広島大学学位請求論文

Search for sub-eV scalar and pseudoscalar fields via four-wave mixing with table-top lasers

(テーブルトップレーザーを用いた四光波混合によるsub-eVスカラー・擬スカラー場の探索)

2016年

広島大学大学院理学研究科
物理科学専攻

長谷部　孝

目次

1. 主論文
Search for sub-eV scalar and pseudoscalar fields via
four-wave mixing with tabletop lasers
(テーブルトップレーザーを用いた四光波混合による sub-eV
スカラー・擬スカラー場の探索)

2. 公表論文
(1) Search for sub-eV scalar and pseudoscalar resonances
via four-wave mixing with a laser collider
Takashi Hasebe, Kensuke Homma, Yoshihide Nakamiya,
Kayo Matsuura, Kazuto Otani, Masaki Hashida,
Shunsuke Inoue, and Shuji Sakabe
Progress of Theoretical and Experimental Physics
073C01 (2015)

3. 参考論文
(1) The first search for sub-eV scalar fields via
four-wave mixing at a quasi-parallel laser collider
Kensuke Homma, Talashi Hasebe, and Kazuki Kume
Progress of Theoretical and Experimental Physics
083C01 (2014)

(2) 真空内四光波混合による sub-eV 中性ボゾンの共鳴探索
本間 謙輔, 長谷部 孝, 久米 一輝, 阪部 周二, 橋田 昌樹
高エネルギーニュース, Vol.32, No.3, (2013) 171-177

主論文

Search for sub-eV scalar and pseudoscalar fields via four-wave mixing with table-top lasers

Takashi Hasebe

Department of Physics Science, Graduate School of Science
Hiroshima University
2016

Abstract

More than 90% of the energy density in the universe is supposed to be occupied by dark matter and dark energy. Hypothetical low mass neutral bosons can be the candidates for such dark components.

For example, the low mass scalar field called dilaton is predicted above neV mass scale as the candidate for origin of dark energy. It predicted by the scalar-tensor theory with Λ (STTΛ) which is one of the alternative gravitational theories. The pseudoscalar field, axion predicted by the quantum chromodynamics (QCD) below sub-eV mass region can be one of the reasonable candidates for cold dark matter. These scalar and pseudoscalar fields may couple to photons via extremely weak interactions. Therefore, search for low mass scalar and pseudoscalar fields with extremely high intensity laser fields has been proposed.

Quasi parallel colliding system (QPS) is a system to produce resonance states of low mass scalar and pseudoscalar fields via photon scatterings in a focusing laser. By focusing two-color lasers on the same optical axis, the frequency-shifted photon is emitted from the focal volume as the signature of the resonance production. This phenomenon is regarded as the four-wave mixing process in vacuum.

In this thesis, a search for scalar and psudoscalar fields via QPS was performed by combining a 9.3 μJ/0.9 ps Ti-Sapphire laser and 100 μJ/9 ns Nd:YAG laser at 2.3×10^{-2} Pa. As a result, no significant signal was observed and the exclusion limits for scalar and psudoscalar fields were obtained below 0.15 eV mass range.

Furthermore, the four-wave mixing process occurring in atoms was observed at an atmospheric pressure. The pressure dependence of the four-wave mixing photons emitted from residual gas in the vacuum chamber were measured. The number of them were negligible at 2.3×10^{-2} Pa.

The experimental methods established in this thesis can be basically applicable to higher intensity laser experiments.

Contents

List of Figures

List of Tables

1 Introduction

1.1 Physics Motivation

Ordinary matter composed of quarks and leptons occupies only 5% of the energy density of our universe. Unknown components called dark energy and dark matter occupy the remaining density. This indicates that modifications of standard theories of cosmology and elementary particle physics are required for describing the true nature of the universe. Therefore, uncovering dark energy and dark matter is one of the most crucial subjects in modern physics.

The existence of dark matter is strongly indicated by a number of astronomical observations. Some reasonable candidates for dark matter are predicted by theories beyond the standard model in particle physics. On the other hand, the mechanism for creating dark energy has not been understood yet. A number of dark energy models have been suggested. However, there is no experimental result strongly supports a specific dark energy model.

Hypothetical low mass neutral bosons can be candidates for these dark components. For example, a scalar type boson called dilaton is predicted above neV mass scale by one of the alternative gravitational theory. Dilaton can be the candidate for the origin of dark energy. Furthermore, a pseudoscalar type boson called axion is predicted below meV mass range by the quantum chromodynamics (QCD) as the reasonable candidate for cold dark matter. Both dilaton and axion are interpreted as Numbu-Goldstone (NB) bosons [1, 2] as a result of spontaneous symmetry breakings occurred in the early universe. Therefore they supposed to be have extremely light masses. They also interact with matter fields very weakly. If these bosons interact with electromagnetic fields, even if only slightly, they can be proved by pumping enormous amount of coherent photons to a local space in the vacuum.

1.2 Dark energy models with scalar fields

The accelerating universe was discovered by observations of redshifts of type Ia supernova[3, 4, 5]. It is supposed that unknown energy called dark energy expands the universe. In modern cosmology, the cosmological constant Λ is interpret as the origin of dark energy.

Based on the assumption that Λ is the vacuum energy at the energy scale of the quantum gravity field, the theoretical value of Λ is estimated as $\Lambda_{\mathrm{vac}} \sim M_P^4 \sim 1$ with Planck units $c = \hbar = M_P = 1$, where Planck mass $M_P = \sqrt{\frac{\hbar c}{8\pi G}} = 2.43 \times 10^{18}$ GeV with the gravitational constant G. On the other hand, the observation value of Λ is $\Lambda_{\mathrm{obs}} \sim 10^{-120}$. This unreasonable deviation is called "cosmological constant problem". Introduced the decaying behavior of $\Lambda \propto t^{-2}$ as a function of time t is an inartificial solution. This is because, the present age of universe $t_0 = 1.37 \times 10^{10}$ years is expressed as $t_0 \sim 10^{60}$ with Planck units.

Scalar-tensor theory with Λ (STTΛ) [6] is the alternative gravitational theory which can solve the cosmological constant problem. In this theory, decaying Λ as t^{-2} is obtained as a result of spontaneous breaking of a conformal symmetry. It predicts a light scalar field "dilaton" as the NB boson as a result of the conformal symmetry breaking. Based on the prediction from STTΛ, dilaton has the extremely light mass $\sim 10^{-9} - 10^{-6}$ eV [7] and interacts with matter via extremely weak coupling as weak as that of gravity. In STTΛ, two photon coupling to a dilaton via quantum anomaly are allowed. Therefore, dilaton can be searched directly via $\gamma\gamma \to \phi \to \gamma\gamma$ process, where γ and ϕ represent photon and dilaton, respectively. Dilaton has been searched indirectly by testing the deviation from the Newtonian gravity at short distances. For example, the modification to the Newtonian gravity as following form has been tested

$$V_r = -G\frac{m_1 m_2}{r}\left(1 + \alpha e^{-r/\lambda}\right), \tag{1}$$

where m_1 and m_2 are masses of samples, α is the strength of the hypothetical potential as compared to the Newtonian potential, and λ is its propagation length.

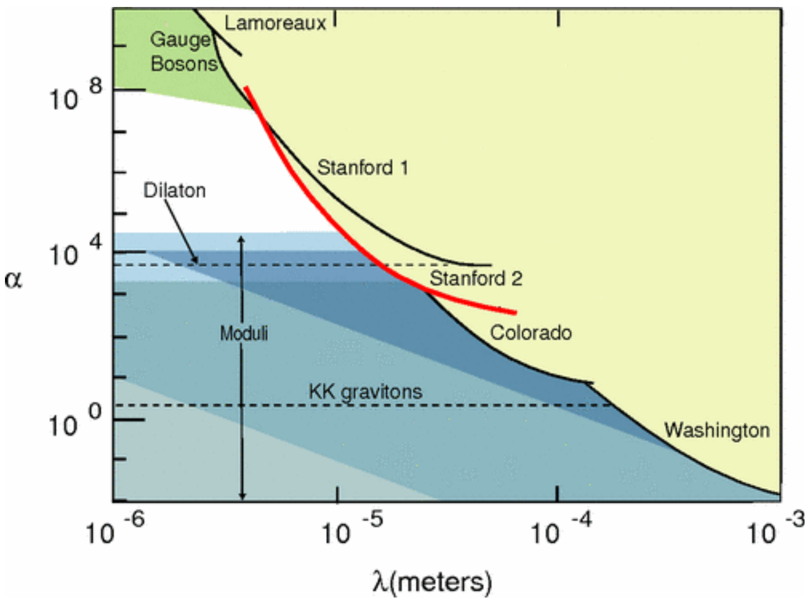

Figure 1. Exclusion limits of non-Newtonian forces in $\alpha - \lambda$ space [8]. The solid lines show upper limits obtained from previous experiments, Casimir force measurements "Lamoreaux"[9] and "Washington"[10], measurements of gravitational force between two bodies at short range "Stanford1"[11] and "Stanford2"[8], and measurement with torsion balance technique "Colorado"[12]. Shaded areas show the rough predictions for the dilaton based on the string theory [13], and KK gravitons which is predicted by extra dimension scenarios [14].

1.3 Search for pseudoscalar field, axion

The pseudoscalar field, "axion"[15, 16] is a possible candidate for cold dark matter [17, 18]. The expected mass scale of axion is $\sim 10^{-6} - 10^{-3}$ eV. Axion is a hypothetical boson introduced in order to solve "strong CP problem". In the QCD theory, the Charge conjugate - Parity (CP) symmetry is not guaranteed. Nevertheless, the CP violation in the QCD are strongly suppressed according to measurements of the electric dipole moment of neutron [19]. To solve this unnaturalness, an additional symmetry called "Peccei-Quinn (PQ) symmetry" [20] is introduced in the QCD Lagrangian. In this scenario, the CP symmetry is realized by spontaneous breaking of the PQ symmetry. As a result, axion appears as a Nambu-Goldstone mode.

Axion can also coupling to two photon as well as dilaton. Therefore axion (σ) has been searched via the $\gamma\gamma \to \sigma \to \gamma\gamma$ process by a number of experiments. For example, solar axion searches [21, 22, 23, 24, 25, 26, 27], searches via vacuum magnetic birefringence [28, 29, 30], light shining through a wall (LSW) [31, 32], and axion dark matter search (ADMX) [33, 34]. The exclusion limits of axion by previous searches are shown in Fig.2.

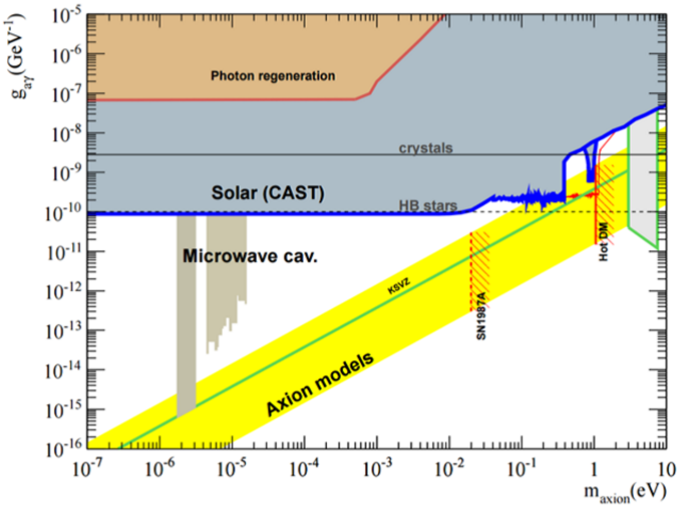

Figure 2. Exclusion limits of axion[35]. The horizontal and vertical axes indicate the mass of axion and the coupling constant between axion and photon, respectively. The brown area represents the exclusion limit by the LSW. The blue lines indicate the limit by the solar axion search experiments. The gray area shows the limit by the microwave cavity search like the ADMX. The yellow band represents the expected area of axion based on the prediction from the KSVZ axion model [36, 37].

Here the experimental strategy of LSW is introduced. The schematic view of experimental setup of LSW is shown in Fig.3.

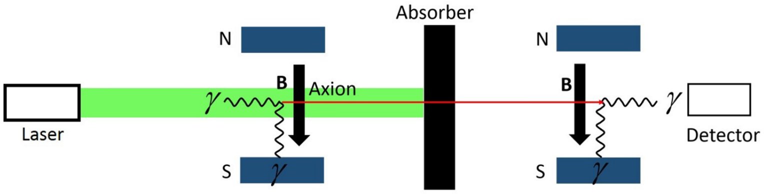

Figure 3. The schematic view of experimental setup of LSW

The LSW searches axion via the $\gamma\gamma \to \sigma \to \gamma\gamma$ process. Two photons at the initial state are provided from a laser and a external magnetic field. The photon propagating in the static magnetic field converts into an axion with a certain probability. The axion can be separated from laser photons by penetrating the absorber placed between two magnets and it converts into photon in the second magnetic fields.

The conversion probability of $\gamma \to \sigma \to \gamma$ is given by

$$P_{\gamma\to\sigma\to\gamma} \propto (gBL)^4 \left(\frac{1 - cos(qL)}{(qL)^2}\right)^2, \tag{2}$$

where $g = \alpha/M_a$ is a coupling constant of $\gamma - \sigma$, $\alpha \sim 1/137$ is the fine-structure constant and M_a is the energy scale parameter corresponding to the PQ symmetry breaking, B is the strength of the magnetic field, L is its length, q is the momentum difference between axion and photon.

1.4 Quasi parallel colliding system

Here a direct search for dilaton-like scalar fields and axion-like pseudoscalar fields by creating the resonance states of them in laboratory is discussed. Photon is a suitable probe for creating resonant states of extremely low mass fields due to zero mass of itself. At head-on photon-photon collisions, the colliding energy at the center- of-mass system E_{CMS} is expressed as 2ω, where ω is the energy of incident photons. When we assume optical photons whose energies are approximately 1 eV, we cannot capturing sub-eV mass resonances in head-on collisions.

Quasi parallel colliding system (QPS) [39, 40] is the system to realize the low colliding energy by colliding photons at small incident angles. The center-of-mass energy is expressed as

$$E_{\mathrm{CMS}} = 2\omega \sin\vartheta, \tag{3}$$

where ϑ is half of the incident angle of the photon pair. By introducing small ϑ, the colliding system to create resonances below sub-eV mass range is achieved. It is possible to realize the QPS by focusing a laser at a long focal length. In this method, search for scalar (ϕ) and pseudoscalar (σ) fields are performed by observing the $\gamma\gamma \to \phi/\sigma \to \gamma\gamma$ process.

In the QPS, the enhancement of the scattering rate is given by introducing another coherent field to stimulate the two photon decay of the resonance field. The initial and final states photons follow the energy conservation

$$\omega + \omega \to (2-u)\omega + u\omega \tag{4}$$

where ω is the energy of photon which create a resonance, $u\omega$ is the energy of photon which induces the resonance decay with $0 < u < 1$. The photon whose energy is $(2-u)\omega$ is emitted as the signature of the resonance decay. The schematic view of the QPS is illustrated in Fig.4.

The similar relation in Eq.(4) is applied to the "four-wave mixing" process which is the third-order nonlinear quantum optical process in atoms [41, 42]. Therefore, search for low mass fields via QPS by combining two-color lasers is regarded as observing the four-wave mixing process in the vacuum. The four-wave mixing measurement in the vacuum is also used as a method for testing photon-photon scattering via nonlinear QED effects in different collision geometry [43, 44, 45, 46] .

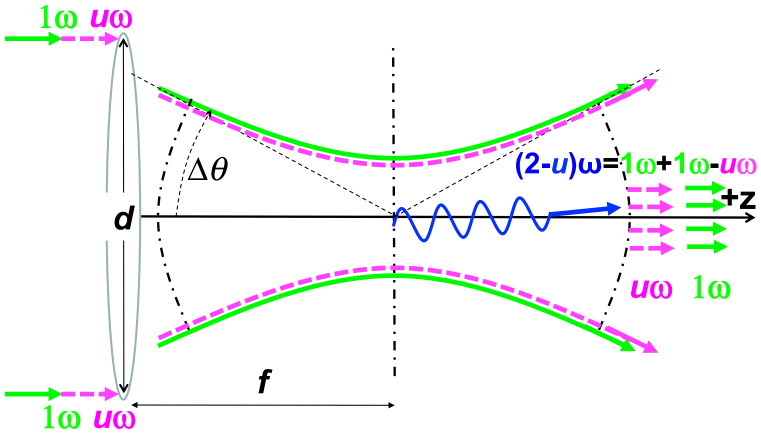

Figure 4. The schematic view of QPS. The photons to create resonance state are provided from the creation laser which is drawn by green. The inducing laser drawn by magenta induce the decay of resonances. The inducing laser is combined on the same optical axis of the creation laser. The parameters d, f, $\Delta\vartheta$ denote the beam diameter, the focal length, the upper range of incident angles of photons, respectively. The signal photon (blue) is emitted from the focal volume as a result of the exchanging of a resonance field via two photons scattering process [40].

The QPS has the characteristics that the signal yield has ${N_\gamma}^3$ dependence by the inducing mechanism, where N_γ is the number of photon per laser pulse. With taking the rapid developments of high intensity lasers into account, N_γ^3 dependence become prominent at experiments with higher intensity lasers. It encourage us to search unknown fields by QPS with laser fields.

1.4.1 Kinematics of QPS

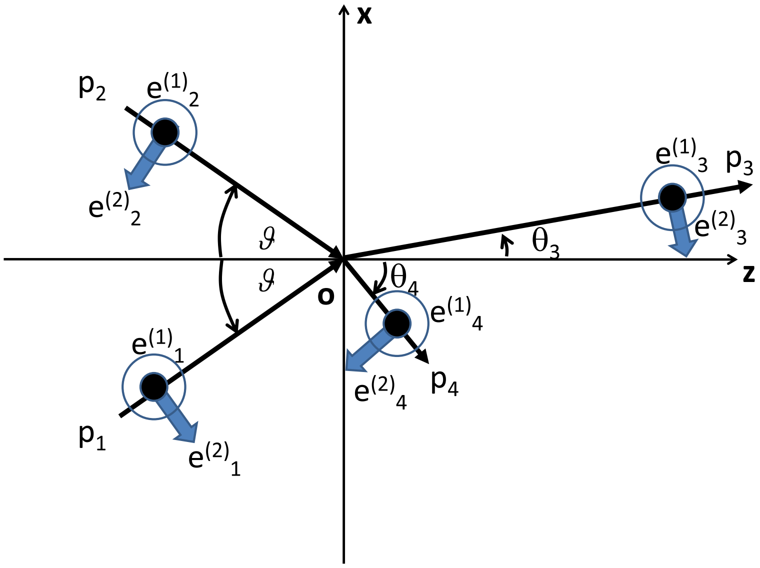

Figure 5. The definitions of kinematics variables in QPS [40].

The variables to describe the kinematics of QPS are introduced as illustrated in Fig.5. The 4-momentum vectors of incident photons p_1 and p_2 are defined on the z-x plane as follows:

$$p_1 = (\omega \sin\vartheta, 0, \omega \cos\vartheta; \omega), \tag{5}$$

$$p_2 = (-\omega \sin\vartheta, 0, \omega \cos\vartheta; \omega). \tag{6}$$

The energy conservation is expressed as

$$\omega + \omega = (2-u)\omega + u\omega, \tag{7}$$

where u is an arbitrary number which satisfies $0 < u < 1$. Then, the energies of final state photons are re-defined as follows:

$$\omega_3 \equiv (2-u)\omega, \tag{8}$$

$$\omega_4 \equiv u\omega, \tag{9}$$

where ω_3 and ω_4 are energies of a pair of final state photons The momenta of a pair of final state photons p_3 and p_4 are expressed as

$$p_3 = (\omega_3 \sin\theta_3, 0, \omega_3 \cos\theta_3; \omega_3), \tag{10}$$

$$p_4 = (-\omega_4 \sin\theta_4, 0, \omega \cos\theta_4; \omega_4). \tag{11}$$

The relation of linear polarization states between initial and final state photons correlates the property of the exchanged resonance. In the case of scalar field exchange, the relations of linear polarizations when all wave vectors are on the same plane are expressed as

$$\begin{aligned} \omega\{1\} + \omega\{1\} &= \omega_3\{1\} + \omega_4\{1\}, \\ \omega\{1\} + \omega\{1\} &= \omega_3\{2\} + \omega_4\{2\}, \end{aligned} \tag{12}$$

where {1} and {2} denote linear polarization states orthogonal each other. In the case of pseudoscalar field exchange, the relations of linear polarizations are expressed as

$$\begin{aligned} \omega\{1\} + \omega\{2\} &= \omega_3\{1\} + \omega_4\{2\}, \\ \omega\{1\} + \omega\{2\} &= \omega_3\{2\} + \omega_4\{1\}. \end{aligned} \tag{13}$$

The linear polarization relations in Eq.(12) and Eq.(13) are applicable to the situation that all momentum vectors of photons are on the same reaction plane. In a focusing laser, the incident $p_1 - p_2$ reaction plane and the outgoing $p_3 - p_4$ plane rotate independently. Therefore, even if a {1}-polarized incident laser is provided at an actual experimental situation, the incident $p_1 - p_2$ plane rotates from the fixed {1}-polarized plane in the focal region. As a result, the focused QPS has sensitivity to both scalar and pseudoscalar fields simultaneously, even though we fix the linear polarization state of incident laser before focusing. Hence, the sensitivity for scalar and pseudoscalar fields are evaluated by introducing the incident plane rotation factor $\mathcal{G}$. The evaluation of $\mathcal{G}$ is discussed in Appendix A of this thesis.

1.4.2 Mechanism for inducing effect

The Feynman diagram of the $\gamma\gamma \to \phi/\sigma \to \gamma\gamma$ process is shown in Fig.6. The effective interaction Lagrangians coupling between two photons and ϕ / σ are expressed as

$$-L_\phi = gM^{-1}\frac{1}{4}F_{\mu\nu}F^{\mu\nu}\phi, \quad -L_\sigma = gM^{-1}\frac{1}{4}F_{\mu\nu}\tilde{F}^{\mu\nu}\sigma, \tag{14}$$

where M is the energy scale parameter and g is the coupling constant, F is the electro magnetic tensor and $\tilde{F}$ is its duel.

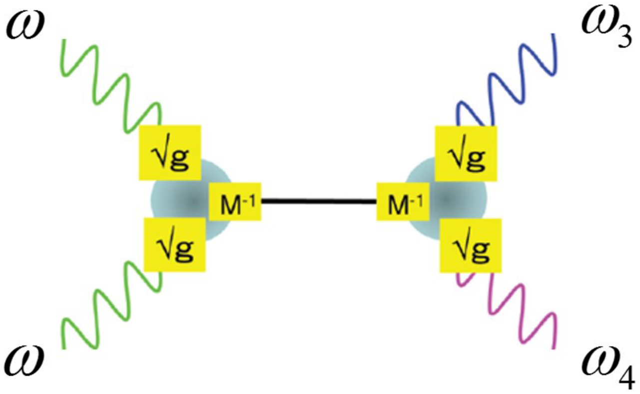

Figure 6. The Feynman diagram of the $\gamma\gamma \to \phi/\sigma \to \gamma\gamma$ process.

The photon-photon scattering probability is enhanced in the background coherent field as following mechanism. The Feynman amplitude of the $\gamma\gamma \to \phi/\sigma \to \gamma\gamma$ process as shown in Fig.6 is expressed as

$$V_2\left((p_1+p_2)^2+m^2\right)^{-1}V_1. \tag{15}$$

where V_1 and V_2 are the matrix elements at the first and second vertices, respectively. Based on the interaction Lagrangian of the scalar filed exchange, V_1 and V_2 are expressed as

$$\begin{aligned} V_1 &= \frac{g}{M}\langle 0|F_{\mu\nu}|p_1\rangle\langle 0|F^{\mu\nu}|p_2\rangle, \\ V_2 &= \frac{g}{M}\langle p_3|F_{\mu\nu}|0\rangle\langle p_4|F^{\mu\nu}|0\rangle. \end{aligned} \tag{16}$$

We now simplify the expression of $\langle 0|F_{\mu\nu}|p_1\rangle$ as

$$\langle 0|a|p_1\rangle = 1, \tag{17}$$

by introducing the creation operator a and the annihilation operator $a^\dagger$. This description is applied in one photon state. In the case of coherent photons state, Eq.(17) substitute for

$$\langle\langle p_1, N|a|p_1, N\rangle\rangle = \sqrt{N}, \tag{18}$$

where N is the number of photons in the coherent state. In the case that the incident photons are provided from the coherent laser, V_1 is re-expressed as

$$V_1 = \frac{g}{M}\langle\langle p_1, N|F_{\mu\nu}|p_1, N\rangle\rangle\langle\langle p_2, N|F^{\mu\nu}|p_2, N\rangle\rangle. \tag{19}$$

It obtains the enhancement of N compared with Eq.(16). The similar enhancement mechanism can be applied at the second vertex V_2 when the inducing laser field is provided. If the momenta of inducing photons are equivalent to p_4, V_2 is expressed as follows:

$$V_2 = \frac{g}{M}\langle p_3|F_{\mu\nu}|0\rangle\langle\langle p_4, N|F^{\mu\nu}|p_4, N\rangle\rangle. \tag{20}$$

As compared to the second line of Eq.(16), V_2 in Eq.(20) obtains the enhancement of $\sqrt{N}$. Therefore the scattering rate has the enhancement of $\sqrt{N}^2 = N$ by the effect of the inducing laser field.

1.4.3 The effect of averaging the squared scattering amplitude

In general, the resonance of a particle is produced when the center-of-mass energy of a collision E_{CMS} is equivalent to the mass of a resonance m. The mass of a resonance has the finite width duo to the uncertainty principle and the mass distribution takes the Breit-Wigner resonance distribution. At the Breit-Wigner distribution, the value of the full width at half maximum takes $\Gamma = \hbar/\tau$, where τ is the lifetime of the resonance. Therefore, the resonance condition is satisfied when E_{CMS} is included in the mass range of the resonance.

In the case of QPS, we now define the experimental parameters which satisfy the following resonance condition.

$$E_{\mathrm{CMS}} = 2\omega_r \sin\vartheta_r = m. \tag{21}$$

Based on the interaction Lagrangian at Eq.(14), the squared scattering amplitude in the s-channel $|\mathcal{M}_s|^2$ at the $\gamma\gamma \to \phi/\sigma \to \gamma\gamma$ process is expressed as

$$|\mathcal{M}_S|^2 \approx (4\pi)^2 \frac{a^2}{\chi^2 + a^2}. \tag{22}$$

with $\chi = \omega - \omega_r$.
a is defined as

$$a = \frac{\omega_r^2}{8pi}\left(\frac{gm}{M}\right)^2 = \frac{m\Gamma}{2\sin{\vartheta_r}^2}, \tag{23}$$

with

$$\Gamma = \frac{1}{16\pi}\left(\frac{g}{M}\right)^2 m^3. \tag{24}$$

When capturing the resonance of the low mass and weak coupling fields, the resonance width Γ becomes extremely narrow due to its small values of g/M and m. Therefore, satisfying the resonance condition is quite difficult, if E_{CMS} takes a unique value at a individual collision like charged particle collisions. In the case of the off-resonance condition, in fact, $\chi \gg a$ duo to the small value of M^{-1}, $|\mathcal{M}_S|^2$ is strongly suppressed since $a^2 \propto M^{-2}$.

In QPS, however, the momentum vectors of photons fluctuate around its diffraction limit according to the uncertainty principle. The fluctuation appears as the uncertainty of the incident angle of photon ϑ. Therefore, E_{CMS} at QPS intrinsically has the uncertainty, even through it is a single collision. Thus, the quite narrow resonance can be captured if E_{CMS} includes the mass of the resonance in its fluctuation range.

Considering the uncertainty of the incident angles of the photons, the squared amplitude should be averaged over the possible incident angles as follows:

$$\overline{|\mathcal{M}_S|^2} = \int_0^{\pi/2} \rho(\vartheta)|\mathcal{M}_S(\vartheta)|^2 d\vartheta, \tag{25}$$

where $\rho(\vartheta)$ is the angler distribution of incident two photons in the Gaussian beam. $\rho(\vartheta)$ is expressed as

$$\rho(\vartheta) = \frac{2}{\sqrt{\pi}\Delta\theta} \exp\left\{-\left(\frac{\vartheta}{\Delta\theta}\right)^2\right\}, \tag{26}$$

where ϑ is the angle between a pair of incident photons, $\Delta\theta = d/2f$ is the possible maximum incident angle, and ϑ is given as

$$\vartheta = \frac{1}{2}|\theta_1 - \theta_2| \tag{27}$$

with the incident angle of single photon θ_1 and θ_2. Then, Eq.(25) is rewritten as follows:

$$\overline{|\mathcal{M}_S|^2} = \frac{(4\pi)^2}{\sqrt{\pi}\omega^2}\left(\frac{\vartheta_r}{\Delta\theta}\right) a\mathcal{W}, \tag{28}$$

with

$$\mathcal{W} \sim \frac{\pi}{2} \exp\left\{-\left(\frac{\vartheta_r}{\Delta\theta}\right)^2\right\}. \tag{29}$$

In Eq.(28), $\overline{|\mathcal{M}_S|^2}$ has a dependence but not a^2 dependence as shown in Eq.(22). We find that $a \propto M^2$ enhancement is obtained by operating the averaging process originating from the angler ambiguity of the incident photons. .

1.4.4 Coupling-mass relation

The signal yield $\mathcal{Y}$ is expressed with experimental parameters as follows:

$$\begin{aligned}\mathcal{Y} &= \frac{1}{64\sqrt{2}\pi^4}\left(\frac{\lambda_c}{c\tau_c}\right)\left(\frac{\tau_c}{\tau_i}\right)\left(\frac{f}{d}\right)^3 \tan^{-1}\left(\frac{\pi d^2}{4f\lambda_c}\right)\frac{(\overline{u}-\underline{u})^2}{\overline{u}\underline{u}} \\ &\times \left(\frac{gm[\mathrm{eV}]}{M[\mathrm{eV}]}\right)^2\left(\frac{m[\mathrm{eV}]}{\omega[\mathrm{eV}]}\right)^3 \mathcal{W}\mathcal{G}\mathcal{F}_s C_{\mathrm{mb}} {N_c}^2 N_i, \end{aligned} \tag{30}$$

where the subscripts c and i indicate the creation and inducing lasers, respectively, λ is the wavelength, τ is the pulse duration, f is the focal length, d is the beam diameter, $\overline{u}$ and $\underline{u}$ are the upper and lower values on u determined by the spectrum width of ω_4, respectively, $\mathcal{W} \sim \pi/2$ is the numerical factor relevant to the integral of the weighted resonance function, $\mathcal{G}$ is the incident plane rotation factor , $\mathcal{F}_{\mathcal{S}}$ is the polarization dependent axially asymmetric factor originated from rotation of $p_3 - p_4$ plane (the detail of evaluation of $\mathcal{G}$ and $\mathcal{F}_S$ are described in Appendix A and B of this paper), $C_{\mathrm{mb}} = 1/2$ is the combinatorial factor originating from selecting a pair of photons among multimode frequency states and N is the average numbers of photons in the coherent state. The detail of the formulation of the signal yield is summarized in Appendix D of this paper. The coupling constant g/M is expressed as

$$\frac{g}{M[\mathrm{eV}]} = 2^{1/4}8\pi^2\sqrt{\frac{\mathcal{Y}\omega^3[\mathrm{eV}]}{\left(\frac{\lambda_c}{c\tau_c}\right)\left(\frac{\tau_c}{\tau_i}\right)\left(\frac{f}{d}\right)^3\tan^{-1}\left(\frac{\pi d^2}{4f\lambda_c}\right)\frac{(\overline{u}-\underline{u})^2}{\overline{u}\underline{u}}\mathcal{W}\mathcal{G}\mathcal{F}_s C_{\mathrm{mb}} {N_c}^2 N_i}}\, m^{-5/2}[\mathrm{eV}]. \tag{31}$$

1.5 Four-wave mixing process in atoms

A four-wave mixing process is the nonlinear quantum optical process occurs via interactions between electric fields and matter. Atoms polarize when electric fields are applied. The polarizability of atoms have non-linearity in strong electric fields as follows:

$$\boldsymbol{P} = \epsilon_0(\chi^{(1)}\boldsymbol{E} + \chi^{(2)}\boldsymbol{E}^2 + \chi^{(3)}\boldsymbol{E}^3 + \cdots), \tag{32}$$

where $\boldsymbol{P}$ is the polarizability of atom, ϵ_0 is the permittivity of vacuum, $\chi^{(i)}$ is the i-th-order nonlinear susceptibility with $i = 1, 2, 3\cdots$, and $\boldsymbol{E}$ is the strength of electric field. Incident photons induce an oscillating dipole moment in atom and the induced dipole moment radiates other photon fields.

The four-wave mixing is the third-order nonlinear process. The incident wave includes three separated frequencies, ω_1, ω_2, and ω_3 generates a new wave at ω_4 in polarized materials. The relation of the frequencies between incident and generated photons is expressed as

$$\omega_1 + \omega_2 - \omega_3 = \omega_4. \tag{33}$$

The energy diagram of the four-wave mixing process is drawn in Fig.7.

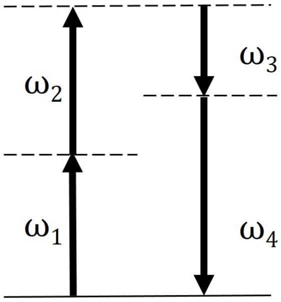

Figure 7. The energy diagram of four-wave mixing process.

When the frequencies of two absorbed photons have the relation of $\omega_1 = \omega 2$, this process is specially called "degenerate four-wave mixing", then, Eq.(33) is rewritten as

$$2\omega - \omega_3 = \omega_4, \tag{34}$$

with $\omega = \omega_1 = \omega_2$. This equation is similar to the energy conservation of the resonance production at QPS with two-colors laser fields expressed in Eq.(7). Therefore, the photons generated via the degenerate four-wave mixing process in atoms can be the background source at the unknown fields search in QPS.

The intensity of the generated photon by the degenerate four-wave mixing process, $\omega_4 = 2\omega_1 - \omega_2$ at the plane waves condition is expressed [38] as

$$I_4 = \frac{576\pi^6 {|\chi^{(3)}|}^2}{{n_1}^2 n_2 n_4 {\lambda_4}^2 c^2} {I_1}^2 I_2 \frac{L^2 \sin^2(\Delta k L/2)}{{(\Delta k L/2)}^2}, \tag{35}$$

where I_i is the intensity of photons at frequency ω_i, n_i is the reflective index at ω_i, L is the interaction length, and Δk is the phase matching factor $\Delta k = k_4 - (2k_1 - k_2)$ with the wavenumber at ω_i.

I_4 has the cubic dependence of the strength of incident photon fields as $I_4 \propto {I_1}^2 I_2$, which is similar to the laser pulse energy dependence of the signal yields at the QPS with two-colors laser fields shown in Eq.(30).

1.6 Step-by-step searches in QPS

The concept for scalar and pseudoscalar fields search in QPS has been already advocated [39, 40]. However, the verification of the practical experimental approach is still developing. Therefore, thrashing out problems by increasing the laser intensities in step by step is important.

In QPS, the signal photon is emitted to the same optical axes of two-color lasers. Therefore, for example, if we use 1 J pulse laser, the signal photon has to be separated from $\sim 10^{18}$ photons per pulse. We developed the optical system of QPS for the first time at Hiroshima university in 2014 [48] . The schematic view of the optical system is shown in Fig.8.

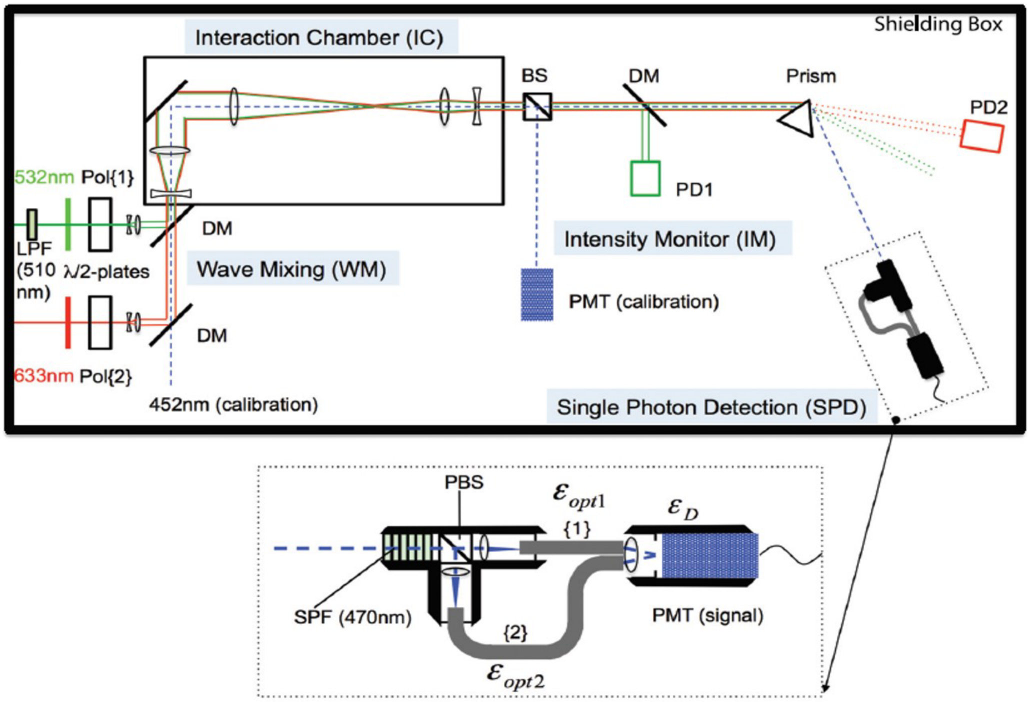

Figure 8. The schematic view of the experimental setup search for scalar fields by QPS [48].

We used a 0.2μJ/0.75 ns pulse laser as the creation laser which provides the initial photons create resonances and a 2 mW CW laser as the inducing laser which induces the decay of resonances. The wavelengths of the creation and inducing lasers are 532 nm and 633 nm, respectively. The wavelength of signal photon is 459 nm. Therefore, 452 nm CW laser is used as the calibration source to determine the trajectory of the signal photon.

The creation and inducing lasers are combined by the dichroic mirror (DM) and they focused in the vacuum chamber. Then, both lasers are separated from signal waves by the prism and the photomultiplier tube (PMT) is placed on the trajectory of the signal photon. Optical filters to cut the creation and inducing photons are place in front of the PMT.

The scalar fields search was performed at 1.2×10^{-4} Pa with approximately 6.0×10^{-8} shot statistics. The leak photons from the creation and inducing lasers were suppressed at a level of less than 10^{-4} photons per pulse. Furthermore, no significant four-wave mixing signal is observed. From this pilot search experiment, we confirmed that the experiment setup for detect the four-wave mixing signal with 1 photon sensitivity is feasible. Figure 9 shows the exclusion limit of scalar fields obtained at a 95% confidence level.

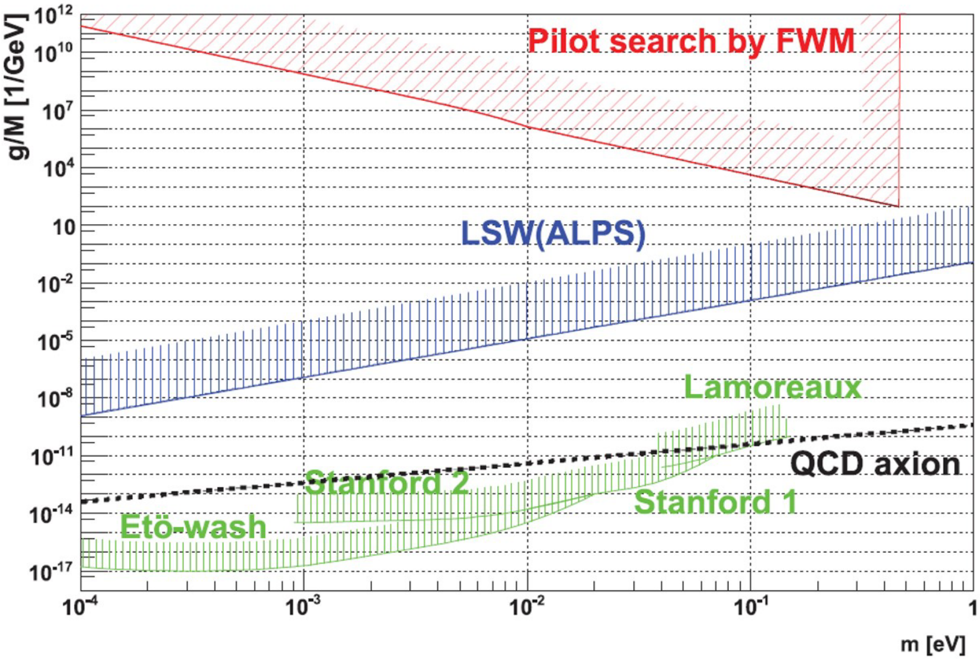

Figure 9. Exclusion limits for scalar fields are shown in m - g/M space [48], where m is the mass of the scalar field and g/M is the coupling constant to photon. The red shaded area indicates the exclusion limit by the pilot search by the QPS at a 95% confidence level. The blue shaded area represents the exclusion limit of scalar fields by LSW experiment "ALPS". The green shaded areas show the exclusion limits by non-Newtonian force measurements introduced in section 1.2. The expected line of axion is drawn by the black dotted line as a reference for future pseudoscalar search.

1.7 Aim of the thesis

The first search for scalar fields by QPS was performed with weak intensity lasers, thus, the effect of the four-wave mixing process in atoms was negligible. However, the atomic four-wave mixing process can be the main background source in the future search with higher intensity lasers.

In this thesis, a search experiment performed at Kyoto university with much higher beam intensities than that of the pilot search. In this experiment, the four-wave mixing photons originating from the residual gas are anticipated due to the higher beam intensities. This thesis gives the experimental methods to obtain the exclusion limits of scalar and pseudoscalar fields under the circumstance where a finite amount of background photons must be evaluated.

2 Experimental setup

2.1 Overview

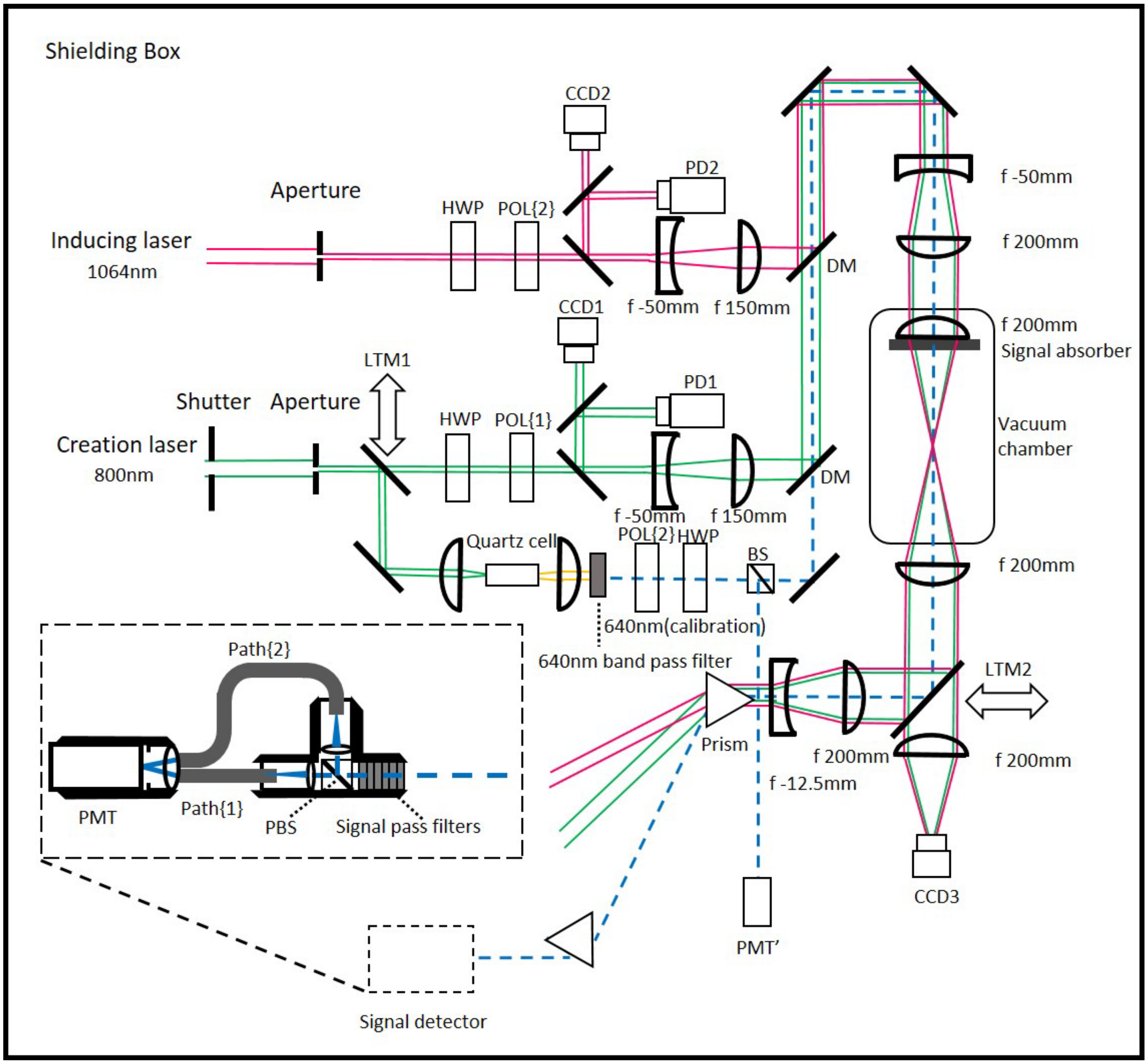

Figure 10. Schematic view of the experimental setup for the scalar and pseudoscalar fields search.

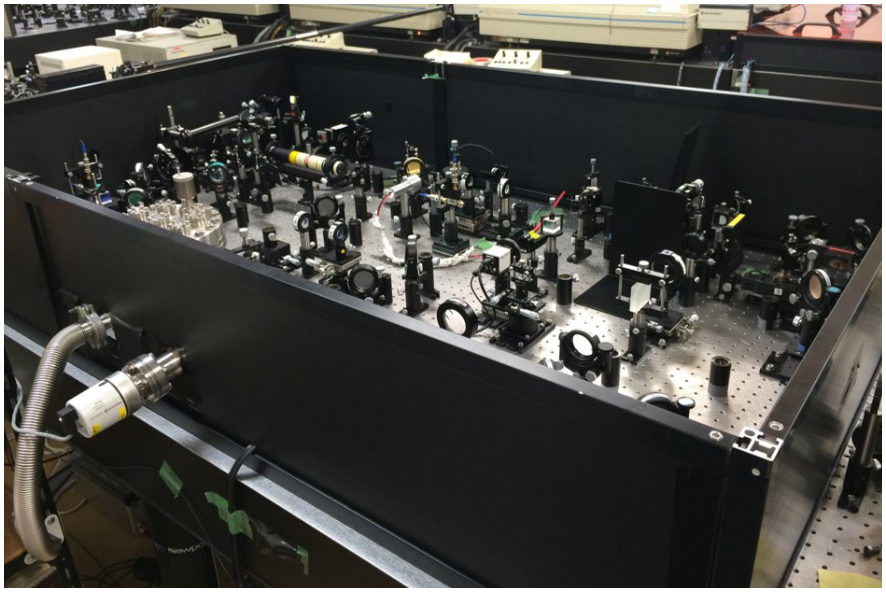

Figure 11. The picture of the optical systems.

Figure 10 illustrates the experimental setup for scalar and pseudoscalar fields search. A mode-locked Ti-sapphire laser, wavelength $\lambda_c = 800$ nm, and a Q-switched Nd:YAG laser, wavelength $\lambda_i = 1064$ nm are used as the creation and inducing lasers, respectively. The linear polarization states of the creation and inducing lasers are adjusted by polarization angles of the linear polarizers "POL$\{1\}$" and "POL$\{2\}$", respectively. POL$\{1\}$ and POL$\{2\}$ transmit only $\{1\}$ and $\{2\}$-polarization components, respectively, where $\{1\}$ and $\{2\}$ are linear polarization states orthogonal each other. The half wave plate (HWP) placed on each beam line rotates the linear polarization angle of each beam, and rotation angles of them are fixed as transmitted lights from POL$\{1\}$ and POL$\{2\}$ are maximized.

The linear polarization vectors of the creation and inducing lasers are orthogonal because the number of the four-wave mixing photons in atoms are minimized when the polarization vectors of the two incident lasers are orthogonal each other. At this condition, the polarization relation between the initial and final state photons for the scalar field exchange in the focusing laser fields is expressed as

$$\omega\{1\} + \omega\{1\} = \omega_3\{2\} + \omega_4\{2\}. \tag{36}$$

In the case of the pseudoscalar field exchange, the relation is written as

$$\omega\{1\} + \omega\{2\} = \omega_3\{2\} + \omega_4\{1\}. \tag{37}$$

Thus, the polarization state of ω_4 depends on the property of the resonance.

Figure 12. The pictures of the creation laser (left: Hurricane, manufactured by Spectra-Physics) and the inducing laser (right: GCR350, manufactured by Spectra-Physics).

The beam profiles of the creation and inducing lasers are shaped to Gaussian-like profiles by going through the beam apertures with approximately 2mm clear apertures. Then a few percents of photons in lasers are split and the photo diodes "PD1" and "PD2" monitor the beam energies of the creation and inducing lasers, respectively, and CCD cameras "CCD1" and "CCD2" monitor the beam alignments of them, respectively.

The beam diameters of them are expanded to approximately 5 - 6 mm by the telescope on each beam line, and they are combined with the dichroic mirror (DM) and the beam diameters are expanded to approximately 20 mm by the common telescope. The combined beam is guided into the vacuum chamber and focused by the convex lens at a 200 mm focal length.

The signal absorber consists of five optical filters which absorb below 750 nm wavelength photons is placed in front of the convex lens in the vacuum chamber. It eliminates the background photons emitted from the optical components.

The agreement of the optical axes between the creation and inducing lasers are ensured at a precision of 2-3 μm by adjusting the focal spots of them at the near side and the far side of the interaction point with CCD camera.

The center of wavelength of the signal photon λ_s is evaluated as

$$\lambda s = \frac{\lambda i \lambda c/2}{\lambda i - \lambda c/2} = 641\text{nm}. \tag{38}$$

To make sure the detection efficiency and the trajectory of the signal photons, the calibration light, $\lambda = 640$ nm, is combined to the same optical axes of the creation and inducing lasers. The 640nm calibration light is pick up from the white light source created by "self phase modulation (SPM)", which is the third-order nonlinear quantum optical effect occurring by alteration in the refractive index which has the dependence of the electric field strength. Now SPM effect is given by focusing the creation laser to the quartz cell target filled with water as shown in Fig.13. As a result, the energy spectrum of the creation laser has a broadening effect by SPM. The 640nm light is obtained from the white light source by placing the band pass filter which transmits 640 ± 5 nm photons. The beam splitter (BS) splits the calibration light evenly and the photomultiplier tube (PMT') monitors the beam energy of the calibration light. Whether the creation laser is guided into the vacuum chamber or the quartz cell to produce the calibration light is selected by switching the linear translation mirror (LTM1).

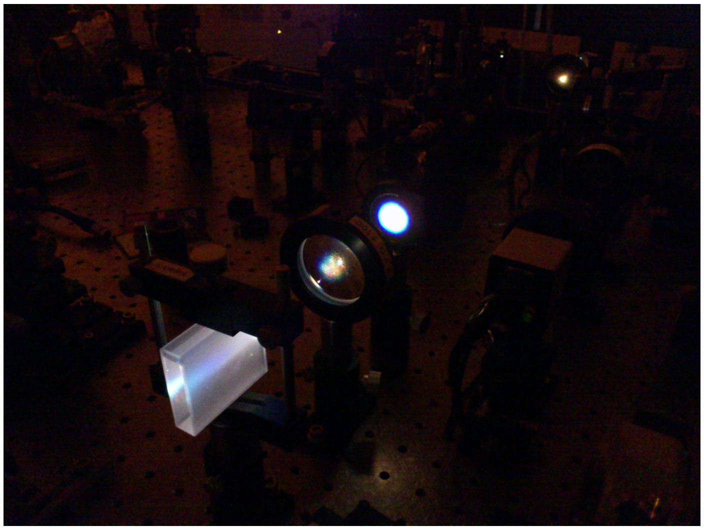

Figure 13. White light are emitted by focusing the creation laser in the quartz cell filled with water.

The linear translation mirror (LTM2) switches the beam line of the combined beam whether the beam goes to the signal detector or the CCD camera (CCD3). The agreement of the focal spots of the creation and inducing lasers are confirmed by monitoring the images of beam spots by CCD3 before and after the physics run.

The combined beam and signal photons are separated by a pair of prism and the signal detector is placed on the trajectory of the signal photons.

The signal pass filters which transmit 580 - 690 nm wavelength photons are set to eliminate residual photons from the creation and inducing lasers. The polarization beam splitter (PBS) split the signals to $\{1\}$- polarized and $\{2\}$-polarized components, respectively. The $\{1\}$-polarized and $\{2\}$-polarized signals through the short (Path$\{1\}$) and the long (Path$\{2\}$) optical fiber paths, respectively, with having a 23ns of time delay. Then photons from each path enter a common photo device. A single-photon-sensitive photomultiplier tube (PMT; R7400-01, manufactured by HAMAMATSU) is used as the signal detector.

2.2 Data acquisition trigger

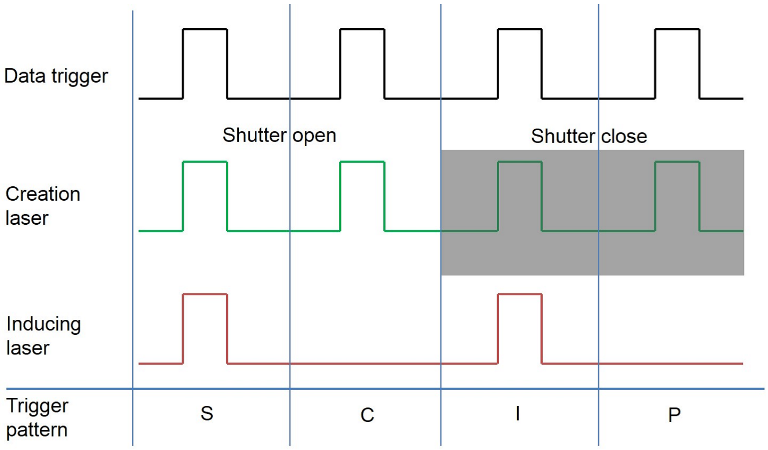

Figure 14. The image of the trigger logic

The repetition rate of the creation and inducing lasers are 1 kHz and 10 Hz, respectively. The coincidence of the pulse timing of them is adjusted so that the yields of the four-wave mixing photons emitted from gas in the focal volume are maximized. The shutter is placed on the beam line of the creation laser and it repeats open and close every 5 seconds. The image of the trigger logic is illustrated in Fig.14. The 20 Hz data acquisition trigger synchronizes to both pulses and it makes four trigger patterns, which are "the both lasers are incident (S)", "only the creation laser is incident (C)", "only the inducing laser is incident (I)", and "neither lasers is incident (P)". A digital oscilloscope records the waveform data from PD1, PD2 and PMT triggered by the data acquisition trigger.

3 Waveform analysis

3.1 Peak finding algorithm

The recorded waveform data from the PMT consists of 500 sampling points p_1 - p_{500} in 200 ns time range. Peak structures originating from observed photons are searched by a peak finding algorithm. The algorithm is operated as following steps:

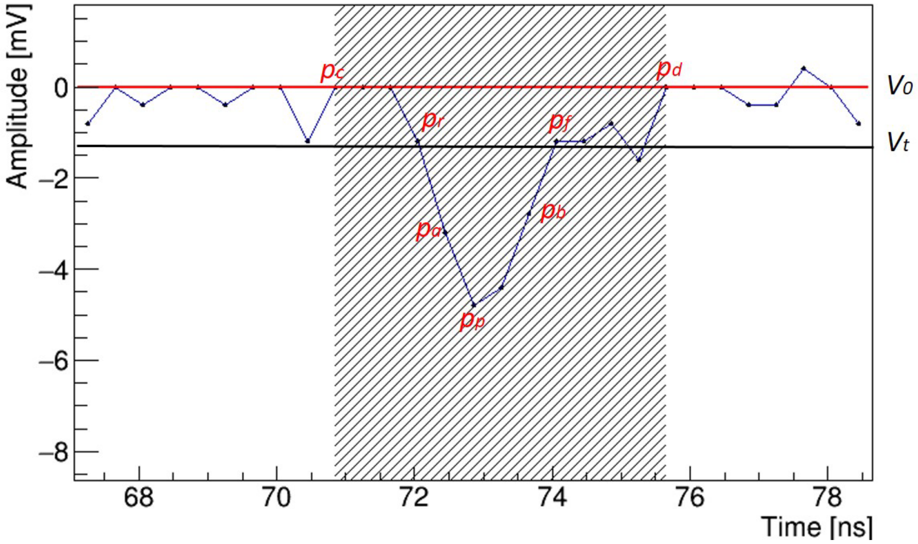

Figure 15. The waveform example to show peak finding procedures. The red horizontal line indicates the pedestal value and the black horizontal line means the threshold value for peak finding. The gray shaded area shows the integral range to evaluate the charge sum.

1. The pedestal value V_0 is defined as the average voltage of p_1 - p_{100} and p_{400} - p_{500}.
2. Set a threshold voltage V_t and search points p_a and p_b satisfy the following requirements:
   $V_\mathrm{t} - V_0 < V_{p_{(\mathrm{a}-1)}}$ and $V_{p_\mathrm{a}} \geq V_\mathrm{t} - V_0$,
   $V_\mathrm{t} - V_0 \leq V_{p_\mathrm{b}}$ and $V_{p_{(\mathrm{b}+1)}} > V_\mathrm{t} - V_0$.
3. Find the point p_p which has the minimum voltage from p_a to p_b and regard p_p as a peak point.
4. Search points p_r and p_f which satisfy following conditions:
   $1/2(V_{p_\mathrm{p}} - V_0) \geq V_{p_\mathrm{r}}$ and $V_{p_{(\mathrm{r}+1)}} < 1/2(V_{p_\mathrm{p}} - V_0)$,
   $1/2(V_{p_\mathrm{p} - V_0}) < V_{p_{(\mathrm{f}-1)}}$ and $V_{p_\mathrm{f}} \geq 1/2(V_{p_\mathrm{p}} - V_0)$.
5. Define points p_c and p_d as below:
   $\mathrm{c} = 2(\mathrm{p} - \mathrm{r}) - 1$ and $\mathrm{d} = 2(\mathrm{f} - \mathrm{p}) + 1$.

Then, the peak structure is defined as data points from p_c to p_d. The charge sum of the peak structure Q is calculated as

$$Q = \sum_{n=c}^{d} \frac{(V_{p_\mathrm{n}} - V_0)\,\Delta t}{R}, \tag{39}$$

where $\Delta t = 0.4$ ns is the time interval between V_n and $V_{\mathrm{n}+1}$, and $R = 50\ \Omega$ is the impedance. The charge sum of the peak structure is converted into the unit of the number of photons by dividing it from the single-photon equivalent charge.

3.2 Noise event subtraction

The recorded data contains some noisy waveforms originating from the ambient noises in the laboratory. These noisy waveforms should be removed before search photon-like peaks because the noises could be misidentified as photon-like peak structures.

The noisy waveforms are identified by analyzing the frequencies of the waveforms since the frequencies of noise events tend to be lower than those of normal events. The frequencies are estimated by counting the nodes, which is defined as the intersection between a waveform and the average line of amplitudes within the 200ns time window.

Figure 16 shows the distributions of the number of nodes for trigger patterns S, C, I, and P. A waveform the number of node is lower than 150 is defined as a noise event. The typical waveforms identified as noisy and normal events are shown in Fig.17.

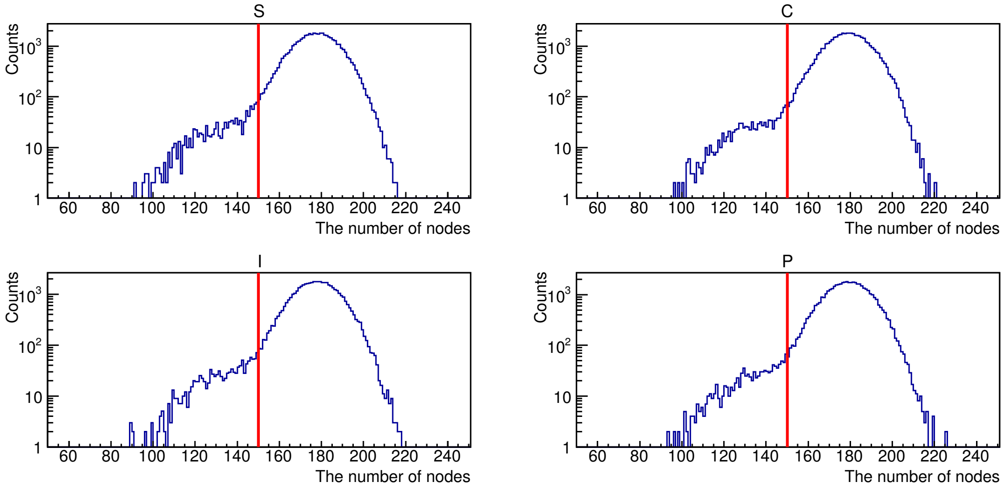

Figure 16. The distributions of the number of nodes for trigger patterns S, C, I, and P [47]. The red vertical lines indicate the boundary of 150 nodes. All trigger patterns have similar distributions.

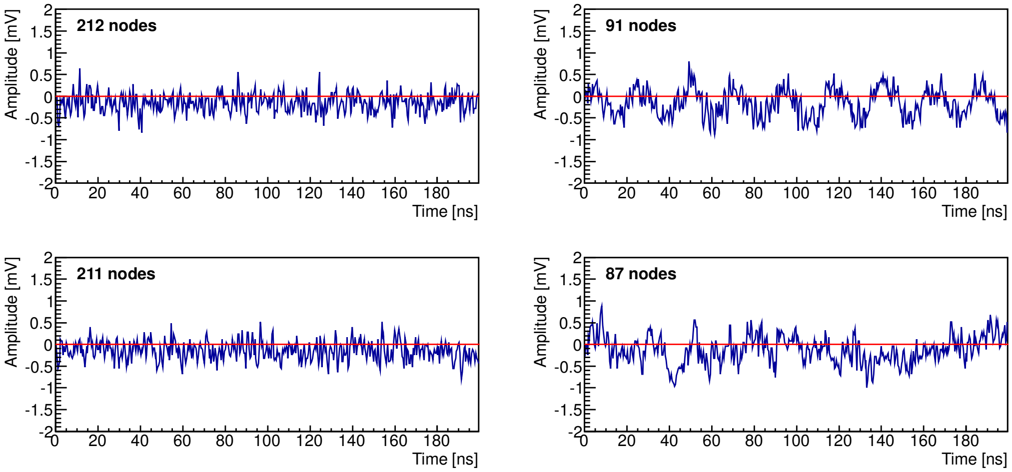

Figure 17. The two panels on the left and right sides show the example of waveforms identified as normal and noise events, respectively [47]. The red horizontal lines indicate the averages of the amplitudes of 500 sampling points in each waveform.

3.3 Trigger pattern selection

The beam energies of the creation and inducing lasers are monitored by photo diodes PD1 and PD2, respectively. The trigger pattern is classified according to the charge correlation between the waveforms from PD1 and PD2. The waveform examples from PD1 and PD2 are shown in Fig.18 and Fig.19, respectively.

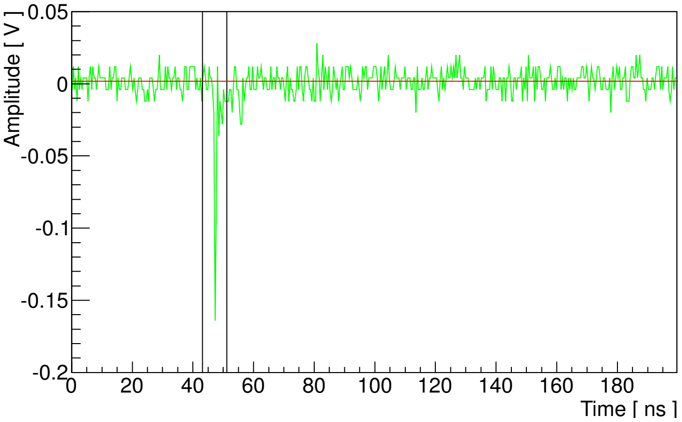

Figure 18. The waveform example from PD1. The red horizontal lines indicate the pedestal line. The black vertical lines show the integral range for evaluating the charge sum.

The charge sum of the creation laser Q_c is evaluated as

$$Q_c = \sum_{t=\mathrm{a}}^{\mathrm{b}} \frac{(V_{p_{\mathrm{t}}} - V_0)\,\Delta t}{R}, \tag{40}$$

where a = 43.2 nm and b = 51.2 nm are integral ranges for all waveforms from PD1, and V_0 is the pedestal value evaluated for event by event as the average of amplitudes from 1 - 100 and 400 - 500 data points.

The charge sum of the inducing laser Q_i is evaluated as integral of the amplitudes over 1 - 500 points.

The recorded waveforms from PMT are tagged with trigger patterns S, C, I, or P. Which pattern the waveform belongs to is determined by the charge correlation between PD1 and PD2 shown in Fig.20.

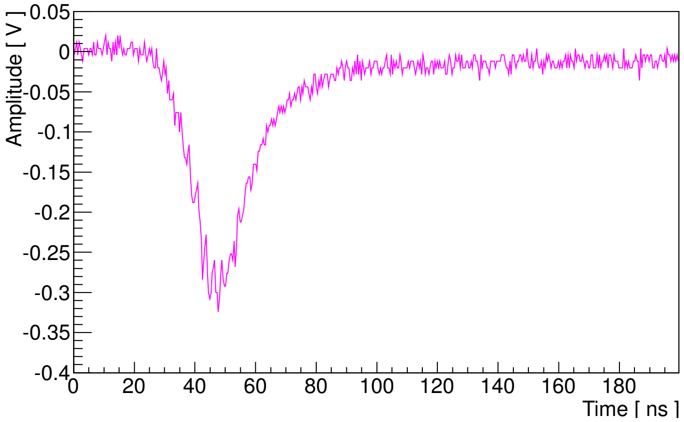

Figure 19. The waveform example from PD2.

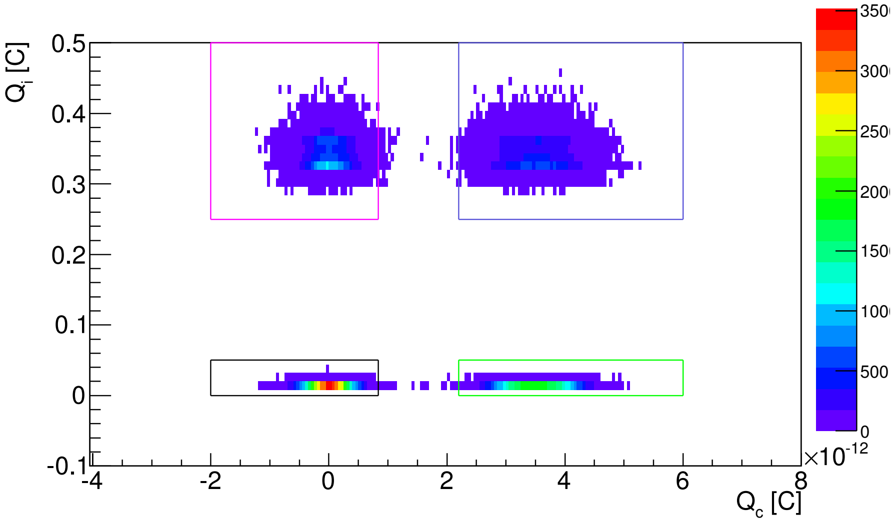

Figure 20. The distributions of charge correlation between the creation and inducing lasers. The data points in the blue, green, magenta and black rectangles indicate trigger patterns S, C, I and P, respectively.

Table 1 shows the number of events in each trigger pattern.

Table 1: Data table for the number of events in each trigger pattern

Trigger pattern	The number of events
S	46120
C	46203
I	46044
P	46169

3.4 Threshold value for peak identification

The threshold value V_{t} for identifying the photon-like peak is determined by checking the correlation between V_{t} and the charge sum of peak structures shown in Fig.21. From Fig.21, V_{t} becomes lower, the negative charge value increase. These negative charges are come from misidentifying the noise as peak structures. Therefore, the effectual threshold value should be set to the region the negative charges are not contained. Therefore, $V_{\mathrm{t}} = -1.3$ mV is given as the effectual threshold value.

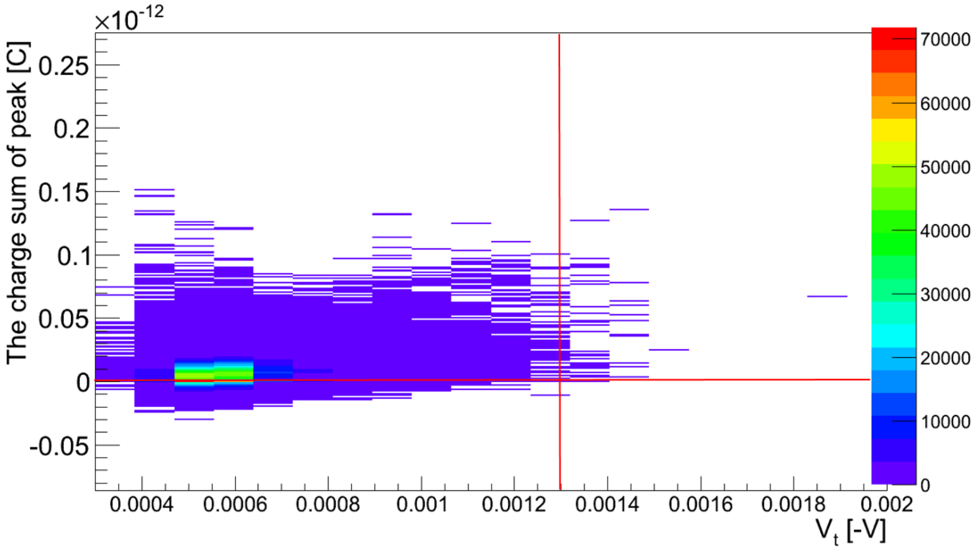

Figure 21. The correlation between V_{t} and the charge sum of peak structure. The red horizontal line shows 0 charge line and the red vertical line indicates the adopted threshold value $V_{\mathrm{t}} = -1.3$ mV.

3.5 Signal-like peak position

The photons which propagate from the focal spot to the detection point make the characteristic peak structures at specific time domains. The time domains that signal expected be observed are determined by observing the four-wave mixing photons emitted from gas in the focal volume. Figure 22 shows the time distributions of observed photons at 5.0×10^4 Pa.

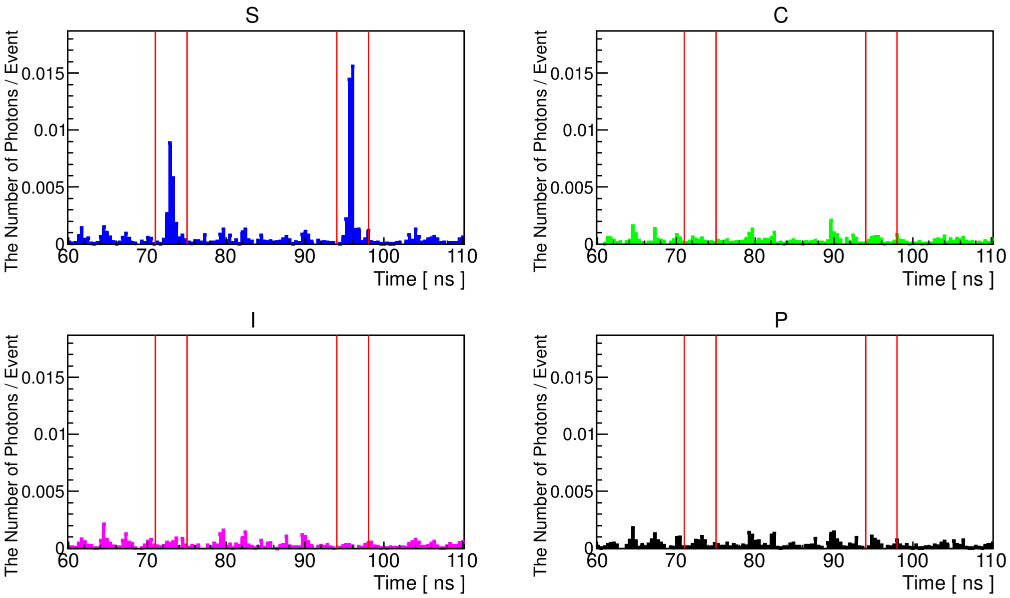

Figure 22. The time distributions of observed photons (efficiency-uncorrected) per triggered event at 5.0×10^4 Pa [47]. The left and right bands bounded by two neighboring vertical lines indicate the time domains $T\{1\}$ and $T\{2\}$ where $\{1\}$ and $\{2\}$-polarized photons are expected to be observed. The signal-like peaks are observed only in S-pattern.

The time domains in 71-75 ns ($T\{1\}$) and 94-98 ns ($T\{2\}$) indicate the arrival times of $\{1\}$ and $\{2\}$-polarized photons traveling the short optical fiber path Path$\{1\}$ and the long optical fiber Path$\{2\}$, respectively. The relative time difference between $T\{1\}$ and $T\{2\}$ is 23 ns. It is consistent to the time difference between Path$\{1\}$ and Path$\{2\}$.

4 Detector calibration

4.1 Evaluation of 1 photon equivalent charge

To convert the charge sum from the PMT into the number of photons, the 1 photon equivalent (1 P.E.) charge of the PMT has to be evaluated. The 1 P.E. charge was measured with a 532 nm pulse laser in advance of the search experiment. It is assumed that the charge distribution are consisted from multiple Gaussian distributions corresponding to the incident photon counts. The charge distribution are fitted by multiple Gaussian distributions based on following assumptions:

- The 0 photon distribution does not correlate with the finite photons distributions.
- $\mu_N - \mu_0$ is proportional to the number of incident photons N. Where μ_N is the mean of the N photons distribution.
- The variance of the N photons distribution σ_N^2 is proportional to the number of incident photons N.
- The incident photon counts conform to Poisson distribution.

Therefore, the multiple Gaussian fitting is operated as we fix the free parameters μ_0, σ_0, μ_1, and σ_1.

The 0 photon distribution are determined by recording waveform data without photon injection. The charge distribution with 45000 statistics are shown in Fig. 23. From the fitting gauss function,

$$\mu_0 = -2.785 \times 10^{-15}, \quad (41)$$

$$\sigma_0 = 1.090 \times 10^{-14} \quad (42)$$

are given.

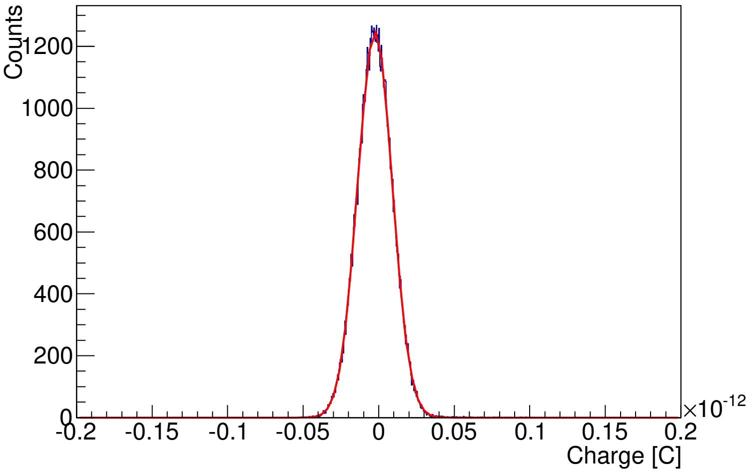

Figure 23. The charge distribution without photon injection.

Then, the intensity of the incident laser is adjusted to extremely low to determine the 1 photon distribution. The intensity of the laser becomes higher, the contribution of 1 photon distribution is clearly appeared as right side tail of the charge distribution. The obtained charge distributions are fitted by 0 photon + 1 photon + 2 photon distributions by increasing the laser intensity moderately. Where μ_0 and σ_0 are fixed and the other μ_N and σ_N are given as free parameters at this time.

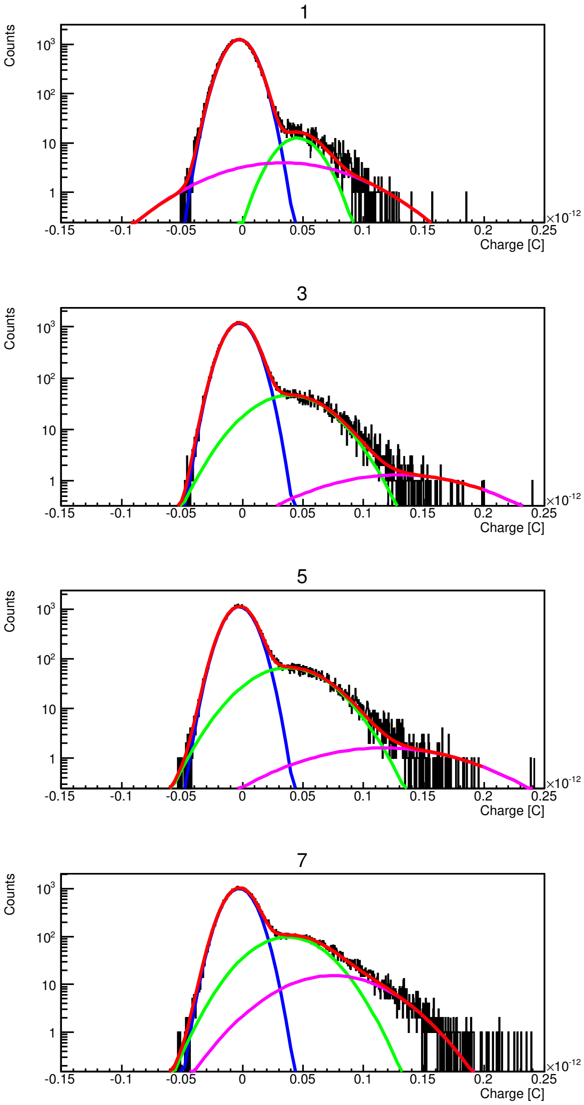

Figure 24. The charge distributions fitted by 3 Gaussians. The blue, green, and magenta lines represent 0,1, and 2 photon(s) distribution, respectively. The red line shows the sum of 3 Gaussians.

The fitting parameters of the 1 photon distribution should not fluctuate by changing of the laser intensity. The laser intensity dependence of μ_1 and σ_1 are shown in Fig.25. The fluctuations of μ_1 and σ_1 are converged from No.2 to No.7. Thus, we evaluate μ_1 and σ_2 as the average values in these range,

$$\mu_1 = 3.838 \times 10^{-14}, \tag{43}$$
$$\sigma_1 = 2.807 \times 10^{-14}. \tag{44}$$

.

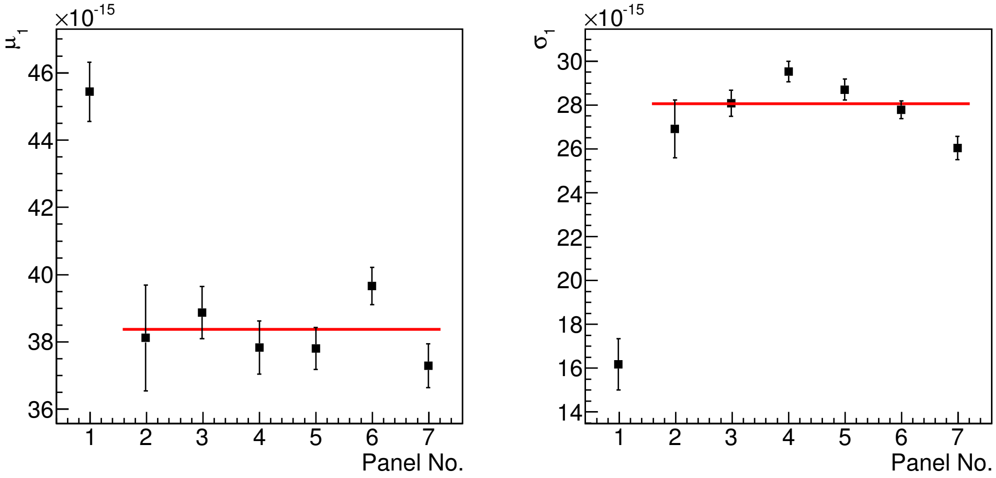

Figure 25. The laser intensity dependence of μ_1 and σ_2 are shown at the left and right panels, respectively. The integer numbers in x-axis indicate the corresponding panel No. in Fig. 24. The red horizontal lines stand for the average value from No.2 to No.7.

Then, the charge distributions are fitted by the multiple Gaussians at the higher intensities setting. Now μ_N and σ_N become fix parameters, thus, the multiple Gaussian fitting function are given uniquely by calibrating the average number of incident photons λ. The best suited value of λ are determined when the minimum χ^2 are given. Figure 26 shows the charge distributions fitted by multiple Gaussian functions.

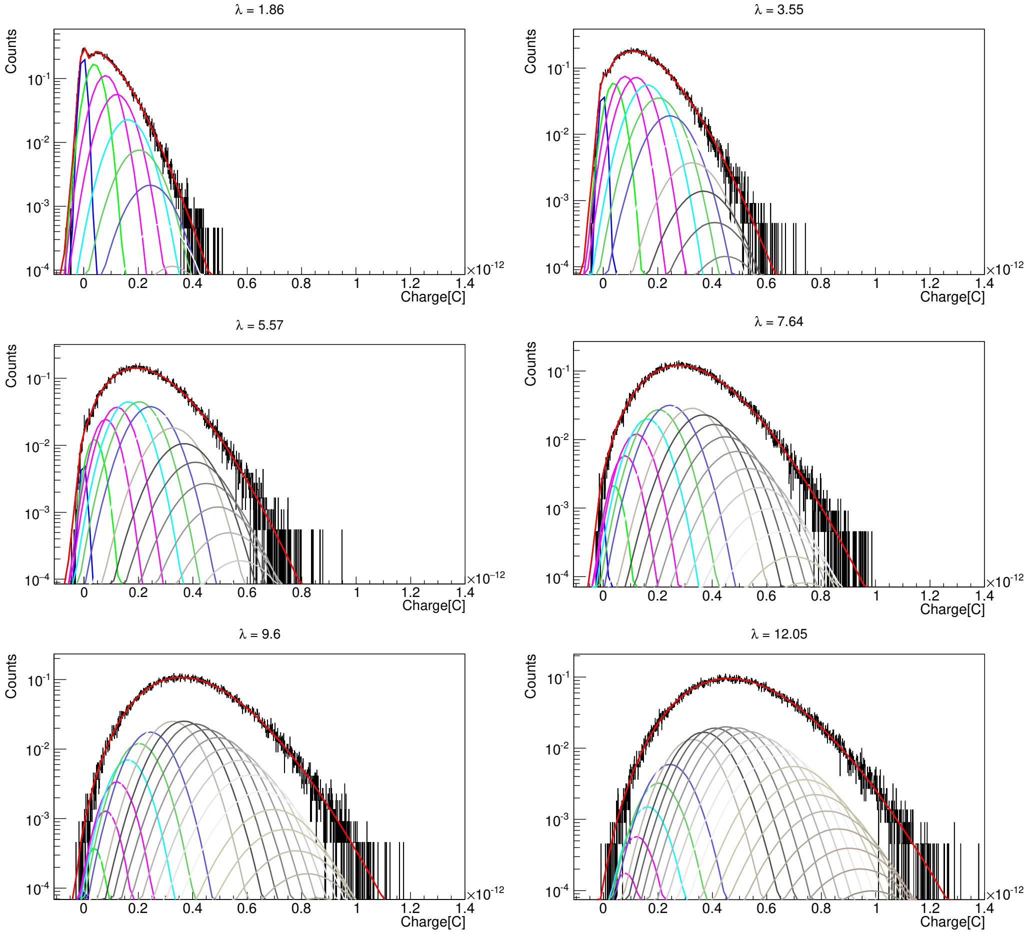

Figure 26. Charge distributions fitted by multiple Gaussians at the higher intensities setting.

The correlation between λ and the mean value of charge distributions are shown in Fig.27 with the fitting linear function. The charge mean are proportion to the average number of incident photons λ. Finally, the 1 photon equivalent charge $Q_{\text{p.e.}}$ is given as the slope of the linear function as

$$Q_{\text{p.e.}} = 4.13 \pm 0.06 \times 10^{-14}\ \text{C}. \tag{45}$$

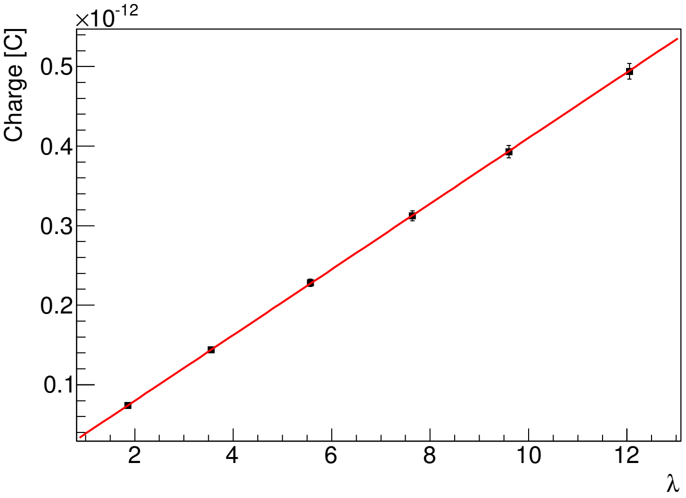

Figure 27. The correlation between λ and the mean value of charge distributions

4.2 Detection efficiency

The detection efficiency of the PMT is evaluated by comparing the number of observed photons at the PMT and the power of the incident laser by using a 532nm pulse laser. The measurement setup is shown in Fig.28.

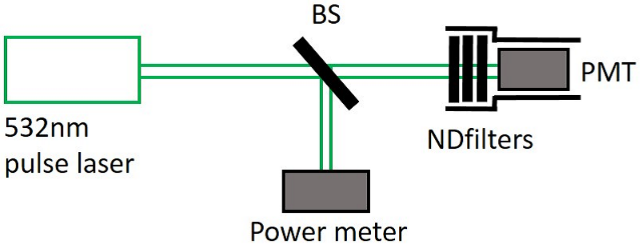

Figure 28. Setup to measure the detection efficiency of the PMT

The pulse laser is split to two optical paths eventually by a beam splitter (BS). The power of incident laser is measured by a calibrated power meter. The laser at another path is attenuate by three optical filters (ND filters) and guided to the PMT.

The average power of the incident laser measured by the power meter is 1.09 ± 0.01 mW. The pulse energy is evaluated to 55.1 ± 0.5 nJ by taking the repetition rate of the incident laser 19.8 Hz into account. The number of photons per pulse N_{PM} is evaluated as

$$N_{\mathrm{PM}} = (1.49 \pm 0.01) \times 10^{11}. \tag{46}$$

N_{PMT}, the number of observed photons at the PMT, is given by converting the average value of the charge distribution from the PMT.

$$N_{\mathrm{PMT}} = 16.0 \pm 0.1. \tag{47}$$

Then attenuation factor of three optical filters placed in front of PMT are measured as

$$\xi = 4.6 \times 10^{-9}. \tag{48}$$

The detection efficiency ϵ_D is calculated as follows:

$$\epsilon_D = \frac{N_{\mathrm{PMT}}}{\xi N_{\mathrm{PM}}} = 2.4 \pm 0.1\ \%. \tag{49}$$

5 Experimental parameters

5.1 Beam diameters

The beam diameters of the creation and inducing lasers before expanded by telescopes are measured by CCD cameras directly.

The x-y beam profile of the creation laser averaged of 50 pulses are shown in upper-left of Fig.29. The beam diameter is determined by fitting the 3D beam profile by the 2D gauss function shown in upper-right of Fig.29, where the form of the fitting function is

$$f(x,y) = A \exp\left(-\frac{(x-\mu_x)^2}{2\sigma}\right) \exp\left(-\frac{(y-\mu_x)^2}{2\sigma}\right) + C, \tag{50}$$

where A is the amplitude, C is the offset, μ_x and μ_y are the mean values in x and y axis, respectively, and σ is the standard deviation. The common σ is applied in x and y axes due to making the parametrization simply in the QPS.

The under-left and under-right panels in Fig.29 show x and y projections fitted by the 2D gauss function, respectively. The similar plots in the case of the inducing laser are shown in Fig.30.

The beam diameters of the creation and inducing lasers d_c and d_i are defined as 2σ of the 2D gauss function fit to each profile. As a result,

$$\begin{aligned} d_c &= 1.64 \pm 0.01 \text{ mm}, && (51) \\ d_i &= 1.69 \pm 0.01 \text{ mm} && (52) \end{aligned}$$

are obtained, where the unit of [pixel] are converted into [mm] by taking a 11.2 μm pixel size of the CCD camera into account .

Both beam are expanded 3 times lager by the telescopes and further expanded 4 times larger after they are combined. The expanded beam diameters of the creation and inducing lasers D_c and D_i are estimated as

$$\begin{aligned} D_c &= 19.6 \pm 1.6 \text{ mm}, && (53) \\ D_i &= 20.3 \pm 1.7 \text{ mm}, && (54) \end{aligned}$$

respectively, with taking the total enlargement factor 12 ± 1 into account.

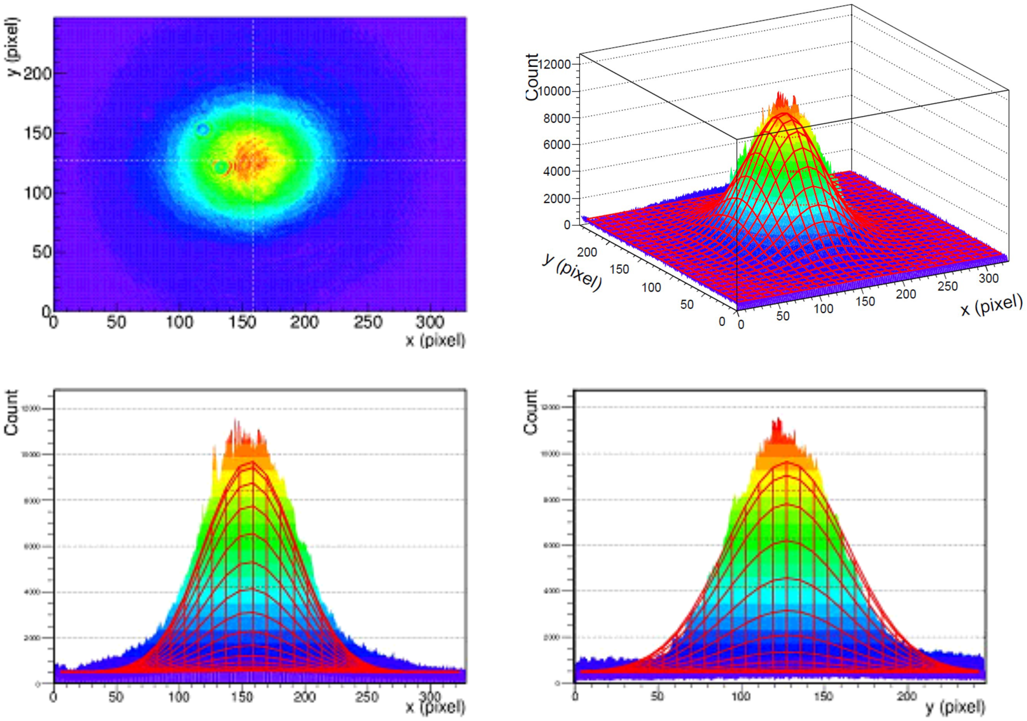

Figure 29. The beam profile of the creation laser

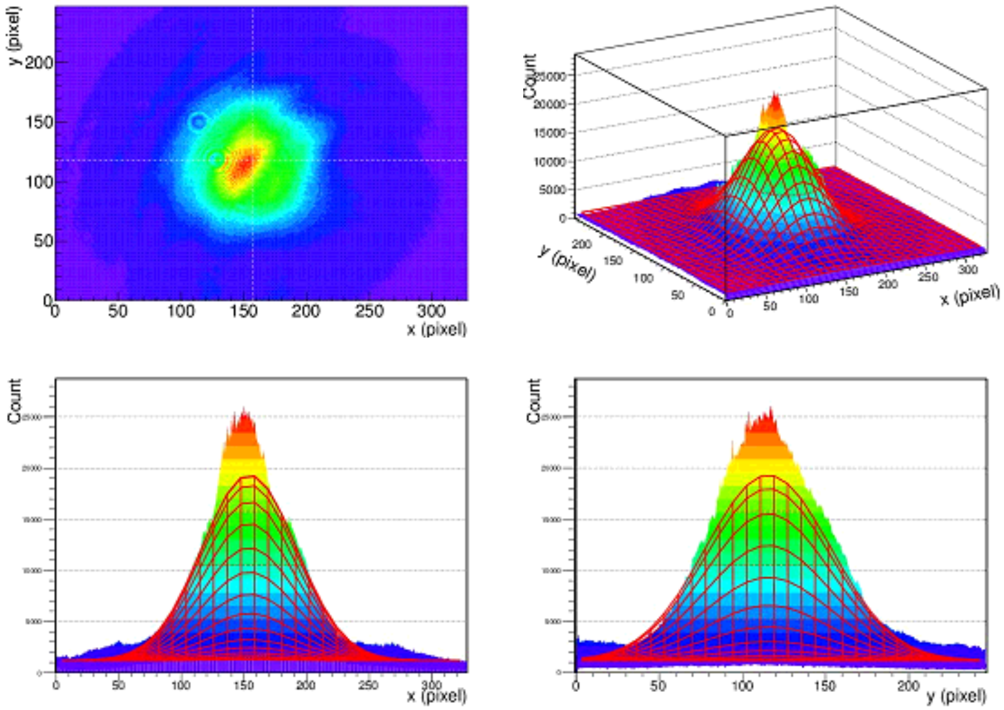

Figure 30. The beam profile of the inducing laser

5.2 Beam overlapping factor at the focal spot

The number of photons contribute to the inducing mechanism in the inducing laser should be considered. It estimated by measuring how much beam energies of the creation laser overlap to that of the inducing laser at the interaction point in the vacuum chamber. Since the correction of this overlapping factor are most sensitive around the focal spot.

The beam profiles of the creation and inducing lasers at the focal spot are measured at the interaction point by the common CCD camera. The incident beams are expanded by the telescope install in front of the CCD camera due to the small size of images captured at the focal spot.

The x-y projection of the creation and inducing beams are shown in Fig.31. The spot size of them are defined as well as in the case of determining the beam diameter of them. The common mean values of the 2D gauss function μ_x and μ_y are assigned to the beam profiles of the creation and the inducing lasers.

The measured spot diameters of the creation and inducing lasers are 20.9 ± 0.1 μm and 23.1 ± 0.1 μm, respectively. A ideal spot diameter of a coherent Gaussian beam d_f is evaluated as

$$d_\mathrm{f} = \frac{4\lambda f}{\pi d}. \tag{55}$$

From Eq.(55), the spot diameters of the creation and inducing lasers are evaluated as 10μm and 12μm, respectively. The measured spot diameters are broadened compared with the ideal values due to the incoherence of the beams come from their intrinsic properties and the effect of optical materials.

The beam energy overlapping factor

$$\eta = 0.87 \tag{56}$$

is evaluated by integrating the counts in the beam profiles of the inducing laser over the area that the spot of the creation laser covers.

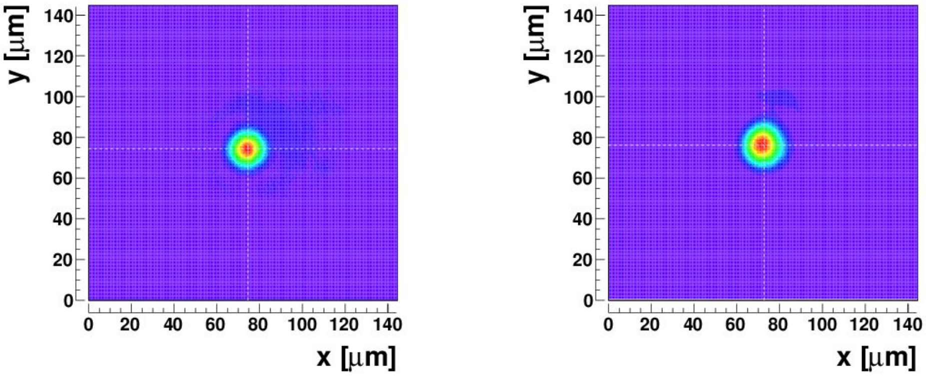

Figure 31. The beam profiles of the creation (left) and inducing (right) lasers at the focal spot

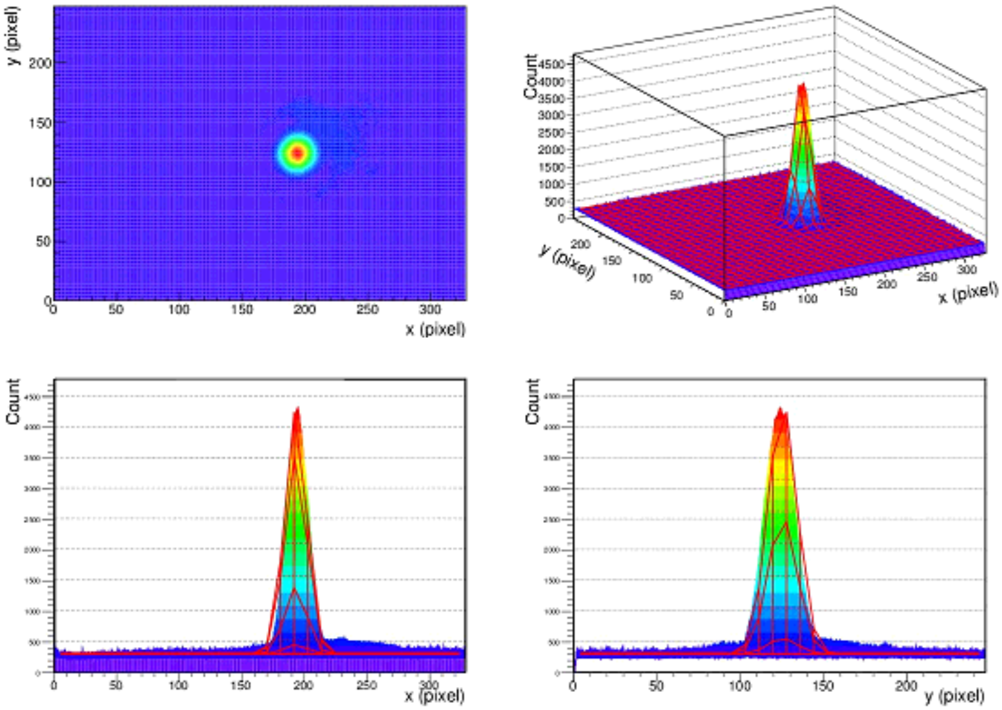

Figure 32. The beam profile of the creation laser at the focal spot

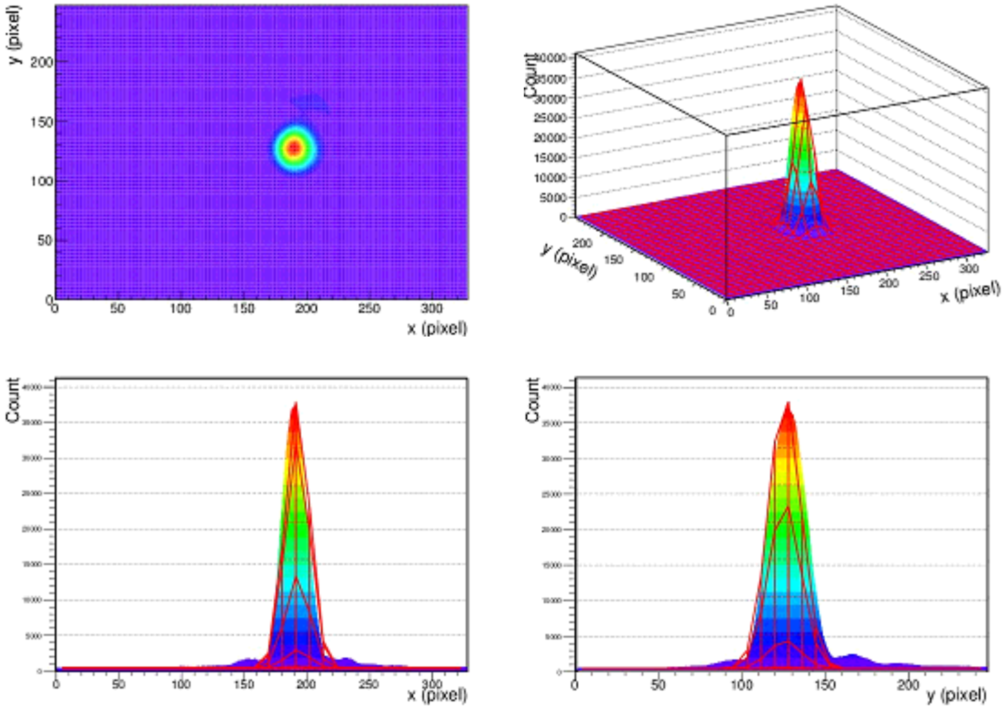

Figure 33. The beam profile of the inducing laser at the focal spot

5.3 Beam energies

The beam energies of the creation and inducing lasers are monitored by photo diodes PD1 and PD2, respectively.

The beam energy of the creation laser are calibrated by the charge sum of waveform data from PD1. The energy of the inducing laser are calibrated by the peak voltage of waveforms from PD2, because the charge sum is not sensitive to in the case of the inducing laser duo to its long time duration.

The beam energies are measured by a power meter at a backward of the beam aperture on each beam line. The waveforms of photo diodes and the beam energies measured by the power meter are recorded in parallel by changing the beam energies with inserting optical filters.

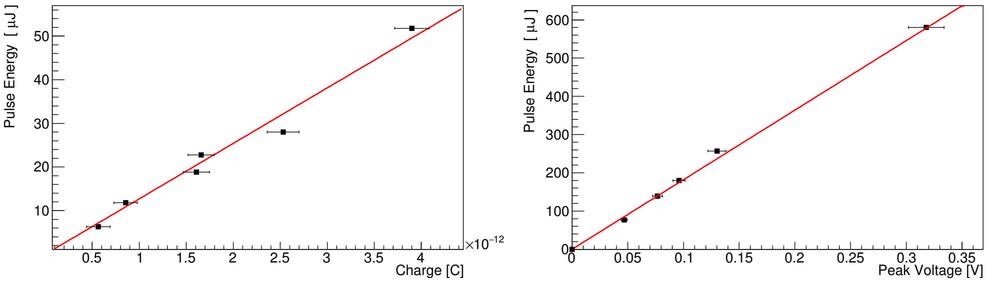

Figure 34. The correlation between the charge sum and the pulse energy of the creation laser is shown in the left panel. The correlation between the peak voltage and the pulse energy of the inducing laser is shown in the right panel. They are fitted by the linear functions drawn by the red lines.

The charge distribution of the creation laser and the peak voltage distribution of the inducing laser are shown at left and right panels in Fig. 35, respectively. The mean of the charge distribution of the creation laser is $5.31 \pm 0.78 \times 10^{-12}$ C and the mean of the peak voltage distribution of the inducing laser is -0.34 ± 0.01 V. The pulse energies at the sampling points are evaluate by extrapolate the mean values to the linear functions drawn in Fig. 34.

The pulse energies of the creation and inducing lasers at the sampling points are $E_c^* = 44.6 \pm 5.9\ \mu$J and $E_i^* = 617.4 \pm 3.5\ \mu$J, respectively.

However, the beam energies attenuate by propagating from the sampling points to the focal spot. The attenuation factors are evaluated by measuring the beam energies at the sampling points and the focal spot with the power meter after the physics run. The measured attenuation factor of the creation laser is $\kappa_c = 0.21$, and that of the inducing laser is $\kappa_c = 0.19$. The pulse energies of the creation and inducing lasers at the focal spot E_c and E_i are evaluate as follows:

$$\begin{aligned} E_c &= \kappa_c E_c^* = 9.3 \pm 1.2\ \mu\text{J}, \\ E_i &= \kappa_i E_i^* = 117 \pm 1\ \mu\text{J}. \end{aligned} \tag{57}$$

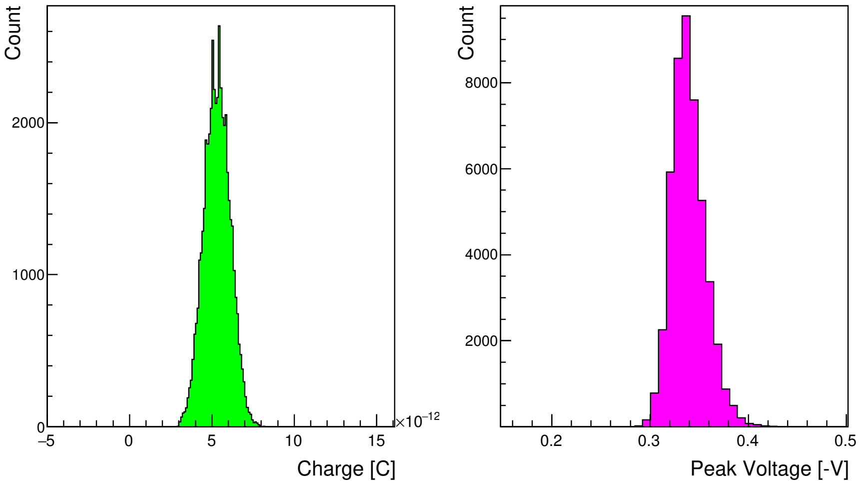

Figure 35. The charge distribution of the creation laser (left) and the peak voltage distribution of the inducing laser (right).

5.4 The pulse duration of the creation laser

The pulse duration of the creation laser τ_c is measured by using the autocorrelation method. Figure 36 illustrates the measurement setup. The creation laser are split by a beam splitter (BS). The two beams travel the different optical length and the split beams are combined by BS again.

The combined pulse is composed of the two pulses which have a tiny amount of time difference due to their different optical lengths. The relative time delay between two pulses are adjustable by sliding the linear transition stage.

The combined beam enters a BBO (BaB_2O_4) crystal and converts into the second harmonic wave ($\lambda = 400$ nm). The intensity of the second harmonic wave depends on the number of time-coincidental photons in the combined pulse. Therefore, the time duration of the laser pulse are evaluated by measuring correlation between a time delay and the intensity of the second harmonic wave.

The intensity of the second harmonic wave are measured by the PMT. The optical filters transmit 380-430nm wavelength photons are placed in front of the PMT. The pulse duration of the creation laser τ_c is evaluated as

$$\tau_c = \frac{\Delta\tau}{\alpha}, \tag{58}$$

where $\Delta\tau$ is the time duration of the autocorrelated signal shown in Fig.36, and α is the autocorrelation factor.

$\Delta\tau$ is defined as $\Delta\tau = 2\Delta L/c$, where $\Delta L = 0.2$ mm is the full width at half maximum of the fitting gauss function of the autocorrelated signal shown in Fig.37. The autocorrelation factor $\alpha = \sqrt{2}$ is assigned with the assumption that the time structure of the laser pulses follow a Gaussian distribution. From Eq.(58), the pulse duration of the creation laser τ_c is given as

$$\tau_c = 900 \text{ fm}. \tag{59}$$

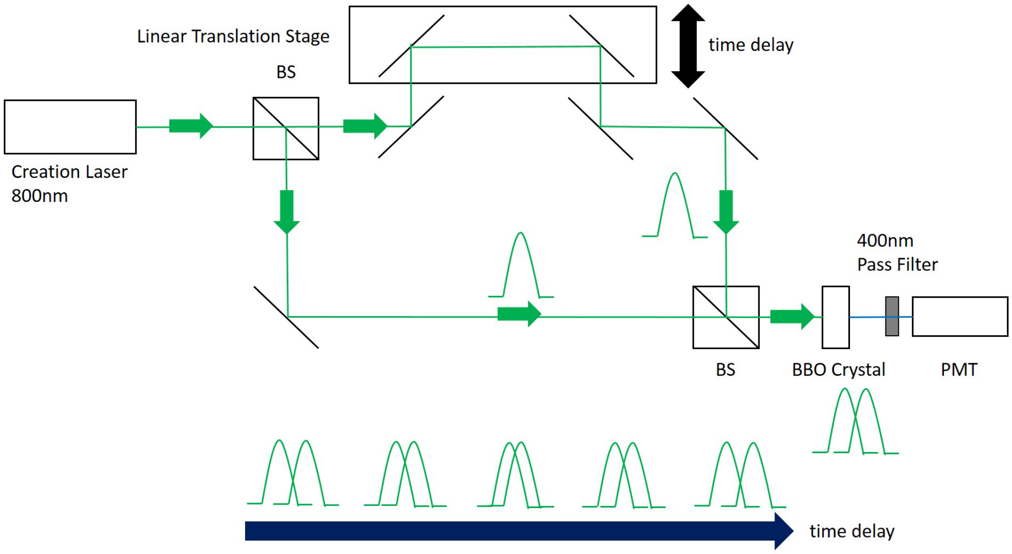

Figure 36. The setup to measure the pulse duration of the creation laser via the autocorrelation method.

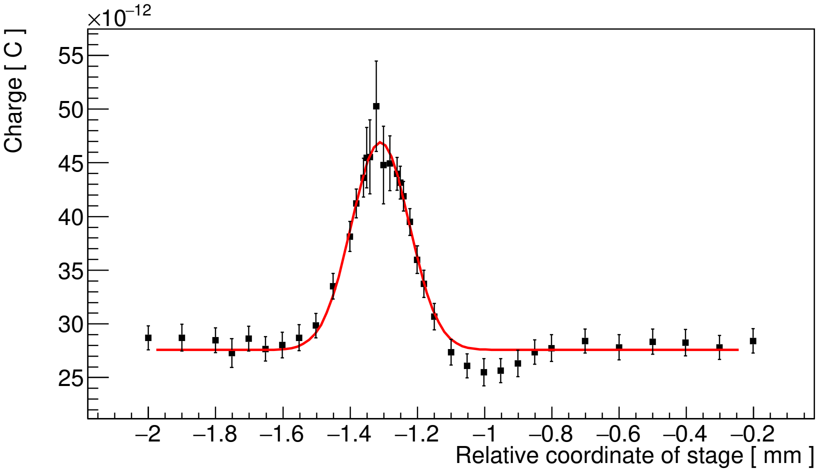

Figure 37. The intensity of the second harmonic wave depends on the relative coordination of the linear transformed stage.

5.5 The energy spectrum of the creation laser

The energy spectrum of the creation laser is measured in front of the focal spot by a spectrum analyzer. The measured wavelength distribution are shown in Fig.38. The effective spectrum width of the creation laser $\delta\omega_c$ is defined as

$$\delta\omega_c\,[\mathrm{eV}] = \frac{1}{2}\frac{hc}{e\delta\lambda_c}, \tag{60}$$

where h is the Planck constant, c is the velocity of light, e is the elementary charge. $\delta\lambda_c = 3$ nm is defined as the root mean square of the wavelength distribution shown in Fig.38. The spectrum width of the creation laser is evaluated from Eq.(60) as

$$\delta\omega_c \sim 0.005 \text{ eV} \tag{61}$$

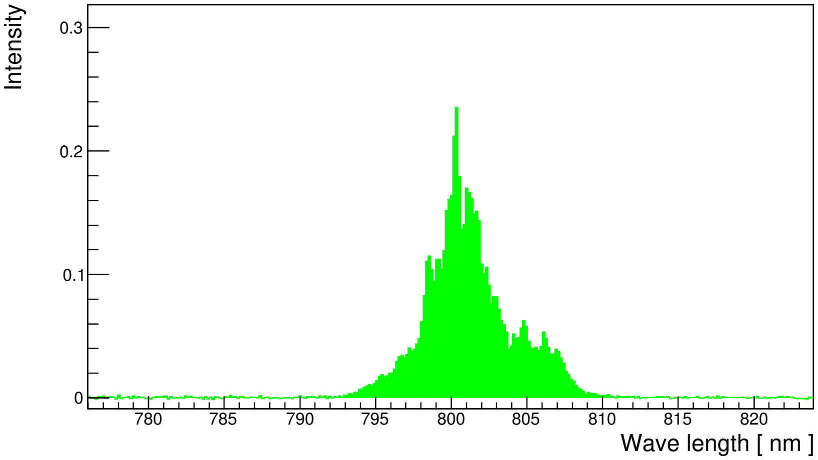

Figure 38. The wavelength spectrum of the creation laser.

5.6 Signal attenuation factor

The signal attenuation factor from the focal spot to the end of the long optical fiber, ϵ_{opt2} is measured. This attenuation factor is composed of the transmittance of optical devices and the signal acceptance of the PMT.

The intensities of the {2}-polarized calibration light at in front of the vacuum chamber and at the PMT are measured in parallel. The calibration light are split by the BS and the energy at in front of the vacuum chamber is measured by a photo-multiplier-tube (PMT') which is the same model of the PMT used as the signal detector.

ϵ_{opt2} is evaluate from following equation,

$$\epsilon_{\mathrm{opt2}} = \frac{N_{\mathrm{PMT}}}{N_{\mathrm{PMT}'}} R_{\mathrm{att}} R_{\epsilon_D}, \tag{62}$$

where N_{PMT} is the mean number of the incident photons per pulse measured at the signal detection point by PMT and $N_{\mathrm{PMT}'}$ is measured at in front of vacuum chamber by PMT', R_{att} is the attenuation factor from the sampling point to the focal spot, and R_{ϵ_D} is the ratio of detection efficiency of PMT and PMT'.

The measurement values of N_{PMT} and $N_{\mathrm{PMT}'}$ are

$$\begin{aligned} N_{\mathrm{PMT}} &= 2.09 \pm 0.01, & (63) \\ N_{\mathrm{PMT}'} &= (4.17 \pm 0.20) \times 10^2. & (64) \end{aligned}$$

$R_{\mathrm{att}} = 0.26 \pm 0.06$ is measured at the sampling point and the focal spot by PMT' after physics run.

$R_{\epsilon_D} = 0.45 \pm 0.01$ is also measured when the detection efficiency of PMT are measured.

As a result, ϵ_{opt2} is given as

$$\epsilon_{opt2} = 0.9 \pm 0.2\ \%. \tag{65}$$

5.7 Efficiency ratio between two optical fiber paths

ϵ_{opt1}, the signal attenuation factor for Path{1}, is evaluated from the ratio of path efficiencies B, where

$$B \equiv \frac{\epsilon_{\mathrm{opt1}}}{\epsilon_{\mathrm{opt2}}}. \tag{66}$$

B is measured by rotating the polarization angle Θ of the calibration light with the half wave plate, and counting the number of photons in $T\{1\}$ and $T\{2\}$.

The Θ dependences of the number of $\{1\}$ and $\{2\}$- polarized photons are plotted in Fig 39.

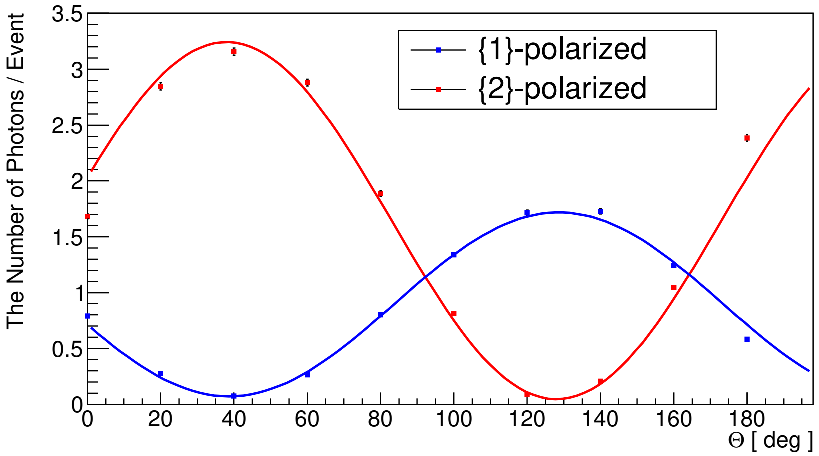

Figure 39. The number of $\{1\}$ and $\{2\}$-polarized photons as a function of the linear polarized angle Θ.

The data points for each polarization state are fitted by following function,

$$f(\Theta) = A(\cos 2\Theta + \phi) + C, \tag{67}$$

where A is the amplitude, ϕ is the phase, and C is the constant. B is re-expressed as $B = A_{\{1\}}/A_{\{2\}}$, where $A_{\{1\}}$ and $A_{\{2\}}$ are the amplitudes of the fitting functions of $\{1\}$ and $\{2\}$-polarized data, respectively. From Fig.39,

$$B = 0.51 \pm 0.01 \tag{68}$$

is given and

$$\epsilon_{\mathrm{opt1}} = B\epsilon_{\mathrm{opt2}} = 0.5 \pm 0.1\ \% \tag{69}$$

is obtained.

6 Results

6.1 Observed photon counts in vacuum

The physics run search for scalar and pseudoscalar fields was performed at 2.3×10^{-2} Pa. The time distributions of observed photons are shown in Fig.40.

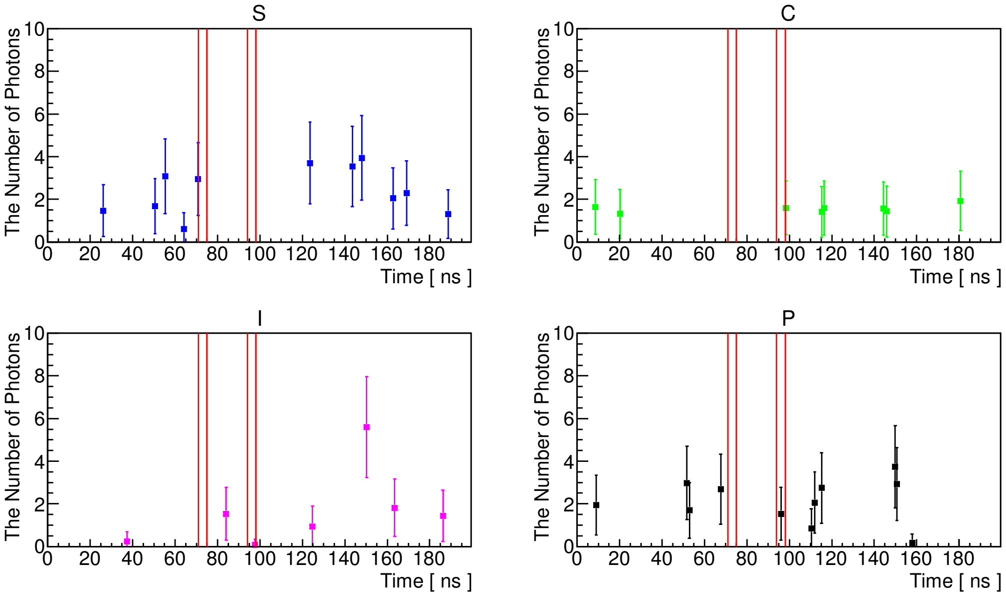

Figure 40. The time distributions of the observed photons (efficiency-uncorrected) at $2.3 \times 10^{-}2$ Pa [47]. The data points in each trigger pattern are normalized to the number of triggered events of S trigger pattern.

From Tab.2, it is confirmed that no four-wave mixing photon is observed in vacuum. Furthermore, residual photons in the creation and inducing lasers are also not observed at the detection point.

The number of the four-wave mixing photons are evaluated with following strategy. It is assumed that the number of observed photon n_i for each

Table 2: The numbers of observed photons in $T\{1\}$ and $T\{2\}$ for each trigger pattern. n_{i1} and n_{i2} are the number of signals in trigger pattern i with $\{1\}$ and $\{2\}$-polarized states, respectively. W_i is the number of events in trigger pattern i.

Trigger i	n_{i1}	n_{i2}	W_i
S	0	0	46120
C	0	0	46203
I	0	0.07	46044
P	0	1.53	46169

trigger pattern i are composed of following components

$$\begin{aligned} n_S &= N_P + N_C + N_I + N_S, && (70) \\ n_C &= N_P + N_C, && (71) \\ n_I &= N_P + N_I, && (72) \\ n_P &= N_P, && (73) \end{aligned}$$

with an assumption that the observed photons at P-pattern n_P are comes from thermal noises from the PMT and ambient noises such as cosmic rays (N_P). All trigger patterns should contain N_P by considering the event weights of the four trigger patterns. N_C and N_I are come from the residual photons in the creation and inducing lasers, respectively. They furthermore contains the photons produced by nonlinear interactions at optical materials or gas when the creation or inducing laser is incident, individually. N_S is the number of signal photons originating from the four-wave mixing process. This should appears at S-pattern.

N_S is evaluate from Eq.(73), as follows:

$$\begin{aligned} N_S &= n_S - \frac{W_S}{W_P} n_P - \frac{W_S}{W_C}(n_C - n_P) - \frac{W_S}{W_I}(n_I - n_P) \\ &= n_S - \frac{W_S}{W_C} n_C - \frac{W_S}{W_I} n_I + \frac{W_S}{W_P} n_P. \qquad (74) \end{aligned}$$

The time distribution of N_S is shown in Fig.41. It is obtained by subtractions among the time distributions of the four-trigger patterns shown in Fig.40 based on the relation in Eq.(74). Figure 41 indicates that no excess is shown in time domains $T\{1\}$ and $T\{2\}$. It means the four-wave mixing signals are not observed in this search.

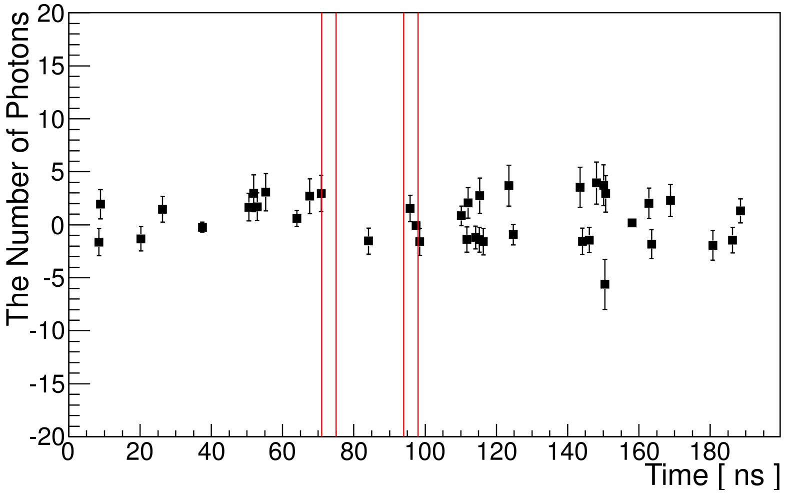

Figure 41. The time distribution of the number of signal photons N_S (efficiency-uncorrected) at 2.3×10^{-2} Pa.

As a result, the number of observed signal photons with {1} and {2}-polarized states are obtained as follows:

$$
\begin{aligned}
N_{S1} = &\quad 0 \pm 0(\text{stat.}) \pm 2.16(\text{syst.I}) \pm 0.30(\text{syst.II}) \pm 0(\text{syst.III}), \\
N_{S2} = &\quad 1.46 \pm 1.27(\text{stat.}) \pm 2.16(\text{syst.I}) \pm 0.04(\text{syst.II}) \pm 3.59(\text{syst.III}).
\end{aligned}
$$

6.2 Systematic errors

Systematic error I is come from the number of the photons outside of the two arrival time domains $T\{1\}$ and $T\{2\}$. This is evaluated by calculating the root mean square of N_S except in $T\{1\}$ and $T\{2\}$.

Systematic error Ⅱ is originating from the ambiguity of the number of signals depends on the uncertainty of the threshold value V_{t} for the peak finding. It is estimated by changing V_{t} from -1.2 mV to -1.4 mV.

Systematic error Ⅲ is relevant to the ambiguities of threshold value n_{node} for the rejection of noisy events shown in Fig.16.

The number of signals by changing V_{t} and n_{node} are listed in Tab.3. V_{t} and n_{node} are changed independently. When estimate syst.I, n_{node} is fixed to 150. In the case of syst.Ⅱ estimation, V_{t} is fixed to -1.3 mV.

Table 3: The data table of N_{S1} and N_{S2} depends on V_{t} and n_{node}.

V_{t} [mV]	N_{S1}	N_{S2}	n_{node}	N_{S1}	N_{S2}
-1.2	0.52	1.46	145	0	-4.75
-1.3	0	1.46	150	0	1.46
-1.4	0	1.53	155	0	1.46

It is assumed that uncertainties of N_{S1} and N_{S2} originating from the ambiguities of V_{t} and n_{node} are based on uniform distributions. Here syst.Ⅱ and syst.Ⅲ are defined as the standard deviation of uniform distributions.

7 Background Estimation

7.1 Four-wave mixing process in residual gas

The four-wave mixing photons can be emitted from the focal volume by interaction between high intensity lasers and residual gas into the vacuum chamber.

The four-wave mixing process by interacting with atoms is interpreted as the third-order nonlinear quantum optical process[41, 42]. It is considerable background source since it can be the main background component at higher intensity laser experiments in the future.

In this experiment, the expected number of the four-wave mixing photons from gas are estimated by measuring its pressure dependence. The number of the four-wave mixing photons in gas are evaluated with similar analysis method at the vacuum condition.

Figure 42 shows the pressure dependence of the number of the four-wave mixing photons. The black and red data points indicate {1} and {2}-polarized photons, respectively, and they are fitted by the quadratic functions.

The expected number of the four-wave mixing photons with the same shot statistics as the vacuum data at 2.3×10^{-2} Pa (an equivalent condition to the vacuum data) are estimated as

$$\begin{aligned} \mathcal{N}_{\text{gas1}} &= 1.7 \pm 1.1 \times 10^{-5}, \\ \mathcal{N}_{\text{gas2}} &= 1.7 \pm 1.1 \times 10^{-5}, \end{aligned} \tag{75}$$

where $\mathcal{N}_{\text{gas1}}$ and $\mathcal{N}_{\text{gas2}}$ are the number of {1} and {2}-polarized photons (efficiency-corrected), respectively. Thus the number of the four-wave mixing photons emitted from residual gas are negligible small in this search experiment.

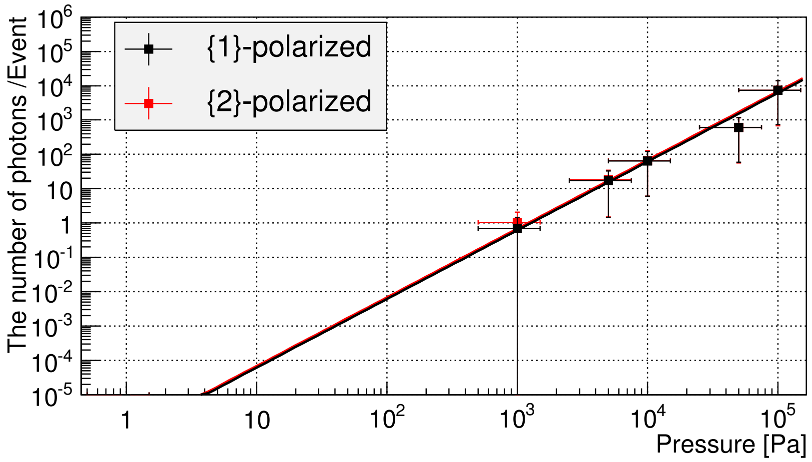

Figure 42. The pressure dependence of the number of four-wave mixing photons per pulse [47].

The correlations between the energies of the incident lasers and the number of the four-wave mixing photons in gas are also measured. The beam energies of the creation and inducing lasers are changed independently by inserting optical filters on each beam line. The energies of the creation and inducing lasers dependences are shown in Fig.43 and Fig.44, respectively.

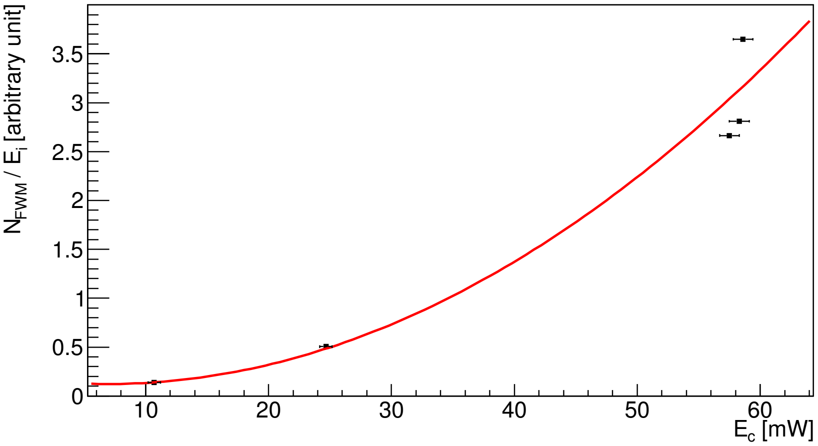

Figure 43. The correlations between the pulse energy of the creation laser E_c and the number of the four-wave mixing photons in gas N_{FWM} fitted by the quadratic function. The vertical axis is scaled by E_i and the numerical values are notated in arbitrary unit.

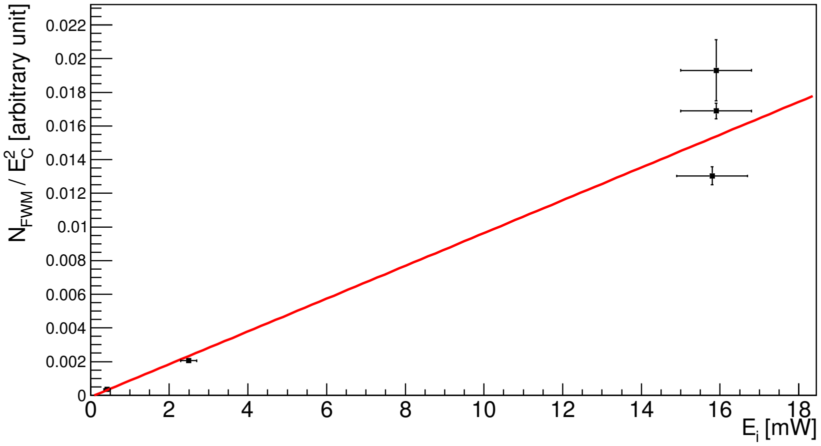

Figure 44. The correlations between the pulse energy of the inducing laser E_i and N_{FWM} fitted by the linear function. The vertical axis is scaled by E_c and the numerical values are notated in arbitrary unit.

In addition, the number of the four-wave mixing photons N_{FWM} divided by ${E_c}^2 E_i$ at the different beam energies conditions are plotted in Fig.45. They become constant among the different beam energies conditions. It agrees with the intensity dependence of the four-wave mixing photons $I_4 \propto {I_1}^2 I_2$ shown in Eq.(35).

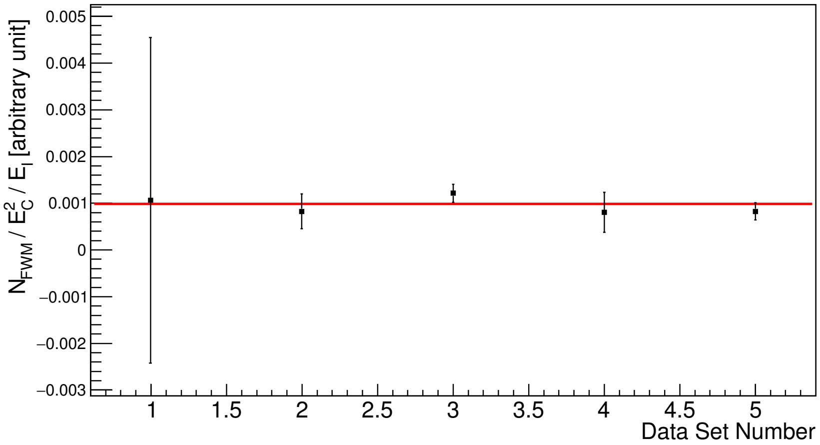

Figure 45. $N_{\mathrm{FWM}}/E_c^2/E_i$ at the different beam energies conditions fitted by constant.

7.2 Photon-photon scattering by nonlinear QED effect

The QED (Quantum Electro Dynamics) predicts photon-photon interaction by the contribution of the electron loop originating from the nonlinear quantum effect of vacuum (Fig.46). The background photons can be produced via this process in QPS. The cross section of photon-photon scattering in the QED process is expressed as

$$\sigma_{\mathrm{QED}} = \frac{973}{10125\pi}\alpha^2\gamma_e^2\left(\frac{\hbar\omega_{\mathrm{cms}}}{m_e c^2}\right), \tag{76}$$

where $\alpha \sim 1/137$ is the fine-structure constant, $\gamma_e \sim 2.8 \times 10^{-13}$ cm is the classical electron radius, ω_{cms} is the photon energy in the center-of-mass system, and $m_e \sim 0.5$ MeV is the electron mass .

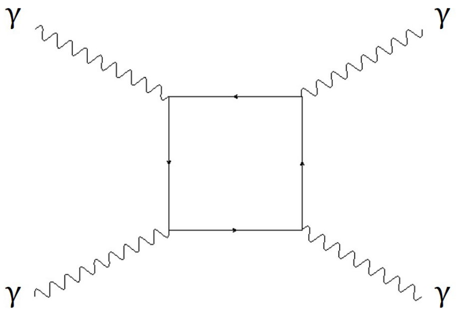

Figure 46. The Feynman diagram of the photon-photon scattering via nonlinear QED process.

We now roughly estimate the order of σ_{QED} with $\omega = 0.1$ eV,

$$\sigma_{\mathrm{QED}} \sim 10^{-75}\ \mathrm{m}^2. \tag{77}$$

The luminosity L of the photon-photon scattering in QPS including the inducing photons per shot are expressed simply as

$$L = \frac{N_c^2 N_i}{2\pi W_0^2}\sin\Delta\vartheta^2, \tag{78}$$

where $N_c \sim 10^{14}$ and $N_i \sim 10^{15}$ are the number of photons in the pulse of the creation and inducing lasers, respectively, $W_0 \sim 10\ \mu$m is the focal spot radius, and $\Delta\vartheta \equiv d/2f \sim 0.1$.

L is evaluated as

$$L \sim 10^{47}\ \mathrm{m}^{-2}. \tag{79}$$

The number of the photon-photon scattering processes expected with whole shot statistics in this experiment are expressed as

$$\mathcal{N}_{\mathrm{QED}} = \sigma_{\mathrm{QED}} L W_S, \tag{80}$$

where $W_S \sim 50000$ is the number of S-triggered events.
N_{QED} is roughly estimated as

$$N_{\mathrm{QED}} \sim 10^{-23}. \tag{81}$$

We note that these calculation overestimates the scattering rate, since we now assume that all inducing photons contribute to the inducing effect. A rigorous derivation of the photon-photon scattering rate by the QED process in the QPS geometry can be evaluated by taking the phase matching between the creation and inducing photons into account. We overestimate the scattering rate, nevertheless, it is negligible small in this experimental condition. Therefore, the background signals originating from the nonlinear QED process are no less negligible in this experiment.

8 Exclusion limits for scalar and pseudoscalar fields

8.1 Coupling - mass relations

The coupling-mass relations of scalar and pseudoscalar fields are evaluated from Eq.(31). The efficiency-corrected number of {1}-polarized photons $\mathcal{N}_{S1}$ and that of {2}-polarized photons $\mathcal{N}_{S2}$ are evaluated with the experiment parameters as

$$\mathcal{N}_{S1} = \frac{N_{S1}}{\epsilon_{\mathrm{opt1}}\epsilon_D}, \quad \mathcal{N}_{S2} = \frac{N_{S2}}{\epsilon_{\mathrm{opt2}}\epsilon_D}. \tag{82}$$

The upper limits of the signal yields per shot in the case of scalar and pseudo scalar fields exchange at a 95% confidence level are evaluated as

$$\mathcal{Y}_{\mathrm{sc}} = \frac{2.24\delta N_{S2}}{\epsilon_{\mathrm{opt2}}\epsilon_D W_S}, \quad \mathcal{Y}_{\mathrm{ps}} = \frac{2.24\delta N_{S1}}{\epsilon_{\mathrm{opt1}}\epsilon_D W_S}, \tag{83}$$

respectively.

We now assume the true number of signal yield is 0, since no significant signal is observed and the expected number of backgrounds are negligible. Therefore, the number of observed signals should follows the Poisson distribution whose mean is 0. δN_{S1} and δN_{S2} are defined as the standard deviations of the Poisson distributions and they are evaluated from the quadratic sum of the statistical and systematic errors of N_{S1} and N_{S2}, respectively. The upper limits of the searched mass ranges of both fields are given as

$$m < 2\omega \sin\Delta\theta \sim 2\omega\frac{d}{2f} = 0.15 \text{ eV}. \tag{84}$$

The exclusion limits for scalar and pseudoscalar fields obtained from this experiment are shown in Fig.47 and Fig.48, respectively.

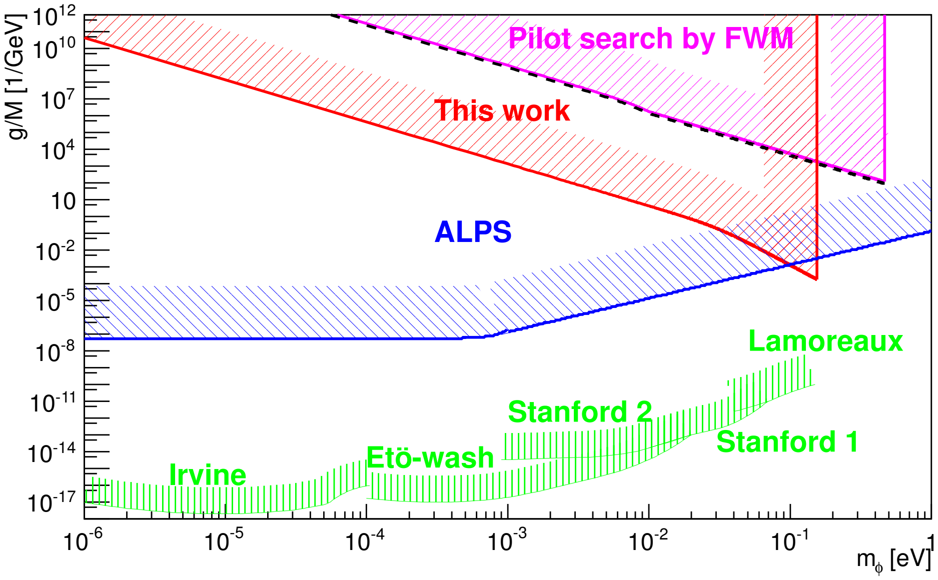

Figure 47. Exclusion limits for scalar fields (ϕ) in ϕ-photon coupling (g/M) as a function of mass of ϕ (m_ϕ) [47]. The excluded region at a 95% confidence level obtained from this experiment is drawn by the red shaded area. The magenta shaded area shows the excluded region by previous search in QPS [48], which is renewed from the black dotted line obtained from Ref.[48] by taking the incident-plane-rotation factor $\mathcal{G}$ into account. The blue shaded area represents the excluded region for scalar fields by light shining through a wall experiment "ALPS" [32] (the sine function part of the sensitivity curve is simplified to unity for drawing purposes at the mass region above 10^{-3}eV,). The green shaded areas indicate the limits given by non-Newtonian force searches by torsion balance experiments "Irvine" [49], "Eto-wash" [50, 51], "Stanford1" [11], "Stanford2" [8] and Casimir force measurement "Lamoreaux"[9].

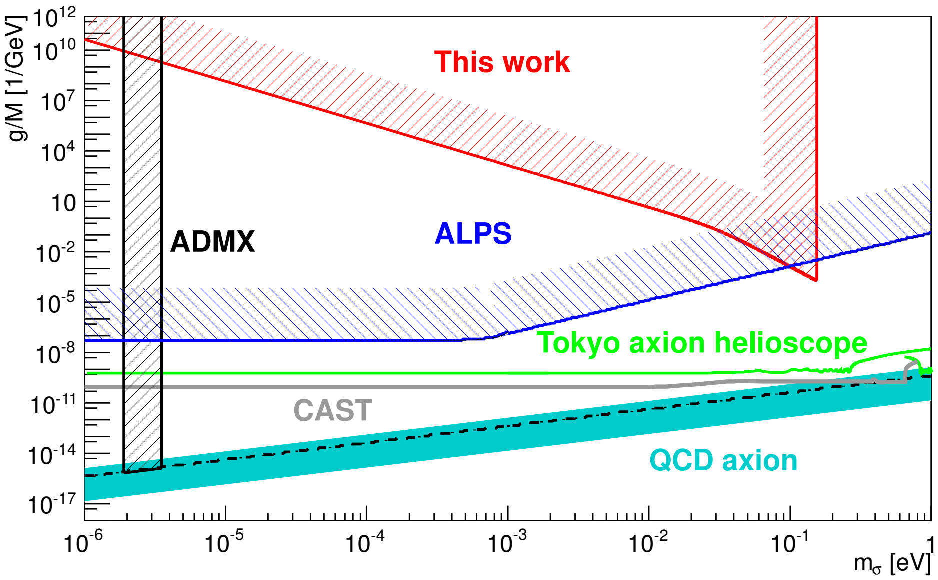

Figure 48. Exclusion limits for pseudoscalar fields (σ) in σ-photon coupling (g/M) as a function of mass of σ (m_σ) [47]. The blue shaded area shows the excluded region by the pseudoscalar search, "ALPS". The green and gray solid line show the exclusion limits from the solar axion experiments "Tokyo Axion Helioscope" [21, 22, 23] and "CAST" [25, 26, 27] , respectively. The black shaded area represents the result from the dark matter axion search using a microwave cavity "ADMX" [33, 34]. The cyan band indicates the expected coupling-mass relation of QCD axion predicted by KSVZ model[36, 37] with $|E/N - 1.95|$ in the range 0.07-7, furthermore, in the case of $E/N = 0$ is shown by the black dotted line.

8.2 Data table of experimental parameters

The experimental parameters are summarized in Tab.4. $\mathcal{G}^{\mathrm{sc}}$ and $\mathcal{G}^{\mathrm{ps}}$ represent $\mathcal{G}$ in the case of scalar and pseudoscalar fields exchange, respectively. The evaluation of $\mathcal{G}$ is discussed in Appendix A of this thesis.

$\mathcal{F}^{\mathrm{sc}}_{1122}$ and $\mathcal{F}^{\mathrm{ps}}_{1212}$ denote $\mathcal{F}_S$ in the case of scalar and pseudoscalar fields exchange, respectively. See the detail in Appendix B of this thesis.

The center of the wavelength of the inducing laser λ_i, the line width of the inducing laser $\delta\omega_4$, and the pulse duration of the inducing laser τ_i are referred from the values published by Spectra Physics.

The energy of the inducing laser per τ_i is evaluated as $E_i = \eta E_i^*$, where $\eta = 0.87$ is the overlapping factor given from section 5.2, and $E_i^* = 117.4 \pm 0.7\ \mu\mathrm{J}$ is obtained from Eq.(57).

The single-photon detection efficiency at 641nm is evaluated as $\epsilon_D = \xi\epsilon_D^*$, where $\xi = 0.67$ is the relative quantum efficiency between 532nm and 641nm lights provided by HAMAMATSU, and $\epsilon_D^* = 2.4 \pm 0.1$ % is given from Eq.(49).

Table 4: Data table of experimental parameters.

Parameters	Values
Center of wavelength of creation laser λ_c	800 nm
Relative line width of creation laser $(\delta\omega/\langle\omega\rangle)$	3.8×10^{-3}
Center of wavelength of inducing laser λ_i	1064 nm
Relative line width of inducing laser $(\delta\omega_4/\langle\omega_4\rangle)$	5.0×10^{-5}
Duration time of creation laser pulse per injection τ_c	900 fs
Duration time of inducing laser pulse per injection τ_i	9 ns
Creation laser energy per τ_c	9.3 ± 1.2 μJ
Inducing laser energy per τ_i	100 ± 1 μJ
Focal length f	200 mm
Beam diameter of laser beams d	20 mm
Upper mass range given by $\theta < \Delta\theta$	0.15 eV
$u = \omega_4/\omega$	0.75
Incident plane rotation factor $\mathcal{G}$	$\mathcal{G}^{\rm sc}_{11}$=19/32 $\mathcal{G}^{\rm ps}_{12}$=1/2
Axially asysmmetric factor $\mathcal{F}_S$	$\mathcal{F}^{\rm sc}_{1122}$=19.4 $\mathcal{F}^{\rm ps}_{1212}$=19.2
Combinatorial factor in luminosity C_{mb}	1/2
Single-photon detection efficiency at 641nm ϵ_D	1.4 ± 0.1 %
Efficiency of optical path from interaction point to path{1} $\epsilon_{\rm opt1}$	0.5 ± 0.1 %
Efficiency of optical path from interaction point to path{2} $\epsilon_{\rm opt2}$	0.9 ± 0.2 %
δN_{S1}	2.2
δN_{S2}	4.4

9 Conclusion

The search for scalar and psudoscalar fields via the quasi parallel colliding system (QPS) was performed by combining a 9.3 μJ/0.9 ps Ti-Sapphire laser and 100 μJ/9 ns Nd:YAG laser at 2.3×10^{-2} Pa.

The number of {1} and {2}-polarized signal-like photons are $N_{S1} = 0 \pm 0(\mathrm{stat.}) \pm 2.16(\mathrm{syst.I}) \pm 0.30(\mathrm{syst.II}) \pm 0(\mathrm{syst.III})$ and $N_{S2} = 1.46 \pm 1.27(\mathrm{stat.}) \pm 2.16(\mathrm{syst.I}) \pm 0.04(\mathrm{syst.II}) \pm 3.59(\mathrm{syst.III})$, respectively.

As a result, no significant signal was observed and the exclusion limits for scalar and psudoscalar fields were obtained at a 95% confidence level below 0.15 eV mass range. The most sensitive coupling limits $g/M = 2.05 \times 10^{-4}$ GeV^{-1} for scalar search and $g/M = 2.12 \times 10^{-4}$ GeV^{-1} for pseudoscalar search are obtained at $m = 0.15$ eV.

The pressure dependences of the four-wave mixing photons emitted from residual gas in the vacuum chamber were measured. The expected number of {1} and {2}-polarized photon per shot are $\mathcal{N}_{\mathrm{gas1}} = 1.7 \pm 1.1 \times 10^{-5}$, and $\mathcal{N}_{\mathrm{gas2}} = 1.7 \pm 1.1 \times 10^{-5}$ at 2.3×10^{-2} Pa.

The experimental methods developed in this thesis can be applicable to the future experiments with higher intensity lasers.

10 Future prospects

Here prospects for the future experiments with higher intensity lasers are discussed. There are several issues which can be considerable in the conditions using higher intensity lasers.

- How to suppress the number of background signals and how to estimate the number of them?

  The four-wave mixing photons from gas are negligible in this experiment. However, the finite number of background signals can be observed in higher intensity laser fields. They can be suppressed by achieving a higher vacuum pressure since the background signals have the quadratic dependence of the pressure as shown in Fig.42.

  If we use 1PW (10^{15} W) lasers in the future experiments, the vacuum pressure 10^{-10} Pa are necessary to suppress the four-wave mixing photon in gas less than 1 photon per shot. Achieving 10^{10}Pa is not easy since a large volume of vacuum components, for example, a vacuum chamber and beam transporting pipes, are used in high intensity laser systems. The reasonable solution is introducing the differential pumping system near the focal spot.

  In the high vacuum pressure, the quadratic pressure dependence of background signals can no be assured since the partial pressure should no be similar to that of near an atmospheric pressure. Therefore, the number of background signals should be estimated by considering what atoms dominate the measured pressure, and how many background photons expected to be emitted from them.

  Furthermore, the four-wave mixing photons emitted from optical components are also considerable. The material which through the intense laser can be main background sources. Thus, they should not be placed before signals are separated from incident lasers. For example, beam focusing should be done by not a convex lens but a parabolic mirror.

- How much sensitivity can future experiments reach?

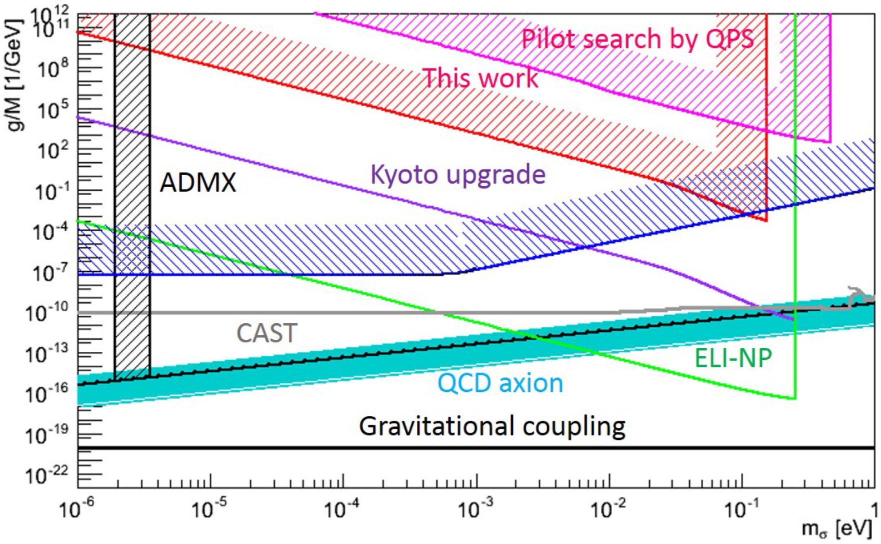

Figure 49. The expected sensitivities obtained by future experiments.

An upgraded experiment is developing with 10TW laser at Kyoto university and 10PW laser at ELI-NP (Extreme Light Infrastructure - Nuclear Physics) [52], which is being constructed in Romania and it will run from 2018. The expected sensitivities are shown in Fig.49. The purple line is expected sensitivity by Kyoto 10TW experiment and it will reach to QCD axion line at sub-eV mass region. The green line indicates the expected sensitivity in ELI-NP. The sensitivity by ELI-NP experiment will not reach to the gravitational coupling. Therefore, an extremely higher intensity lasers are required for the dilaton search.

Here the worldwide laser community IZEST (International center on Zette-Exawatt Science and Technology) [53] is introduced. This is associated from more than 30 institutions including Kyoto university and ELI-NP to develop the extremely high intensity lasers and contributing to fundamental physics research. The dark field search experiment via QPS is positioned as one of the important researches in IZEST community. Therefore, the dilaton search will become factual in the future.

Acknowledgement

First of all, I express my gratitude to Assist. Prof. K. Homma. for giving me the opportunity for studying this exiting subject. Enormous amount of time for discussion with him guide my doctoral thesis to complete.

I gratefully thank my supervisor Prof. T. Sugitate for his general support and advice for my academic life.

I cordially appreciate Prof. S. Sakabe for his much support and tutelage for my research in Kyoto University. I express my gratitude to Assoc. Prof. M. Hashida, Assist. Prof. S. Inoue, Assist. Prof. S. Tokita, Dr. K. Otani and Dr. Y. Miyasaka for giving me a lot of advice about the experimental knowledges and techniques about laser optics. They always provided high quality experimental environment to me during my stay in Kyoto University.

K. Kume contributes a lot to develop the analysis method and the experimental setup at the early phase of this experimental research.

I acknowledge Y. Inoue providing the data list of the sensitive curve for the Tokyo axion helioscope.

I appreciate T. Takahashi for his appropriate advice and discussion for my doctoral thesis.

I gratefully thank all members of quark physics laboratory at Hiroshima University and members of Sakabe lab. in Kyoto University.

Finally, I would like to thank my parents for their long-term support during my academic life.

Appendix A: Incident plane rotation factor $\mathcal{G}$

The relations of the linear polarization states between the initial and final state photons can be written as

$$\begin{aligned} \omega\{1\} + \omega\{1\} &= \omega_3\{1\} + \omega_4\{1\}, \\ \omega\{1\} + \omega\{1\} &= \omega_3\{2\} + \omega_4\{2\}, \end{aligned} \tag{85}$$

or

$$\begin{aligned} \omega\{1\} + \omega\{2\} &= \omega_3\{1\} + \omega_4\{2\}, \\ \omega\{1\} + \omega\{2\} &= \omega_3\{2\} + \omega_4\{1\}. \end{aligned} \tag{86}$$

Equations(85) and (86) correspond to the case of scalar and pseudoscalar fields exchange, respectively. We note that these descriptions can be applied when all photons are on the same reaction plane. However, in the focused geometry in QPS, the theoretical incident polarization plane consists of the incident photon pair p_1 and p_2 has a rotational degree of freedom. Therefore, if we fix the polarization vector of the incident laser to $\{1\}$ or $\{2\}$, the theoretical polarization vectors (1) and (2) are defined independently. As a result, the focusing QPS has the sensitivity for scalar and pseudoscalar fields, simultaneously, even we fix the polarization vectors of the incident photons to $\{1\}$ or $\{2\}$.

The outgoing $p_3 - p_4$ plane also has the rotation degree of freedom with the rotation angle φ independent of the rotation of the incident $p_1 - p_2$ plane.

To evaluate the signal yields of scalar and pseudoscalar fields in the focused QPS, a weighted averaging factor $\mathcal{G}$ over the rotation angle of the incident plane Φ is introduced.

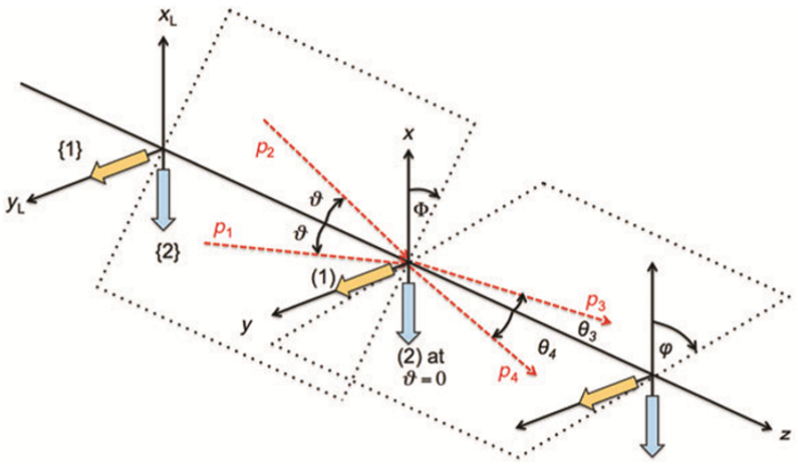

Figure 50. The definitions of polarization vectors and rotation angles in QPS [47].

First of all, the s-channel scattering amplitude is expressed as

$$\mathcal{M}_S = -(gM^{-1})^2 \frac{\mathcal{V}_{ab}^{[1]} \mathcal{V}_{cd}^{[2]}}{(p_1 + p_2)^2 + m^2}, \tag{87}$$

where $S \equiv$ abcd with a,b,c,d = 1 or 2, respectively, denotes a sequence of polarization states of four photons.

The Φ-dependent squared transition amplitude should be averaged over the possible rotation angle from 0 to 2π. Thus, we define the incident plane rotation factor as follows:

$$\mathcal{G}_{ab} \equiv \frac{\int_0^{2\pi} |\mathcal{V}_{ab}^{[1]}(\Phi)|^2 d\Phi}{\int_0^{2\pi} |\mathcal{V}_{ab}^{[1]}(\Phi = 0)|^2 d\Phi}. \tag{88}$$

The vertex factors for the scalar fields exchange (SC) are expressed as

$$\begin{aligned} \mathcal{V}_{ab}^{[1]\mathrm{SC}} &= (p_1 p_2)(e_1^{(a)} e_2^{(b)}) - (p_1 e_2^{(a)})(p_2 e_1^{(b)}), \\ \mathcal{V}_{cd}^{[2]\mathrm{SC}} &= (p_3 p_4)(e_3^{(c)} e_4^{(d)}) - (p_3 e_4^{(c)})(p_4 e_3^{(d)}). \end{aligned} \tag{89}$$

In the pseudoscalar fields exchange (PS),

$$\begin{aligned} \mathcal{V}_{ab}^{[1]\mathrm{PS}} &= -\epsilon^{\mu\nu\rho\sigma} p_{1\mu} p_{2\rho} e_{1\nu}{}^{(a)} e_{2\sigma}{}^{(b)}, \\ \mathcal{V}_{cd}^{[2]\mathrm{PS}} &= -\epsilon^{\mu\nu\rho\sigma} p_{3\mu} p_{4\rho} e_{3\nu}{}^{(c)} e_{4\sigma}{}^{(d)}, \end{aligned} \tag{90}$$

(91)

where ϵ is the Levi-Civita tensor.

The momenta and polarization vectors of four photons are expressed as follows:

$$\begin{aligned}
e_i^{(1)} &= (0,1,0), \\
e_1^{(2)} &= (-\cos\vartheta, 0, \sin\vartheta), \\
e_2^{(2)} &= (-\cos\vartheta, 0, -\sin\vartheta), \\
e_3^{(2)} &= (-\cos\theta_3, 0, \sin\theta_3), \\
e_4^{(2)} &= (-\cos\theta_4, 0, -\sin\theta_4), \\
p_1 &= (\omega\sin\vartheta\cos\Phi, -\omega\sin\vartheta\sin\Phi, \omega\cos\vartheta), \\
p_2 &= (-\omega\sin\vartheta\cos\Phi, \omega\sin\vartheta\sin\Phi, \omega\cos\vartheta), \\
p_3 &= (\omega_3\sin\theta_3\cos\varphi, -\omega_3\sin\theta_3\sin\varphi, \omega_3\cos\theta_3), \\
p_4 &= (-\omega_4\sin\theta_4\cos\varphi, \omega_4\sin\theta_4\sin\varphi, \omega_4\cos\theta_4). \qquad (92)
\end{aligned}$$

We evaluate the first vertex factor in case of $ab = 11$ for the scalar exchange as

$$\begin{aligned}
\mathcal{V}_{11}^{[1]\mathrm{SC}} &= (p_1p_2)(e_1^{(1)}e_2^{(1)}) - (p_1e_2^{(1)})(p_2e_1^{(1)}) \\
&= \omega^2(\cos 2\vartheta - 1 + \sin^2(\vartheta)\sin^2\Phi) \sim \omega^2\vartheta^2(2-\sin^2\Phi), \qquad (93)
\end{aligned}$$

where the approximation is based on $\vartheta \sim \vartheta_r \ll 1$.

In the case of $ab = 12$ for the pseudoscalar exchange,

$$\begin{aligned}
\mathcal{V}_{12}^{[1]\mathrm{PS}} &= -\epsilon^{\mu\nu\rho\sigma}p_{1\mu}p_{2\rho}{e_{1\nu}}^{(1)}{e_{2\sigma}}^{(2)} \\
&= -2\omega^2\sin^2\vartheta\cos\Phi. \qquad (94)
\end{aligned}$$

We obtain the incident plane rotation factor in case of scalar exchange as

$$\mathcal{G}_{11}^{\mathrm{SC}} = \frac{\int_0^{2\pi}(2-\sin^2\Phi)^2 d\Phi}{8\pi} = \frac{19}{32}. \qquad (95)$$

In the case of the pseudoscalar exchange, we obtain

$$\mathcal{G}_{12}^{\mathrm{PS}} = \frac{\int_0^{2\pi}(\cos^2\varphi)d\varphi}{8\pi} = \frac{1}{2}. \qquad (96)$$

Appendix B: Axially asymmetric factor $\mathcal{F}_S$

The outgoing $p_3 - p_4$ plane has the rotation degree of freedom as well as the incident $p_1 - p_2$ plane. From Eq.(89), the second vertex factor in case of *cd* = 22 for the scalar exchange is given as

$$\begin{aligned} \mathcal{V}_{22}^{[2]\mathrm{SC}} &= (p_3 p_4)(e_3^{(2)} e_4^{(2)}) - (p_3 e_4^{(2)})(p_4 e_3^{(2)}) \\ &= \omega_3 \omega_4 \{\cos(\theta_3 + \theta_4)(\cos(\theta_3 + \theta_4) - 1) + (1 + \cos^2\varphi)\sin\theta_3 \sin\theta_4 \cos\theta_3 \cos\theta_3 \\ &+ (\sin^2\theta_3 \cos^2\theta_4 + \sin^2\theta_4 \cos^2\theta_3)\cos\varphi\}. \end{aligned} \tag{97}$$

For a small ϑ, the approximations $\sin\vartheta_3 \sim \sqrt{\mathcal{R}}\vartheta$ and $\sin\vartheta_4 \sim 1/\sqrt{\mathcal{R}}\vartheta$ are used with $\mathcal{R} \equiv \sin\theta_3 / \sin\theta_4 = \omega_4/\omega_3$.

Then, $\cos(\theta_3 + \theta_4)$ is rewritten as

$$\cos(\theta_3 + \theta_4) \sim 1 - \vartheta^2(1 + \hat{\mathcal{R}}), \tag{98}$$

with

$$\hat{\mathcal{R}} \equiv \frac{1}{2}(\mathcal{R} + \mathcal{R}^{-1}). \tag{99}$$

Equation (97) is approximated as

$$\mathcal{V}_{22}^{[2]\mathrm{SC}} \sim \omega_3 \omega_4 \vartheta^2 \{\cos^2\varphi + (2\cos\varphi - 1)\hat{\mathcal{R}}\} \equiv \omega_3 \omega_4 \vartheta^2 F(\vartheta). \tag{100}$$

The axially asymmetric factor $\mathcal{F}_S$ for the scalar exchange case are defined as

$$\mathcal{F}_{1122}^{\mathrm{SC}} \equiv \int_0^{2\pi} F^2(\varphi) d\varphi \sim 2\pi \left(\frac{3}{8} + 3\hat{\mathcal{R}}^2 - \hat{\mathcal{R}} \right). \tag{101}$$

In the case of pseudoscalar exchange, the second vertex factor at *cd* = 12 are evaluated as

$$\begin{aligned} \mathcal{V}_{12}^{[2]\mathrm{PS}} &= -\epsilon^{\mu\nu\rho\sigma} p_{3\mu} p_{4\rho} e_{3\nu}{}^{(1)} e_{4\sigma}{}^{(2)} \\ &= -\omega_3 \omega_4 \{\cos\theta_4(-\cos\theta_3 + \cos\theta_4) + \sin\theta_4(\sin\theta_4 + \sin\theta_3 \cos\varphi) \\ &\sim -\omega_3^2 \omega_4^2 \vartheta^2 \{\check{\mathcal{R}} + (\mathcal{R}^{-1} + 1)\cos\varphi\} \equiv -\omega_3^2 \omega_4^2 \vartheta^2 G(\varphi), \end{aligned} \tag{102}$$

with

$$\check{\mathcal{R}} \equiv \frac{1}{2}(\mathcal{R} - \mathcal{R}^{-1}). \tag{103}$$

As a result, the axially asymmetric factor for the pseudoscalar exchange is given as

$$\mathcal{F}_{1122}^{\rm PS} \equiv \int_0^{2\pi} G^2(\varphi) d\varphi \sim 2\pi \left(\check{\mathcal{R}} + \frac{1}{2}(\mathcal{R}^{-1}+1)^2 \right). \tag{104}$$

Appendix C: The effect of finite spectrum widths of the creation and the inducing lasers

The description of the $\gamma\gamma \to \phi/\sigma \to \gamma\gamma$ process in QPS are based on the condition that the incident photon pair have the same photon energy ω and the same incident angle ϑ. However, the incident photons have the energy uncertainties due to the finite spectrum width of the creation laser. Therefore, the energy-asymmetric collisions of the incident photon pairs should be considered when evaluate the signal yield.

Here the energy conservation is introduced again.

$$\begin{aligned} \omega &+ \omega \to (2-u)\omega + u\omega \\ = \omega &+ \omega \to \omega_3 + \omega_4 \end{aligned} \tag{105}$$

The finite spectrum widths of the creation and inducing lasers give the uncertainty of u as $\underline{u} \leq u \leq \overline{u}$. As a result, the signal photon also has the finite spectrum width.

We now introduce the following notations for the photon energies as

$$\begin{aligned} \omega &= \langle\omega\rangle \pm \delta\omega \\ \omega_3 &= \langle\omega_3\rangle \pm \delta\omega_3 \\ \omega_4 &= \langle\omega_4\rangle \pm \delta\omega_4 \end{aligned} \tag{106}$$

where $\langle\omega\rangle$, $\langle\omega_3\rangle$, and $\langle\omega_4\rangle$ are the average of the energies of the creation, signal, and inducing photons, respectively, and $\delta\omega$, $\delta\omega_3$, and $\delta\omega_4$ are their energy fluctuations. $\delta\omega$ and $\delta\omega_4$ are given by the spectrum width of the creation and inducing lasers, respectively. These notations are based on the practical laboratory frame, referred to as L-system, with different incident photon energies ω_1 and ω_2 and corresponding incident angles ϑ_1 and ϑ_2. To apply the ideal description that the incident photon pair have the same incident photon energy and incident angle, referred to as $\langle L\rangle$-system, the following notations are introduced.

$$\begin{aligned} \omega &= \langle\omega\rangle \\ \omega_3 &= \langle\omega_3\rangle \pm \Delta\omega_3 \\ \omega_4 &= \langle\omega_4\rangle \pm \Delta\omega_4 \end{aligned} \tag{107}$$

In the $\langle L\rangle$-system, δ_ω is effectively invisible by operating the transverse Lorentz boost. $\Delta\omega_3$ and $\Delta\omega_4$ include not only $\delta\omega_3$ and $\delta\omega_4$ but also the energy uncertainties originating from absorbing $\delta\omega$ by transition from L-system to $\langle L\rangle$-system. The energy and the transverse momentum of the incident photons ω and p_{T} have relations between L-system and $\langle L\rangle$-system as follows:

$$\begin{aligned}
\begin{pmatrix} \omega_1 \\ p_{1T} \end{pmatrix} &= \gamma \begin{pmatrix} 1 & -\beta \\ -\beta & 1 \end{pmatrix} \begin{pmatrix} \langle\omega\rangle \\ \langle\omega\rangle \sin\vartheta \end{pmatrix}, \\
\begin{pmatrix} \omega_2 \\ p_{2T} \end{pmatrix} &= \gamma \begin{pmatrix} 1 & -\beta \\ -\beta & 1 \end{pmatrix} \begin{pmatrix} \langle\omega\rangle \\ -\langle\omega\rangle \sin\vartheta \end{pmatrix},
\end{aligned} \tag{108}$$

where β is the relative velocity with respect to the velocity of light c and $\gamma = (1-\beta^2)^{-1/2}$. From Eq.(108), ω_1 and ω_2 are expressed as

$$\begin{aligned}
\omega_1 &= \gamma\langle\omega\rangle(1-\beta\sin\vartheta) \equiv \langle\omega\rangle - \delta\omega \equiv \langle\omega\rangle\,(1-\delta r)\,, \\
\omega_2 &= \gamma\langle\omega\rangle(1+\beta\sin\vartheta) \equiv \langle\omega\rangle + \delta\omega \equiv \langle\omega\rangle\,(1+\delta r)\,,
\end{aligned} \tag{109}$$

where $\delta r \equiv \delta\omega/\langle\omega\rangle$ is the relative line width with respect to the mean energy of the creation laser.

β for ω_1 and ω_2 satisfies the following equations with introducing the notation β_1 and β_2 corresponds to ω_1 and ω_2, respectively with $\delta r \ll 1$.

$$\begin{aligned}
(1+\sin^2\vartheta - 2\delta r)\beta_1^2 - 2\sin\vartheta\beta_1 + 2\delta r = 0, \\
(1+\sin^2\vartheta + 2\delta r)\beta_2^2 + 2\sin\vartheta\beta_2 - 2\delta r = 0.
\end{aligned} \tag{110}$$

In the case of β_1, the following solution is given with $\vartheta \ll 1$.

$$\beta_{1\pm} \equiv \frac{\vartheta \pm \sqrt{D}}{1+\vartheta^2-2\delta r} \sim (1-\vartheta^2+2\delta r)\left(\vartheta \pm \sqrt{D}\right), \tag{111}$$

where

$$D \sim \vartheta^2 - (1+\vartheta^2-2\delta r)2\delta r \sim \vartheta^2 - 2\delta r. \tag{112}$$

The constraint of $D \geq 0$ gives

$$2\delta r \leq \vartheta^2. \tag{113}$$

If this is satisfied, $\sqrt{D} \sim (\vartheta^2 - 2\delta r)^{1/2} \sim \vartheta - \delta r/\vartheta$ with $\delta r \ll 1$ gives

$$\vartheta \pm \sqrt{D_1} \sim \vartheta \pm \left(\vartheta - \frac{\delta r}{\vartheta}\right). \tag{114}$$

As a result, $\beta_{1\pm}$ are expressed as

$$\begin{aligned}\beta_{1+} &\sim (1-\vartheta^2+2\delta r)\left(2\vartheta-\frac{\delta r}{\vartheta}\right)\sim 2\vartheta-\frac{\delta r}{\vartheta},\\ \beta_{1-} &\sim (1-\vartheta^2+2\delta r)\left(\frac{\delta r}{\vartheta}\right)\sim\frac{\delta r}{\vartheta}>0,\end{aligned}\tag{115}$$

where β_{1+} is not acceptable because the limit of $\delta r \to 0$ indicates $\beta = 0$.

β_2 is similarly obtained as

$$\begin{aligned}\beta_{2+} &\sim (1+\vartheta^2+2\delta r)\left(\frac{\delta r}{\vartheta}\right)\sim\frac{\delta r}{\vartheta}>0,\\ \beta_{2-} &\sim (1+\vartheta^2+2\delta r)\left(-2\vartheta-\frac{\delta r}{\vartheta}\right)\sim -2\vartheta-\frac{\delta r}{\vartheta},\end{aligned}\tag{116}$$

where β_{2-} is not acceptable because the limit of $\delta r \to 0$ indicates $\beta = 0$ as well as β_{1+}.

As a result, β is given as

$$\beta \sim \beta_{1-} = \beta_{2+} = \frac{\delta r}{\vartheta}.\tag{117}$$

By substituting δr in Eq.(117) into Eq.(113), the range of β is expressed as

$$\beta < \frac{\vartheta}{2}.\tag{118}$$

Among ϑ within $\Delta\vartheta$, ϑ_r is effectively enhanced based on the Breit-Wigner distribution in the averaging process of the square of the invariant scattering amplitude around $E_{\mathrm{CMS}} = 2\sin\vartheta_r\langle\omega\rangle$. Therefore, for a given mass $m \sim 2\langle\omega\rangle\vartheta_r$ with $\vartheta_r \ll 1$, the effective physical limit on β is expressed as

$$\beta_r \equiv \frac{\delta r}{\vartheta_r} < \frac{\vartheta_r}{2}.\tag{119}$$

On the other hand, the full line width of a creation laser $\Delta r \equiv \delta\omega_{\mathrm{full}}/\langle\omega\rangle$ is intrinsically determined. Therefore, the maximum range of β is given as

$$0 < \beta < \beta_c \equiv \frac{\Delta r}{\vartheta}.\tag{120}$$

If β_c is smaller than β_r, the upper limit of β_r is constrained as $\beta_r \le \beta_c$ duo to the instrumental limit of the spectrum width of the creation laser. Therefore smaller β, either β_c or β_r has to be chosen.

The range of u originating from the spectrum width of the creation laser in the $\langle L\rangle$-system is notated as $\underline{u}_c \le u \le \overline{u}_c$. $\underline{u}_c$ and $\overline{u}_c$ are evaluated as

$$\begin{aligned}
\overline{u}_c\langle\omega\rangle &\sim l_{i+}u\langle\omega\rangle\gamma(1+\beta\vartheta) \equiv l_{i-}u\langle\omega\rangle \min\{\gamma_c(1+\Delta r), \quad \gamma_r(1+\frac{1}{2}\vartheta_r^2)\} \\
\underline{u}_c\langle\omega\rangle &\sim l_i u\langle\omega\rangle\gamma(1-\beta\vartheta) \equiv l_i u\langle\omega\rangle \min\{\gamma_c(1-\Delta r), \quad \gamma_r(1-\frac{1}{2}\vartheta_r^2)\}
\end{aligned} \tag{121}$$

where l_i represents the process to choose a ω_4 within the relative line width of the inducing laser with $l_{i\pm} \equiv 1 \pm \delta\omega_4/\langle\omega_4\rangle$, γ_c and γ_i are defined as $\gamma_c = (1-\beta_c^2)^{-1/2}$ and $\gamma_r = (1-\beta_r^2)^{-1/2}$ respectively, and $\min\{A, B\}$ requires to choose smaller one between A and B.

The effective spectrum width of the inducing laser broadens by absorbing that of the creation laser in $\langle L\rangle$-system. We introduce a following notation as including the effect of the spectrum widths of the creation and the inducing lasers

$$\omega_{<4>} \equiv l_c l_i u\langle\omega\rangle, \tag{122}$$

where $l_c \equiv 1 \pm \delta u_c/u$ with $\delta u_c \equiv (\overline{u_c} - \underline{u_c})/2$. The inclusive uncertainty on ω_4 in the $\langle L\rangle$-system is evaluated as

$$\delta^2\omega_{<4>} = \left(\frac{\partial\omega_{<4>}}{\partial l_i}\right)^2 \delta^2 l_i + \left(\frac{\partial\omega_{<4>}}{\partial l_c}\right)^2 \delta^2 l_c = u^2\langle\omega\rangle^2 \left[\left(\frac{\delta u_4}{u}\right)^2 + \left(\frac{\delta u_c}{u}\right)^2\right]. \tag{123}$$

The inclusive uncertainty on u is given as

$$\delta u_{\mathrm{inc}} \equiv \frac{\delta\omega_{<4>}}{\langle\omega\rangle} = u\sqrt{\left(\frac{\delta u_4}{u}\right)^2 + \left(\frac{\delta u_c}{u}\right)^2}. \tag{124}$$

The upper and lower limits of u is obtained as

$$\begin{aligned}
\overline{u} &\equiv u + \delta u_{\mathrm{inc}}, \\
\underline{u} &\equiv u - \delta u_{\mathrm{inc}},
\end{aligned} \tag{125}$$

respectively.

Appendix D: Evaluation of the signal yield in QPS

The signal yield $\mathcal{Y}$ in QPS is evaluated as following policy.

$$\mathcal{Y} = \mathcal{D}[\mathrm{s/L^3}]\overline{\Sigma}[\mathrm{L^3/s}], \tag{126}$$

where $\mathcal{D}$ is the time-integrated density and Σ is the interaction volume per unit time.

From Eq.(2.5) of Ref.[39], the differential cross section per solid angle of the signal photon is expressed as

$$\frac{d\sigma}{d\Omega_3} = \left(\frac{1}{8\pi\omega}\right)^2 \sin\vartheta^{-4} \left(\frac{\omega_3}{2\omega}\right)^2 |\mathcal{M}_S(\vartheta)|^2. \tag{127}$$

The output angle of the signal photon θ_3 fluctuates by the effect of the spectrum width of the inducing laser $\delta\omega_4$. The integrated cross section over the range of θ_3 is expressed as

$$\sigma(\vartheta) = \frac{\mathcal{F}_S|\mathcal{M}_S(\vartheta)|^2}{(8\pi\omega)^2\sin^4\vartheta}\int_{\underline{\theta_3}}^{\overline{\theta_3}} \left(\frac{\omega_3}{2\omega}\right)^2 \sin\theta_3 d\theta_3, \tag{128}$$

where $\overline{\theta_3}$ and $\underline{\theta_3}$ are the upper and lower limits of θ_3, respectively. The interaction cross section into the interaction volume per unit time $\Sigma(\vartheta)$ is denoted as

$$\Sigma(\vartheta) = K(\vartheta)\sigma(\vartheta) \sim \frac{2c^3\mathcal{F}_S|\mathcal{M}_S(\vartheta)|^2}{(8\pi)^2}\left(\frac{\lambda_c}{2\pi c}\right)^2 \frac{\delta u}{4} \quad \left[\mathrm{L^3/s}\right] \tag{129}$$

where $K(\vartheta)$ is the relative velocity of incoming particle beams defined as

$$K(\vartheta) \equiv \sqrt{(\vec{v_1}-\vec{v_2})^2 - \frac{(\vec{v_1}\times\vec{v_2})^2}{c^2}} = 2c\sin^2\vartheta, \tag{130}$$

λ_c is the wavelength of the creation laser, $\delta u \equiv \overline{u} - \underline{u}$. The averaged value of $\Sigma(\vartheta)$ over ϑ is expressed as

$$
\begin{aligned}
\overline{\Sigma} &= \int_0^{\pi/2} d\vartheta \rho(\vartheta)\Sigma(\vartheta) \\
&= \frac{c\mathcal{F}_S \lambda_c^2 \delta u}{2(16\pi^2)^2} \int_0^{\pi/2} d\vartheta \rho(\vartheta) |\mathcal{M}_S(\vartheta)|^2 \\
&\sim \frac{c\mathcal{W}\mathcal{F}_S \lambda_c^2 \delta u}{4\sqrt{\pi}(4\pi)^3} \left(\frac{\vartheta_r}{\Delta\theta}\right) \left(\frac{gm}{M}\right)^2 . \qquad (131)
\end{aligned}
$$

Then, we evaluate the time-integrated density factor $\mathcal{D}$ based on the Gaussian laser beam propagation. The density profile of an incident Gaussian laser at the focal point $z = 0$ with the pulse duration time τ_c propagating over the focal length f along z-axis are expressed as

$$
\rho_c(x, y, z, t) = \frac{2N_c}{\pi w^2(z)} \exp\left\{-2\frac{x^2 + y^2}{w^2(z)}\right\} \frac{1}{\sqrt{\pi} c\tau_c} \exp\left\{-\left(\frac{z'}{c\tau_c}\right)^2\right\}, \quad (132)
$$

where N_c is the number of creation photons per pulse.

The time-integrated density factor for the creation laser $\mathcal{D}_c$ is expressed as

$$
\begin{aligned}
\mathcal{D}_c &= \int_{-f/c}^{0} dt \int_{-\infty}^{\infty} dx \int_{-\infty}^{\infty} dy \int_{-\infty}^{\infty} dz {\rho_c}^2(x, y, z, t) \\
&= \frac{N_c^2}{\sqrt{2\pi}} \frac{1}{\pi {w_0}^2} \frac{1}{c\tau_c} \frac{z_R}{c} \tan^{-1}\left(\frac{f}{z_R}\right) \quad \left[s/L^3\right], \qquad (133)
\end{aligned}
$$

where the time integration is performed during the pulse propagation from $z = -f$ to $z = 0$, since the photon-photon scattering never occurs after they pass through the focal point.

The effect of the inducing laser beam under the practical experimental condition is should be considered. The inducing effect is expected only when the momentum of the one of the final state photon p_4 coincides with a photon momentum included in the coherent state of the inducing beam. When the final state of photons accept the inducing effect, it should satisfies following resonance condition,

$$
E_{\mathrm{CMS}} = m = 2\omega \sin\vartheta_r. \qquad (134)
$$

Therefore, p_4 has to be expressed with the condition $\vartheta = \vartheta_r$. Then, following relations are obtained with approximation $\vartheta_r \ll 1$,

$$
\theta_4 \sim \mathcal{R}^{-1/2}\vartheta_r \quad \text{and} \quad \theta_3 \sim \mathcal{R}^{1/2}\vartheta_r, \qquad (135)
$$

where

$$\mathcal{R} \equiv \frac{\sin\theta_3}{\sin\theta_4} = \frac{\omega_4}{\omega_3} = \frac{u}{2-u}. \tag{136}$$

These relations indicate that the final state photons emitted as a ring-like patterns.

Next, the overlapping between the p_4 and the fraction of photon momenta in the inducing beam is discussed. The electric field distribution at $z = 0$ is described as following expression,

$$\begin{aligned} \vec{E}(k_x, k_y; z=0) &= \vec{E_0}\frac{w_0^2}{4\pi}\exp\left\{-\frac{w_0^2}{4}(k_x^2+k_y^2)\right\} \\ &\equiv \vec{E_0}\frac{w_0^2}{4\pi}\exp\left\{-\frac{w_0^2}{4}k_T^2\right\}, \end{aligned} \tag{137}$$

where the transverse wave vector component $k_T^2 = k_x^2 + k_y^2$ is introduced.

The electric filed distribution of the inducing beam is expressed as

$$\vec{E_4}(k_x, k_y; z=0) = \vec{E_{04}}\frac{w_{04}^2}{4\pi}\exp\left\{-\frac{w_{04}^2}{4}(k_{T4}^2)\right\} \tag{138}$$

The acceptance factor $\mathcal{A}_i$ is evaluated as

$$\begin{aligned} \mathcal{A}_i &\equiv \frac{\int_{\underline{k_{T4}}}^{\overline{k_{T4}}} 2\pi k_{T4} E_4^2 dk_{T4}}{\int_0^\infty 2\pi k_{T4} E_4^2 dk_{T4}} = e^{-\frac{w_{04}^2}{2}\underline{k_{T4}}^2} - e^{-\frac{w_{04}^2}{2}\overline{k_{T4}}^2} \\ &\sim \frac{w_{04}^2}{2}(\overline{k_{T4}}^2 - \underline{k_{T4}}^2) \sim \frac{w_{04}^2 k_4^2}{2}\vartheta_r^2(\underline{\mathcal{R}}^{-1} - \overline{\mathcal{R}}^{-1}) \\ &\sim 2(\underline{\mathcal{R}}^{-1} - \overline{\mathcal{R}}^{-1})\left(\frac{\vartheta_r}{\Delta\theta}\right)^2 = 4\frac{\overline{u}-\underline{u}}{\overline{u}\underline{u}}\left(\frac{\vartheta_r}{\Delta\theta}\right)^2, \end{aligned} \tag{139}$$

with

$$k_{T4} \equiv k_4 \sin\theta_4 \sim k_4 \mathcal{R}^{-1/2}\vartheta_r, \tag{140}$$

where $\underline{k_{T4}}$ and $\overline{k_{T4}}$ defined as the lower and upper values of k_{T4}, the approximation $w_{04}k_{T4} \ll 1$ and $k_{T4} \sim k_4\mathcal{R}^{-1/2}\vartheta_r$ are applied in the first and second lines, respectively, and

$$w_{04}k_4 = \frac{2\pi w_{04}}{\lambda_i} \equiv \frac{2}{\Delta\theta_4} \sim \frac{2}{\Delta\theta} \tag{141}$$

is substituted in the third line.

Furthermore, the overlapping effect of pulse durations of the creation and inducing lasers should be considered. This is because the inducing photons contribute the enhancement effect have to coincide with the creation photons at the time-dimension. When we simulate the pulse duration of the creation laser τ_c is shorter that that of the inducing laser τ_i, the entire inducing effect is expressed as

$$\mathcal{I} = \mathcal{A}_i \left(\frac{\tau_c}{\tau_i}\right) N_i = 4\frac{\overline{u} - \underline{u}}{\overline{u}\underline{u}} \left(\frac{\vartheta_r}{\Delta\theta}\right)^2 \left(\frac{\tau_c}{\tau_i}\right) N_i. \tag{142}$$

The density factor including the inducing laser effect $\mathcal{D}_{c+i}$ is expressed as follows:

$$\begin{aligned} \mathcal{D}_{c+i} &= C_{\mathrm{mb}} \mathcal{D}_c \mathcal{I} \\ &= C_{\mathrm{mb}} \frac{N_c^2}{\sqrt{2\pi}} \frac{1}{\pi {w_0}^2} \frac{1}{c\tau_c} \frac{z_R}{c} \tan^{-1}\left(\frac{f}{z_R}\right) 4\delta\mathcal{U} \left(\frac{\vartheta_r}{\Delta\theta}\right)^2 \left(\frac{\tau_c}{\tau_i}\right) N_i \\ &= \frac{4}{\sqrt{2\pi}} \frac{1}{c^2\lambda_c\tau_c} \left(\frac{\tau_c}{\tau_i}\right) \tan^{-1}\left(\frac{\pi d^2}{4\ f\lambda_c}\right) \left(\frac{\vartheta_r}{\Delta\theta}\right)^2 \\ &\times \frac{\overline{u} - \underline{u}}{\overline{u}\underline{u}} C_{\mathrm{mb}} N_c^2 N_i, \end{aligned} \tag{143}$$

where $C_{\mathrm{mb}} = 1/2$ is the combinatorial factor originating from the combination of choosing two photons among frequency multimode states in creation and inducing lasers.

The signal yield $\mathcal{Y}$ is finally expressed as

$$\begin{aligned} \mathcal{Y} &= \mathcal{D}_{c+i} \overline{\Sigma} \\ &= \frac{4}{\sqrt{2\pi}} \frac{1}{c^2\lambda_c\tau_c} \left(\frac{\tau_c}{\tau_i}\right) \tan^{-1}\left(\frac{\pi d^2}{4\ f\lambda_c}\right) \left(\frac{\vartheta_r}{\Delta\theta}\right)^2 \frac{\overline{u} - \underline{u}}{\overline{u}\underline{u}} C_{\mathrm{mb}} N_c^2 N_i \\ &\times \frac{c\mathcal{W}\mathcal{F}_S\lambda_c^2\delta u}{4\sqrt{\pi}(4\pi)^3} \left(\frac{\vartheta_r}{\Delta\theta}\right) \left(\frac{gm}{M}\right)^2 \\ &\sim \frac{1}{64\sqrt{2}\pi^4} \left(\frac{\lambda_c}{c\tau_c}\right) \left(\frac{\tau_c}{\tau_i}\right) \left(\frac{f}{d}\right)^3 \tan^{-1}\left(\frac{\pi d^2}{4\ f\lambda_c}\right) \\ &\times \frac{(\overline{u} - \underline{u})^2}{\overline{u}\underline{u}} \left(\frac{gm[eV]}{M[eV]}\right)^2 \left(\frac{m[eV]}{\omega[eV]}\right)^3 \mathcal{W}\mathcal{F}_S C_{\mathrm{mb}} N_c^2 N_i, \end{aligned} \tag{144}$$

where the parameters specified with [eV] apply natural units.

Appendix E: Scalar-tensor theory and dilaton

Here physics backgrounds for the scalar-tensor theory and dilaton fields are introduced by referring to Ref.[13]. The accelerating universe was discovered by observations of redshifts of type Ia supernova. It is supposed that unknown energy called dark energy expands the universe. In modern cosmology, the cosmological constant Λ is interpreted as the origin of dark energy.

The cosmological constant Λ is appeared in Einstein field equations as follows:

$$R_{\mu\nu} - \frac{1}{2}Rg_{\mu\nu} + \Lambda g_{\mu\nu} = \frac{8\pi}{c^4}GT_{\mu\nu}, \tag{145}$$

where $R_{\mu\nu}$ is the Ricci tensor, R is the scalar curvature, $g_{\mu\nu}$ is the metric tensor, G is the gravitational constant, and $T_{\mu\nu}$ is the stress-energy tensor. If we assume the cosmological constant Λ as the vacuum energy, the theoretical value of Λ is estimated as $\Lambda_{\text{vac}} \sim M_P^4 \sim 1$ with Planck units $c = \hbar = M_P = 1$, where Planck mass $M_P = \sqrt{\frac{\hbar c}{8\pi G}} = 2.43 \times 10^{18}$ GeV. On the other hand, the observation value of Λ is given as $\Lambda_{\text{obs}} \sim 10^{-120}$. This unreasonable deviation is called "cosmological constant problem".

Scalar-tensor theory is the alternative gravitational theory which can solve the cosmological constant problem. Scalar-tensor theory is propounded by P.Jordan in 1955 to discuss about the time variability of the gravitational constant G. The first motivation is come from considering why gravitational force is so weak compared to other forces. The time variability of G is obtained by introducing scalar field ϕ.

The Lagrangian is expressed as follows:

$$\mathcal{L} = \sqrt{-g}\left(\frac{1}{2}\xi\phi^2 R - \frac{1}{2}\epsilon g^{\mu\nu}\partial_\mu\phi\partial_\nu\phi + L_{\text{matter}} - \Lambda\right), \tag{146}$$

where ξ is the dimensionless constant, $\epsilon \pm 1$, L_{matter} is the matter field Lagrangian. The time variability of G is expressed as $\xi\phi^2 = (8\pi G_{\text{eff}})^{-1}$. However, the scale factor of universe $a(t) = \text{const}$ is given from Eq.(147). This means the universe is static, which is not consistent with the observations of the expanding universe.

The physical frame which has the invariable G is obtained from the conformal transformation of Eq.(147). The transformation satisfies

$$g_{*\mu\nu} = \Omega^2 g_{\mu\nu}, \tag{147}$$

where

$$\Omega^2 = \xi\phi^2, \tag{148}$$

$$\phi = \xi^{-1/2}\exp(\zeta\sigma), \tag{149}$$

with $\zeta^{-2} = 6 + \epsilon\xi^{-1}$. Then Eq.(147) is converted as

$$\mathcal{L} = \sqrt{-g_*}\left(\frac{1}{2}R_* - \frac{1}{2}g_*^{\mu\nu}\partial_\mu\sigma\partial_\nu\sigma + L_{*matter} - \Lambda\exp(-4\zeta\sigma)\right). \tag{150}$$

The transformed conformal frame is named "Einstein frame". The invariable G is expressed in the first term of right side. The Einstein frame has the highly important aspects that

$$a = t^{1/2}, \tag{151}$$

$$\rho_\sigma = \frac{1}{2}\left(\frac{d\sigma}{dt}\right)^2 + \Lambda\exp(-4\zeta\sigma) = \frac{3}{16}\zeta^{-2}t_*^{-2}, \tag{152}$$

where a is the scale factor of the universe and ρ_σ is the energy density of the scalar field σ. The expansion of the universe is expressed in Eq.(151) and the time dependence of it is consistent with the expected result.

Equation (152) gives t^{-2} dependence of $\Lambda_{\rm obs}$. Now we go back to the cosmological constant problem. The age of universe $t_0 = 1.37 \times 10^{10}$ years is expressed as $t_0 \sim 10^{60}$ with Planck units. On the other hand, $\Lambda_{\rm obs} \propto t^{-2}$ is obtained from Eq.(152). As a result,

$$\Lambda_{\rm obs} = \Lambda_{\rm vac}t_0^{-2} = \Lambda_{\rm vac} \times 10^{-120} \tag{153}$$

is derived. Thus, the descriptions of the Einstein frame can be the solution of the cosmological constant problem.

The Einstein frame seems to be having good agreement with our realistic universe. However, the Einstein frame have the crucial problem that the mass of particles m has the time variability. This property is come from $L_{\rm matter}$ in Eq.(147). Here $L_{\rm matter}$ is expressed as

$$L_{\rm matter} = \sqrt{-g}\left(-\frac{1}{2}g^{\mu\nu}\partial_\mu\psi\partial_\nu\psi - \frac{1}{2}m^2\psi^2\right), \tag{154}$$

where ψ is the neutral scalar field. In the Einstein frame $L_{*\rm matter}$ is expressed as

$$L_{*\rm matter} = \sqrt{-g_*}\left(-\frac{1}{2}g_*^{\mu\nu}\partial_\mu\psi_*\partial_\nu\psi_* - \frac{1}{2}m_*^2\psi_*^2\right), \tag{155}$$

where m_* has the time dependence with $m_* \propto t_*^{-1/2}$.

To introduce the constant mass to the Einstein frame, the second term of the right side in Eq.(154) is rewritten as

$$L_{\phi\psi} = -\frac{1}{2}\sqrt{-g}h^2\phi^2\psi^2, \tag{156}$$

where h is the dimensionless coupling constant. In the Einstein frame, Eq. (157) is expressed as

$$L_{\phi\psi} = -\frac{1}{2}\sqrt{-g_*}m_\sharp^2\psi_*^2, \tag{157}$$

where $m_\sharp^2 = h^2\xi^{-1}$= const. The Einstein frame, finally, has consistency with our realistic universe.

Our nature has chosen the Einstein frame as the specific conformal frame in spite of the nature has the degree of freedom of what frame choose. It is interpreted as the spontaneous breaking of the conformal symmetry. From Eq.(149), σ is regarded as the Nambu-Goldstone field called dilaton.

Dilaton has a nonzero mass duo to the self-energy. The mass of dilaton m_σ is given by [39]

$$m_\sigma^2 \sim \frac{m_q^2 M_{\rm ssb}^2}{M_P^2} \sim (10^{-9}\ {\rm eV})^2, \tag{158}$$

where m_q is a typical mass of the light quarks $\sim$ MeV, $M_{\rm ssb} \sim$ TeV is the effective cutoff of the self-energy of dilaton relevant to the mass scale of the supersymmetry-braking. This calculation is based on the one-loop diagram of the light quarks and leptons couple to dilaton. When the two-loop diagram of the σ - Higgs coupling is taken into the account, $m_\sigma \sim$ sub-eV is obtained.

The coupling constant for the σ - photon coupling is expressed as [39]

$$\frac{g}{M} = \frac{(2\alpha/3\pi)\mathcal{Z}\xi}{M_P}, \tag{159}$$

where $\mathcal{Z} = 5$ is the effective number of the fundamental charged particles (the light quarks and leptons) in the loop, and ξ is a constant of the order unity. The magnitude of the coupling constant is roughly estimated to $g/M \sim 10^{-20}$ eV $\sim G^{1/2}$.

Appendix F: Axion theory

Axion is the pseudoscalar NG boson as a result of the breaking of the Peccei-Quinn (PQ) symmetry. Theoretical backgrounds of axion is introduced in this section by referring to [54].

The PQ symmetry is the chiral symmetry introduced to solve the strong CP problem. The QCD Lagrangian has the term violates the CP invariance as [55]

$$L_\theta = \theta \frac{g_s^2}{32\pi^2} F_a^{\mu\nu} \tilde{F}_{a\mu\nu}, \tag{160}$$

where θ is the phase parameter relevant to the chiral transformation, g_s is the coupling constant of the QCD, $F_a^{\mu\nu}$ is the strength of the gluon field, and $\tilde{F}_{a\mu\nu}$ is its dual. θ has a degree of freedom corresponds to the chiral transition, however, its experimental value is constrained to $\theta_{\mathrm{obs}} < 10^{-9}$ by the measurements of the electric dipole moment of neutron. Why is θ_{obs} so small is known as the strong CP problem.

To solve the strong CP problem, a global chiral symmetry $U(1)_{\mathrm{PQ}}$ is introduced. As a result, Eq.(160) substitute for

$$L_\theta = \left(\theta + \frac{a}{v} N\right) \frac{g_s^2}{32\pi^2} F_a^{\mu\nu} \tilde{F}_{a\mu\nu}, \tag{161}$$

where a indicates the axion field, v is the vacuum expectation value of the Higgs field, and N is the model-dependent factor. a takes the following form.

$$a = \langle a \rangle + a_{\mathrm{phys}}, \tag{162}$$

where $\langle a \rangle$ is given by the minimum value of the potential of a, and a_{phys} is indicates the excitation of the potential. Therefore, a_{phys} represents the observable axion.

When the PQ symmetry breaks spontaneously to satisfy

$$\left(\theta + \frac{\langle a \rangle}{v} N\right) = 0, \tag{163}$$

the strong CP problem can be solved and axion appears as the NB boson.

The interaction Lagrangian coupling between two photons and axion introduced in Eq.(14) is given again.

$$-L_\sigma = g M^{-1} \frac{1}{4} F_{\mu\nu} \tilde{F}^{\mu\nu} \sigma. \tag{164}$$

The original PQ model predicts that axion may also couple to the charged particles directly and the mass scale of the PQ symmetry braking takes

$M \sim (\sqrt{2}G_F)^{-1/2} \equiv v_F$, where G_F is the coupling constant of the weak interactions. However, this prediction is excluded by the previous axion search experiments, for example, $K^+ \to \pi + a$ search at KEK [56] and $J/\psi \to \gamma + a$ search at SLAC [57], where a represents axion.

From the previous experimental results, a "invisible axion" model with $M \gg v_F$ has been advocated. Here the typical invisible axion model called the "KSVZ model" [36, 37] is introduced. The KSVZ model predicts that a scalar field σ with $M_\sigma \gg v_F$ carries PQ charge and a superheavy quark Q plays a role as the only fields carry PQ charge with $M_Q \sim M_\sigma$. As a result, axion does not interact with leptons and it only interacts with the light quarks via the strong and electromagnetic anomalies [55].

In the invisible axion model, the mass of axion is given as

$$m_\sigma = \frac{m_\pi F_\pi}{M_\sigma}\frac{\sqrt{z}}{1+z} = 0.62 \text{ eV} \left(\frac{10^7 \text{ GeV}}{\mathrm{M}_\sigma}\right), \tag{165}$$

where $m_\pi = 135$ MeV is the mass of π_0, $F_\pi = 93$ MeV is the decay constant of π_0, $z = \frac{m_u}{m_d} = 0.568 \pm 0.042$ with the masses of up quark and down quark, m_u and m_d, respectively.

The coupling constant for the axion - photon coupling is expressed as

$$\frac{g}{M} = \frac{e^2}{8\pi^2 M_\sigma}\left(\frac{E}{N} - 1.92\right), \tag{166}$$

with

$$\begin{aligned} N &= \sum_j Q_5(PQ)_j, \\ E &= 2\sum_j Q_5(PQ)_j Q_j^2 N_{cj}, \end{aligned} \tag{167}$$

where $Q_5(PQ)_j$ is the PQ charge of the fermions, Q_j is the electromagnetic charge in unit of e, and N_{cj} is the color degree of freedom. Thus the values of N and E are the model-dependent because the number of species carry the PQ charge depends on the model.

References

[1] Y.Numbu, Phys. Rev. Lett **4**, 380 (1960).

[2] J.Goldstone, Nuevo Cim. **19**, 154 (1961).

[3] B.Schmidt et al., Astrophys.J **507**, 46 (1998).

[4] A.G.Riess et al., Astron.J **116**, 1009 (1998).

[5] S.Perlmutter et al., Astrophys.J **517**, 565 (1999).

[6] Y. Fujii and K. Maeda, *The Scalar-Tensor Theory of Gravitation*, Cambridge Univ. Press (2003).

[7] Y.Fujii, arxiv:1502.1360 [gr-qc] (2015)

[8] S. J. Smullin et al., Phys. Rev. D **72**, 122001 (2005); **72**, 129901 (2005) [erratum].

[9] S. K. Lamoreaux, Phys. Rev. Lett. **78**, 5 (1997); **81**, 5475 (1998) [erratum].

[10] M. Bordag et al., Phys. Rev. D. **58**, 075003 (1998); **81**, 5475 (1998) [erratum].

[11] J. Chiaverini et al., Phys. Rev. Lett. **90**, 151101 (2003).

[12] J.C.Long et al., Nature **421**, 922 (2003).

[13] D.B.Kaplan and M.B.Wise, J.High Energy Phys. **07**, 037 (2000).

[14] N.A.Hamed, S.Dimopoulos, and G.Dvali. Phys. Rev. D **59**, 086004 (1999).

[15] S. Weinberg, Phys. Rev. Lett **40**, 223 (1978).

[16] F. Wilczek, Phys. Rev. Lett **40**, 271 (1978).

[17] M. P. Hertzberg, M. Tegmark, and F. Wilczek, Phys. Rev. D **78**, 083507 (2008).

[18] O. Wantz and E. P. S. Shellard, Phys. Rev. D **82**, 123508 (2010).

[19] J.H.Smith, E.M.Purcell, and N.F.Ramsey. Phys.Rev. **108**, 120 (1957).

[20] R. D. Peccei and H. R. Quinn, Phys. Rev. Lett **38**, 1440 (1977).

[21] S. Moriyama et al., Phys. Lett. B **434**, 147 (1998).

[22] Y. Inoue et al., Phys. Lett. B **536**, 18 (2002).

[23] Y. Inoue et al., Phys. Lett. B **668**, 93 (2008).

[24] K. Zioutas et al. (CAST Collaboration), Phys. Rev. Lett. **94**, 121301 (2005).

[25] S. Andriamonje et al. (CAST Collaboration), J. Cosmol. Astropart. Phys. **04**, 010 (2007).

[26] E. Arik et al. (CAST Collaboration), J. Cosmol. Astropart. Phys. **02**, 008 (2009).

[27] M. Arik et al. (CAST Collaboration), Phys. Rev. Lett. **107**, 261302 (2011).

[28] R. Cameron et al. (BRFT Collab.), Phys. Lett. D **57**, 3873 (1993).

[29] E. Zavattini et al. (PVLAS Collab.), Phys. Lett. D **77**, 032006 (2008).

[30] F. D. Valle et al. (PVLAS Collab.), Phys. Lett. D **90**, 092003 (2014).

[31] P. Pugnat et al. (OSQAR Collab.), Phys. Lett. D **78**, 092003 (2008).

[32] K. Ehret et al. (ALPS Collab.), Phys. Lett. B **689**, 149 (2010).

[33] S.J.Asztalos et al. (ADMX Collab.), Phys. Rev. D **69**, 01101 (2004).

[34] S.J.Asztalos et al. (ADMX Collab.), Phys. Rev. Lett. **104**, 041301 (2010).

[35] I.G.Irastorza et al., JCAP **06**, 013 (2011).

[36] J. E. Kim, Phys. Rev. Lett. **43**, 103 (1979).

[37] M. A. Shifman, A. I. Vainshtein and V. I. Zakharov, Nucl. Phys. B **166**, 493 (1980).

[38] J. F. Reintjes, *Nonlinear Optical Parametric Processes in Liquids and Gases*, ACADEMIC PRESS, INC. (1984).

[39] Y. Fujii and K. Homma, Prog. Theor. Phys **126**, 531 (2011); Y. Fujii and K. Homma, Prog. Theor. Exp. Phys. (2014) 089203.

[40] K. Homma, Prog. Theor. Exp. Phys. (2012) 04D004; K. Homma, Prog. Theor. Exp. Phys. (2014) 089201.

[41] S. A. J. Druet and J.-P. E. Taran, Prog. Quant. Electr. **7**, 1 (1981).

[42] Amnon Yariv, *Optical Electronics in Modern Communications* Oxford University Press (1997).

[43] F. Moulin and D. Bernard, Opt. Commun. **164**, 137 (1999).

[44] E. Lundström et al., Phys. Rev. Lett. **96**, 083602 (2006).

[45] J. Lundin et al., Phys. Rev. A **74**, 043821 (2006).

[46] D. Bernard et al., Eur. Phys. J. D **10**, 141 (2000).

[47] T.Hasebe et al., Prog. Theor. Exp. Phys. 073C01 (2015).

[48] K. Homma, T. Hasebe, and K.Kume, Prog. Theor. Exp. Phys. 083C01 (2014).

[49] Y. Su et al., Phys. Rev. D **50**, 3614 (1994); **51**, 3135 (1995) [erratum].

[50] E. G. Adelberger et al., Phys. Rev. Lett. **98**, 131104 (2007);

[51] D. J. Kapner et al., Phys. Rev. Lett. **98**, 021101 (2007).

[52] ELI-NP web site; http://www.eli-np.ro.

[53] IZEST web site; http://www.izest.polytechnique.edu/jsp/accueil.jsp.

[54] 長島　順清, 高エネルギー物理学の発展, 朝倉書店 (1999).

[55] R. D. Peccei, Lect. Notes Phys. **741**, 3 (2008).

[56] Y. Asano et al., Phys. Lett. B. **107**, 159 (1981).

[57] C. Edwards et al., Phys. Rev. Lett. **48**, 903 (1982).

公表論文

(1) Search for sub-eV scalar and pseudoscalar resonances via four-wave mixing with a laser collider

Takashi Hasebe, Kensuke Homma, Yoshihide Nakamiya,
Kayo Matsuura, Kazuto Otani, Masaki Hashida,
Shunsuke Inoue, and Shuji Sakabe

Progress of Theoretical and Experimental Physics
073C01 (2015)

Prog. Theor. Exp. Phys. **2015**, 073C01 (19 pages)
DOI: 10.1093/ptep/ptv101

Search for sub-eV scalar and pseudoscalar resonances via four-wave mixing with a laser collider

Takashi Hasebe[1], Kensuke Homma[1,2,*], Yoshihide Nakamiya[3], Kayo Matsuura[1], Kazuto Otani[4], Masaki Hashida[3,5], Shunsuke Inoue[3,5], and Shuji Sakabe[3,5]

[1] *Graduate School of Science, Hiroshima University, Kagamiyama, Higashi-Hiroshima, Hiroshima 739-8526, Japan*
[2] *International Center for Zetta-Exawatt Science and Technology, Ecole Polytechnique, Route de Saclay, Palaiseau, F-91128, France*
[3] *Institute for Chemical Research, Kyoto University Uji, Kyoto 611-0011, Japan*
[4] *Institut national de la recherche scientifique–Energie Materiaux Telecommunications, 1650 Boulevard Lionel-Boulet, C.P.1020, Varennes (Quebec) J3X 1S2, Canada*
[5] *Graduate School of Science, Kyoto University, Sakyouku, Kyoto 606-8502, Japan*
*E-mail: homma@hepl.hiroshima-u.ac.jp

Received February 4, 2015; Revised June 12, 2015; Accepted June 17, 2015; Published July 28, 2015

Quasi-parallel photon–photon scattering by combining two-color laser fields is an approach to producing resonant states of low-mass fields in the laboratory. In this system resonances can be probed via the four-wave mixing process in the vacuum. A search for scalar and pseudoscalar fields was performed by combining a 9.3 μJ/0.9 ps Ti-sapphire laser and a 100 μJ/9 ns Nd:YAG laser. No significant signal of four-wave mixing was observed. We provide the upper limits on the coupling–mass relation for scalar and pseudoscalar fields, respectively, at a 95% confidence level in the mass region below 0.15 eV.

Subject Index C15, C19, C23, C33, C41

1. Introduction

Uncovering the nature of dark energy and dark matter is one of the most crucial problems in modern physics. Low-mass and weakly coupling fields predicted by theoretical models in cosmology and particle physics can be candidates for such dark components. For instance, based on the scalar–tensor theory with the cosmological constant Λ (STTΛ) [1], dark energy is interpreted as decaying Λ while the universe becomes older due to the gravitational coupling between extremely light dilatons, a kind of scalar field (ϕ), and matter fields. Observing the $\gamma\gamma \rightarrow \phi \rightarrow \gamma\gamma$ process with extremely high intensity laser fields can be a method of searching for ϕ in the laboratory [2]. The same approach can also be applied to searches for low-mass pseudoscalar fields (σ), if the photon spin states are properly chosen [3]. The axion [4,5], a pseudoscalar field associated with the breaking of Peccei–Quinn symmetry [6], is a suitable candidate to which this method is directly applicable. The axion is supposed to be one of the most reasonable candidates for cold dark matter [7,8]. Therefore, these theoretical models strongly motivate us to search for such fields in the laboratory in general.

Axion searches via two-photon coupling processes have been performed by a number of experiments, for example, solar axion searches [9–15], light shining through a wall [16–19], and the axion

Funded by SCOAP^3

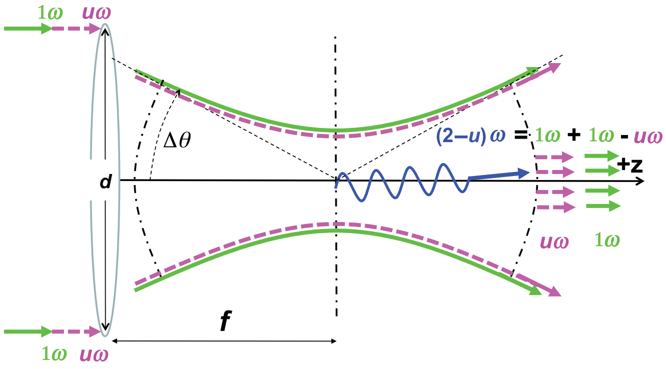

Fig. 1. Quasi-parallel colliding system by combining two-color laser fields [2], where d is the beam diameter, f the focal length, and the incident angle ϑ takes $0 < \vartheta \le \Delta\theta$, which is unavoidable due to the ambiguity of the wave vectors of incident photons by the nature of focused lasers.

dark matter experiment [20,21]. Following the first search for scalar fields at a quasi-parallel colliding system (QPS) [22], the upgraded search for sub-eV scalar and pseudoscalar fields is presented in this paper.

With the schematic view of QPS in Fig. 1, we briefly explain the essence of our method as follows. By using variables defined at QPS, the center of mass system (CMS) energy between a randomly selected photon pair is expressed as

$$E_{\text{CMS}} = 2\omega \sin\vartheta, \tag{1}$$

where ω is the energy of incident photons and ϑ is half of the incident angle of the photon pair. Extremely low collision energies are realizable at QPS by focusing a laser field because small values of ϑ can be automatically introduced.

In order to overcome low scattering amplitudes of $\gamma\gamma \to \phi/\sigma \to \gamma\gamma$ processes due to weak coupling, we first utilize the character of the integrated resonance effect by capturing E_{CMS} within ΔE_{CMS} via $\Delta\theta$ prepared by a creation laser field. Secondly, we let another laser field propagate into the optical axis common to the creation laser. This laser induces decay of resonance states into a specific energy–momentum space by the coherent nature of the inducing field. The scattering probability is thus proportionally increased by the number of photons in the inducing laser field [2,3,23,24].

The energies of decayed photons are defined by the energy conservation

$$\omega + \omega = (2-u)\,\omega + u\omega, \tag{2}$$

where u is an arbitrary number which satisfies $0 < u < 1$. We redefine the energies of final state photons as

$$\begin{aligned} \omega_3 &\equiv (2-u)\,\omega, \\ \omega_4 &\equiv u\omega, \end{aligned} \tag{3}$$

where ω_3 and ω_4 are the energies of the signal photon and inducing photons, respectively.

In the case of the scalar field exchange, the relation of linear polarization states between initial and final state photons when the wave vectors are on the same reaction plane are expressed as follows:

$$\begin{aligned} \omega\{1\} + \omega\{1\} &= \omega_3\{1\} + \omega_4\{1\}, \\ \omega\{1\} + \omega\{1\} &= \omega_3\{2\} + \omega_4\{2\}, \end{aligned} \tag{4}$$

where $\{1\}$ and $\{2\}$ are linear polarization states orthogonal to each other. In the pseudoscalar field exchange, the polarization relations are expressed as

$$\begin{aligned}\omega\{1\} + \omega\{2\} &= \omega_3\{1\} + \omega_4\{2\},\\ \omega\{1\} + \omega\{2\} &= \omega_3\{2\} + \omega_4\{1\}.\end{aligned} \tag{5}$$

We emphasize that the above relations are limited only to the theoretically ideal case where all four photons are on the same reaction plane within the treatment based on plane waves. In the focused QPS, however, we must accept independent rotations of the incident p_1–p_2 plane and the outgoing p_3–p_4 plane as illustrated in Fig. A1 with respect to an experimentally given linear polarization plane. This implies that even if we supply ω as the pure $\{1\}$-state by a polarizer at the moment of plane wave propagation in advance of focusing, mixing of $\{1\}$ and $\{2\}$ states for randomly selected incident photon pairs is unavoidable while lasers are focused. Therefore, the focused QPS with a fixed initial linear polarization plane has sensitivity to both scalar and pseudoscalar fields simultaneously. We discuss this nature in detail in Appendix A.

The relation in Eq. (2) is similar to "four-wave mixing" in matter corresponding to the third-order nonlinear quantum optical process in atoms [25,26]. Therefore, the observation of the four-wave mixing process in the vacuum may be interpreted as a replacement of the atomic nonlinear process by the exchange of unknown scalar or pseudoscalar fields. The observation of four-wave mixing in the vacuum is also used as a method for testing higher-order QED effects [27–30].

Photons produced via the atomic four-wave mixing process can be the main background source for this search. The first search for scalar fields at QPS [22] was performed with weak intensity lasers, and thus the effect of the four-wave mixing process in atoms was negligible. In this experiment, however, four-wave mixing photons originating from the residual gas are anticipated due to much higher beam intensities. In this paper the method to obtain the exclusion limits in the search at QPS sensitive to both scalar and pseudoscalar fields is provided under the circumstance where a finite number of background photons must be evaluated.

2. The coupling–mass relation

The effective interaction Lagrangians coupling between two photons and ϕ/σ are expressed as

$$-L_\phi = gM^{-1}\tfrac{1}{4}F_{\mu\nu}F^{\mu\nu}\phi, \quad -L_\sigma = gM^{-1}\tfrac{1}{4}F_{\mu\nu}\tilde{F}^{\mu\nu}\sigma, \tag{6}$$

where M has the dimension of energy and g is a dimensionless constant. The yield of signal photons, $\mathcal{Y}$, is expressed with experimental parameters relevant to lasers and optical elements as follows:

$$\begin{aligned}\mathcal{Y} = {}& \frac{1}{64\sqrt{2}\pi^4}\left(\frac{\lambda_c}{c\tau_c}\right)\left(\frac{\tau_c}{\tau_i}\right)\left(\frac{f}{d}\right)^3 \tan^{-1}\left(\frac{\pi d^2}{4f\lambda_c}\right)\frac{(\bar{u}-\underline{u})^2}{\bar{u}\underline{u}}\\ & \times\left(\frac{gm\,[\mathrm{eV}]}{M\,[\mathrm{eV}]}\right)^2\left(\frac{m\,[\mathrm{eV}]}{\omega\,[\mathrm{eV}]}\right)^3 \mathcal{W}\mathcal{G}\mathcal{F}_s C_{mb} {N_c}^2 N_i,\end{aligned} \tag{7}$$

where the subscripts c and i indicate the creation and inducing laser, respectively, λ is the wavelength, τ is the pulse duration, f is the focal length, d is the beam diameter, $\bar{u}$ and $\underline{u}$ are the upper and lower values on u determined by the spectrum width of ω_4, respectively, m is the mass of the exchanging field, $\mathcal{W}$ is the numerical factor relevant to the integral of the weighted resonance function which is refined in Eq. (B21) in Appendix B compared to $\mathcal{W} \sim \pi/2$ in Ref. [22], $\mathcal{G}$ is the incident plane rotation factor described in Appendix A, $\mathcal{F}_S$ is the polarization-dependent axially asymmetric factor for outgoing photons [3], C_{mb} is the combinatorial factor originating from selecting a pair of photons among multimode frequency states, and the N are the average numbers of photons in the coherent state. The detail of the formulation of the signal yield is summarized in the Appendix of Ref. [22]. The coupling constant g/M is expressed as

$$\frac{g}{M\,[\mathrm{eV}]} = 2^{1/4} 8\pi^2 \sqrt{\frac{\mathcal{Y}\omega^3\,[\mathrm{eV}]}{\left(\frac{\lambda_c}{c\tau_c}\right)\left(\frac{\tau_c}{\tau_i}\right)\left(\frac{f}{d}\right)^3 \tan^{-1}\left(\frac{\pi d^2}{4f\lambda_c}\right)\frac{(\bar{u}-\underline{u})^2}{\bar{u}\underline{u}}\mathcal{W}\mathcal{G}\mathcal{F}_s C_{mb} {N_c}^2 N_i}}\, m^{-5/2}\,[\mathrm{eV}]. \quad (8)$$

3. Experimental setup

We explain the experimental setup to detect signals of four-wave mixing in the vacuum. The schematic view of the setup is shown in Fig. 2.

A Ti-sapphire laser (wavelength 800 nm) and a Nd:YAG laser (wavelength 1064 nm) are used as the creation and inducing lasers, respectively. To reduce the number of background photons emitted from the residual gas via four-wave mixing, the linear polarization states of the creation and inducing lasers are configured to linear polarization states $\{1\}$ and $\{2\}$, respectively. The beam alignments of the lasers are monitored by CCD cameras (CCD) and the pulse energies of the creation and inducing lasers are measured by photodiodes (PD). These beams are combined by a dichroic mirror (DM). The combined beams are guided into the vacuum chamber at the 20 mm beam diameter and focused with the convex lens at the focal length of 200 mm.

The expected wavelength of the corresponding signal photon is evaluated from the following equation:

$$\lambda_s = \frac{\lambda_i \lambda_c/2}{\lambda_i - \lambda_c/2} = 641\ \mathrm{nm}. \quad (9)$$

A light source with a central wavelength of 640 nm is combined with the creation and inducing lasers by DM to evaluate the detection efficiency and to trace the trajectory of signal photons for the detector alignment.

The agreement of the optical axes between the two lasers is adjusted at a precision of 2–3 µm by monitoring individual beam profiles at the near side and the far side of the focal spot with the CCD camera. The beam profiles at the focal spot are shown in Fig. 3. The spot sizes of the creation and inducing lasers, which are defined as 2σ of the 2D Gauss functions fitting the beam profiles, are 21 µm and 23 µm, respectively. The creation laser overlaps with 87% of the beam energy of the inducing laser at the focal spot. Thus, the effective beam energy of the inducing laser is evaluated by correcting the measured beam energy with this overlapping factor.

Signal photons generated within the focal volume travel along the common optical axis of the combined lasers. Signal photons are separated from the creation and inducing lasers by the prism, and signal wave filters are placed to further eliminate the residual photons from the combined lasers. The polarization beam splitter (PBS) transmits $\{1\}$-polarized photons and reflects $\{2\}$-polarized photons. Incident photons are split between the shorter optical fiber Path$\{1\}$ and the longer Path$\{2\}$. The incident photons to PBS are eventually observed by the common photo-device having relative time delay

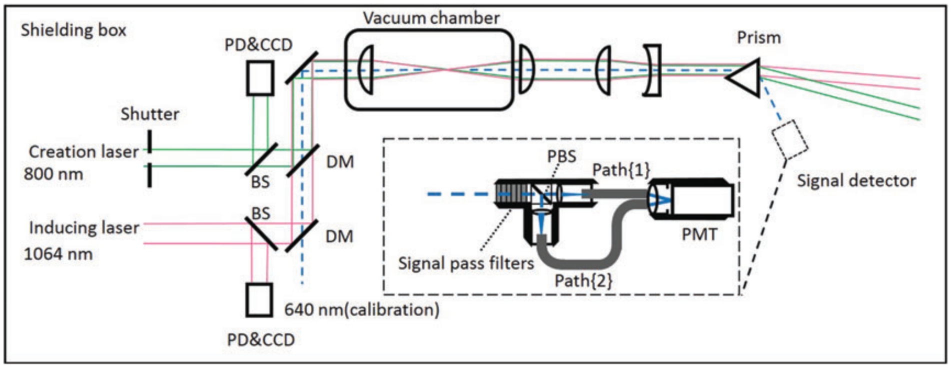

Fig. 2. Schematic view of the experimental setup.

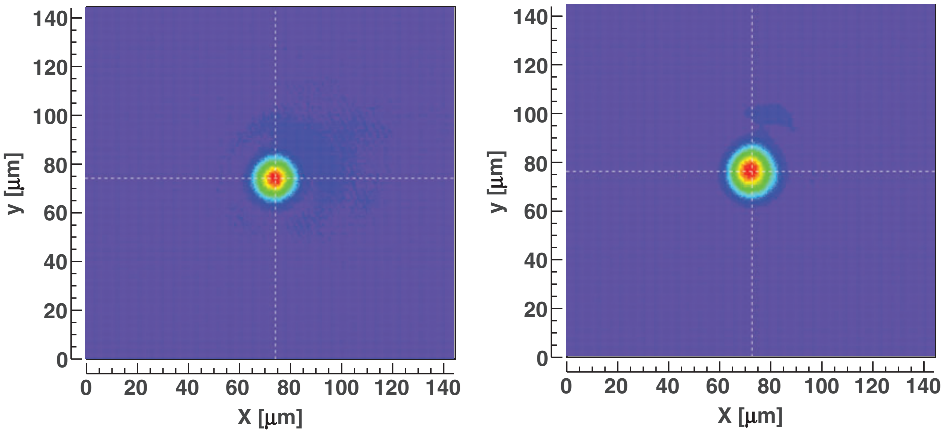

Fig. 3. The beam profiles of the creation laser (left) and the inducing laser (right) at the common focal point captured by a common CCD camera.

of 23 ns. We use a single-photon-countable photomultiplier tube (PMT; R7400-01, manufactured by HAMAMATSU) as the photo-device.

The repetition rate of the creation laser is 1 kHz and that of the inducing laser is 10 Hz by synchronizing the trigger with the 1 kHz creation pulsing. The data acquisition trigger of 20 Hz is synchronized with the 1 kHz creation laser pulsing which includes pedestal triggers in order to provide four patterns of triggers. The time coincidence between creation and inducing pulses is performed by adjusting the relative injection timing between the two lasers so that the relative time maximizes the four-wave mixing yield in the air. The shutter is placed on the creation laser beam line and it repeatedly opens and closes every 5 seconds. We acquire data with the four patterns of triggers, which are "both lasers are incident (S)," "only the creation laser is incident (C)," "only the inducing laser is incident (I)," and "neither laser is incident (P)." The digital oscilloscope recorded waveform data from the PMT and two photodiodes synchronized with the 20 Hz data acquisition trigger. The recorded waveform data from the PMT are sorted into the four types of trigger pattern: S, C, I, and P. The four trigger patterns are classified by checking the charge correlations between the waveform data from the two photodiodes for intensity monitoring.

4. Method of waveform analysis

The observed photon counts are estimated by analyzing the waveform data from the PMT. The individual waveform consists of 500 sampling data points within a 200 ns time window. We search

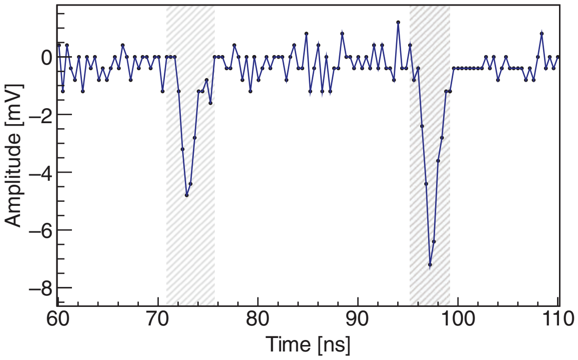

Fig. 4. A waveform data sample with two peak structures. The black shaded areas show the integral ranges to evaluate the charge sums of individual peak structures.

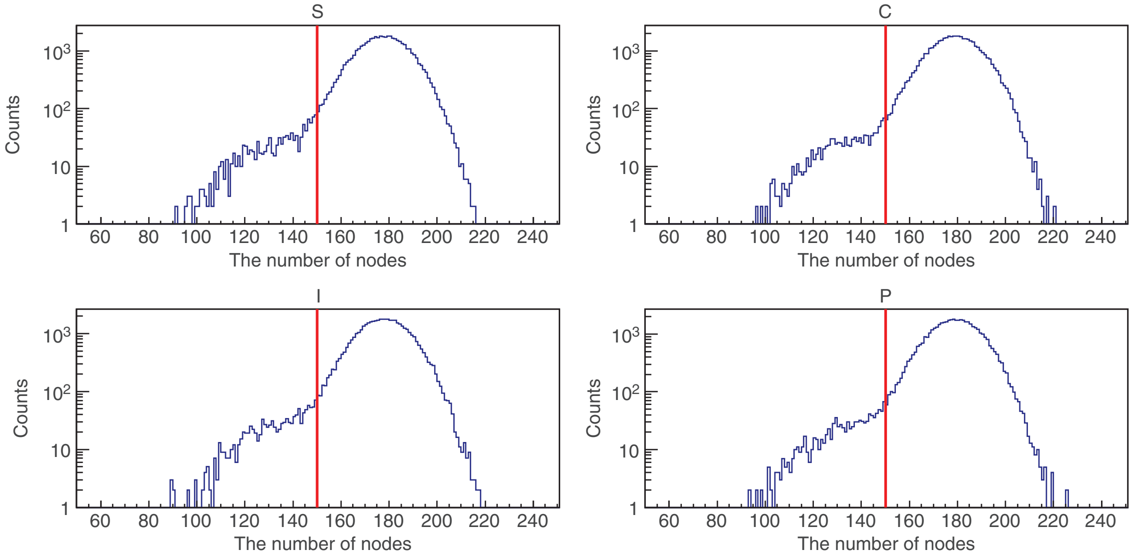

Fig. 5. Distributions of the number of nodes for trigger patterns S, C, I, and P. The events with fewer numbers of nodes below the red vertical line are identified as noisy events.

for negative peaks whose amplitude exceeds a given threshold. We then calculate charge sums of the peak structures. Figure 4 shows a sample of waveform data where peak structures are identified. Charge sums of peak structures are evaluated in units of the single-photon equivalent charge, -4.21×10^{-14} C.

There are some accidental noisy events among the recorded waveform data. In our analysis method, these noise structures could be misidentified as large photon-like peak structures. Therefore, it is necessary to remove such noisy events from the analyzed waveform data before counting photon-like peaks. We can identify noisy events by analyzing the frequencies of the waveforms. Noisy waveforms tend to have lower frequencies than those of normal waveforms. The frequencies are estimated by counting the number of nodes, which is defined as the intersections between a waveform and the average line of amplitudes within the 200 ns time window. The distributions of the number of nodes for each trigger pattern are shown in Fig. 5. We regard a waveform of which the number of nodes is lower than 150 as a noisy event in all trigger patterns by confirming that the differences of the distributions among four trigger patterns are not prominent. Typical waveforms of noisy events and normal events identified by this method are shown in Fig. 6.

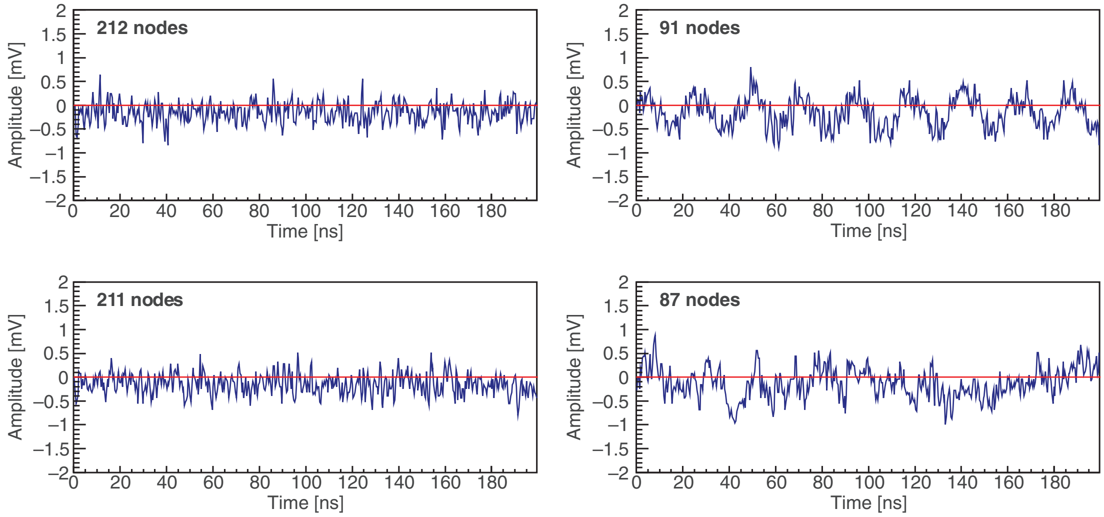

Fig. 6. Examples of waveforms of noisy events and normal events. The two panels on the left and right sides show waveforms of normal events and noisy events, respectively. The red horizontal lines indicate the averages of the amplitudes of sampling points for each waveform.

5. Measurement of the four-wave mixing process in the residual gas

Background photons can be produced via the four-wave mixing process occurring in residual atoms in the vacuum chamber. To estimate the expected number of background photons, we measured the pressure dependence of the number of four-wave mixing photons in gas. Figure 7 shows arrival time distributions of observed photons in the air at 5.0×10^4 Pa among four trigger patterns. Specific two-peak structures appear only for the S pattern. These peak structures have approximately a 23 ns time interval, which agrees with the optical path length difference between Path$\{1\}$ and Path$\{2\}$. We count the number of photons within a time domain $T\{1\}$ (71–75 ns) for the $\{1\}$-polarized state and $T\{2\}$ (94–98 ns) for the $\{2\}$-polarized state.

The number of four-wave mixing signals N_S are evaluated from the following equation (see Eqs. (18) and (19) in Ref. [22]):

$$N_{\mathrm{S}} = n_{\mathrm{S}} - \frac{W_{\mathrm{S}}}{W_{\mathrm{C}}} n_{\mathrm{C}} - \frac{W_{\mathrm{S}}}{W_{\mathrm{I}}} n_{\mathrm{I}} + \frac{W_{\mathrm{S}}}{W_{\mathrm{P}}} n_{\mathrm{P}}, \tag{10}$$

where n_i and W_i denote the number of photon-like peaks in the signal domains and the number of events in trigger pattern i, respectively.

The pressure dependence of the number of four-wave mixing photons per S-trigger event are shown in Fig. 8. Data points are fit by the quadratic function of pressure. We extrapolate the number of four-wave mixing photons in the residual gas at 2.3×10^{-2} Pa (an equivalent condition to the vacuum data we discuss later) from the fitting function. The efficiency-corrected number of $\{1\}$-polarized and $\{2\}$-polarized photons in residual gas $\mathcal{N}_{\mathrm{gas1}}$ and $\mathcal{N}_{\mathrm{gas2}}$ with the same shot statistics as the vacuum data are evaluated as follows:

$$\begin{aligned} \mathcal{N}_{\mathrm{gas1}} &= 1.7 \pm 1.1 \times 10^{-5}, \\ \mathcal{N}_{\mathrm{gas2}} &= 1.7 \pm 1.1 \times 10^{-5}. \end{aligned} \tag{11}$$

We confirmed that the expected value of four-wave mixing photons from the residual gas is negligibly small in the vacuum data for a given total statistics.

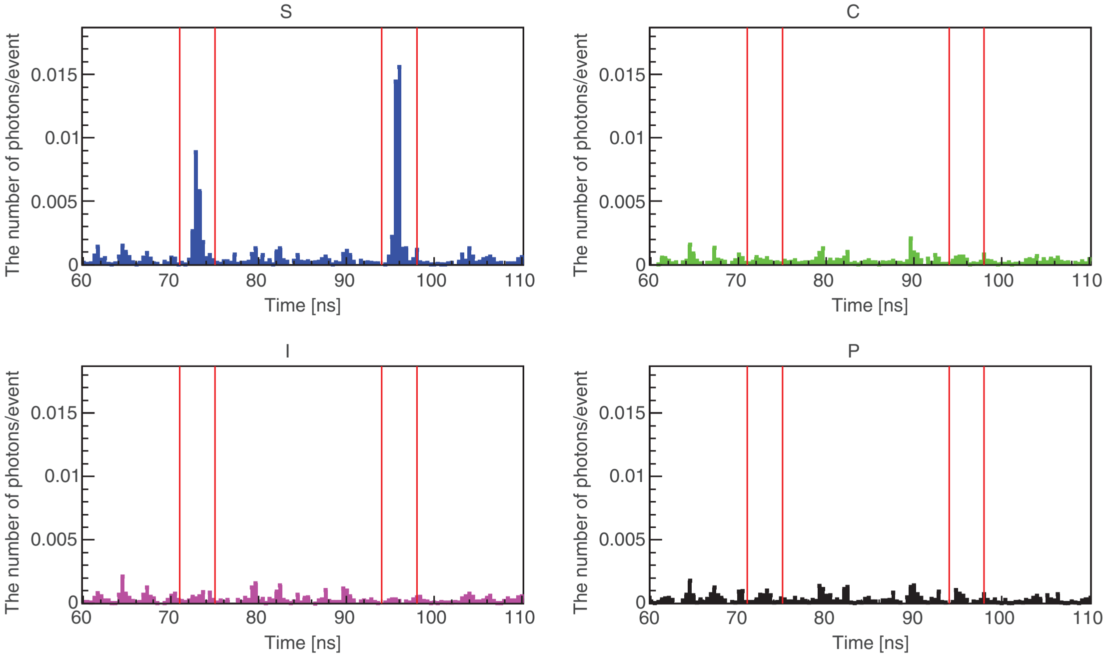

Fig. 7. The arrival time distributions of observed photons per triggered event (efficiency-uncorrected) at 5.0×10^4 Pa. The left and right bands bounded by two neighboring red lines in each panel indicate the time domains $T\{1\}$ and $T\{2\}$ where $\{1\}$- and $\{2\}$-polarized photons are expected to be observed, respectively. In this figure, the threshold value for peak identification is set lower than that of the actual data analysis on purpose to show typical pedestal structures in each trigger pattern.

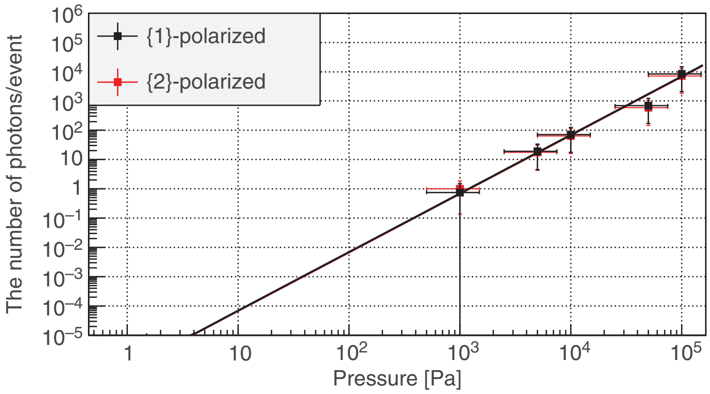

Fig. 8. The pressure dependence of the number of four-wave mixing photons in the residual gas inside the interaction chamber per S-trigger event. The red and black lines represent the fitting functions for the $\{1\}$- and $\{2\}$-polarized states, respectively.

6. The search for four-wave mixing signals in the vacuum

We acquired data at 2.3×10^{-2} Pa in the search for the resonant states of the ϕ and σ fields. Figure 9 shows the arrival time distributions of observed photon counts. Table 1 summarizes the numbers of observed photon-like signals evaluated in units of the single-photon equivalent charge with $\{1\}$- and $\{2\}$-polarized states for each trigger pattern, respectively.

After performing subtractions between the four patterns of the histograms in Fig. 9 based on the relation in Eq. (10), we obtained the time distribution of N_S as shown in Fig. 10. The numbers of

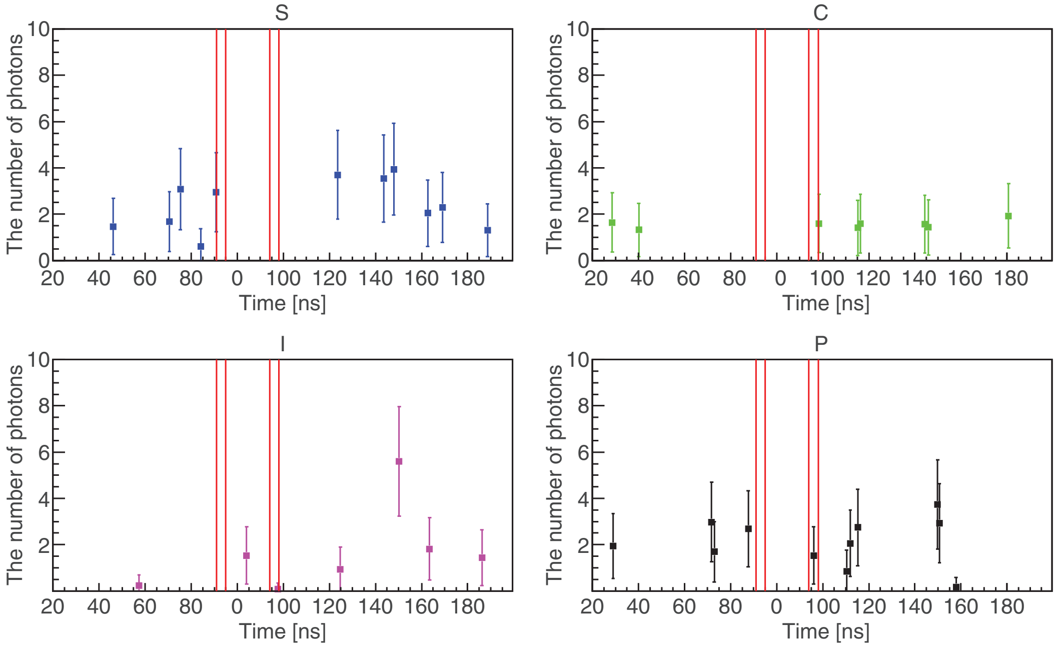

Fig. 9. Arrival time distributions of observed photons at 2.3×10^{-2} Pa. The data points in each trigger pattern are normalized to the number of triggered events of the S trigger pattern.

Table 1. The numbers of observed photons in $T\{1\}$ and $T\{2\}$ for each trigger pattern. n_{i1} and n_{i2} are the numbers of photons evaluated in units of single-photon equivalent charge in trigger pattern i with $\{1\}$- and $\{2\}$-polarized states, respectively. W_i is the number of events in trigger pattern i.

Trigger i	n_{i1}	n_{i2}	W_i
S	0	0	46120
C	0	0	46203
I	0	0.07	46044
P	0	1.53	46169

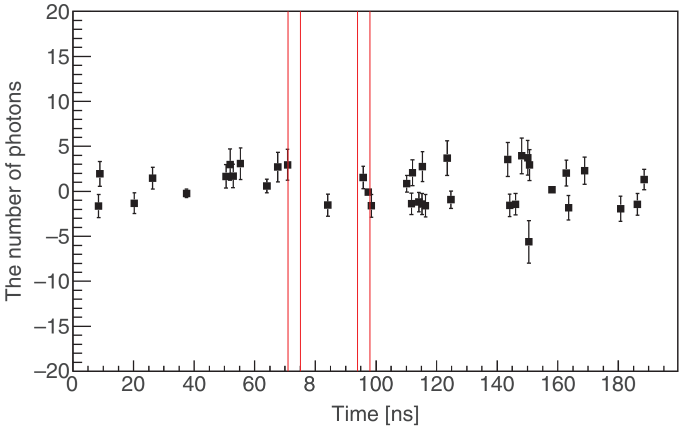

Fig. 10. The arrival time distribution of N_S defined in Eq. (10).

Table 2. Data table of experimental parameters. $\mathcal{G}_{11}^{\mathrm{sc}}$ and $\mathcal{G}_{12}^{\mathrm{ps}}$ represent the incident plane rotation factor for the scalar and pseudoscalar field exchanges, respectively. The evaluation of $\mathcal{G}$ is discussed in Appendix A. $\mathcal{F}_{1122}^{\mathrm{sc}}$ and $\mathcal{F}_{1212}^{\mathrm{ps}}$ denote the axially asymmetric factor for scalar and pseudoscalar field exchanges, respectively. See the detail in the Appendix of Ref. [3].

Parameters	Values
Center of wavelength of creation laser λ_c	800 nm
Relative line width of creation laser $(\delta\omega/\langle\omega\rangle)$	7.5×10^{-3}
Center of wavelength of inducing laser λ_i	1064 nm
Relative line width of inducing laser $(\delta\omega_4/\langle\omega_4\rangle)$	1.0×10^{-4}
Duration time of creation laser pulse per injection τ_c	900 fs
Duration time of inducing laser pulse per injection τ_i	9 ns
Creation laser energy per τ_c	$9.3 \pm 1.2\,\mu$J
Inducing laser energy per τ_i	$100 \pm 1\,\mu$J
Focal length f	200 mm
Beam diameter of laser beams d	20 mm
Upper mass range given by $\theta < \Delta\theta$	0.15 eV
$u = \omega_4/\omega$	0.75
Incident plane rotation factor $\mathcal{G}$	$\mathcal{G}_{11}^{\mathrm{sc}} = 19/32$
	$\mathcal{G}_{12}^{\mathrm{ps}} = 1/2$
Axially asymmetric factor $\mathcal{F}_s$	$\mathcal{F}_{1122}^{\mathrm{sc}} = 19.4$
	$\mathcal{F}_{1212}^{\mathrm{ps}} = 19.2$
Combinatorial factor in luminosity C_{mb}	1/2
Single-photon detection efficiency ϵ_D	1.4 ± 0.1 %
Efficiency of optical path from interaction point to Path{1} ϵ_{opt1}	0.5 ± 0.1 %
Efficiency of optical path from interaction point to Path{2} ϵ_{opt2}	0.9 ± 0.2 %
δN_{S1}	2.2
δN_{S2}	4.4

signals with {1}- and {2}-polarized states are, respectively, given as follows:

$$N_{S1} = 0 \pm 0\ (\mathrm{stat.}) \pm 2.16\ (\mathrm{syst.I}) \pm 0.30\ (\mathrm{syst.II}) \pm 0\ (\mathrm{syst.III}),$$
$$N_{S2} = 1.46 \pm 1.27\ (\mathrm{stat.}) \pm 2.16\ (\mathrm{syst.I}) \pm 0.04\ (\mathrm{syst.II}) \pm 3.59\ (\mathrm{syst.III}). \qquad (12)$$

The systematic error I originates from the number of photons outside of the two arrival time windows for the {1}- and {2}-polarized states. This was evaluated by calculating the root mean square of N_S, except in the $T\{1\}$ and $T\{2\}$ windows. The systematic error II originates from the dependence on the threshold values for the peak finding -1.3 ± 0.1 mV. The systematic error III is relevant to the ambiguities of the rejection of noisy events, 150 ± 5 nodes.

7. The excluded coupling–mass limits for scalar and pseudoscalar fields

There is no significant four-wave mixing signal in this search from the result in (12). We thus evaluate the exclusion regions on the coupling–mass relation as follows.

We estimate the upper limit on the sensitive mass range as

$$m < 2\omega \sin\Delta\theta \sim 2\omega\frac{d}{2f} = 0.15\,\mathrm{eV} \qquad (13)$$

based on the values summarized in Table 2, where ϑ in Fig. 1 varies from 0 to $\Delta\theta$ defined by a focal length f and a beam diameter d.

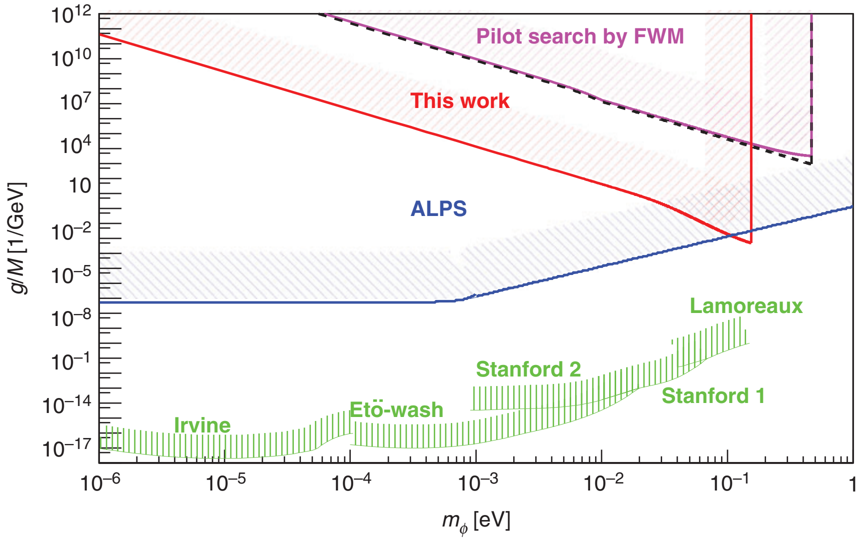

Fig. 11. Exclusion limits for scalar fields (ϕ) in ϕ–photon coupling (g/M) as a function of the mass of ϕ (m_ϕ). The region excluded by this experiment is shown by the red shaded area. The magenta shaded area shows the region excluded by our previous search, which is renewed from the black dotted line obtained from Ref. [22] by taking the incident plane rotation factor $\mathcal{G}$ and the mass-dependent $\mathcal{W}$ factor in Appendix B into account. The blue shaded area represents the region excluded for scalar fields by the light shining through a wall experiment "ALPS" [19] (for the mass region above 10^{-3} eV, the sine function part of the sensitivity curve is simplified to unity for drawing purposes). The green shaded areas indicate the limits given by non-Newtonian force searches by the torsion balance experiments "Irvine" [32], "Eto-wash" [33,34], "Stanford1" [35], "Stanford2" [36], and Casimir force measurement "Lamoreaux" [37].

The number of efficiency-corrected $\{1\}$-polarized signal photons $\mathcal{N}_{S1}$ and that of $\{2\}$-polarized signal photons $\mathcal{N}_{S2}$ are evaluated from the following relations with the experimental parameters:

$$\mathcal{N}_{S1} = \frac{N_{S1}}{\epsilon_{\text{opt1}}\epsilon_{\text{D}}}, \quad \mathcal{N}_{S2} = \frac{N_{S2}}{\epsilon_{\text{opt2}}\epsilon_{\text{D}}}, \tag{14}$$

where ϵ_{opt1} and ϵ_{opt2} are the attenuation ratios of the signal photons propagating from the interaction point through Path$\{1\}$ and Path$\{2\}$, respectively.

These attenuation factors are composed of the transmittance of optical devices and the acceptance of signal paths with respect to the actual location of the PMT. They are inclusively evaluated by sampling the beam energies of the 640 nm calibration light at the focal point and the detection point, respectively, and taking the ratio between them. The matching of beam paths between the calibration light and four-wave mixing signals is ensured by adjusting the beam center of the calibration light with respect to those of the creation and inducing lasers at the near side and the far side of the focal spot, respectively. ϵ_{D} is the signal detection efficiency of the PMT mainly caused by the quantum efficiency of the device. ϵ_{D} is evaluated using a 532 nm pulse laser in advance of the search. We evaluate the absolute detection efficiency by splitting the 532 nm beam equally and taking the ratio between these energies. One is measured by a calibrated beam energy meter and the other is measured by the PMT with neutral density filters with measured attenuation factors. We then corrected the difference of the quantum efficiencies between the 532 nm and 641 nm lights by taking the relative quantum efficiencies provided by HAMAMATSU into account.

We then evaluate upper limits on the coupling–mass relation at a 95% confidence level on the basis that the fluctuation of the number of signal yields forms a Gaussian distribution. We define δN_S as the one standard deviation of N_S. It is evaluated from the quadratic sum of statistical and systematic

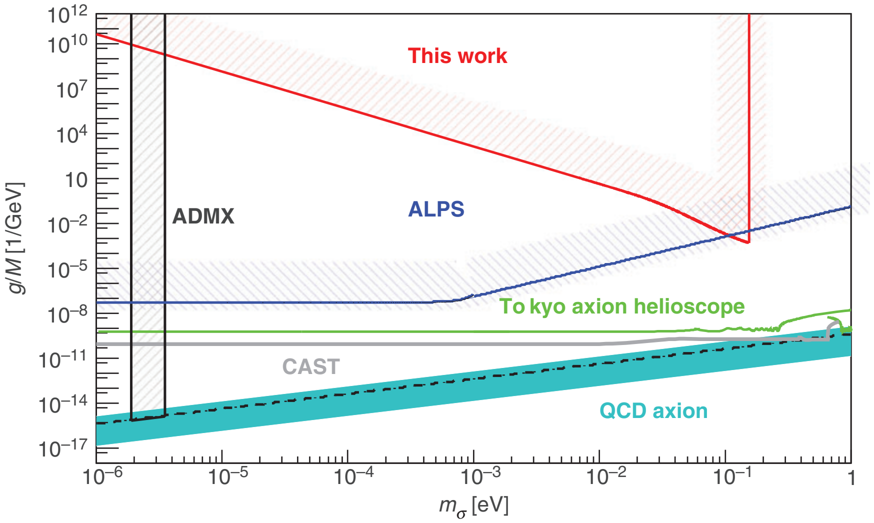

Fig. 12. Exclusion limits for pseudoscalar fields (σ) in σ–photon coupling (g/M) as a function of the mass of σ (m_σ). The blue shaded area shows the region excluded by the pseudoscalar search, "ALPS." The green and gray solid lines show the exclusion limits from the solar axion experiments "Tokyo Axion Helioscope" [9–11] and "CAST" [13–15], respectively. The black shaded area represents the result from the dark matter axion search using a microwave cavity "ADMX" [20,21]. The cyan band indicates the expected coupling–mass relation of the QCD axion predicted by the KSVZ model [38,39] with $|E/N - 1.95|$ in the range 0.07–7; furthermore, the case of $E/N = 0$ is shown by the black dotted line.

errors in Eq. (12), and $2.24\delta N_S$ is the upper limit of N_S when we obtain a 95% confidence level (see Eq. (36.56) in Ref. [31]). The upper limit of signal yields per shot $\mathcal{Y}_{sc}$ (for the scalar field exchange) and $\mathcal{Y}_{ps}$ (for the pseudoscalar field exchange) are evaluated as follows:

$$\mathcal{Y}_{sc} = \frac{2.24\delta N_{S2}}{\epsilon_{opt2}\epsilon_D W_S}, \qquad \mathcal{Y}_{ps} = \frac{2.24\delta N_{S1}}{\epsilon_{opt1}\epsilon_D W_S}. \tag{15}$$

As we briefly mention in Sect. 1 and in detail in Appendix A, even though we fix the linear polarization planes for the creation and inducing laser fields by the polarizers at the moment of plane wave propagation, mixing of $\{1\}$- and $\{2\}$-polarization states is unavoidable in the focused QPS. By this effect, the focused system has sensitivity to both scalar and pseudoscalar fields simultaneously.

We obtain the coupling–mass relation from Eq. (8). The exclusion limits for scalar and pseudoscalar fields at a 95% confidence level are shown in Figs. 11 and 12, respectively.

8. Conclusions

A search for scalar and pseudoscalar fields via the four-wave mixing precess at QPS has been performed by focusing 10 μJ/0.9 ps and 100 μJ/9 ns pulse lasers. The number of $\{1\}$- and $\{2\}$-polarized signal-like photons are $N_{S1} = 0 \pm 0$ (stat.) $\pm\, 2.16$ (syst.I) $\pm\, 0.30$ (syst.II) $\pm\, 0$ (syst.III) and $N_{S2} = 1.46 \pm 1.27$ (stat.) $\pm\, 2.16$ (syst.I) $\pm\, 0.04$ (syst.II) $\pm\, 3.59$ (syst.III), respectively. We confirmed that the expected number of four-wave mixing photons in the residual gas is negligibly small by measuring the pressure dependence. As a result, no significant four-wave mixing signal is observed in this experiment. We obtained the upper limits on the coupling–mass relation for scalar and pseudoscalar fields at a 95% confidence level, respectively. The most sensitive coupling limits $g/M = 5.24 \times 10^{-4}\,\mathrm{GeV}^{-1}$ for scalar search and $g/M = 5.42 \times 10^{-4}\,\mathrm{GeV}^{-1}$ for pseudoscalar search are obtained at $m = 0.15$ eV.

Acknowledgements

We gratefully thank S. Tokita and Y. Miyasaka for operation and maintenance of laser systems. We appreciate Y. Inoue providing the data list of the sensitive curve for the Tokyo axion helioscope.

K. Homma, as the corresponding author, cordially thanks Y. Fujii for the detailed discussions and careful checks with him on the polarization dependence of the scattering probability. He expresses his gratitude to T. Tajima and G. Mourou for many aspects relevant to this subject. He finally acknowledges the strong financial supports by Grants-in-Aid for Scientific Research nos. 24654069, 25287060, and 26104709 from MEXT of Japan, the Collaborative Research Program of the Institute for Chemical Research, Kyoto University (grants No. 2012-6, No. 2013-56, and No. 2014-72), and the MATSUO FOUNDATION.

Funding

Open Access funding: SCOAP^3.

Appendix A. Evaluation of the incident plane rotation factor $\mathcal{G}$

Figure A1 illustrates the relation between the experimentally defined linear polarization directions $\{1\}$ and $\{2\}$ and those theoretically defined (1) and (2). It also depicts the relations between the p_1–p_2 and p_3–p_4 planes with respect to the x–z plane, where the theoretically allowed coupling of an exchanged field to the linear polarization states can be evaluated in the clearest way. In Ref. [3], we have assumed the incident photons p_1 and p_2 are both plane waves with different wave vectors on the same reaction plane, which always ensures the clearest condition. In the general three-dimensional incident case such as a focused Gaussian beam, however, the p_1–p_2 plane can rotate with respect to the x–z plane, which results in a deviation from the theoretically clearest condition. We therefore introduce a weighted averaging factor $\mathcal{G}$ over the clockwise rotation angle Φ of the incident reaction plane with respect to the x-axis as follows.

As discussed in Ref. [3], the Lorentz invariant s-channel scattering amplitude for the Lagrangian defined in Eq. (6) has the following basic form:

$$\mathcal{M}_S = -\left(gM^{-1}\right)^2 \frac{\mathcal{V}_{ab}^{[1]}\mathcal{V}_{cd}^{[2]}}{(p_1+p_2)^2+m^2}, \tag{A1}$$

where $S \equiv abcd$ with $a, b, c, d = 1$ or 2, respectively, denotes a sequence of four-photon polarization states and m is the mass of the scalar or pseudoscalar field. With the vectors defined below, the vertex factors for the scalar case (SC) are expressed as

$$\begin{aligned} \mathcal{V}_{ab}^{[1]\mathrm{SC}} &= (p_1 p_2)\left(e_1^{(a)} e_2^{(b)}\right) - \left(p_1 e_2^{(a)}\right)\left(p_2 e_1^{(b)}\right), \\ \mathcal{V}_{cd}^{[2]\mathrm{SC}} &= (p_3 p_4)\left(e_3^{(c)} e_4^{(d)}\right) - \left(p_3 e_4^{(c)}\right)\left(p_4 e_3^{(d)}\right), \end{aligned} \tag{A2}$$

and those for the pseudoscalar case (PS) are expressed as

$$\begin{aligned} \mathcal{V}_{ab}^{[1]\mathrm{PS}} &= -\epsilon^{\mu\nu\rho\sigma} p_{1\mu} p_{2\rho} e_{1\nu}^{(a)} e_{2\sigma}^{(b)}, \\ V_{cd}^{[2]\mathrm{PS}} &= -\epsilon^{\mu\nu\rho\sigma} p_{3\mu} p_{4\rho} e_{3\nu}^{(c)} e_{4\sigma}^{(d)}. \end{aligned} \tag{A3}$$

We must first take into account the clockwise rotation angle φ of the p_3–p_4 plane with respect to the given x–z plane independent of the p_1–p_2 plane, because these two planes are not coplanar in QPS, contrary to the situation where the coplanar condition of p_1 through p_4 is always satisfied

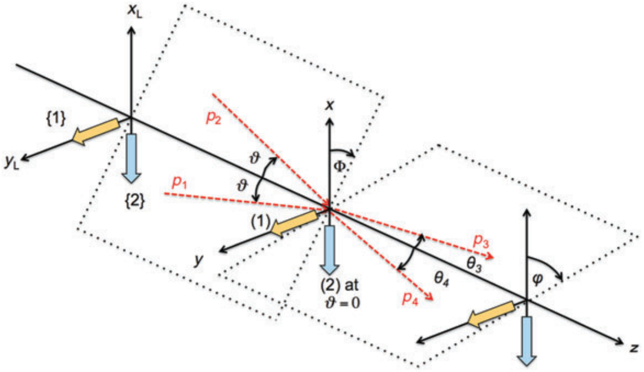

Fig. A1. Definitions of polarization vectors and rotation angles in QPS.

in CMS. This implies that the simple summation factor 2π on the azimuthal degree of freedom of the solid angle cannot be applied to QPS; instead, the φ-dependent squared transition amplitude must be summed over the possible rotation φ from 0 to 2π. We have already introduced this axially asymmetric factor $\mathcal{F}_S$ with respect only to the incident reaction plane at $\Phi = 0$ in [3]. This factor essentially depends only on the second vertex factors above, while the incident plane rotation factor $\mathcal{G}$ is relevant only to the first vertex factors. We thus define the incident plane rotation factor as a weighted average with respect to $\mathcal{F}_S$ at $\Phi = 0$ as follows:

$$\mathcal{G}_{ab} \equiv \frac{\int_0^{2\pi} \left|\mathcal{V}_{ab}^{[1]}(\Phi)\right|^2 d\Phi}{\int_0^{2\pi} \left|\mathcal{V}_{ab}^{[1]}(\Phi = 0)\right|^2 d\Phi}, \tag{A4}$$

because experiments cannot fix the incident reaction plane and the intensity of the creation laser field must be shared over the possible incident reaction planes.

By requiring (1)={1} and (2)={2} at $\Phi = \varphi = 0$ where the theoretically clearest polarization relations can interface with the experimental condition, we describe the polarization vectors and momentum vectors for four photons with rotation angles Φ and φ as follows:

$$e_i^{(1)} = (0, 1, 0), \tag{A5}$$

$$e_1^{(2)} = (-\cos\vartheta, 0, \sin\vartheta), \quad e_2^{(2)} = (-\cos\vartheta, 0, -\sin\vartheta),$$
$$e_3^{(2)} = (-\cos\theta_3, 0, \sin\theta_3), \quad e_4^{(2)} = (-\cos\theta_4, 0, -\sin\theta_4),$$
$$p_1 = (\omega\sin\vartheta\cos\Phi, -\omega\sin\vartheta\sin\Phi, \omega\cos\vartheta; \omega),$$
$$p_2 = (-\omega\sin\vartheta\cos\Phi, \omega\sin\vartheta\sin\Phi, \omega\cos\vartheta; \omega),$$
$$p_3 = (\omega_3\sin\theta_3\cos\varphi, -\omega_3\sin\theta_3\sin\varphi, \omega_3\cos\theta_3; \omega_3),$$
$$p_4 = (-\omega_4\sin\theta_4\cos\varphi, \omega_4\sin\theta_4\sin\varphi, \omega_4\cos\theta_4; \omega_4). \tag{A6}$$

We note here that we cannot rotate polarization vectors because the experiment must introduce fixed polarization vectors. This implies that the clear distinction between scalar and pseudoscalar couplings cannot be stated due to non-zero rotation angles because non-identical linear polarization planes between photon 1 and 2 or photon 3 and 4 are implicitly introduced.

Based on these vectors, we summarize the relations between momenta and polarization vectors with photon labels $i = 1, 2, 3, 4$ as follows:

$$\begin{aligned} \left(p_1 e_j^{(1)}\right) &= -\omega \sin\vartheta \sin\mathit{\Phi}, \quad \left(p_2 e_j^{(1)}\right) = \omega \sin\vartheta \sin\mathit{\Phi}, \\ \left(p_3 e_j^{(1)}\right) &= -\omega_3 \sin\theta_3 \sin\varphi, \quad \left(p_4 e_j^{(1)}\right) = \omega_4 \sin\theta_4 \sin\varphi, \end{aligned} \tag{A7}$$

$$\left(e_i^{(1)} e_j^{(1)}\right) = 1 \quad \text{and} \quad \left(e_i^{(1)} e_j^{(2)}\right) = 0 \tag{A8}$$

for any pair i, j, and

$$\begin{aligned} \left(e_i^{(2)} e_j^{(2)}\right) &= 1 \quad \text{for} \quad i = j, \\ \left(e_1^{(2)} e_2^{(2)}\right) &= \cos 2\vartheta, \left(e_3^{(2)} e_4^{(2)}\right) = \cos(\theta_3 + \theta_4) \equiv \cos\theta_+, \\ \left(e_1^{(2)} e_3^{(2)}\right) &= \cos(\vartheta - \theta_3)\,, \left(e_2^{(2)} e_4^{(2)}\right) = \cos(\vartheta - \theta_4)\,, \\ \left(e_1^{(2)} e_4^{(2)}\right) &= \cos(\vartheta + \theta_4)\,, \left(e_2^{(2)} e_3^{(2)}\right) = \cos(\vartheta + \theta_3)\,, \end{aligned} \tag{A9}$$

and

$$(p_1 p_2) = \omega^2(\cos 2\vartheta - 1) = (p_3 p_4) = \omega_3\omega_4(\cos\theta_+ - 1)\,, \tag{A10}$$

where $(p_1 + p_2)^2 = (p_3 + p_4)^2$ is required for massless photons.

We are now ready to estimate the factor $\mathcal{G}$ included in the partially integrated cross section at Eq. (A24) in Ref. [22]. We evaluate the case of $ab = 11$ for the scalar exchange. From the first of Eq. (A2), we obtain

$$\begin{aligned} \mathcal{V}_{11}^{[1]\mathrm{SC}} &= (p_1 p_2)\left(e_1^{(1)} e_2^{(1)}\right) - \left(p_1 e_2^{(1)}\right)\left(p_2 e_1^{(1)}\right) \\ &= \omega^2\left(\cos 2\vartheta - 1 + \sin^2\vartheta \sin^2\mathit{\Phi}\right) \sim \omega^2\vartheta^2\left(2 - \sin^2\mathit{\Phi}\right), \end{aligned} \tag{A11}$$

where the first of Eq. (A10), Eq. (A5), and $\left(p_1 e_2^{(1)}\right)\left(p_2 e_1^{(1)}\right) = -\left(\omega \sin\vartheta \sin\mathit{\Phi}\right)^2$ are substituted. The last approximation is based on $\vartheta \sim \vartheta_r \ll 1$.

This yields the following averaging factor on the incident reaction plane:

$$\mathcal{G}_{11}^{\mathrm{SC}} = \frac{\int_0^{2\pi}\left(2 - \sin^2\mathit{\Phi}\right)^2 d\mathit{\Phi}}{8\pi} = \frac{19}{32}. \tag{A12}$$

We also provide the case of $ab = 12$ for the pseudoscalar exchange as follows. Based on the first of Eq. (A3), the first vertex factor with vector definitions above is expressed as

$$\begin{aligned} \mathcal{V}_{12}^{[1]\mathrm{PS}} &= -\epsilon^{\mu\nu\rho\sigma} p_{1\mu} p_{2\rho} e_{1\nu}^{(1)} e_{2\sigma}^{(2)} = -p_{1\mu} p_{2\rho} \epsilon^{\mu y\rho\sigma} e_{2\sigma}^{(2)} \\ &= -p_{1\mu} p_{2\rho}\left[\epsilon^{\mu y\rho x}(-\cos\vartheta) + \epsilon^{\mu y\rho z}(-\sin\vartheta)\right] \\ &= p_{2\rho}\left[\left(p_{10}\epsilon^{0y\rho x} + p_{1z}\epsilon^{zy\rho x}\right)\cos\vartheta + \left(p_{10}\epsilon^{0y\rho z} + p_{1x}\epsilon^{xy\rho z}\right)\sin\vartheta\right] \\ &= p_{2\rho}\left[\left(-\omega\epsilon^{0y\rho x} + \omega\cos\vartheta\,\epsilon^{zy\rho x}\right)\cos\vartheta + \left(-\omega\epsilon^{0y\rho z} + \omega\sin\vartheta\cos\mathit{\Phi}\,\epsilon^{xy\rho z}\right)\sin\vartheta\right] \\ &= \left[\left(-\omega\epsilon^{0yzx} p_{2z} + \omega\cos\vartheta\,\epsilon^{zy0x} p_{20}\right)\cos\vartheta\right. \\ &\quad \left. + \left(-\omega\epsilon^{0yxz} p_{2x} + \omega\sin\vartheta\cos\mathit{\Phi}\,\epsilon^{xy0z} p_{20}\right)\sin\vartheta\right] \\ &= \omega^2\left[(-\cos\vartheta + \cos\vartheta)\cos\vartheta + (-\sin\vartheta - \sin\vartheta)\cos\mathit{\Phi}\sin\vartheta\right] = -2\omega^2\sin^2\vartheta\cos\mathit{\Phi}. \end{aligned} \tag{A13}$$

This yields the following averaging factor on the incident reaction plane:

$$\mathcal{G}_{12}^{\mathrm{PS}} = \frac{\int_0^{2\pi} \cos^2 \varphi d\varphi}{2\pi} = \frac{1}{2}. \tag{A14}$$

Appendix B. Refinement of the weight factor $\mathcal{W}$

In Ref. [3,22], we approximated $\mathcal{W}$ as the constant $\pi/2$ for a mass region much smaller than that covered by $\Delta\theta$ as a conservative estimate. This is because we preferred simplicity of the parametrization to accuracy. However, once we need to compare the sensitivity for the higher mass region with the other search methods, the validity of the approximation applicable only to the smaller mass region must be reconsidered. In the following, we first exactly repeat the relevant part of Ref. [22] and then refine $\mathcal{W}$ as a function of the sensitive mass regions by quoting the necessary equations.

We first express the squared scattering amplitude for the case when a low-mass field is exchanged in the s-channel via a resonance state with the symbol to describe polarization combinations of initial and final states S:

$$|\mathcal{M}_S|^2 \approx (4\pi)^2 \frac{a^2}{\chi^2 + a^2}, \tag{B1}$$

where $\chi = \omega^2 - \omega_r^2$ with the resonance condition $m = 2\omega_r \sin\vartheta_r$ for a given mass m, and a is expressed as

$$a = \frac{\omega_r^2}{8\pi}\left(\frac{gm}{M}\right)^2 = \frac{m\Gamma}{2\sin^2\vartheta_r} \tag{B2}$$

with the resonance decay rate of the low-mass field

$$\Gamma = (16\pi)^{-1}\left(gM^{-1}\right)^2 m^3. \tag{B3}$$

The resonance condition is satisfied when the center-of-mass system (CMS) energy between two incident photons $E_{\mathrm{CMS}} = 2\omega\sin\vartheta$ coincides with the given mass m. At a focused geometry of an incident laser beam, however, E_{CMS} cannot be uniquely specified due to the momentum uncertainty of the incident waves. Although the incident laser energy has an intrinsic uncertainty, the momentum uncertainty or the angular uncertainty between a pair of incident photons dominates that of the incident energy. Therefore, we consider the case where only angles of incidence ϑ between randomly chosen pairs of photons are uncertain within $0 < \vartheta \le \Delta\vartheta$ for a given focusing parameter by fixing the incident energy. The treatment for the intrinsic energy uncertainty is explained in detail in the Appendix B of Ref. [22]. We fix the laser energy ω at the optical wavelength

$$\omega_{opt}^2 = \frac{m^2}{4\vartheta_r^2} \sim 1\,\mathrm{eV}^2, \tag{B4}$$

while the resonance condition depends on the incident angle uncertainty. This gives an expression for χ as a function of ϑ:

$$\chi(\vartheta) = w_{\mathrm{opt}}^2 - w_r^2(\vartheta) = \frac{m^2}{4\vartheta_r^2} - \frac{m^2}{4\vartheta^2} = \left(1 - (\vartheta_r/\vartheta)^2\right)\omega_{\mathrm{opt}}^2, \tag{B5}$$

where

$$d\vartheta = \frac{\vartheta_r}{2\omega_{\mathrm{opt}}^2}\left(1 - \frac{\chi}{\omega_{\mathrm{opt}}^2}\right)^{-3/2} d\chi. \tag{B6}$$

We thus introduce the averaging process for the squared amplitude $\overline{|\mathcal{M}_S|^2}$ over the possible uncertainty on incident angles

$$\overline{|\mathcal{M}_S|^2} = \int_0^{\pi/2} \rho(\vartheta)|\mathcal{M}_S(\vartheta)|^2 d\vartheta, \tag{B7}$$

where $\mathcal{M}_S$ specified with a set of physical parameters m and gM^{-1} is expressed as a function of ϑ, and $\rho\,(\vartheta)$ is the probability distribution function as a function of the uncertainty on ϑ within an incident pulse.

We review the expression for the electric field of the Gaussian laser propagating along the z-direction in spatial coordinates (x, y, z) [26] as follows:

$$\vec{E}(x, y, z) = \vec{E}_0 \frac{w_0}{w(z)} \exp\left\{-i[kz - H(z)] - r^2\left(\frac{1}{w(z)^2} + \frac{ik}{2R(z)}\right)\right\}, \tag{B8}$$

where E_0 is the electric field amplitude, $k = 2\pi/\lambda$, $r = \sqrt{x^2 + y^2}$, w_0 is the minimum waist, which cannot be smaller than λ due to the diffraction limit, and the other definitions are as follows:

$$w(z)^2 = {w_0}^2\left(1 + \frac{z^2}{{z_R}^2}\right), \tag{B9}$$

$$R = z\left(1 + \frac{{z_R}^2}{z^2}\right), \tag{B10}$$

$$H(z) = \tan^{-1}\left(\frac{z}{z_R}\right), \tag{B11}$$

$$z_R \equiv \frac{\pi {w_0}^2}{\lambda}. \tag{B12}$$

With θ being an incident angle of a single photon in the Gaussian beam, the angular distribution $g(\theta)$ can be approximated as

$$g(\theta) \sim \frac{1}{\sqrt{2\pi}\Delta\theta} \exp\left\{-\frac{\theta^2}{2\Delta\theta^2}\right\}, \tag{B13}$$

where the incident angle uncertainty in the Gaussian beam $\Delta\theta$ is introduced within the physical range $|\theta| < \pi/2$ as

$$\Delta\theta \sim \frac{\lambda_c}{\pi w_0} = \frac{d}{2f}, \tag{B14}$$

with the wavelength of the creation laser λ_c, the beam diameter d, the focal length f, and the beam waist $w_0 = \frac{f\lambda_c}{\pi d/2}$, as illustrated in Fig. 1. For a pair of photons 1, 2, each of which follows $g\,(\theta)$, the incident angle between them is defined as

$$\vartheta = \tfrac{1}{2}|\theta_1 - \theta_2|. \tag{B15}$$

With the variance $\Delta\vartheta^2 = 2\left(\frac{1}{4}\Delta\theta^2\right)$, the pair angular distribution $\rho\,(\vartheta)$ is then approximated as

$$\rho\,(\vartheta) \sim \frac{2}{\sqrt{\pi}\Delta\theta} \exp\left\{-\left(\frac{\vartheta}{\Delta\theta}\right)^2\right\} \sim \frac{2}{\sqrt{\pi}\Delta\theta} \quad \text{for} \quad 0 < \vartheta < \pi/2, \tag{B16}$$

where the coefficient 2 of the amplitude is caused by limiting ϑ to the range $0 < \vartheta < \pi/2$, and $\left(\frac{\vartheta}{\Delta\theta}\right)^2 \ll 1$ is taken into account because $\Delta\theta$ in Eq. (B14) also corresponds to the upper limit by the focusing lens based on geometric optics. This distribution is consistent with the flat-top distribution applied to Refs. [3,24] apart from the coefficient.

We now re-express the average of the squared scattering amplitude as a function of $\chi \equiv a\xi$ in units of the width of the Breit–Wigner (BW) distribution a by substituting Eqs. (B1) and (B16) into Eq. (B7) with Eq. (B6):

$$\overline{|\mathcal{M}_S|^2} = \frac{(4\pi)^2}{\sqrt{\pi}\,\omega_{\mathrm{opt}}^2}\left(\frac{\vartheta_r}{\Delta\theta}\right) a\mathcal{W}, \tag{B17}$$

where we introduce the constant

$$\mathcal{W} \equiv \int_{-\infty}^{\frac{\omega_{\mathrm{opt}}^2}{a}\left\{1-(\vartheta_r/(\pi/2))^2\right\}} W(\xi)\,\frac{1}{\xi^2+1}\,d\xi \tag{B18}$$

with

$$W(\xi) \equiv \left(1 - \frac{a\xi}{\omega_{\mathrm{opt}}^2}\right)^{-3/2}. \tag{B19}$$

In Eq. (B18) the weight function $W(\xi)$ is a positive and monotonic function within the integral range and the second term is the BW function with a width of unity. Note that $\overline{|\mathcal{M}_S|^2}$ is now explicitly proportional to a but not a^2. This gives the enhancement factor a compared to the case $\overline{|\mathcal{M}_S|^2} \propto a^2$ where no resonance state is contained in the integral range controlled by $\Delta\theta$ experimentally. The integrated value of the pure BW function from $\xi = -1$ to $\xi = +1$ gives $\pi/2$, while that from $\xi = -\infty$ to $\xi = +\infty$ gives π. The difference is only a factor of two. The weight function $W(\xi)$ of the kernel is almost unity for small $a\xi$, that is, when a is small enough with a small mass and a weak coupling. Therefore, we will consider only the region of $\xi \pm 1$ as a conservative estimate. By taking only this integral range, we can be released from trivial numerical modifications originating from $\xi = -\infty$ and the behavior of $W(\xi)$ at $\xi = \frac{\omega_{\mathrm{opt}}^2}{a}\left\{1 - (\vartheta_r/(\pi/2))^2\right\}$ which are not essential due to the strong suppression by the BW weight.

We now refine $\mathcal{W}$ in order to apply it more accurately even to the case for $\vartheta_r/\Delta\theta \sim 1$ where, exactly speaking, the second approximation in Eq. (B16) is not valid. In this case, by using the first of Eq. (B16) with substitution of the relation between $\chi \equiv a\xi$ and ϑ expressed in Eq. (B5), Eq. (B19) is modified as follows:

$$W(\xi) \equiv \exp\left\{-\frac{(\vartheta_r/\Delta\theta)^2}{1-\frac{a}{\omega_{\mathrm{opt}}^2}\xi}\right\}\left(1-\frac{a}{\omega_{\mathrm{opt}}^2}\xi\right)^{-3/2} \sim \exp\left\{-\left(\frac{\vartheta_r}{\Delta\theta}\right)^2\right\}, \tag{B20}$$

where the last approximation is based on $a/\omega_{opt}^2 \ll 1$ with respect to the integral range $\xi \pm 1$ in Eq. (B18) for the conservative estimate. This is justified in the mass–coupling range we are interested in via the first relation in Eq. (B2), for instance, $a/\omega_{\mathrm{opt}}^2 \sim 10^{-29}$ for $m \sim 0.1$ eV and $g/M \sim 10^{-4}\,\mathrm{GeV}^{-1}$. By substituting Eq. (B20) into Eq. (B18), the conservative evaluation on $\mathcal{W}$ over $\xi \pm 1$ is expressed as

$$\mathcal{W} \sim \int_{-1}^{+1} W(\xi)\,\frac{1}{\xi^2+1}\,d\xi \sim \frac{\pi}{2}\exp\left\{-\left(\frac{\vartheta_r}{\Delta\theta}\right)^2\right\}. \tag{B21}$$

This factor is dependent on ϑ_r, equivalently dependent on mass, especially for larger ϑ_r close to $\Delta\theta$, while it is almost $\pi/2$ for smaller ϑ_r.

References

[1] Y. Fujii and K. Maeda, *The Scalar–Tensor Theory of Gravitation* (Cambridge University Press, Cambridge, 2003).

[2] Y. Fujii and K. Homma, Prog. Theor. Phys. **126**, 531 (2011); Prog. Theor. Exp. Phys. **2014**, 089203 (2014) [erratum].
[3] K. Homma, Prog. Theor. Exp. Phys. **2012**, 04D004 (2012); **2014**, 089201 (2014) [erratum].
[4] S. Weinberg, Phys. Rev. Lett. **40**, 223 (1978).
[5] F. Wilczek, Phys. Rev. Lett. **40**, 279 (1978).
[6] R. D. Peccei and H. R. Quinn, Phys. Rev. Lett. **38**, 1440 (1977).
[7] M. P. Hertzberg, M. Tegmark, and F. Wilczek, Phys. Rev. D **78**, 083507 (2008).
[8] O. Wantz and E. P. S. Shellard, Phys. Rev. D **82**, 123508 (2010).
[9] S. Moriyama et al., Phys. Lett. B **434**, 147 (1998).
[10] Y. Inoue et al., Phys. Lett. B **536**, 18 (2002).
[11] Y. Inoue et al., Phys. Lett. B **668**, 93 (2008).
[12] K. Zioutas et al. [CAST Collaboration], Phys. Rev. Lett. **94**, 121301 (2005).
[13] S. Andriamonje et al. [CAST Collaboration], J. Cosmol. Astropart. Phys. **04**, 010 (2007).
[14] E. Arik et al. [CAST Collaboration], J. Cosmol. Astropart. Phys. **02**, 008 (2009).
[15] M. Arik et al. [CAST Collaboration], Phys. Rev. Lett. **107**, 261302 (2011).
[16] R. Cameron et al., BFRT Phys. Rev. D **47**, 3707 (1993).
[17] E. Zavattini et al. [PVLAS Collaboration], Phys. Rev. D **77**, 032006 (2008).
[18] P. Pugnat et al. [OSQAR Collaboration], Phys. Rev. D **78**, 092003 (2008).
[19] K. Ehret et al. [ALPS Collaboration], Phys. Lett. B **689**, 149 (2010).
[20] S. J. Asztalos et al. [ADMX Collaboration], Phys. Rev. D **69**, 01101 (2004).
[21] S. J. Asztalos et al. [ADMX Collaboration], Phys. Rev. Lett. **104**, 041301 (2010).
[22] K. Homma, T. Hasebe, and K. Kume, Prog. Theor. Exp. Phys. **2014**, 083C01 (2014).
[23] T. Tajima and K. Homma, Int. J. Mod. Phys. A **27**, 1230027 (2012).
[24] K. Homma, D. Habs, and T. Tajima, Appl. Phys. B **106**, 229 (2012).
[25] S. A. J. Druet and J.-P. E. Taran, Prog. Quant. Electr. **7**, 1 (1981).
[26] A. Yariv, *Optical Electronics in Modern Communications* (Oxford University Press, Oxford, 1997).
[27] F. Moulin and D. Bernard, Opt. Commun. **164**, 137 (1999).
[28] E. Lundström et al., Phys. Rev. Lett. **96**, 083602 (2006).
[29] J. Lundin et al., Phys. Rev. A **74**, 043821 (2006).
[30] D. Bernard et al., Eur. Phys. J. D **10**, 141 (2000).
[31] J. Beringer et al. [Particle Data Group], Phys. Rev. D **86**, 010001 (2012).
[32] Y. Su et al., Phys. Rev. D **50**, 3614 (1994); **51**, 3135 (1995) [erratum].
[33] E. G. Adelberger et al., Phys. Rev. Lett. **98**, 131104 (2007).
[34] D. J. Kapner et al., Phys. Rev. Lett. **98**, 021101 (2007).
[35] J. Chiaverini et al., Phys. Rev. Lett. **90**, 151101 (2003).
[36] S. J. Smullin et al., Phys. Rev. D **72**, 122001 (2005); **72**, 129901 (2005) [erratum].
[37] S. K. Lamoreaux, Phys. Rev. Lett. **78**, 5 (1997); **81**, 5475 (1998) [erratum].
[38] J. E. Kim, Phys. Rev. Lett. **43**, 103 (1979).
[39] M. A. Shifman, A. I. Vainshtein, and V. I. Zakharov, Nucl. Phys. B **166**, 493 (1980).

参考論文

(1) The first search for sub-eV scalar fields
via four-wave mixing at a quasi-parallel laser collider

Kensuke Homma, Takashi Hasebe, and Kazuki Kume

Progress of Theoretical and Experimental Physics
083C01 (2014)

(2) 真空内四光波混合光による sub-eV 中性ボゾンの
共鳴探索

本間謙輔, 長谷部孝, 久米一輝, 阪部周二, 橋田昌樹

高エネルギーニュース, vol32, No3, (2013) 171 - 177

PTEP

Prog. Theor. Exp. Phys. **2014**, 083C01 (25 pages)
DOI: 10.1093/ptep/ptu087

The first search for sub-eV scalar fields via four-wave mixing at a quasi-parallel laser collider

Kensuke Homma[1,2,*], Takashi Hasebe[1], and Kazuki Kume[1]

[1] *Graduate School of Science, Hiroshima University, Kagamiyama, Higashi-Hiroshima, Hiroshima 739-8526, Japan*
[2] *International Center for Zetta-Exawatt Science and Technology, Ecole Polytechnique, Route de Saclay, Palaiseau, F-91128, France*
*E-mail: homma@hepl.hiroshima-u.ac.jp

Received August 19, 2013; Revised April 30, 2014; Accepted May 16, 2014; Published August 7, 2014

A search for sub-eV scalar fields coupling to two photons has been performed via four-wave mixing at a quasi-parallel laser collider for the first time. The experiment demonstrates the novel approach of searching for resonantly produced sub-eV scalar fields by combining two-color laser fields in the vacuum. The aim of this paper is to provide the concrete experimental setup and the analysis method based on specific combinations of polarization states between incoming and outgoing photons, which is extendable to higher-intensity laser systems operated at high repetition rates. No significant signal of four-wave mixing was observed by combining a 0.2 μJ/0.75 ns pulse laser and a 2 mW CW laser on the same optical axis. Based on the prescription developed for this particular experimental approach, we obtained the upper limit at a confidence level of 95% on the coupling–mass relation.

Subject Index C15, C19, C23, C33, C41

1. Introduction

The large proportion of dark components in the universe motivates us to search for yet undiscovered fields to naturally interpret the relevant observations. In high-energy scales, several bosons have been discovered that can be understood as a result of spontaneous symmetry breaking, such as pions based on chiral symmetry at the 0.1 GeV scale and W/Z bosons based on gauge symmetry via the Higgs mechanism at the 100 GeV scale. The relevant experimental results show the evidence of coupling to two photons of boson states via, for instance, the decay process of the neutral pion and the Higgs-like particle. These facts encourage further experimental searches for similar types of fields via two-photon coupling at very different energy scales, apart from any theoretical speculations. In addition, there are actually theoretical rationales for expecting sub-eV particles such as the axion (pseudoscalar boson) [1–3] and the dilaton (scalar boson) [4–6] associated with breaking of fundamental symmetries in the context of particle physics and cosmology. Therefore, we are led to probe such fields via their coupling to two photons in the sub-eV mass range. Furthermore, the advent of high-intensity laser systems and the rapid leap of the intensity encourage the approach of probing weakly coupling dark fields with optical photons by the enhanced luminosity factor [7,8].

We advocated the concept of the quasi-parallel laser collider to produce a resonance state of a hypothetical boson in the sub-eV mass range and simultaneously induce the decay in the background of a coherent laser field [9–11]. The exchange of such a low-mass field is interpreted as the

Funded by SCOAP^3

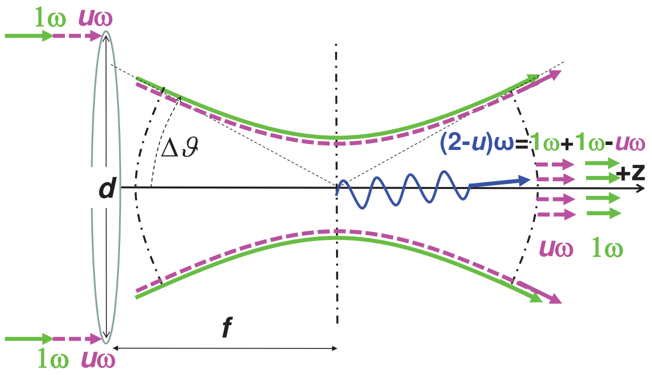

Fig. 1. Quasi-parallel colliding system (QPS) between two incident photons out of a focused laser beam with focal length f, beam diameter d, and with the upper range of incident angles $\Delta\vartheta$ determined by geometric optics. The signature $(2-u)\omega$ is produced via the four-wave mixing process, $1\omega + 1\omega \to (2-u)\omega + u\omega$ with $0 < u < 1$, by mixing two-color waves with different frequencies 1ω and $u\omega$ in advance at the incidence.

four-wave mixing process in the vacuum. Figure 1 illustrates the four-wave mixing process where two photons with degenerate energy ω are used for resonance production, the inducing laser field has the energy $u\omega$ with $0 < u < 1$, and a photon with the energy $(2-u)\omega$ is created as the signature of the interaction. This four-wave mixing process is well known in quantum optics [12,13], where atomic dynamics governs the phenomenon instead of the exchange of the hypothetical resonance state, and the application to test the higher-order QED effect can also be found in Refs. [14–17]. We identify this wave-mixing system as a special kind of photon–photon collider intentionally; it has the significant advantage that the interaction rate has cubic dependence on the laser intensity, while conventional particle colliders have quadratic dependence on the number of charged particles per colliding bunch [11]. The cubic dependence of the interaction rate highly motivates us to extend the method to much higher pulse energy and higher-intensity laser systems.

The proposed method can in principle distinguish whether the exchanged boson is scalar or pseudoscalar based on combinations of polarization states in the initial and final state photons [11]. Therefore, the method has impacts on searches for axion-like particles as well as the fifth force [18,19]. In this paper, however, we focus only on the case of the scalar field exchange, because the experimental setup is simpler. The aim of this paper is to demonstrate the pilot experiment to search for sub-eV scalar fields via the four-wave mixing process in the vacuum, in which the basic elements necessary for the proposed experimental method and data analysis are provided so that they can be extended to much higher-intensity systems operated at high repetition rates in the near future [20].

2. Coupling–mass relation

In this section we summarize the formulae necessary to obtain the coupling–mass relation from experimental parameters. The formulae are basically from Ref. [11]; however, we re-evaluate the relations to apply to the realistic experimental conditions in the pilot search. We thus provide the details of the corrections in Appendices A and B compared with those in Ref. [9,11].

The effective interaction Lagrangian between two photons and a hypothetical low-mass scalar field has the generic form expressed as

$$-L_\phi = gM^{-1}\frac{1}{4}F_{\mu\nu}F^{\mu\nu}\phi, \tag{1}$$

where M has the dimension of energy while g is a dimensionless constant.

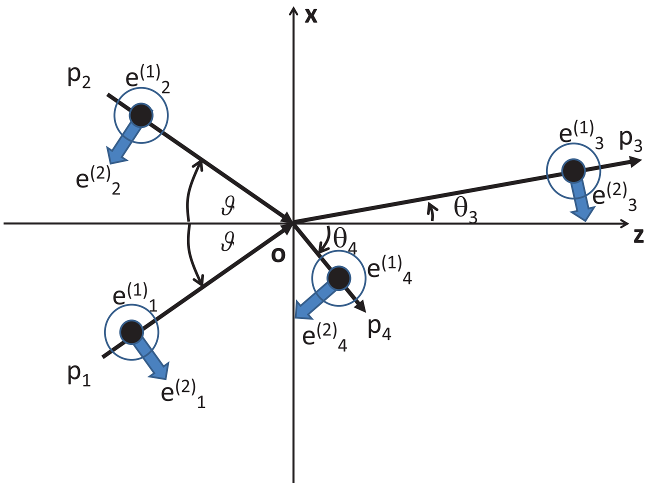

Fig. 2. Definitions of kinematic variables [9].

In the case of scalar field exchange, the possible linear polarization states in the four-wave mixing process when all wave vectors are on the same plane, as illustrated in Fig. 2, are expressed as follows:

$$\omega\{1\} + \omega\{1\} \to (2-u)\omega\{1\} + u\omega\{1\},$$
$$\omega\{1\} + \omega\{1\} \to (2-u)\omega\{2\} + u\omega\{2\}, \quad (2)$$

where photon energies from the initial to the final states are denoted by the linear polarization states $\{1\}$ and $\{2\}$, which are orthogonal to each other. In this pilot experiment, we pursue the second case of Eq. (2).

We then introduce notations to describe the kinematics of four photons as illustrated in Fig. 2, where the incident angle ϑ is assumed to be symmetric around the z-axis in the average sense, because we focus lasers symmetrically by a lens element. We introduce an arbitrary number u with $0 < u < 1$ to redefine the momenta of the final state photons as

$$\omega_4 \equiv u\omega \quad \text{and} \quad \omega_3 \equiv (2-u)\omega, \quad (3)$$

where we require $0 < \omega_4 < \omega_3 < 2\omega$. We look to measure ω_3 with the specific polarization states as the signature of the interaction. With these definitions, energy–momentum conservation is expressed as [11]

$$(2-u)\omega + u\omega = 2\omega, \quad (4)$$
$$(2-u)\omega\cos\theta_3 + u\omega\cos\theta_4 = 2\omega\cos\vartheta, \quad (5)$$
$$(2-u)\omega\sin\theta_3 = u\omega\sin\theta_4, \quad (6)$$
$$\mathcal{R} \equiv \frac{\sin\theta_3}{\sin\theta_4} = \frac{\omega_4}{\omega_3} = \frac{u}{2-u} = \frac{\sin^2\vartheta}{1 - 2\cos\vartheta\cos\theta_4 + \cos^2\vartheta}. \quad (7)$$

Given a set of physical parameters of the scalar field exchange–mass m, coupling to two photons g/M, and the polarization-dependent factor $\mathcal{F}_S$ with a specified set of linear polarizations S as explained below–the yield is parameterized as

$$\mathcal{Y} \equiv \frac{1}{64\sqrt{2}\pi^4}\left(\frac{\lambda_c}{c\tau_c}\right)\left(\frac{\tau_c}{\tau_i}\right)\left(\frac{f}{d}\right)^3 \tan^{-1}\left(\frac{\pi d^2}{4f\lambda_c}\right)\frac{(\overline{u}-\underline{u})^2}{\overline{u}\underline{u}}\left(\frac{gm\,[\mathrm{eV}]}{M\,[\mathrm{eV}]}\right)^2 \times \left(\frac{m\,[\mathrm{eV}]}{\omega\,[\mathrm{eV}]}\right)^3 \mathcal{W}\mathcal{F}_S C_{\mathrm{mb}} N_c^2 N_i, \tag{8}$$

which is quoted from Eq. (A35) in Appendix A, where the subscripts c and i denote creation and inducing lasers, respectively, λ the wavelength, τ the pulse duration, f a common focal length, d a common beam diameter, $\overline{u}$ and $\underline{u}$ upper and lower values on u determined by the spectrum width of ω_4, respectively, $C_{\mathrm{mb}} = 1/2$ is the combinatorial factor originating from the consideration on multimode frequency states [11], N the average numbers of photons in coherent states, $\mathcal{W} \sim \pi/2$ the numerical factor relevant to the integral of the weighted resonance function defined by Eq. (A22) in Appendix A, and we partially apply natural units to parameters specified with [eV].

Reference [11] discussed the effect of the spectrum width in the case that the spectrum width of the creation laser is negligibly small compared to that of the inducing laser. However, this is not always the case. For example, this pilot experiment is actually performed with the condition that both widths are nearly equal, as we explain in the next section. We provide the details of the effective choice of $\overline{u}$ and $\underline{u}$ applicable to the most general case in Appendix B.

In the case of $S = 1122$ as specified by the second of Eqs. (2) applied to the scalar field exchange (SC), the polarization-dependent factor is estimated as [11]

$$\mathcal{F}^{SC}_{1122} \sim 2\pi\left(\frac{3}{8} + 3\hat{\mathcal{R}}^2 - \hat{\mathcal{R}}\right), \tag{9}$$

with $\hat{\mathcal{R}} \equiv \frac{1}{2}(\mathcal{R} + \mathcal{R}^{-1})$ for a given u via $\mathcal{R}$ in Eq. (7). This factor originates from a degree of freedom on the azimuthal rotation of the plane including p_3 and p_4 around the z-axis in Fig. 2 with respect to that defined by p_1 and p_2. The other polarization combinations can also be calculated based on the appendix of Ref. [11].

From Eq. (8) we express the coupling parameter g/M to discuss the sensitivity as a function of m for a given set of experimental parameters via the equation

$$\frac{g}{M\,[\mathrm{eV}]} = 2^{1/4}8\pi^2\sqrt{\frac{\mathcal{Y}\omega^3\,[\mathrm{eV}]}{\left(\frac{\lambda_c}{c\tau_c}\right)\left(\frac{\tau_c}{\tau_i}\right)\left(\frac{f}{d}\right)^3\tan^{-1}\left(\frac{\pi d^2}{4f\lambda_c}\right)\frac{(\overline{u}-\underline{u})^2}{\overline{u}\underline{u}}\mathcal{W}\mathcal{F}_S C_{\mathrm{mb}} N_c^2 N_i}}\,m^{-5/2}\,[\mathrm{eV}] \tag{10}$$

under the condition $\tau_c \le \tau_i$, because the pulse energy of the creation laser is more important for enhancing the signal yield due to the quadratic dependence on the energy.

3. Experimental setup to detect four-wave mixing

Figure 3 shows a schematic view of the experimental setup. The setup consists of the wave mixing part (WM), the interaction vacuum chamber (IC), the intensity monitoring part (IM), and the single-photon detection part (SPD).

WM combines a pulsed laser beam to create a resonance state with a continuous-wave (CW) laser beam which induces the decay with specified linear polarization states. For the purpose of calibration, a laser beam containing the signal energy $(2-u)\omega$ is also combined. The wave mixing can be achieved by a set of dichroic mirrors.

The pulsed laser is the linearly polarized NanoLaser, a monolithic passively Q-switched microchip laser. The laser cavity consists of a 2 mm^3 Nd:YAG gain medium bonded to a chromium-doped

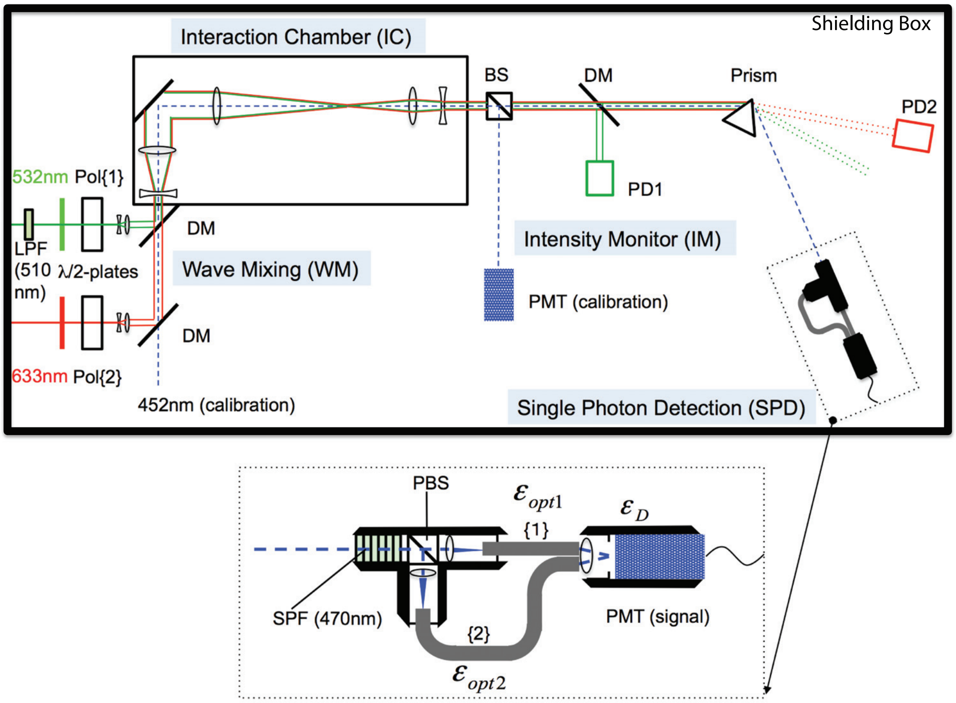

Fig. 3. Schematic view of the experimental setup to measure the four-wave mixing process in the vacuum.

YAG saturable absorber. The repetition rate depends on the diode pumping power: the higher the pumping power, the faster the absorber saturates and becomes transparent. The measured repetition rate is 18.5 kHz. The cavity's mirrors are vapor deposited on the both sides of the crystal to form a monolithic oscillator pumped by a CW diode laser. The second-harmonic wavelength of 532 nm is produced by converting the fundamental wavelength of 1064 nm. The pulse energy of the 532 nm wave is typically 0.8 μJ per 0.75 ns pulse duration with the transverse mode close to TEM00 at the ejection point of the laser.

The CW laser is a linearly polarized helium–neon laser at the wavelength 632.8 nm with power 10 mW at the ejection point of the laser and the transverse mode TEM00.

The relative line widths of these lasers with respect to their central frequencies are summarized in Table 2. In addition, as we discuss in Appendix B concerning the relation on line widths between creation and inducing lasers which is relevant to $\overline{u}$ and $\underline{u}$ in Eq. (8), we evaluate the effective line width in the averaged quasi-parallel frame based on Eq. (B26) in Appendix B.

Given wavelengths for the creation laser ($\lambda_c = 532$ nm) and inducing laser ($\lambda_i = 633$ nm) beams which result in $u = \lambda_c/\lambda_i = 0.84$, the corresponding wavelength of four-wave mixing is expected to be

$$\lambda_s = \frac{\lambda_c/2 \cdot \lambda_i}{\lambda_i - \lambda_c/2} = 459\,\text{nm}. \tag{11}$$

Thus, in addition to the creation and inducing laser beams, a blue diode laser covering the 452 ± 10 nm wavelength range is used to supply the calibration source to align the detection system and to obtain the detector efficiency with respect to the signal photon of $(2 - u)\omega$.

The linear polarizers made of calcite with an extinction ratio of $O(10^{-4})$ specify the incident linear polarization states of the creation and inducing laser fields, as well as the calibration laser field. The linear polarization state {1} is determined by the polarizer (Pol{1}) for the creation laser, while the state {2} is set by the polarizer (Pol{2}) for the inducing laser, which is adjusted so that the planes of the linear polarizations become orthogonal to each other. In front of the linear polarizers, $\lambda/2$-plates are placed and adjusted so that the transmittance of almost linearly polarized lasers at the output of the laser systems is maximized. In front of the ejection point of the creation pulse laser, we put a long-pass filter to accept wavelengths only above 510 nm to suppress wavelengths close to the signal wavelength of 459 nm in advance of the wave mixing with the optical density OD ~ 4, where OD is defined as OD $\equiv -\log_{10}(I/I_0)$ with output and input photon intensities I and I_0, respectively.

After wave mixing with specified polarization states, the combined laser beams share the common optical axis, and they are guided into the interaction chamber (IC) which is maintained at 1.2×10^{-4} Pa. Inside IC, a set of achromatic lenses expands the beam diameter to 40 mm and focuses the combined beams with a focal length of $f = 200$ mm. The focal spots are monitored by a beam profile monitor and the centers of the two-color beam profiles at a point near the common focal spot are aligned with each other with $\sim$10 μm precision. The agreement of the optical axes between the two beams is also confirmed by checking the profile overlap at a different point from the focal spot along the common optical axis. After focusing the combined beams inside IC, the divergent beams are parallelized by a set of achromatic lenses with a reduced beam diameter of 10 mm and guided outside the IC through the chamber window. The beam-focusing parameter is important, because this gives the upper limit of the sensitive mass range by the possible range of the incident angle ϑ via Eqs. (A18)–(A20) in Appendix A. The resonance production is enhanced when $m = 2\omega \sin\vartheta$ is satisfied, that is, when the CMS-energy between two incident photons coincides with the exchanged mass. If the angular coverage $\Delta\vartheta$ is too small compared to the mass we are interested in, the resonance condition is never satisfied. Therefore, the focusing parameter can adjust the sensitive mass range via the upper limit on the incident angles. In this pilot experiment the upper limit on mass is thus 0.46 eV for the creation laser wavelength of 532 nm (2.3 eV).

The absolute beam intensities are monitored by the beam profile monitor. The non-interacting creation and inducing laser fields are kicked out by individual dichroic mirrors and the reflected waves are measured by the photo diodes PD1 and PD2 for 532 nm and 633 nm, respectively. This amplitude information is used to monitor the relative intensity variation on a shot-by-shot basis.

The signal wave is further guided to an equilateral prism made of N-SF11 glass with a MgF_2 anti-reflection coat, and thus refracted to the detection system, while the residual non-interacting creation and inducing beams are refracted in different directions. These non-interacting waves are further reflected by mirrors and dumped apart from the detection point of the signal wave.

For the scalar field search, we require the initial and final state photon energies with their linear polarization states as follows:

$$\omega\{1\} + \omega\{1\} \to u\omega\{2\} + (2-u)\omega\{2\}, \tag{12}$$

where {1} and {2} specify orthogonal linear polarization states for photons in the creation beam and in the inducing beam, respectively. As a reference polarization combination, we also simultaneously measure the case

$$\omega\{1\} + \omega\{1\} \to u\omega\{2\} + (2-u)\omega\{1\}, \tag{13}$$

which is not allowed when all the wave vectors in Fig. 2 are on the same plane. Due to a degree of freedom on the relative rotation angle between the $p_1 - p_2$ and $p_3 - p_4$ planes around the z-axis, however, there is a finite probability of accepting this polarization combination. In order to measure both cases on a shot-by-shot basis, we introduced the polarization beam splitter (PBS) whose polarization directions are aligned to the incident laser polarizations {1} and {2} respectively in advance

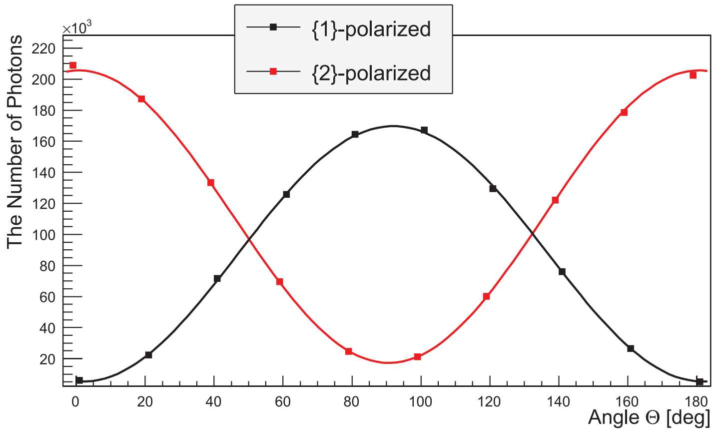

Fig. 4. The number of photons in $T\{1\}$ and $T\{2\}$ as a function of the relative rotation angle between the polarization plane of the pulsed creation laser and that of the polarization beam splitter (PBS).

(see the enlarged view of the SPD part in Fig. 3). For the two polarization paths behind the PBS, two plastic optical fibers whose transmittances are independent of the incident linear polarization states are attached with different lengths by introducing a relative time delay of 23.75 ns. These two optical fibers are attached to a common photomultiplier tube (PMT), which is a metal package PMT with the rise time of 0.78 ns (R7400-01 manufactured by HAMAMATSU), through lenses so that we can count the number of photons in the two different time domains $T\{1\}$ and $T\{2\}$ separated by that time difference on the digitized wave form of the analog output from the common PMT. By using the fiber-coupled PMT, the degree of linear polarization is measured by rotating the polarization plane of the pulsed creation laser with respect to that of the PBS. Figure 4 shows how the numbers of photons in $T\{1\}$ and $T\{2\}$ change as a function of the relative rotation angle Θ in units of degrees. The fit results with the functional form $\sin(\pi\Theta/180)$ are consistent with a nearly linear polarized state after transmission through all the optics, including the dichroic mirrors.

In order to shut out residual non-interacting creation and inducing laser photons, five short-pass filters (SPF) with nominal OD ∼4 for each to accept only wavelengths below 470 nm are placed inside the tube in front of the PBS. The detection efficiency for the signal wavelength is evaluated in advance of the pilot measurement with two PMTs of the same type using the beam splitter (BS) in Fig. 3.

The readout of the analog signal from the photomultiplier is performed by a four-channel waveform digitizer (10-bit cPCI High-Speed Digitizers, Acqiris DC282 type U1065A provided by Agilent Technologies) without any electronics for amplification to avoid adding noise sources. The measured maximum rate of the readout by requiring simple online preselections is ∼10 kHz. The digitizer is similar to a digital oscilloscope; however, the readout speed is three orders of magnitude higher. Thus, online selections based on an algorithm are applicable before waveforms are actually stored.

Trigger signals are created by discriminating pulse heights of analog signals on PD1 and the digitizer is synchronized with these trigger signals. By denoting the existence or absence of green (532 nm) and red (633 nm) lasers as g and r or $\bar{g}$ and $\bar{r}$, respectively, we can consider the following four wave-mixing patterns: $g + r$, $\bar{g} + \bar{r}$, $g + \bar{r}$, and $\bar{g} + r$, representing the cases including signal (S), dark currents or pedestal (P), residual of creation laser photons (C), and residual of inducing laser photons (I), respectively. The pedestal trigger is produced immediately after every 18.5 kHz green triggers by adding a constant delay at which the green laser pulse is physically absent.

We put a physical shutter on the CW red laser beam line, repeating open and close every 2 s. Monitoring the green and red laser amplitudes at individual triggers allows the identification of the four patterns of wave-mixing S, P, C, and I based on offline analysis of the recorded digitized waveform. Waveforms are recorded with 500 sampling points during the 250 ns time window corresponding to 0.5 ns/division, which is consistent with the time resolution on the leading edge of the photomultiplier (PMT) used for the single photon detection.

As the online level trigger, we required that at least one signal-like signature below a -1.00 mV threshold after online pedestal subtraction is found in either $T\{1\}$ or $T\{2\}$ time domain within the two 15 ns windows (see the green bands in Figs. 4 and 6), and only waveforms containing such a signature are recorded on the disk for offline analysis.

The number of total triggers reached 2.5×10^9 during the pilot measurement over four days.

4. Offline data analysis

In order to test the statistical significance of the four-wave mixing signals, the quantities we discuss are N_{Si} which are the acceptance-uncorrected numbers of photons found in the time domains $T\{i\}$ with the linear polarization states $i = 1, 2$ in the case of the signal pattern (S). For the following paragraphs, we abbreviate the symbols of the time domains with specified polarization states, unless confusion is expected.

First, the four patterns: signal (S), pedestal (P), residual of green laser photons (C), and residual of red laser photons (I) are each identified by looking at the amplitudes of the photodiodes recorded in the waveform data, and the number of events of individual patterns, W_S, W_P, W_C, and W_I, respectively, are counted. These numbers are used as the weights to evaluate the number of photons in the signal pattern by subtracting those in the other patterns.

Since there are no perfect wave-filters, we must expect non-zero numbers of residual photons in the three patterns except for the pedestal pattern where the dominant background is the thermal noise from the photomultiplier. We therefore interpret the observed raw numbers of photons n in the four patterns specified with individual subscripts as

$$\begin{aligned} n_S &= N_P + N_C + N_I + N_S \\ n_C &= N_P + N_C \\ n_I &= N_P + N_I \\ n_P &= N_P, \end{aligned} \tag{14}$$

where we assume that the observed pedestal counts include thermal noise from the photodevice and ambient noise such as cosmic rays, and hence the pedestal counts should be commonly included in the other three patterns in the average sense. By considering the event weights of the four trigger patterns, we then deduce the true number of photons in the signal pattern as follows

$$\begin{aligned} N_S &= n_S - \frac{W_S}{W_P} n_P - \frac{W_S}{W_C}(n_C - n_P) - \frac{W_S}{W_I}(n_I - n_P) \\ &= n_S - \frac{W_S}{W_C} n_C - \frac{W_S}{W_I} n_I + \frac{W_S}{W_P} n_P. \end{aligned} \tag{15}$$

We note that, exactly speaking, the physical meaning of n_P is different from the number of photons, because the dominant pedestal charges are produced by thermal noise in the photodevice. As long as the observed charges are expressed in units of single-photon equivalent charge, however, this treatment is justified.

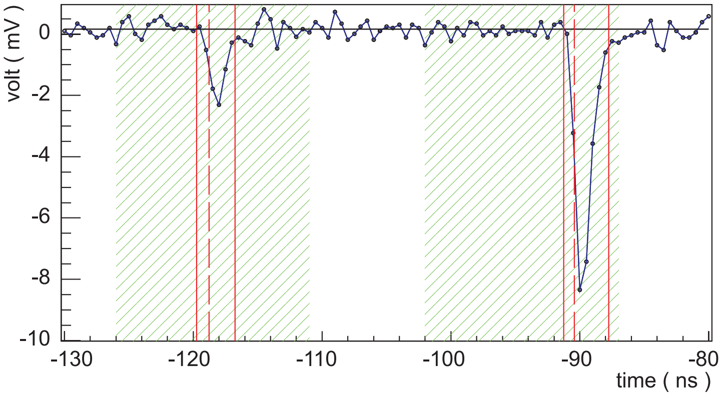

Fig. 5. Single-shot example of a digitized waveform with peaks within the 50 ns time window.

The analysis steps to obtain the observed raw numbers n_{ij} with trigger patterns $i = \mathrm{S, C, I, P}$ and linear polarization states $j = 1, 2$ are as follows. Figure 5 shows a single-shot example of the digitized waveform within a 50 ns time window. The two time domains within 3.5 ns intervals subtended by two solid vertical lines are equally defined and are separated by the known time difference of 23.75 ns due to the different optical fiber lengths. The shorter (earlier time domain) and longer (later time domain) fibers correspond to the linear polarization states {1} and {2}, respectively.

Photon-like signals or thermal noise signals are identified by negative peak finding. After finding a time bin with the largest amplitude in the negative direction, a global pedestal amplitude is determined by averaging over the 250 ns window excluding the peak region, as shown by the horizontal line in Fig. 5. We then find the falling edge and define the signal arrival time t_0 at the detector as the time bin at the half value of the peak amplitude after subtracting the pedestal value, which is indicated by the dotted vertical line. We require that a peak structure is identified by a pair of falling and rising edges around the peak position t_{p}. By defining time intervals from the falling edge to the peak and the peak to the rising edge as Δt_{f} and Δt_{r}, respectively, the time window of a signal, t_{sig}, is defined as $t_{\mathrm{p}} - 2.0\Delta t_{\mathrm{f}} \leq t_{\mathrm{sig}} \leq t_{\mathrm{p}} + 2.25\Delta t_{\mathrm{r}}$, indicated by solid vertical lines. The charge sum in that time window is evaluated in units of single-photon equivalent charge, -4.21×10^{-14} C.

The single-photon equivalent charge from the PMT used when operated at −800 V was evaluated with weak pulsed-photon sources ranging from 0 to several tens of photons as the average number of incident photons per pulse injection. Based on the Poisson probability distribution for a given set of pulsed photon sources, we can estimate the expected charge when a single photon is injected so that this charge is common to all the weak photon sources.

We then choose the waveforms satisfying the condition that at least one peak above 0.6 photon-equivalent charge $(-2.60 \times 10^{-14} / -4.21 \times 10^{-14})$ is contained for counting the number of photons in the four patterns. The offline cut is indicated by the dotted vertical line in Fig. 6 with respect to the single-photon equivalent charge denoted by the solid vertical line, where the charge sums within the time windows of photon-like signals are shown in all four trigger patterns.

Figure 7 shows charge sums within time windows of peak-like structures, equivalently the numbers of photon-like signals, as a function of the observed arrival time t_0 for the four trigger patterns. The number of photons is counted in units of single-photon equivalent charge within the time domains $T\{1\}$ and $T\{2\}$, respectively. Table 1 summarizes the numbers of photons in units of single-photon equivalent charge in the four trigger patterns in the time domains $T\{1\}$ and $T\{2\}$, and the numbers of analyzed events in trigger patterns $i = \mathrm{S, C, I, P}$.

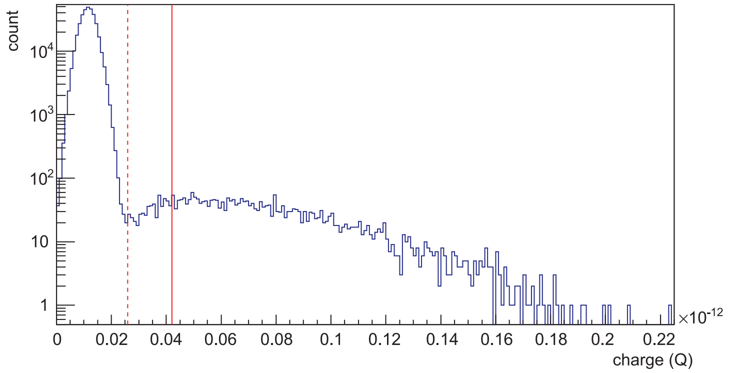

Fig. 6. Charge sums within time windows of photon-like signals in all four trigger patterns. The offline cut is indicated by the dotted vertical line with respect to the solid vertical line corresponding to single-photon equivalent charge.

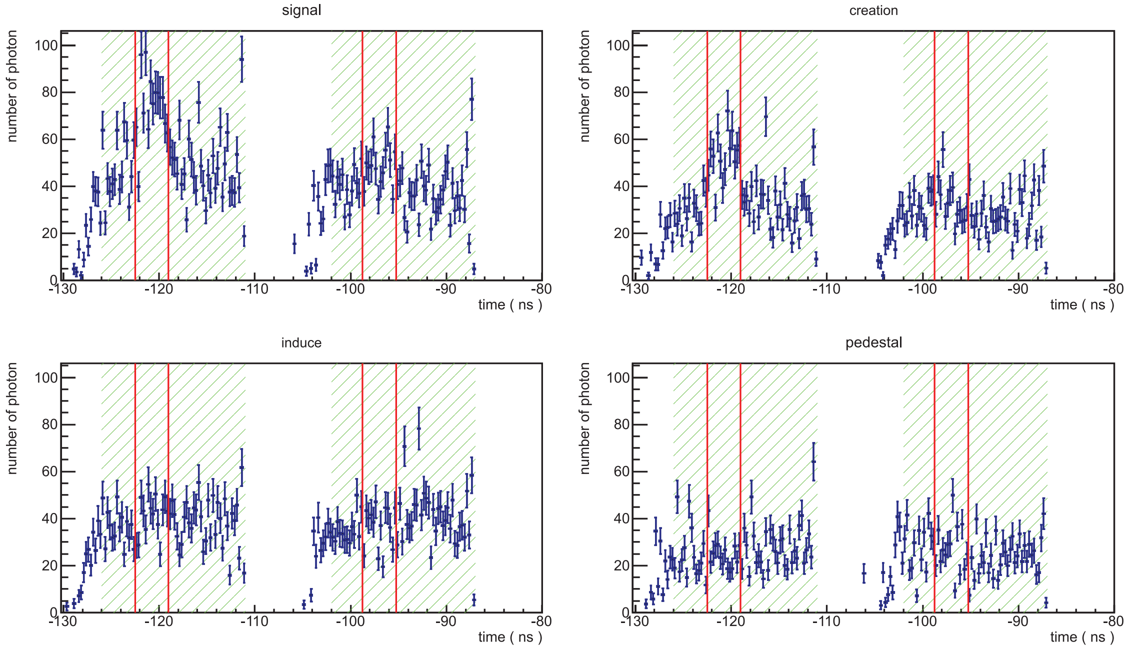

Fig. 7. Charge sums within time windows of peak-like structures in units of single-photon equivalent charge that correspond to the numbers of photon-like signals, as a function of the arrival time t_0 for the four trigger patterns, signal, pedestal, green residual, and red residual, within the time domains $T\{1\}$ and $T\{2\}$ with a 3.5 ns interval subtended by the red vertical lines, respectively. The green shaded bands indicate the online analysis windows of 15 ns time duration.

Table 1. Observed raw numbers of photon-like signals n_{ij} in two time domains specified with the polarization states $j = 1, 2$ for each trigger pattern $i = \mathrm{S}$ (signal), P (pedestal dominated by thermal noise), C (green laser), and I (red laser), where W_i indicates the number of analyzed events in trigger pattern i.

Trigger i	n_{i1}	n_{i2}	W_i
S	1036	675	5.97317383×10^8
P	391	422	6.65181553×10^8
C	822	513	6.65200665×10^8
I	574	510	5.97300398×10^8

5. Results

We take two steps to discuss the existence of signal photons from the four-wave mixing process. First, we investigate whether the acceptance-uncorrected N_{S1} and N_{S2} indicate deviations from zero beyond the inclusive errors in individual polarization paths. We then set upper limits on the coupling–mass relation, if there is no statistically significant number of four-wave mixing signals. Otherwise, we discuss the polarization dependence of the observed finite numbers of four-wave mixing signals.

The acceptance-uncorrected numbers of photon-like signals N_{S1} and N_{S2} with signal triggers (S) after subtraction between four patterns of triggers were obtained based on the relation in Eq. (15) as follows:

$$\begin{aligned} N_{S1} &= 75 \pm 51(\text{stat.}) \pm 96(\text{syst. I}) \pm 7(\text{syst. II}), \\ N_{S2} &= 83 \pm 44(\text{stat.}) \pm 96(\text{syst. I}) \pm 7(\text{syst. II}). \end{aligned} \tag{16}$$

The statistical errors were calculated by taking propagation of statistical errors associated with the subtraction using the photon numbers in Table 1 into account. The systematic errors I associated with the subtraction between four trigger patterns were evaluated by focusing on the behavior of the numbers of photon-like signals in the time windows outside the $T\{1\}$ or $T\{2\}$ domains, denoted by $\overline{T\{1\}}\,\&\,\overline{T\{2\}}$, where only unpolarized background photon-like signals are expected,[1] hence, the difference between $N_{S\bar{1}}$ and $N_{S\bar{2}}$ should not appear and the deviation from zero gives the systematic uncertainty on the subtraction method. We randomly combined 14 independent time bins of 0.25 ns interval among the $\overline{T\{1\}}\,\&\,\overline{T\{2\}}$ domain and counted the number of photon-like signals within the same time window as that of the $T\{1\}$, $T\{2\}$ domains, i.e., 3.5 ns = 0.25 ns × 14. The root mean square of such counts eventually gives the systematic uncertainty on the baseline counts in the $T\{1\}$ and $T\{2\}$ domains associated with the subtraction method. The systematic errors II originate from the ambiguity on the offline cut to define a peak to count the number of photon-like signals. These are estimated by changing the offline cut value from 0.5 to 2.0 photon-equivalent charge. The numbers in Eq. (16) indicate that there is no significant four-wave mixing signal within one standard deviation in both polarization states {1} and {2}.[2]

In order to evaluate the acceptance-corrected photon numbers $\mathcal{N}_{S1}$ and $\mathcal{N}_{S2}$, we need to correct the bias due to the difference of detection efficiencies in the two optical fibers in Fig. 3 for selecting states {1} and {2}, respectively. We thus parameterize the overall efficiencies, $\epsilon_{1,2}$ for the {1} and {2}

---

[1] The residual of the pulsed creation laser beam is only found either in $T\{1\}$ or $T\{2\}$ domains, even though the polarization states can be distinguished by the two optical fiber paths. On the other hand, the residual of the CW inducing laser beam can be found in any time domains, however, the polarization states cannot be distinguished by the two optical fiber paths eventually, because photons even with one polarization state can produce signals in the two time domains equally as long as these incident timings are randomly distributed. Therefore, if the $\overline{T\{1\}}\,\&\,\overline{T\{2\}}$ domain is chosen, no polarization dependence of the number of residual photon-like signals is expected after all, as long as the subtraction between the four trigger patterns is ideally performed. Needless to say, thermal noise should not have any polarization dependence.

[2] The expected acceptance-uncorrected numbers of photons with {2}-state from atomic four-wave mixing processes are evaluated as $\sim 10^{-22}$ and $\sim 10^{-9}$ photons from the residual gas and optical elements for the same shot statistics as the present search, respectively, based on supplementary measurements with higher-intensity laser fields where four-wave mixing yields were evaluated as a function of residual gas pressures. We estimated these numbers of photons by scaling the results in the supplementary measurement down to the laser peak power of the two-color laser fields with the same optical elements and focusing geometry as the present search by taking differences of detector acceptances and shot statistics between the present search and the supplementary measurements into account.

states, respectively, as

$$\epsilon_1 \equiv \epsilon_{\mathrm{opt1}}\epsilon_{\mathrm{D}}, \qquad \epsilon_2 \equiv \epsilon_{\mathrm{opt2}}\epsilon_{\mathrm{D}}, \tag{17}$$

where $\epsilon_{\mathrm{opt1,2}}$ express the optical collection efficiencies of the combination of the polarization beam splitter and optical fibers equipped with two lenses, and ϵ_{D} is the pure detection efficiency of the photomultiplier not including the optical paths (see the enlarged SPD part in Fig. 3). What we directly measure experimentally is a branching ratio between two paths containing exactly the same optical components and detector as those used for the pilot measurement, which corresponds to the ratio of these two efficiencies:

$$B \equiv \frac{\epsilon_1}{\epsilon_2}. \tag{18}$$

This quantity is determined by taking the ratio between the numbers of photons in $T\{1\}$ and $T\{2\}$ at $\Theta = 90°$ and $\Theta = 0°$, respectively, in Fig. 4. With B, the acceptance-uncorrected photon numbers are expressed as

$$\mathcal{N}_{\mathrm{S1}} = \frac{N_{\mathrm{S1}}}{\epsilon_1} = \frac{N_{\mathrm{S1}}}{B\epsilon_2} = \frac{N_{\mathrm{S1}}}{B\epsilon_{\mathrm{opt2}}\epsilon_{\mathrm{D}}}, \qquad \mathcal{N}_{\mathrm{S2}} = \frac{N_{\mathrm{S2}}}{\epsilon_2} = \frac{N_{\mathrm{S2}}}{\epsilon_{\mathrm{opt2}}\epsilon_{\mathrm{D}}}, \tag{19}$$

where the second of Eqs. (17) is substituted, and ϵ_{D} is known from the other measurement in advance.

As the second step, we evaluate the upper limit on the coupling–mass relation, where we regard the acceptance-uncorrected uncertainty δN_{S2} in the polarization state $\{2\}$ as the one standard deviation σ in the following Gaussian type of distribution with the mean value $\mu = N_{\mathrm{S2}}$:

$$1 - \alpha = \frac{1}{\sqrt{2\pi}\sigma}\int_{\mu-\delta}^{\mu+\delta} \mathrm{e}^{-(x-\mu)^2/(2\sigma^2)}\mathrm{d}x = \mathrm{erf}\left(\frac{\delta}{\sqrt{2}\sigma}\right), \tag{20}$$

where the estimator x corresponds to N_{S2} in our case, and the confidence level is given by $1-\alpha$—see Eq. (36.56) in [21]. As the upper limit estimate, we apply $2\alpha = 0.05$ with $\delta = 2.24\sigma$ to give a confidence level of 95% in this analysis.

We then require that the expectation value of N_{S2} coincides with 2.24σ to obtain the upper limit at the 95% confidence level. In order to relate the upper limit on N_{S2} with the upper limit on the coupling–mass relation directly, we further need to deduce $\mathcal{N}_{\mathrm{S2}}$ corresponding to the unbiased number of signal photons immediately after the focal point via the second of Eqs. (19):

$$\mathcal{N}_{\mathrm{S2}} = \frac{N_{\mathrm{S2}}}{\epsilon_{\mathrm{opt2}}\epsilon_{\mathrm{D}}} = \frac{2.24\delta N_{\mathrm{S2}}}{\epsilon_{\mathrm{opt2}}\epsilon_{\mathrm{D}}}. \tag{21}$$

Figure 8 shows the upper limit on the coupling–mass relation at the 95% confidence level which is calculated by requiring

$$W_s\mathcal{Y} = \mathcal{N}_{\mathrm{S2}} \tag{22}$$

in Eq. (10) with the experimental parameters summarized in Tables 1 and 2. The excluded domain by this pilot search based on four-wave mixing (FWM) in QPS is indicated by the slanted shaded area. For reference, we show existing upper limits from the other types of scalar field searches with vertically shaded areas: the ALPS experiment [22] (the sine function part of the sensitivity curve is simplified to unity for the figure) which is one of the "Light Shining through a Wall" (LSW) experiments, searching for non-Newtonian forces based on torsion balance techniques; Etö-wash [23,24]; Stanford1 [25]; Stanford2 [26]; and the Casimir force measurement (Lamoreaux) [27]. The domains

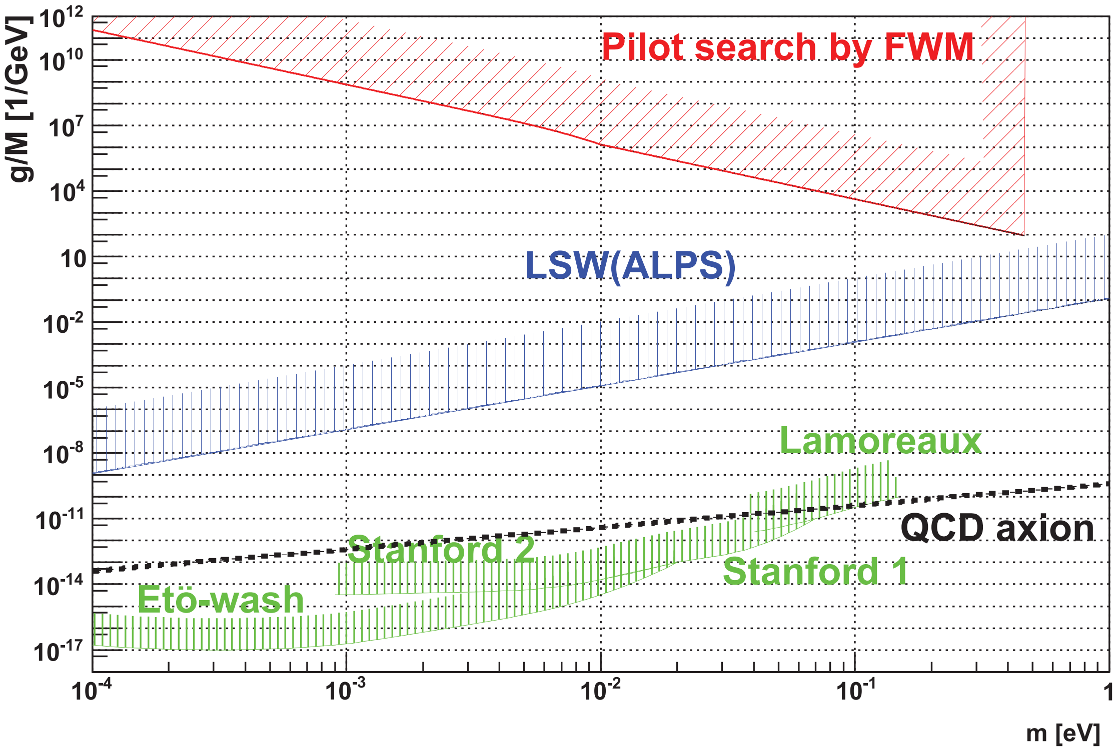

Fig. 8. Upper limits on the coupling(g/M)–mass(m) relation for the scalar field exchange. The excluded region by this pilot search based on four-wave mixing (FWM) in QPS is indicated by the slanted shaded area. The vertically shaded areas show the excluded regions by the other scalar field searches: the ALPS experiment [22] (the sine function part of the sensitivity curve is simplified to unity for drawing purposes) which is one of the "Light Shining through a Wall" (LSW) experiments, searching for non-Newtonian forces based on torsion balance techniques; Etö-wash [23,24]; Stanford1 [25]; Stanford2 [26]; and the Casimir force measurement (Lamoreaux) [27]. As a reference for future pseudoscalar searches, we also show the expected mass–coupling relation based on the QCD axion scenario for $E/N = 0$[3] (KSVZ model [29,30]), indicated by the inclining dotted line.

below the vertically shaded areas are all excluded. We note that if we require the proper polarization combinations between initial and final states for pseudoscalar fields [11], we are able to test the QCD axion models in the near future. As a reference, we show the expected mass–coupling relation based on the QCD axion scenario for $E/N = 0$[3] (KSVZ model [29,30]) which is indicated by the inclining dotted line.

6. Conclusion

We demonstrated the pilot search for scalar fields in the mass region $m \leq 0.46\,\text{eV}$ via four-wave mixing of two-color laser fields. There were no significant four-wave mixing signals. We obtained the upper limit on the coupling–mass relation at a confidence level of 95%, which approximately follows $m^{-5/2}$ scaling with the highest sensitivity $g/M = 92.6\,\text{GeV}^{-1}$ at $m = 0.46\,\text{eV}$. The concept of the experimental setup as well as the analysis procedure is extendable to higher-intensity laser systems in the near future.

---

[3] See the parametrization, for example, in the section "Axions and other similar particles" in [21]. See also [28] on the possible range of the ratio of the electromagnetic to color anomaly factors of the axial current associated with the axion, E/N.

Table 2. Experimental parameters used to obtain the upper limit on the coupling–mass relation.

parameters	values or comments
wavelength of creation laser λ_c	532 nm
relative line width of creation laser $(\delta\omega/\langle\omega\rangle)$	4.6×10^{-6}
wavelength of inducing laser λ_i	633 nm
relative line width of inducing laser $(\delta\omega_4/\langle\omega_4\rangle)$	3.2×10^{-6}
$u = \omega_4/\omega$ based on Eqs. (3) and (7)	0.84
focal length f	200 mm
beam diameter of laser beams d	40 mm
upper mass range given by $\vartheta < \Delta\vartheta$	0.46 eV
azimuthal asymmetric factor $\mathcal{F}_S$	$\mathcal{F}^{SC}_{1122}$ in Eq. (9)
duration time of creation laser pulse per injection τ_c	0.75 ns
duration time of inducing laser per injection τ_i (CW)	1 s
creation laser energy per τ_c	$(0.181 \pm 0.009)\ \mu$J
inducing laser energy per τ_i	(1.87 ± 0.19) mJ
combinatorial factor in luminosity C_{mb}	1/2
single-photon detection efficiency ϵ_D	$(2.94 \pm 0.03)\%$
efficiency of optical path 2 ϵ_{opt2}	$(4.3 \pm 0.1)\%$
branching ratio $B \equiv \epsilon_1/\epsilon_2$	0.824 ± 0.002
δN_{S2} in Eq. (22)	106

Acknowledgements

K. Homma cordially thanks Y. Fujii for long-term discussions on theoretical aspects relevant to the scalar field in the context of cosmology. He has greatly benefited from valuable discussions with S. Sakabe, M. Hashida, and Y. Nakamiya. He expresses his gratitude to T. Tajima and G. Mourou for many aspects relevant to this subject. This work was supported by Grant-in-Aid for Scientific Research nos. 24654069 and 25287060 from MEXT of Japan, and was also supported by the MATSUO FOUNDATION.

Funding

Open Access funding: Funded by SCOAP^3.

Appendix A. Re-evaluation of the signal yield

Given the formulae in Refs. [9–11] and the correction suggested by [31], we re-evaluate the signal yield with a more direct formulation than that based on the concept of *cross section*. The cross section is naturally applied to a beam flux normal to a target or the extension to head-on particle colliders where all beams are on the same axis. In QPS, however, this viewpoint is not necessarily convenient due to the wide distribution of tilted incident fluxes. In such a case, we can adopt the more convenient formulation [32,33], which is useful, for instance, to evaluate the number of interactions in plasma where the concept of *a beam flux to a target* is no longer clear. With the notations in Fig. 2 and the Lorentz invariant phase space factor dL_{ips},

$$\mathrm{d}L_{\mathrm{ips}} = (2\pi)^4\delta(p_3 + p_4 - p_1 - p_2)\frac{d^3p_3}{2\omega_3(2\pi)^3}\frac{d^3p_4}{2\omega_4(2\pi)^3}, \tag{A1}$$

the signal yield can be formulated as [32,33]

$$\begin{aligned}\mathcal{Y} &= \int \mathrm{d}t\mathrm{d}\vec{r}\rho_1(\vec{r},t)\rho_2(\vec{r},t)\int \mathrm{d}\vartheta\frac{1}{2\omega 2\omega}\rho(\vartheta)|\mathcal{M}(\vartheta)|^2\mathrm{d}L_{\mathrm{ips}}\\ &\equiv \mathcal{D}\left[s/L^3\right]\overline{\Sigma}\left[L^3/s\right],\end{aligned} \tag{A2}$$

where $\mathcal{M}(\vartheta)$ is the Lorentz invariant transition amplitude as a function of incident angle ϑ with the normalized statistical weight $\rho(\vartheta)$ due to the uncertainty of the incident angle, $\mathcal{D}$ is time-integrated density, and Σ is the interaction volume per unit time. We note the dimensions explicitly with time s and length L in [] of Eq. (A2). On the other hand, it may be possible to factorize the yield based on the concept of *time-integrated luminosity* × *cross section* as follows:

$$\mathcal{Y} = \int d\vartheta \rho(\vartheta) \left(\int dt d\vec{r} \rho_1(\vec{r}, t) \rho_2(\vec{r}, t) K(\vartheta) \right) \left(\frac{1}{K(\vartheta) 2\omega 2\omega} |\mathcal{M}(\vartheta)|^2 dL_{\text{ips}} \right)$$

$$\equiv \int d\vartheta \rho(\vartheta) \mathcal{L}(\vartheta) \left[s/(L^2 \cdot s) \right] \sigma(\vartheta) \left[L^2 \right], \tag{A3}$$

where K corresponds to the relative velocity of incoming particle beams for a given ϑ based on Møller's Lorentz invariant factor [34]. The relative velocity K is defined as [35]

$$K(\vartheta) \equiv \sqrt{(\vec{v_1} - \vec{v_2})^2 - \frac{(\vec{v_1} \times \vec{v_2})^2}{c^2}} = 2c \sin^2 \vartheta, \tag{A4}$$

with the notation in Fig. 2. If $\rho(\vartheta)$ is a mere number, which is the normal case for collisions with two independent beams with a fixed relative velocity, this factorization is robust. In the case of the photon QPS, however, the concept of relative velocity between a pair of incident photons could be ambiguous due to spreads of single photon wavefunctions near the waist,[4] while the squared scattering amplitude itself has to be averaged over a possible range on ϑ due to that unavoidable uncertainty. In order to have recourse to the concept of a cross section, however, we need to choose a proper relative velocity value to convert a squared scattering amplitude into a cross section. We then face difficulty in uniquely determining a K-factor with respect to the averaged squared scattering amplitude over a range of ϑ in QPS. In the formulation in Eq. (A2) without recourse to the concept of a cross section, on the other hand, ambiguity originating from choices of a proper K-factor is all avoidable. Therefore, we reformulate the signal yield based on Eq. (A2) as follows.

We first express the squared scattering amplitude for the case when a low-mass field is exchanged in the s-channel via a resonance state with the symbol to describe polarization combinations of initial and final states S:

$$|\mathcal{M}_S|^2 \approx (4\pi)^2 \frac{a^2}{\chi^2 + a^2}, \tag{A5}$$

where $\chi = \omega^2 - \omega_r^2$ with the resonance condition $m = 2\omega_r \sin\vartheta_r$ for a given mass m, and a is expressed as

$$a = \frac{\omega_r^2}{8\pi} \left(\frac{gm}{M} \right)^2 = \frac{m\Gamma}{2 \sin^2 \vartheta_r}, \tag{A6}$$

with the resonance decay rate of the low-mass field[5]

$$\Gamma = (16\pi)^{-1} \left(gM^{-1} \right)^2 m^3. \tag{A7}$$

---

[4] Our attitude might be strongly biased by the Copenhagen interpretation. If pre-existing momenta in advance of measurement could be realized in nature, it might allow us to explicitly define relative velocity. The approach expressed in Eq. (A2), however, can circumvent this vague point originating from the different interpretations of *realism* in quantum mechanics.

[5] We note that if $M \sim M_{\text{Planck}} \sim 10^{18}$ GeV and $g \sim \alpha_{\text{qed}} \sim 10^{-2}$, the decay rate for $m \sim 10^{-9}$ GeV becomes $\sim 10^{-41}$ Hz, and hence the lifetime is quite long. Therefore, we need to stimulate the decay at the same time as the production by supplying an inducing laser field in advance of the interaction, that is, we treat the interaction as an instantaneous scattering process where the production and the decay cannot be distinguished in spacetime.

The resonance condition is satisfied when the center-of-mass system (CMS) energy between two incident photons $E_{\mathrm{CMS}} = 2\omega \sin\vartheta$ coincides with the given mass m. At a focused geometry of an incident laser beam, however, E_{CMS} cannot be uniquely specified due to the momentum uncertainty of incident waves. Although the incident laser energy has an intrinsic uncertainty, the momentum uncertainty or the angular uncertainty between a pair of incident photons dominates that of the incident energy. Therefore, we consider the case where only angles of incidence ϑ between randomly chosen pairs of photons are uncertain within $0 < \vartheta \le \Delta\vartheta$ for a given focusing parameter by fixing the incident energy. The treatment for the intrinsic energy uncertainty is explained in Appendix B. We fix the laser energy ω at the optical wavelength,

$$\omega_{\mathrm{opt}}^2 = \frac{m^2}{4\vartheta_r^2} \sim 1\,\mathrm{eV}^2, \tag{A8}$$

while the resonance condition depends on the incident angle uncertainty. This gives an expression for χ as a function of ϑ:

$$\chi(\vartheta) = w_{\mathrm{opt}}^2 - w_r^2(\vartheta) = \frac{m^2}{4\vartheta_r^2} - \frac{m^2}{4\vartheta^2} = \left[1 - (\vartheta_r/\vartheta)^2\right]\omega_{\mathrm{opt}}^2, \tag{A9}$$

where

$$\mathrm{d}\vartheta = \frac{\vartheta_r}{2\omega_{\mathrm{opt}}^2}\left(1 - \frac{\chi}{\omega_{opt}^2}\right)^{-3/2}\mathrm{d}\chi. \tag{A10}$$

We thus introduce the averaging process for the squared amplitude $\overline{|\mathcal{M}_S|^2}$ over the possible uncertainty on incident angles,

$$\overline{|\mathcal{M}_S|^2} = \int_0^{\pi/2} \rho(\vartheta)|\mathcal{M}_S(\vartheta)|^2 \mathrm{d}\vartheta, \tag{A11}$$

where $\mathcal{M}_S$ specified with a set of physical parameters m and gM^{-1} is expressed as a function of ϑ, and $\rho(\vartheta)$ is the probability distribution function as a function of the uncertainty on ϑ within an incident pulse.

We review the expression for the electric field of the Gaussian laser propagating along the z-direction in spatial coordinates (x, y, z) [13] as follows:

$$\vec{E}(x, y, z) = \vec{E}_0 \frac{w_0}{w(z)} \exp\left\{-\mathrm{i}[kz - H(z)] - r^2\left(\frac{1}{w(z)^2} + \frac{\mathrm{i}k}{2R(z)}\right)\right\}, \tag{A12}$$

where E_0 is the electric field amplitude, $k = 2\pi/\lambda$, $r = \sqrt{x^2 + y^2}$, w_0 is the minimum waist, which cannot be smaller than λ due to the diffraction limit, and other definitions are as follows:

$$w(z)^2 = {w_0}^2\left(1 + \frac{z^2}{{z_R}^2}\right), \tag{A13}$$

$$R = z\left(1 + \frac{{z_R}^2}{z^2}\right), \tag{A14}$$

$$H(z) = \tan^{-1}\left(\frac{z}{z_R}\right), \tag{A15}$$

$$z_R \equiv \frac{\pi {w_0}^2}{\lambda}. \tag{A16}$$

With θ being the incident angle of a single photon in the Gaussian beam, the angular distribution $g(\theta)$ can be approximated as

$$g(\theta) \sim \frac{1}{\sqrt{2\pi}\Delta\theta} \exp\left\{-\frac{\theta^2}{2\Delta\theta^2}\right\}, \tag{A17}$$

where the incident angle uncertainty in the Gaussian beam $\Delta\theta$ is introduced within the physical range $|\theta| < \pi/2$ as

$$\Delta\theta \sim \frac{\lambda_c}{\pi w_0} = \frac{d}{2f}, \tag{A18}$$

with the wavelength of the creation laser λ_c, the beam diameter d, the focal length f, and the beam waist $w_0 = \frac{f\lambda_c}{\pi d/2}$, as illustrated in Fig. 1. For a pair of photons 1, 2, each of which follows $g(\theta)$, the incident angle between them is defined as

$$\vartheta = \frac{1}{2}|\theta_1 - \theta_2|. \tag{A19}$$

With the variance $\Delta\vartheta^2 = 2(\frac{1}{4}\Delta\theta^2)$, the pair angular distribution $\rho(\vartheta)$ is then approximated as

$$\rho(\vartheta) \sim \frac{2}{\sqrt{\pi}\Delta\theta} \exp\left\{-\left(\frac{\vartheta}{\Delta\theta}\right)^2\right\} \sim \frac{2}{\sqrt{\pi}\Delta\theta} \quad \text{for} \quad 0 < \vartheta < \pi/2, \tag{A20}$$

where the coefficient 2 of the amplitude is caused by limiting ϑ to the range $0 < \vartheta < \pi/2$, and $\left(\frac{\vartheta}{\Delta\theta}\right)^2 \ll 1$ is taken into account because $\Delta\theta$ in Eq. (18) also corresponds to the upper limit by the focusing lens based on geometric optics. This distribution is consistent with the flat-top distribution applied in Refs. [10,11], apart from the coefficient.

We now re-express the average of the squared scattering amplitude as a function of $\chi \equiv a\xi$ in units of the width of the Breit–Wigner(BW) distribution a by substituting Eqs. (A5) and (A20) into Eq. (A11) with Eq. (A10):

$$\overline{|\mathcal{M}_S|^2} = \frac{(4\pi)^2}{\sqrt{\pi}\omega_{\text{opt}}^2} \left(\frac{\vartheta_r}{\Delta\theta}\right) a\mathcal{W}, \tag{A21}$$

where we introduce the constant

$$\mathcal{W} \equiv \int_{-\infty}^{\frac{\omega_{\text{opt}}^2}{a}\{1-(\vartheta_r/(\pi/2))^2\}} W(\xi) \frac{1}{\xi^2+1} d\xi, \tag{A22}$$

with

$$W(\xi) \equiv \left(1 - \frac{a\xi}{\omega_{\text{opt}}^2}\right)^{-3/2}. \tag{A23}$$

In Eq. (A22), the weight function $W(\xi)$ is a positive and monotonic function within the integral range and the second term is the Breit–Wigner(BW) function with a width of unity. Note that $\overline{|\mathcal{M}_S|^2}$ is now explicitly proportional to a but not a^2. This gives the enhancement factor a compared to the case $\overline{|\mathcal{M}_S|^2} \propto a^2$ where no resonance state is contained in the integral range controlled by $\Delta\theta$ experimentally. The integrated value of the pure BW function from $\xi = -1$ to $\xi = +1$ gives $\pi/2$, while that from $\xi = -\infty$ to $\xi = +\infty$ gives π. The difference is only a factor of two. The weight function $W(\xi)$ of the kernel is almost unity for small $a\xi$, that is, when a is small enough with a small mass and a weak coupling. For instance, the coupling–mass range covered by Fig. 8, $g/M \sim 10^{11}$ GeV^{-1} and $m \sim 10^{-13}$ GeV, gives $a \sim 10^{-5}$, while $g/M \sim 10^2$ GeV^{-1} and $m \sim 10^{-10}$ GeV gives $a \sim 10^{-17}$. In such cases the integrated value of Eq. (A22) is close to that of BW, because the weight function is close to unity and also the upper limit of the integral range in Eq. (A22) is large for $\vartheta_r/\Delta\vartheta < 1$ by the a^{-1} dependence. In Ref. [11], we thus approximate $\mathcal{W}$ as $\pi/2$ as a conservative estimate.

Let us remember the partially integrated cross section over the solid angle of the signal photon ω_3 which corresponds to Eq. (11) in Ref. [11]. The expression before taking the average over ϑ, hence as a function of ϑ, is:

$$\sigma(\vartheta) = \frac{\mathcal{F}_S |\mathcal{M}_S(\vartheta)|^2}{(8\pi\omega)^2 \sin^4\vartheta} \int_{\underline{\theta_3}}^{\overline{\theta_3}} \left(\frac{\omega_3}{2\omega}\right)^2 \sin\theta_3 d\theta_3. \tag{A24}$$

We then convert the interaction cross section $\sigma(\vartheta)$ into the interaction volume per unit time $\Sigma(\vartheta)$ by simply multiplying the relative velocity $K(\vartheta) = 2c\sin^2\vartheta$:

$$\Sigma(\vartheta) = \frac{2c\mathcal{F}_S |\mathcal{M}_S(\vartheta)|^2}{(8\pi\omega)^2 \sin^2\vartheta} \int_{\underline{\theta_3}}^{\overline{\theta_3}} \left(\frac{\omega_3}{2\omega}\right)^2 \sin\theta_3 d\theta_3 \sim \frac{2c^3\mathcal{F}_S |\mathcal{M}_S(\vartheta)|^2}{(8\pi)^2} \left(\frac{\lambda_c}{2\pi c}\right)^2 \frac{\delta u}{4} \quad \left[L^3/s\right], \tag{A25}$$

where λ_c is the creation laser wavelength, $\delta u \equiv \overline{u} - \underline{u}$ with approximations $u^2 \ll 1$ and $\vartheta \ll 1$, and c and $\hbar$ are restored to confirm the dimension explicitly. The averaged value over ϑ is then expressed as

$$\begin{aligned}
\overline{\Sigma} &= \int_0^{\pi/2} d\vartheta \rho(\vartheta) \Sigma(\vartheta) = \frac{c\mathcal{F}_S \lambda_c^2 \delta u}{2(16\pi^2)^2} \int_0^{\pi/2} d\vartheta \rho(\vartheta) |\mathcal{M}_S(\vartheta)|^2 \\
&\sim \frac{c\mathcal{F}_S \lambda_c^2 \delta u}{2(16\pi^2)^2} \frac{(4\pi)^2}{\sqrt{\pi}\omega_{\mathrm{opt}}^2} \left(\frac{\vartheta_r}{\Delta\theta}\right) a\mathcal{W} = \frac{c\mathcal{W}\mathcal{F}_S \lambda_c^2 \delta u}{2\sqrt{\pi}(4\pi)^2 \omega_{\mathrm{opt}}^2} \left(\frac{\vartheta_r}{\Delta\theta}\right) a \\
&= \frac{c\mathcal{W}\mathcal{F}_S \lambda_c^2 \delta u}{2\sqrt{\pi}(4\pi)^2 \omega_{\mathrm{opt}}^2} \left(\frac{\vartheta_r}{\Delta\theta}\right) \frac{\omega_r^2}{8\pi} \left(\frac{gm}{M}\right)^2 \\
&= \frac{c\mathcal{W}\mathcal{F}_S \lambda_c^2 \delta u}{4\sqrt{\pi}(4\pi)^3} \left(\frac{\vartheta_r}{\Delta\theta}\right) \left(\frac{gm}{M}\right)^2,
\end{aligned} \tag{A26}$$

where Eq. (A21) and a in Eq. (A6) are substituted in the second and third lines, respectively, and $\omega_r \equiv \omega_{\mathrm{opt}}$ via Eq. (A8) is identified for the last line.

We now consider the time-integrated density factor $\mathcal{D}$ in Eq. (A2) applicable to free propagation of the Gaussian laser beam for creation, as illustrated in Fig. 1. We first parameterize the density profile of an incident Gaussian laser beam being the focal point at $z = 0$ with the pulse duration time τ_c propagating over the focal length f along the z-axis as [36]

$$\rho_c(x, y, z, t) = \frac{2N_c}{\pi w^2(z)} \exp\left\{-2\frac{x^2 + y^2}{w^2(z)}\right\} \frac{1}{\sqrt{\pi} c\tau_c} \exp\left\{-\left(\frac{z'}{c\tau_c}\right)^2\right\}, \tag{A27}$$

where the central position of the creation pulse in the z coordinate is traced by the relation $z = ct$ as a function of time t while the pulse duration along the z-direction is expressed with the local coordinate z'; hence, $z' = z - ct$, and N_c is the average number of creation photons per pulse. Using the squared expression

$$\rho_c^2(x, y, z, t) = \frac{4{N_c}^2}{\pi^3 (c\tau_c)^2} \frac{1}{w^4(z)} \exp\left\{-4\frac{x^2 + y^2}{w^2(z)}\right\} \exp\left\{-2\left(\frac{z'}{c\tau_c}\right)^2\right\}, \tag{A28}$$

based on Eq. (A2), $\mathcal{D}_\mathrm{c}$ is then expressed as

$$\begin{aligned}\mathcal{D}_\mathrm{c} &= \int_{-f/c}^{0} \mathrm{d}t \int_{-\infty}^{\infty} \mathrm{d}x \int_{-\infty}^{\infty} \mathrm{d}y \int_{-\infty}^{\infty} \mathrm{d}z \rho_\mathrm{c}{}^2(x,y,z,t) \\ &= \frac{4N_\mathrm{c}^2}{\pi^3 (c\tau_\mathrm{c})^2} \int_{-f/c}^{0} \mathrm{d}t \frac{1}{w^4(ct)} \sqrt{\frac{\pi w^2(ct)}{4}} \sqrt{\frac{\pi w^2(ct)}{4}} \int_{-\infty}^{\infty} \mathrm{d}z' \exp\left\{-2\left(\frac{z'}{c\tau_\mathrm{c}}\right)^2\right\} \\ &= \frac{N_\mathrm{c}^2}{\sqrt{2\pi}} \frac{1}{\pi w_0{}^2} \frac{1}{c\tau_\mathrm{c}} \int_{-f/c}^{0} \mathrm{d}t \frac{1}{1+(ct/z_R)^2} \\ &= \frac{N_\mathrm{c}^2}{\sqrt{2\pi}} \frac{1}{\pi w_0{}^2} \frac{1}{c\tau_\mathrm{c}} \frac{z_R}{c} \tan^{-1}\left(\frac{f}{z_R}\right) \quad \left[s/L^3\right], \end{aligned} \tag{A29}$$

where the time integration is performed during the pulse propagation from $z = -f$ to $z = 0$, because photon–photon scattering never takes place when two photons in a pair are apart from each other at $z > 0$.

We now evaluate the effect of the inducing laser beam. The inducing effect is expected only when p_4 as a result of scattering coincides with a photon momentum included in the coherent state of the inducing beam. In order to characterize p_4 from the interaction, we first summarize the kinematic relations specified in Fig. 2. Although the CMS-energy varies depending on the incident angle ϑ, the interaction rate is dominated at the CMS-energy satisfying the resonance condition $E_\mathrm{CMS} = m = 2\omega \sin\vartheta_r$ via the Breit–Wigner weighting. Therefore, p_4 is essentially expressed with the condition $\vartheta = \vartheta_r$ in Eq. (7). With $\vartheta_r \ll 1$, we obtain the following relations:

$$\theta_4 \sim \mathcal{R}^{-1/2}\vartheta_r \quad \text{and} \quad \theta_3 \sim \mathcal{R}^{1/2}\vartheta_r. \tag{A30}$$

These relations imply that the spontaneous interaction causes ring-like patterns of emitted photons with cone angles θ_3 and θ_4 commonly constrained by ϑ_r, because the way to take a reaction plane determined by $p_{1,2,3,4}$ is symmetric around the z-axis.

We then evaluate what fraction of photon momenta in the inducing beam overlaps with p_4; in other words, the acceptance factor applied to the ideal Gaussian laser beam, which was discussed within the plane wave approximation in [11]. In the beam waist at $z = 0$, the angular spectrum representation gives the following electric field distribution as a function of wave vector components k_x and k_y on the transverse plane $z = 0$ based on the Fourier transform of $\vec{E}(x, y, z = 0)$ [37]:[6]

$$\vec{E}(k_x, k_y; z = 0) = \vec{E}_0 \frac{w_0^2}{4\pi} \mathrm{e}^{-\frac{w_0^2}{4}(k_x^2+k_y^2)} \equiv \vec{E}_0 \frac{w_0^2}{4\pi} \mathrm{e}^{-\frac{w_0^2}{4}k_\mathrm{T}^2}, \tag{A31}$$

where the transverse wave vector component $k_\mathrm{T}^2 = k_x^2 + k_y^2$ is introduced. With the paraxial approximation $k_z \sim k - k_\mathrm{T}^2/2k$, we can derive exactly the same expression for $E(x, y, z)$ in Eq. (A12) starting from this representation [37].[6] We apply Eq. (A31) to the inducing beam represented by the subscript 4 with $k_{\mathrm{T}4} \equiv k_4 \sin\theta_4 \sim k_4 \mathcal{R}^{-1/2}\vartheta_r$, using the first relation in Eq. (A30) and $w_{04} \equiv \frac{f\lambda_\mathrm{i}}{\pi d/2}$. For a range from $\underline{k_{\mathrm{T}4}}$ to $\overline{k_{\mathrm{T}4}}$ by denoting with the underline and overline the lower and upper values

---

[6] A similar description can also be found in http://www.photonics.ethz.ch/fileadmin/user_upload/optics/Courses/EM_FieldsAndWaves/AngularSpectrumRepresentation.pdf.

on the corresponding variables, respectively,the acceptance factor $\mathcal{A}_{\rm i}$ is estimated as

$$\begin{aligned}\mathcal{A}_{\rm i} &\equiv \frac{\int_{\underline{k_{\rm T4}}}^{\overline{k_{\rm T4}}} 2\pi k_{\rm T4} E_4^2 {\rm d}k_{\rm T4}}{\int_0^\infty 2\pi k_{\rm T4} E_4^2 {\rm d}k_{\rm T4}} = {\rm e}^{-\frac{w_{04}^2}{2}\underline{k_{\rm T4}}^2} - {\rm e}^{-\frac{w_{04}^2}{2}\overline{k_{\rm T4}}^2} \sim \frac{w_{04}^2}{2}(\overline{k_{\rm T4}}^2 - \underline{k_{\rm T4}}^2)\\ &\sim \frac{w_{04}^2 k_4^2}{2}\vartheta_r^2(\underline{\mathcal{R}}^{-1} - \overline{\mathcal{R}}^{-1})\\ &\sim 2(\underline{\mathcal{R}}^{-1} - \overline{\mathcal{R}}^{-1})\left(\frac{\vartheta_r}{\Delta\theta}\right)^2 = 4\delta\mathcal{U}\left(\frac{\vartheta_r}{\Delta\theta}\right)^2,\end{aligned} \tag{A32}$$

where the approximation in the first line is based on $w_{04}k_{\rm T4} \ll 1$, $k_{\rm T4} \sim k_4\mathcal{R}^{-1/2}\vartheta_r$ is substituted in the second line, and $w_{04}k_4 = \frac{2\pi w_{04}}{\lambda_{\rm i}} \equiv 2/\Delta\theta_4$ with $\Delta\theta_4 \sim \Delta\theta$ due to the common focusing geometry d and f to those of the creation beam is substituted in the third line by defining $\delta\mathcal{U} \equiv \frac{\overline{u}-\underline{u}}{\overline{u}\underline{u}}$. We note that Eq. (A32) now has quadratic dependence on ϑ_r while the corresponding acceptance factor in [11] was proportional to ϑ_r due to the plane wave approximation.

Because of the common optical element sharing the same optical axis, in advance, the spatial overlap between creation and inducing lasers is satisfied in QPS. In actual experiments, however, it is likely that the time durations between the two laser pulses are prepared as $\tau_{\rm i} \ge \tau_{\rm c}$ for inducing i and creation c beams, respectively, because shortness of $\tau_{\rm c}$ is more important to enhance $\mathcal{D}_{\rm c}$ via the quadratic nature of the pulse energy. Therefore, we further introduce a factor representing the spacetime overlap by assuming the pulse peaks in spacetime coincide with each other. Hence, the entire inducing effect is expressed as

$$\mathcal{I} = \mathcal{A}_{\rm i}\left(\frac{\tau_{\rm c}}{\tau_{\rm i}}\right)N_{\rm i} = 4\delta\mathcal{U}\left(\frac{\vartheta_r}{\Delta\theta}\right)^2\left(\frac{\tau_{\rm c}}{\tau_{\rm i}}\right)N_{\rm i}. \tag{A33}$$

Therefore, the overall density factor $\mathcal{D}_{\rm c+i}$ including the inducing laser effect is expressed as

$$\begin{aligned}\mathcal{D}_{\rm c+i} &\sim C_{\rm mb}\mathcal{D}_{\rm c}\mathcal{I}\\ &= C_{\rm mb}\frac{N_{\rm c}^2}{\sqrt{2\pi}}\frac{1}{\pi w_0{}^2}\frac{1}{c\tau_{\rm c}}\frac{z_R}{c}\tan^{-1}\left(\frac{f}{z_R}\right)4\delta\mathcal{U}\left(\frac{\vartheta_r}{\Delta\theta}\right)^2\left(\frac{\tau_{\rm c}}{\tau_{\rm i}}\right)N_{\rm i}\\ &= \frac{4}{\sqrt{2\pi}}\frac{z_R}{\pi w_0{}^2c^2\tau_{\rm c}}\left(\frac{\tau_{\rm c}}{\tau_{\rm i}}\right)\tan^{-1}\left(\frac{f}{z_R}\right)\left(\frac{\vartheta_r}{\Delta\theta}\right)^2\delta\mathcal{U}C_{\rm mb}N_{\rm c}^2N_{\rm i}\\ &= \frac{4}{\sqrt{2\pi}}\frac{1}{c^2\lambda_{\rm c}\tau_{\rm c}}\left(\frac{\tau_{\rm c}}{\tau_{\rm i}}\right)\tan^{-1}\left(\frac{\pi d^2}{4f\lambda_{\rm c}}\right)\left(\frac{\vartheta_r}{\Delta\theta}\right)^2\delta\mathcal{U}C_{\rm mb}N_{\rm c}^2N_{\rm i},\end{aligned} \tag{A34}$$

where $C_{\rm mb} = 1/2$ corresponds to the combinatorial factor originating from the choice of a frequency among the frequency multimode states in the creation and inducing lasers, as discussed in Ref. [11].

Based on Eq. (A2) with Eqs. (A26) and (A34), the re-evaluated signal yield $\mathcal{Y}$ is finally expressed as

$$\begin{aligned}\mathcal{Y} &= \mathcal{D}_{\rm c+i}\overline{\Sigma}\\ &= \frac{4}{\sqrt{2\pi}}\frac{1}{c^2\lambda_{\rm c}\tau_{\rm c}}\left(\frac{\tau_{\rm c}}{\tau_{\rm i}}\right)\tan^{-1}\left(\frac{\pi d^2}{4f\lambda_{\rm c}}\right)\left(\frac{\vartheta_r}{\Delta\theta}\right)^2\delta\mathcal{U}C_{\rm mb}N_{\rm c}^2N_{\rm i}\frac{c\mathcal{W}\mathcal{F}_S\lambda_{\rm c}^2\delta u}{4\sqrt{\pi}(4\pi)^3}\left(\frac{\vartheta_r}{\Delta\theta}\right)\left(\frac{gm}{M}\right)^2\\ &= \frac{1}{\sqrt{2\pi}(4\pi)^3}\left(\frac{\lambda_{\rm c}}{c\tau_{\rm c}}\right)\left(\frac{\tau_{\rm c}}{\tau_{\rm i}}\right)\tan^{-1}\left(\frac{\pi d^2}{4f\lambda_{\rm c}}\right)\left(\frac{\vartheta_r}{\Delta\theta}\right)^3\delta u\delta\mathcal{U}\left(\frac{gm}{M}\right)^2\mathcal{W}\mathcal{F}_SC_{\rm mb}N_{\rm c}^2N_{\rm i}\end{aligned}$$

$$
\begin{aligned}
&= \frac{1}{\sqrt{2}\pi(4\pi)^3}\left(\frac{\lambda_{\mathrm{c}}}{c\tau_{\mathrm{c}}}\right)\left(\frac{\tau_{\mathrm{c}}}{\tau_{\mathrm{i}}}\right)\Delta\theta^{-3}\tan^{-1}\left(\frac{\pi d^2}{4\,f\lambda_{\mathrm{c}}}\right)\delta u\delta\mathcal{U}\left(\frac{gm}{M}\right)^2\left(\frac{m}{2\omega\,[\mathrm{eV}]}\right)^3\mathcal{W}\mathcal{F}_S C_{\mathrm{mb}}N_{\mathrm{c}}^2 N_{\mathrm{i}} \\
&\sim \frac{1}{64\sqrt{2}\pi^4}\left(\frac{\lambda_{\mathrm{c}}}{c\tau_{\mathrm{c}}}\right)\left(\frac{\tau_{\mathrm{c}}}{\tau_{\mathrm{i}}}\right)\left(\frac{f}{d}\right)^3\tan^{-1}\left(\frac{\pi d^2}{4\,f\lambda_{\mathrm{c}}}\right)\frac{(\overline{u}-\underline{u})^2}{\overline{u}\underline{u}}\left(\frac{gm\,[\mathrm{eV}]}{M\,[\mathrm{eV}]}\right)^2 \\
&\quad\times\left(\frac{m\,[\mathrm{eV}]}{\omega\,[\mathrm{eV}]}\right)^3\mathcal{W}\mathcal{F}_S C_{\mathrm{mb}}N_{\mathrm{c}}^2 N_{\mathrm{i}}, \qquad\qquad (\mathrm{A35})
\end{aligned}
$$

where the parameters specified with [eV] apply natural units. We note that the re-evaluated signal yield depends on m^5, compared to the m^2 dependence in Ref. [11]. The additional m^2 dependence is caused by the multiplication of K-factor in Eq. (A25), and an m dependence is further added by Eq. (A32) due to the ring-image acceptance for the inducing effect. The sensitivity to lower mass domains thus diminishes.

Appendix B. The effect of the finite spectrum widths of the creation and inducing laser beams

When the creation and inducing lasers have finite spectrum widths, the effect has impacts on the interaction rate of four-wave mixing as well as the spectrum width of the signal via energy–momentum conservation within the unavoidable uncertainty of photon momenta and energies in QPS. We have considered the effect of the finite line width of the inducing laser field by assuming the line width of the creation laser is negligibly small [11]. In such a case, the energy uncertainties in the process of four-wave mixing with the conventions used in Fig. 2 are described as

$$\omega = \langle\omega\rangle, \quad \omega_4 = \langle\omega_4\rangle \pm \delta\omega_4, \quad \text{and} \quad \omega_3 = \langle\omega_3\rangle \pm \delta\omega_3 \qquad (\mathrm{B1})$$

for the creation laser, the inducing laser, and the signal, respectively, where $\langle\cdot\cdot\rangle$ denotes the average of each spectrum, $\delta\omega_4$ expresses the intrinsic line width caused by the energy uncertainty in the atomic process producing the inducing laser beam, and $\delta\omega_3 = \delta\omega_4$ arises due to energy conservation [11].

In this case, $\overline{u}$ and $\underline{u}$ in Eq. (A35) via Eq. (3) solely originate from the intrinsic line width of the inducing laser field. However, this approximation is not valid for the case where the line width of the creation laser is equal to or wider than that of the inducing laser. We now provide the prescription for the following general case:

$$\omega = \langle\omega\rangle + \delta\omega, \quad \omega_4 = \langle\omega_4\rangle \pm \delta\omega_4, \quad \text{and} \quad \omega_3 = \langle\omega_3\rangle \pm \delta\omega_3, \qquad (\mathrm{B2})$$

where the intrinsic line width of the creation laser $\delta\omega$ is explicitly included. In this case, at a glance, Eq. (6) must be modified so that a finite net transverse momentum along the x-axis in Fig. 2 is introduced by the different incident photon energies ω_1 and ω_2 with corresponding incident angles ϑ_1 and ϑ_2, respectively. These notations are for a *nominal* laboratory frame defined by a pair of asymmetric incident photons, referred to as the L-system. Here, *nominal* implies that we cannot specify an individual photon's incident wavelength as well as its incident angle physically, that is, what we know priori is only the ranges of uncertainties on possible wavelengths and incident angles. Exactly speaking, all the calculations so far are based on the equal incident energy $\langle\omega\rangle$ with the equal incident angle ϑ in the averaged laboratory frame, referred to as the $\langle L\rangle$-system as illustrated in Fig. 2, where the transverse momentum of the incident colliding system is zero on the average. We regard the effect of these *nominally* possible L-systems as fluctuations around the averaged $\langle L\rangle$-system. We therefore attempt to transform L-systems into an $\langle L\rangle$-system so that $\delta\omega$ is effectively invisible as follows:

$$\omega = \langle\omega\rangle, \quad \omega_4 = \langle\omega_4\rangle \pm \Delta\omega_4, \quad \text{and} \quad \omega_3 = \langle\omega_3\rangle \pm \Delta\omega_3, \tag{B3}$$

where $\delta\omega$ in Eq. (B2) is absorbed into the effective line widths of the final state photon energies in the $\langle L\rangle$-system resulting in $\Delta\omega_4 > \delta\omega_4$ denoting Δ as the effective width in the $\langle L\rangle$-system, and accordingly $\Delta\omega_3 > \delta\omega_3$ arises via energy–momentum conservation in that system.

As long as a resonance state with a finite mass is formed, a range $0 < \vartheta \le \Delta\vartheta$ in Fig. 1 eventually contains the resonance angle ϑ_r which satisfies the condition that the center-of-mass system energy $E_{\mathrm{CMS}} = 2\langle\omega\rangle \sin\vartheta_r$ coincides with the mass m in the $\langle L\rangle$-system, and any *nominal* L-systems which satisfy the resonance condition can be generally formed by a transverse Lorentz boost of the $\langle L\rangle$-system with the relative velocity β with respect to the velocity of light c. Assigning the positive direction of β to the positive direction of the x-axis in Fig. 2, the energy and the transverse momentum relations between an L-system and the $\langle L\rangle$-system are connected—see Eq. (43.1) in [21]—via

$$\begin{pmatrix}\omega_1\\ p_{1\mathrm{T}}\end{pmatrix} = \gamma\begin{pmatrix}1 & -\beta\\ -\beta & 1\end{pmatrix}\begin{pmatrix}\langle\omega\rangle\\ \langle\omega\rangle\sin\vartheta\end{pmatrix},$$
$$\begin{pmatrix}\omega_2\\ p_{2\mathrm{T}}\end{pmatrix} = \gamma\begin{pmatrix}1 & -\beta\\ -\beta & 1\end{pmatrix}\begin{pmatrix}\langle\omega\rangle\\ -\langle\omega\rangle\sin\vartheta\end{pmatrix}, \tag{B4}$$

with $\gamma \equiv (1-\beta^2)^{-1/2}$, where the subscripts 1 and 2 correspond to the photon indices in Fig. 2. Since the relations of the energy components in Eq. (B4) indicate that p_1 experiences a frequency down-shift, while p_2 experiences a frequency up-shift, we introduce another definition of the energy components of p_1 and p_2 after the transverse boost:

$$\omega_1 = \gamma\langle\omega\rangle(1-\beta\sin\vartheta) \equiv \langle\omega\rangle - \delta\omega \equiv \langle\omega\rangle\,(1-\delta r)\,,$$
$$\omega_2 = \gamma\langle\omega\rangle(1+\beta\sin\vartheta) \equiv \langle\omega\rangle + \delta\omega \equiv \langle\omega\rangle\,(1+\delta r)\,, \tag{B5}$$

where a relative line width with respect to the mean energy of the creation laser $\delta r \equiv \delta\omega/\langle\omega\rangle$ is implemented. We note the following physical and experimental conditions:

$$0 < \beta < 1 \quad \text{and} \quad 0 < \delta r \ll 1. \tag{B6}$$

For convenience, we tentatively distinguish β for $\omega_{1,2}$ by the subscripts in the following discussion.

As for ω_1, from the first line of Eq. (B5) with $\delta r \ll 1$, we obtain

$$(1+\sin^2\vartheta - 2\delta r)\beta_1^2 - 2\sin\vartheta\beta_1 + 2\delta r = 0, \tag{B7}$$

with solutions, assuming $\vartheta \ll 1$,

$$\beta_{1\pm} \equiv \frac{\vartheta \pm \sqrt{D_1}}{1+\vartheta^2-2\delta r} \sim (1-\vartheta^2+2\delta r)\left(\vartheta \pm \sqrt{D_1}\right), \tag{B8}$$

where

$$D_1 \sim \vartheta^2 - (1+\vartheta^2-2\delta r)2\delta r \sim \vartheta^2 - 2\delta r. \tag{B9}$$

Requiring $D_1 \ge 0$ gives a physical constraint

$$2\delta r \le \vartheta^2. \tag{B10}$$

If this is satisfied, $\sqrt{D_1} \sim (\vartheta^2 - 2\delta r)^{1/2} \sim \vartheta - \delta r/\vartheta$ with $\delta r \ll 1$ gives

$$\vartheta \pm \sqrt{D_1} \sim \vartheta \pm \left(\vartheta - \frac{\delta r}{\vartheta}\right). \tag{B11}$$

The double-sign symbol in Eq. (B8) gives the following two solutions:

$$\beta_{1+} \sim (1-\vartheta^2+2\delta r)\left(2\vartheta-\frac{\delta r}{\vartheta}\right) \sim 2\vartheta-\frac{\delta r}{\vartheta},$$
$$\beta_{1-} \sim (1-\vartheta^2+2\delta r)\left(\frac{\delta r}{\vartheta}\right) \sim \frac{\delta r}{\vartheta} > 0, \tag{B12}$$

where only β_{1-} is physically acceptable, while β_{1+} is not, because the limit of $\delta r \to 0$ must correspond to $\beta = 0$ in our discussion.

Let us move on to discuss ω_2. From the second line of Eq. (B5), with $\delta r \ll 1$, we get

$$(1+\sin^2\vartheta+2\delta r)\beta_2^2+2\sin\vartheta\beta_2-2\delta r=0, \tag{B13}$$

with solutions, assuming $\vartheta \ll 1$,

$$\beta_{2\pm} \equiv \frac{-\vartheta \pm \sqrt{D_2}}{1+\vartheta^2+2\delta r} \sim (1-\vartheta^2-2\delta r)\left(-\vartheta \pm \sqrt{D_2}\right), \tag{B14}$$

where

$$D_2 \sim \vartheta^2+(1+\vartheta^2+2\delta r)2\delta r \sim \vartheta^2+2\delta r > 0. \tag{B15}$$

The approximation $\sqrt{D_2} \sim (\vartheta^2+2\delta r)^{1/2} \sim \vartheta+\delta r/\vartheta$ with $\delta r \ll 1$ gives

$$-\vartheta \pm \sqrt{D_2} \sim -\vartheta \pm \left(\vartheta+\frac{\delta r}{\vartheta}\right). \tag{B16}$$

The double-sign symbol in Eq. (B14) gives the following two solutions:

$$\beta_{2+} \sim (1+\vartheta^2+2\delta r)\left(\frac{\delta r}{\vartheta}\right) \sim \frac{\delta r}{\vartheta} > 0,$$
$$\beta_{2-} \sim (1+\vartheta^2+2\delta r)\left(-2\vartheta-\frac{\delta r}{\vartheta}\right) \sim -2\vartheta-\frac{\delta r}{\vartheta}, \tag{B17}$$

where only β_{2+} is physically acceptable, while β_{2-} is not for the same reason as ω_1, in addition to the positivity condition.

A common β is eventually determined as

$$\beta \sim \beta_{1-} = \beta_{2+} = \frac{\delta r}{\vartheta} \tag{B18}$$

based on Eqs. (B12) and (B17). By substituting δr in Eq. (B18) into Eq. (B6), the range of β is expressed as

$$\beta < \frac{\vartheta}{2}. \tag{B19}$$

Among ϑ within $\Delta\vartheta$, ϑ_r is effectively enhanced based on the Breit–Wigner distribution in the averaging process of the square of the invariant scattering amplitude around $E_{\mathrm{CMS}} = 2\sin\vartheta_r\langle\omega\rangle$ [10]. Therefore, for a given mass $m \sim 2\langle\omega\rangle\vartheta_r$ with $\vartheta_r \ll 1$, the effective physical limit on β is expressed as

$$\beta_r \equiv \frac{\delta r}{\vartheta_r} < \frac{\vartheta_r}{2}. \tag{B20}$$

On the other hand, an instrumental full line width of a creation laser $\Delta r \equiv \delta\omega_{\mathrm{full}}/\langle\omega\rangle$ is given by the creation laser intrinsically. Therefore, the range of β can be maximally covered by

$$0 < \beta < \beta_c \equiv \frac{\Delta r}{\vartheta} \tag{B21}$$

based on the relation in Eq. (B18). If β_c is smaller than β_r, however, the instrumental condition limits β to $\beta \le \beta_c$ before reaching the physical limit β_r for a given mass parameter. Therefore, we are required to choose smaller β, either $\beta_{\rm c}$ or β_r, depending on the relation between an experimentally given line width of the creation laser and a given mass parameter we search for.

Given a possible range of β based on the relation between an intrinsic line width of the creation laser and a given mass m, we can construct a unique $\langle L\rangle$-system by inversely boosting individual L-systems, where the intrinsic line width $\delta\omega_4$ is effectively broadened. This is because a spectrum width is effectively embedded by the possible range of inverse boosts for a ω_4 chosen among $\langle\omega_4\rangle - \delta\omega_4 \le \omega_4 \le \langle\omega_4\rangle + \delta\omega_4$ in individual L-systems. Therefore, combining the inverse-boost-originating spectrum width with the intrinsic line width of the inducing laser provides the effective inclusive range of u defined in Eq. (3) in the $\langle L\rangle$-system.

We first evaluate how much the common inverse boost originating from the line width of the creation laser solely changes the range of u from $\underline{u}_{\rm c}$ to $\overline{u}_{\rm c}$ in the $\langle L\rangle$-system for an ω_4 within the line width of the inducing laser field. By inversely applying the boost in Eq. (B4) to p_4 in Fig. 2, we can express the upper and lower edges of the broadened energy range of ω_4 with the approximation $\vartheta_r \ll 1$ as[7]

$$\begin{aligned} \overline{u}_{\rm c}\langle\omega\rangle &\sim l_{\rm i} u\langle\omega\rangle\gamma(1+\beta\vartheta) \equiv l_{\rm i} u\langle\omega\rangle \min\left\{\gamma_{\rm c}(1+\Delta r), \quad \gamma_r\left(1+\frac{1}{2}\vartheta_r^2\right)\right\}, \\ \underline{u}_{\rm c}\langle\omega\rangle &\sim l_{\rm i} u\langle\omega\rangle\gamma(1-\beta\vartheta) \equiv l_{\rm i} u\langle\omega\rangle \min\left\{\gamma_{\rm c}(1-\Delta r), \quad \gamma_r\left(1-\frac{1}{2}\vartheta_r^2\right)\right\}, \end{aligned} \tag{B22}$$

where $l_{\rm i}$ represents the process to choose an ω_4 within the relative line width $l_{\rm i} \equiv 1 \pm \delta u_4/u$, with $\delta u_4 \equiv (\overline{u} - \underline{u})/2$ being the average value $\langle l_{\rm i}\rangle = 1$, subscripts c and r in the right-hand side denote the cases where $\beta_{\rm c}$ and β_r are used, respectively, and $\min\{A, B\}$ specifies the smaller of A and B.

We then discuss the inclusive range of u by combining the broadened ω_4 in the $\langle L\rangle$-system with the intrinsic line width of the inducing laser. We introduce a notation reflecting the combining process in the $\langle L\rangle$-system,

$$\omega_{<4>} \equiv l_{\rm c} l_{\rm i} u\langle\omega\rangle, \tag{B23}$$

where $l_{\rm c} \equiv 1 \pm \delta u_{\rm c}/u$ with $\delta u_{\rm c} \equiv (\overline{u_{\rm c}} - \underline{u_{\rm c}})/2$, having average value $\langle l_{\rm c}\rangle = 1$, is a coefficient describing the uncertainty by the inverse transverse boost discussed above. Since the intrinsic energy uncertainties of the creation and inducing laser beams are independent, quadratic error propagation gives the following inclusive uncertainty on ω_4 in the $\langle L\rangle$-system:

$$\delta^2\omega_{<4>} = \left(\frac{\partial\omega_{<4>}}{\partial l_{\rm i}}\right)^2 \delta^2 l_{\rm i} + \left(\frac{\partial\omega_{<4>}}{\partial l_{\rm c}}\right)^2 \delta^2 l_{\rm c} = u^2\langle\omega\rangle^2\left[\left(\frac{\delta u_4}{u}\right)^2 + \left(\frac{\delta u_{\rm c}}{u}\right)^2\right]. \tag{B24}$$

Finally, this gives the inclusive uncertainty on u,

$$\delta u_{\rm inc} \equiv \frac{\delta\omega_{<4>}}{\langle\omega\rangle} = u\sqrt{\left(\frac{\delta u_4}{u}\right)^2 + \left(\frac{\delta u_{\rm c}}{u}\right)^2}, \tag{B25}$$

and the upper and lower limits on u, which replace the limits in Eq. (10) with

$$\overline{u} \equiv u + \delta u_{\rm inc} \text{ and } \quad \underline{u} \equiv u - \delta u_{\rm inc}, \tag{B26}$$

respectively, are obtained.

---

[7] Note that the degree of freedom to flip p_3 and p_4 around the z-axis by keeping the angular balance in Fig. 1 results in both frequency up- and down-shifts in ω_3 and ω_4.

As a summary based on Eq. (B22), the effect of the line width of the creation laser is less significant compared to that of the inducing laser for a smaller mass range, while it has some impact for a larger mass range, as long as the line width is comparable to or larger than that of the inducing laser.

References

[1] R. D. Peccei and H. R. Quinn, Phys. Rev. Lett. **38**, 1440 (1977).
[2] S. Weinberg, Phys. Rev. Lett. **40**, 223 (1978).
[3] F. Wilczek, Phys. Rev. Lett. **40**, 271 (1978).
[4] Y. Fujii and K. Maeda, *The Scalar–Tensor Theory of Gravitation* (Cambridge University Press, Cambridge, 2003).
[5] M. P. Hertzberg, M. Tegmark, and F. Wilczek, Phys. Rev. D **78**, 083507 (2008).
[6] O. Wantz and E. P. S. Shellard, Phys. Rev. D **82**, 123508 (2010).
[7] K. Homma, D. Habs, G. Mourou, H. Ruhl, and T. Tajima, Prog. Theor. Phys. Suppl. **193**, 224 (2012).
[8] T. Tajima and K. Homma, Int. J. Mod. Phys. A **27**, 1230027 (2012).
[9] Y. Fujii and K. Homma, Prog. Theor. Phys. **126**, 531 (2011) [arXiv:1006.1762 [gr-qc]].
[10] K. Homma, D. Habs, and T. Tajima, Appl. Phys. B **106**, 229 (2012) [arXiv:1103.1748 [hep-ph]].
[11] K. Homma, Prog. Theor. Exp. Phys. 04D004 (2012).
[12] S. A. J. Druet and J.-P. E. Taran, Prog. Quant. Electr. **7**, 1 (1981).
[13] A. Yariv, *Optical Electronics in Modern Communications* (Oxford University Press, Oxford, 1997).
[14] F. Moulin and D. Bernard, Opt. Commun. **164**, 137 (1999).
[15] E. Lundström et al., Phys. Rev. Lett. **96**, 083602 (2006).
[16] J. Lundin et al., Phys. Rev. A **74**, 043821 (2006).
[17] D. Bernard et al., Eur. Phys. J. D **10**, 141 (2000).
[18] Y. Fujii, Nature Phys. Sci. **234**, 5 (1971).
[19] E. Fischbach and C. Talmadge, *The Search for Non-Newtonian Gravity* (AIP Press, New York, 1998).
[20] G. Mourou, W. Brocklesby, T. Tajima, and J. Limpert, Nature Photonics **7**, 258 (2013).
[21] J. Beringer et al. (Particle Data Group), Phys. Rev. D **86**, 010001 (2012).
[22] K. Ehret et al. (ALPS Collaboration), Phys. Lett. B **689**, 149 (2010).
[23] E. G. Adelberger et al., Phys. Rev. Lett. **98**, 131104 (2007).
[24] D. J. Kapner et al., Phys. Rev. Lett. **98**, 021101 (2007).
[25] J. Chiaverini et al., Phys. Rev. Lett. **90**, 151101 (2003).
[26] S. J. Smullin et al., Phys. Rev. D **72**, 122001 (2005); **72**, 129901 (2005) [erratum].
[27] S. K. Lamoreaux, Phys. Rev. Lett. **78**, 5 (1997); **81**, 5475 (1998) [erratum].
[28] S. L. Cheng, C. Q. Geng, and W. T. Ni, Phys. Rev. D **52**, 3132 (1995).
[29] J. E. Kim, Phys. Rev. Lett. **43**, 103 (1979).
[30] M. A. Shifman, A. I. Vainshtein, and V. I. Zakharov, Nucl. Phys. B **166**, 493 (1980).
[31] D. Bernard, arXiv:1311.5340 [physics.acc-ph].
[32] J. D. Bjorken and S. D. Drell, *Relativistic Quantum Mechanics*, (McGraw-Hill, New York, 1964).
[33] W. Greiner and J. Reinhardt, *Quantum Electrodynamics* (Springer, New York, 1994), 2nd ed., Eq. (3.80).
[34] C. Möller, *General Properties of the Characteristic Matrix in the Theory of Elementary Particles. I* (Munksgaard, Copenhagen, 1946), 1st ed.
[35] M. A. Furman, LBNL-53553, CBP Note-543.
[36] J. F. Reintjes, *Nonlinear Optical Parametric Processes in Liquids and Gases* (Academic Press, Orlando, 1984).
[37] L. Novotny and B. Hecht *Principles of Nano-Optics* (Cambridge University Press, Cambridge, 2012), 2nd ed.

■研究紹介

真空内四光波混合による sub-eV 中性ボゾンの共鳴探索

広島大学大学院理学研究科物理科学専攻
本間 謙輔,　長谷部 孝,　久米 一輝
homma@hepl.hiroshima-u.ac.jp,　hasebe@hepl.hiroshima-u.ac.jp,　kume@hepl.hiroshima-u.ac.jp

京都大学化学研究所先端ビームナノ科学センターレーザー物質科学研究領域
阪部 周二,　橋田 昌樹
sakabe@laser.kuicr.kyoto-u.ac.jp,　hashida@laser.kuicr.kyoto-u.ac.jp

2013 年 11 月 11 日

1　真空の巨大クジラ探索

私たちの目の前にある物体間を埋め尽くしている真空とは何か。仮に，実存しているとすれば，一体どのような構造を有しているのか？ 真空，あるいは時空といったほうが適切かもしれない，得体のしれない「この眼前の容れもの」は，通常光によって計量される。ただし，弱い光線を利用して。もしも計量用の光が極めて強くかつ位相が揃っている場合，一体真空は局所的にどのような応答を示すことになるのであろうか？ これは日常レーザーに触れている著者自身が抱く純粋な疑問である。アインシュタインが類似のことをいうとエレガントである。「重力ならびに空間の計量的な特性に関する筋の通った理論といえば，従来まずあげるべきものは一般相対性理論である。しかし，一般相対性理論によって電磁現象を取り扱うには，この理論のわくのなかに，別にマックスウェルの理論を取り入れることで我慢しなければならなかった。すなわち，線素 ds^2 を与える式で，重力場に関する座標差 dx^ν の 2 次形式のほかに，これと論理的には独立な dx^ν についての 1 次形式を導入しなければならなかった。この係数を電磁場のポテンシャルと解釈した。また，重力場の方程式であるテンソル式には，時空の曲率テンソルのほかに －外面的に，また論理的にも任意にプラス記号を結びつけて －共変形に 書かれた電磁場のエネルギー・運動量テンソルをつけ加えた。マックスウェルの理論が単に第一次近似の場の理論としてだけ，多くの実験結果によって支えられているにすぎないと考えるならば，上に 述べたような電磁場に対する真実の場の方程式は，マックスウェルの式とは少し異なっているのではないかという疑念を一概に否定することはできなかった。」これは，文献[1]の第一パラグラフの抜粋である。

こういった高強度電磁場に対する真空の応答は，やはり，光によって検証するのが妥当であろう。微視的にいえば光子・光子散乱，あるいは 光の非線形性を通じて，真空 あるいは時空の構造をなんとか暴くことはできないであろうか。

私たちは，また強度とは別の尺度を持っている。漠然と真空の光応答といっても，一体それがどのようなスケールで起こっているのかを区別しなければならない。現象が起こる時間・空間のスケール，あるいは真空の光応答のエネルギースケールである。理論は一旦忘れてみよう。LHC で発見された中性粒子は確かに 2 光子に結合する。また，中性中間子も 2 光子に結合する。これらは要するに，3 桁もエネルギースケールの異なったところで類似の共鳴点が存在している事実を示している。3 桁異なったエネルギースケールにおいて，光に結合する共鳴点が複数存在するが，別の桁違いに異なるエネルギー領域には，もはや類似の共鳴点は存在しないと想定するのはむしろ不自然であり，より一般的に探索してみたくなる。探索のために，エネルギーを上げるのは困難だが，エネルギーを徹底的に下げていくのは簡単である。この場合，ナイーブには共鳴の伝播距離は長くなるであろう。つまり，準巨視的なスケールにおける現象を探っていくことになる。言うなれば，「**深海の巨大イカ探索**」ならぬ「**真空の巨大クジラ探索**」を，真空の海をうんと潜って実施してみたくなる。この研究は，このような素朴な観点に端を発している。それでは，ロマンに満ちた探検を始めてみよう。

2　理論的背景

真空にどんなクジラが存在し得るのか。今風の理屈を振りかざしてみよう。暗黒エネルギー (DE)，暗黒物質 (DM) の理解は，現代物理学の最重要課題である。本研究の究極的な観測対象はディラトンと呼ばれるスカラー場の一種である。ディラトンは，有限到達距離の重力源とも捉えられる。これは，スケール変換（グローバルな共形変換）に対して不変であったラグランジアンが，重力定数という次元を持った状態，すなわちスケール変換不変性を自発的に破る際に生じる粒子であり，その自己相互作用により微少な質量を持った南部–ゴールドストーンボゾン（NGB）であ

る。質量 neV 程度以上を有するディラトンが量子アノマリー結合のみを通じて重力程度の強さで物質と相互作用できると，宇宙年齢（10^{60} プランク単位）の 2 乗に反比例して減衰する宇宙項（10^{-120} プランク単位）が自然に導出でき，観測値を無理なく説明できる[2]。したがって，この場の存在を突き止められれば，DE の一つの有力な説明となり得る。この DE 模型は，スカラー・テンソル理論（STT）と呼ばれる流派に属する。その特徴は，時間変動し得る定数を説明できる点にある。この背景には，重力定数が他の結合定数と比較して極めて小さいことを説明するために，定数が時間変動する可能性を考えた，いわゆるディラックの巨大数仮説に端を発して，それをヨルダンが精密に模型化した歴史的経緯がある[3]。加速膨張の発見以来，類似のアプローチとして，クイントエッセンスと呼ばれるスカラー場が，宇宙項の時間変動を生むという模型があるが，これらはむしろ現象論的に導入された原理のない模型である。ここで挙げた STT は，これらとは一線を画する。この宇宙が重力定数を選ぶ際，特定の共形系が定まるのであるが，その系において何が真の定数で，何が時間変動する定数であるかについては，共形系の選び方に依存する。自由度があるといっても，観測と無矛盾である必要がある。この特定の共形系を選ぶという過程が，まさにスケール変換対称性を破り，その結果，NGB が生まれるという考え方に基づいている。ゲージ対称性，カイラル対称性，といった素粒子論にとって馴染みのある対称性に加えて，スケール変換対称性の破れの結果生じるスカラー場である点において，素粒子論的粒子探索の対象として不足のないものである。実際この STT では，質量範囲，力の伝播距離，結合の強さといった力学的な性質まで予言されており，実験的検証に足る理論模型である。このスカラー場の質量が neV 程度であれば，その伝播距離は 100 m のスケールであり，まさしく，真空のクジラと呼べるサイズである。過去においては，第 5 の力として探索されたこともある[4]。一方，その物質場との結合は，重力的であるが故に，これまでの地上探索網にはかかっておらず，まさに，ハンター冥利に尽きるクジラである。

実験の立場からすれば，交換される未知場の質量 m と光子との実効的な結合定数 g/M（g は無次元量で光子との結合を想定するならば α_{QED} 程度，M はエネルギーの次元を有する）さえ与えられれば，未知場の理論的背景に依らず，散乱実験による一般的な探索が可能となる。例えば，ヒッグス場と 2 光子の結合であれば，M として真空期待値つまり，100 GeV の桁を想定すればよい。究極的に実験の感度が重力結合，すなわち，$M = M_{\mathrm{Planck}} \sim 10^{18}$ GeV へ至るのならば，それよりも強い結合領域に予言される軽い DM の候補は，必然的に観測網にかかる。強固な理論的背景を持つ，軽い DM の代表格としてのアクシオン（擬スカラー場）は当然探索対象となる。QCD ラグランジアンの CP 対称性は，QCD の非摂動真空構造（θ 真空）を色濃く反映している。θ 真空の位相値は，元来任意でよい（CP 非保存）にも関わらず，実世界では極めて良い精度でゼロ（CP 保存）となっている。このため自発的に位相値をゼロに収斂させる機構が必要となる。アクシオン場は，このために導入された Peccei-Quinn 対称性の破れに伴う NGB である。π 中間子は元来 NGB として考えられたが，その実質量を説明するためには，カイラル相転移が起る 200 MeV 付近の QCD 非摂動真空を介した擬 NBG 化が必要となる。アクシオン場についても同様であるが，その擬 NBG 化過程を理解することは，QCD 非摂動真空構造の理解に加え，宇宙論的にも重要課題となる。この転移によって得られる質量に依っては，DM の有力な候補になり得るからである。例えば，$M = M_{\mathrm{GUT}} \sim 10^{16}$ GeV かつ $m = 10^{-4} \sim 10^{-6}$ eV であると，アクシオンのみで DM を説明し得る[5]。

こういった理論的背景から，sub-eV の共鳴探索は確かに DE や DM といった現代物理学の最重要課題に関連しており，十分意義のある探検なのである。

3 探索手法

それでは，どのような探索手法があり得るのか模索してみよう。まずは重心系エネルギーを下げて共鳴点の直上を狙うことを考える。厳密な共鳴点上では，弱結合定数部分が分母分子で相殺するからである。ではどのように重心系エネルギーを下げるのか。もしもコライダーで衝突エネルギーを neV 程度にするには，100 m の波長をもった光子同士をぶつけなければならない。無理である。通常，重心系エネルギーを上げるためにコライダーを作っているのであるが，その真逆の発想，つまりほとんど正面でぶつけないことが重要である。そこでわれわれは，準平行系（Quasi Parallel System）というものを考案した[6]。図 1 のような衝突幾何学を考えた場合，その重心系エネルギーは，入射光子のエネルギーを ω，任意に選ばれる 2 光子のなす角を θ とすると，$E = 2\omega\sin\theta$ と表現される。この式から，重心系エネルギーを調整するのに，われわれは光の入射エネルギー

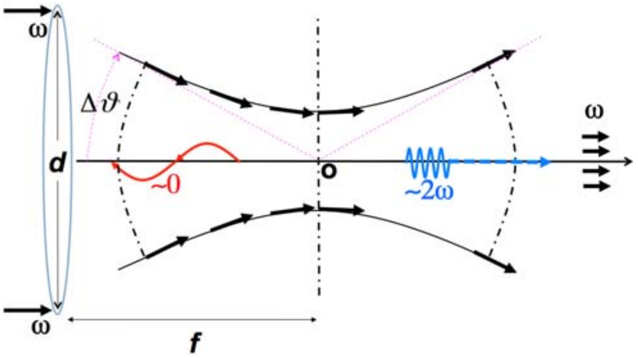

図 1 光子・光子準平衡衝突系(QPS)における周波数シフト

と入射角という 2 つの実験的ノブを持っていることが分かる。現代技術で最も強い光子場を作る手法としては，レーザーしかないであろう。また，できるだけ低いエネルギーのうち，単一光子の検知を可能する波長域は可視光周辺である。したがって光のネルギーを1eV 程度として，あとは長い焦点距離で光を絞れば，必然的に極低エネルギーの重心系エネルギーをもったQPS を内包することになる。図 1 にあるように，概念的にはレンズでレーザーを絞るだけで，なんと桁違いに低い重心系エネルギーを実現する光子・光子コライダーになっていたのである。

QPS には，特筆すべき点が複数ある。第一に，QPS では相互作用が周波数シフトとして観測される点である。QPS は，CMS の衝突軸に垂直な方向へ鋭くローレンツ・ブーストした系と解釈できる。したがって，QPS における光子・光子衝突で，未知場が共鳴的に生成・崩壊する過程において，崩壊後の光子は，その出射方向に応じた周波数シフトを起こす。これはあたかも単色レーザーの集光点から別の色の光が飛び出してくるような現象に映るであろう。第二に，QPS での重心系エネルギーは極めて低いため，標準模型内の粒子交換による相互作用がほとんど寄与しないことである。もっとも寄与が大きいものとしては，QED 過程の光子・光子散乱（いわゆるボックスダイアグラム）が期待される。しかし，その全断面積は重心系ネルギーの 6 乗にスケールするため[7]，sub-eV 領域ではほとんど効かなくなる。例えば，重心系エネルギーが1eV 程度ですら，その全断面積は10^{-42} b と極めて小さい。仮に，neV のスカラー場交換に対して，重心系エネルギーをneV 程度に調整できたならば，さらに 54 桁抑制されることになる。

しかし，ここで最大の難関が立ちはだかる。結合が重力的に弱いところまで感度を持つということは，その共鳴幅は極めて狭いことを受け入れなければならない点である。または長寿命の粒子が生まれてしまうといって良い。通常，共鳴点を狙う実験では，そのビームエネルギーは正確に調整されており，そのエネルギー不定性は，共鳴幅よりも小さい。一方，レーザー光の QPS は，単一レンズで集光して作る以外現実的な方法がないため，特にルミノシティが最も高くなる集光点では，CMS エネルギーが不確定性原理に基づく光子の運動量揺らぎにより，原理的な不定性をもつことになる。例えば，LHC における入射グルーオンの運動量が，陽子内部のパートン分布を通じてしか指定できないことに似た状況かもしれない。今の場合，それが光の波としての性質が浮き彫りになることで不定性が生じると考えられる。それでは，共鳴の影響はなくなるのか？ 実は，そんなことはない。この不定性が原理的なものであるのならば，われわれは散乱振幅の 2 乗を，その不定性の範囲内で平均して求める必要があるからである。つまり，共鳴としての Breit-Wigner（BW）関数を，不定性の範囲にわり積分するような効果が得られるはずである。BW 分布は面白い関数で，その半値幅で積分した値と，無限大の範囲で積分した値の違いが，2 倍しか違わないのである。これの意味することは，もしも，重心系エネルギーの不定性が半値幅よりもずっと大きいのならば，BW の積分効果の半分は保証されることになる。この積分効果により，実際，共鳴幅を一切内包しない場合と比べて，結合定数の 2 乗倍の反応断面積の増大が見込まれる。こういった事情は，QPS で狭い共鳴粒子を捉える場合に特有の事情であり，これを発案した当初，少なくない論文レフリーが疑念を呈したことを告白しておく。その元凶は，あくまでも光子は事前に確定した運動量値をもっているという“古典頭”である。この場合，狭い共鳴点をめったにヒットできないため，無限に統計量が必要になるという思考に陥ってしまう。これに対して，われわれの主張は，統計量とは無関係に，たとえ一対の光子ですら，その重心系エネルギーの原理的な不定性が故に，共鳴の影響を確率的に有限量内包できるという考え方であることを強調しておく。この共鳴の積分的効果により，共鳴点直上のオーダー1 の断面積は得られないが，弱結合定数の 4 乗ではなく，2 乗に比例する散乱確率の中間的増大効果が見込めるのである[6]。クジラの姿は見えずとも，その鳴き声を通じてクジラをある海域内で捕獲したと考えることで満足するアプローチは，あり得るのである。

残念ながら共鳴の積分的効果を考慮しても，重力結合までの感度へ至るには程遠い。これでクジラ探索はおしまいか。ここで，一旦擬スカラー場であるアクシオン探索ではどのような手段が用いられてきたのか概観してみよう。現在最も弱結合まで感度を持ちえる実験として太陽アクシオン探索が挙げられる[8]。太陽内のインコヒーレント光の対により生成されるアクシオンを，地上の磁場を用いて崩壊させる方法を常套手段として探索が行われている。もう一つは純粋に実験室の実験として，太陽内のアクシオン生成のヴァーテックスを，レーザーと静磁場に置き換え，そこで生成されるアクシオンが壁を透過したのち，磁場に再結合する際に生じる光子を，壁の向こうで検知する Light Shining through a Wall(LSW)という手法である[9]。これらの手法に共通するのは，磁場による崩壊の誘導である。LSWにおける相互作用レートは，レーザーの強度に比例し，磁束密度Bの4乗に比例していることを思い出しておこう。

さて，ここまでに考えた共鳴の積分的効果を介した生成・崩壊は，あくまで，真空のプロセスとしてであった。もしも，静磁場に対応する背景場で真空を満たしておいたならば，何が起こるであろうか？ その前に，真空中にレーザー場があるといった場合に，それがどのような状態であるのか思い出しておく必要がある。一般的に，レーザーの場の量子論的な状態は，コヒーレント状態として記述される[10]。このコヒーレント状態とは，“散乱のコヒーレンス”と言葉

は似ているが，全く違う概念であることに留意して欲しい。真空状態$|0\rangle$に対して，励起されたコヒーレント状態を$|N\rangle\rangle$と表現することにしよう。コヒーレント状態は，同一運動量に縮退した個数の異なった状態の線形結合として理解される。このNは，レーザー場に含まれる平均光子数である。さて図 2 を見ていただきたい。生成のヴァーテックスでは，未知場を作り出すために，コヒーレント状態から，2 光子を消滅させる必要がある。1 つ消滅させる演算子の期待値は，$\sqrt{N}$であることが示される。従って，2 光子を消滅させる場合，Nという因子がヴァーテックスに対して，散乱振幅の段階で掛かることになる。散乱振幅の 2 乗をとって相互作用レートに直せば，Nの 2 乗に比例する因子が得られる。これは，平均光子数Nのバンチ同士がぶつかるときに，2 光子対の組み合わせの数がNの 2 乗になるはずであるという直感と矛盾しないが，この一致は偶然でしかない。フェルミオンである荷電粒子のバンチから衝突粒子対を古典的に選ぶ過程とは，厳格な意味では同等には扱えない。一方，真空中で生じた共鳴場が 2 光子へ崩壊する場合，真空状態$|0\rangle$に対して，今度は，2 光子を生成する必要がある。この場合，1 光子を生成する演算子の期待値は 1 となり，2 光子生成しても 1 であることは変わりない。したがって，生成・崩壊の振幅を 2 乗しても，レートはNの 2 乗のままである。通常のコライダー実験では，真空状態に終状態粒子を生成する，いわゆる，自発崩壊過程しか利用して来なかった点に改めて気づくことができよう。ここで上記の静磁場による崩壊の誘導を思い起こそう。もしも真空中に別の運動量状態に縮退したコヒーレント状態があったとしよう。この場合，その運動量状態への 1 光子生成の期待値は，消滅演算と同様に$\sqrt{N}$となる。もう片方の崩壊光子は，真空状態に対して生成することとして，その因子を 1 とすると，その散乱振幅段階の増大は，$\sqrt{N}$の 3 乗となり，散乱レートとしては，結局，Nの 3 乗という因子になる。これは，まさに LSW の反応のレートがレーザー強度とBの 4 乗（強度の 2 乗に相当）の積となっていることと一致する。ただし，その違いは大きい。静磁場では運動量が縮退していない。コヒーレント場の場合には，運動量が縮退しているが故に，上記の共鳴条件をみたしやすい上に，観測すべき終状態の 1 光子の運動量が厳格に定まるからである。加えて，静磁場では恐らく 10 T 程度までが限界であるが，レーザー場の場合にはその強度上昇に陰りが見えていない。

これらを踏まえて，生成用に1ωのレーザー光を用意し，崩壊誘導用にuを$0<u<1$とする$u\omega$の背景レーザー場を用意しておくと，エネルギー・運動量の保存則から$1\omega+1\omega$→共鳴→$u\omega+(2-u)\omega$という反応を介して，崩壊時に一方の光子は$(2-u)\omega$というエネルギーを満たすことになる。つまり，あらかじめ 2 波長のレーザーを混在させておくことにより，真空下でパラメトリックに新たな光波を生成することが可能になる。後になって分かったことであるが，これは Coherent Anti-Stokes Raman Spectroscopy (CARS)というよく知られた分光法そのものであり，量子光学の分野では，一般的に四光波混合過程として詳細に研究されている過程であった[11]。すなわち，上記の誘導過程は，物質中では既知の現象なのである。このような誘導過程を，原子の共鳴ではなく，素粒子の共鳴に対して，そのまま適用できるのかどうか，それ自体大変興味深い研究課題である。たとえば，既知の中性π中間子の崩壊を，コヒーレントな光子場で誘導崩壊させられるのかどうか，是非検証してみたいものである（可視光域レーザー場では，運動学的に難しいが）。

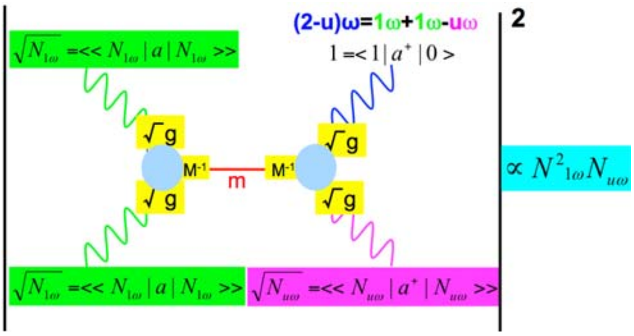

図 2　四光波混合過程による崩壊の誘導

このNの 3 乗に比例する効果は，近未来のレーザー場の高強度化を視野に入れた場合，凄まじい効果となる。たとえば，1 J の光には，10^{18}個程度の可視光光子が存在する。慣性核融合用のレーザー場としては，パルスあたり MJ 級のレーザー照射が可能となっている。つまり，すでにアボガドロ数を超えた光量をハンドルする技術を人類は手に入れている。この光量の 3 乗を考えてみると，コライダー・ルミノシティがどのように頑張っても届かない高感度領域に到達できることは自明である。後にまとめるが，以上の共鳴の積分過程と背景コヒーレント場による誘導過程の導入により，どうやらわれわれは，かろうじて重力結合へ至る感度を，現代テクノロジーの範疇で手に入れられる展望が得られるようである。真空のクジラ探索のための探査手法が原理的には整ったのである。

4　予備実験

それでは，クジラ探索のための具体的な実験系を考えよう。1ω，$u\omega$および$(2-u)\omega$は，すでに述べたように，現状では，すべて可視光付近の波長が妥当である。この条件を満たすのは，全てを同軸上に通す場合である。つまり，2 色の光波1ωと$u\omega$同軸上で混合し，生成した信号光波$(2-u)\omega$を同軸上で検知できる場合に限られる。これは，低質量の共鳴場が，QPS では集光軸方向へ鋭くローレンツ・ブーストしていることに起因している。

もう一つ，レーザーを用いることによる利点がある。それは，未知共鳴場の光子への結合様式を議論できる点にある。レーザー場の偏光状態は，ほぼ完璧に制御可能で，生成用レーザーと誘導用レーザーの偏光状態について，その偏光面も含めて自在に制御でき，かつ，信号光の偏光状態も可視光域であれば，精度よく指定できるためである。この特徴により，少なくとも，スカラー場と擬スカラー場交換の分離も可能になるし，その他の背景事象との分離も可能となる。

それでは，いよいよ実験現場の具体的な話へ移ろう。図 3 は，京都大学化学研究所内で広島大学大学院生らとセットアップを構築している風景である。この測定系は，互いに直交する直線偏光状態 $\left\{1\right\}$，$\left\{2\right\}$ あるいは，その線形結合状態である生成場 ω と，直線偏光状態 $\left\{1\right\}$ または $\left\{2\right\}$ を指定した誘導場 $u\omega$ を，観測対象の未知場の種類に応じて選択的に混合するビーム混合部分，同軸上 2 色集光による準平行衝突系を実現する光子・光子相互作用部分，信号光 $(2-u)\omega$ の直線偏光状態を選んで計数する検出部分からなる。検出部分では，波長選択可能なダイクロックミラーで $(2-u)\omega$ 周辺波長の光子を，相互作用しない残余光の軌道から空間的に切り分ける。その際，混ざり込む生成場と崩壊誘導場の透過光をさらにプリズムで空間的に分離する。波長域を指定された信号光は，偏光ビームスプリッターにて直線偏光状態を指定された後，偏光状態に応じた時差をファイバー中で付けた上で，暗箱内で単一光子計数可能な光電子増倍管で検知される。その際，光電子量の時間構造を波形データとして高速で記録する。さらに，信号波長レーザー光を同軸上に導入でき，検出効率が実測できる。京大化研内で開発・運転している Ti:Sa レーザーシステムのうち，ω として 800 ± 50 nm を使用し，$u\omega$ として Ti:Sa 用の増幅用光源である YAG レーザーからの 1064 nm を用いる。その結果，物理信号となる $(2-u)\omega$ の波長域は，640 nm を中心として 580 ～ 709 nm 程度の範囲をもつことになる。

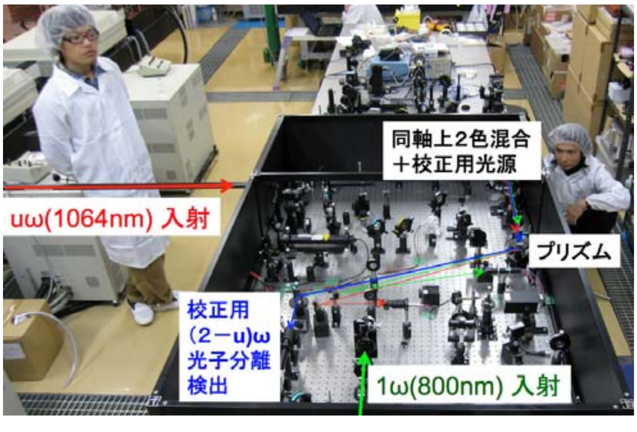

図 3　京都大学化学研究所レーザー実験棟における予備実験の作業風景

この実験提案において最も困難が予想された点は，果たして同軸上にて色の違う 1 光子のみを選択できるのかという点であった。1J のレーザーパルス光でも 10^{18} 個の光子群である。ここから本当に 1 光子のみを特定できるのであろうか？ この問題に対して，結局は，最も単純に屈折率の大きなプリズム群を用いることで解決した。レーザー場が平面波的である限り，大量の光子群は空間的に容易に切り分けられる。勿論，プリズムの表面からは球面波的な散乱も起こる。しかしながら，これらの残光成分は比較的弱い。高性能の色フィルター 1 枚にて，4–5 桁に及ぶフィルターリングが可能となるため，これらを残光の量に応じて適当な枚数重ねていけば，十分な S/N が得られる。高エネルギー実験における前後方のミューオン ID に似ているかもしれないが，分厚い吸収体の壁が，数センチ程度の厚みのフィルター群に置き換えられるため圧倒的に楽である。

次に予想されたのは，物質起因の四光波混合からのバックグラウンド光である。これについては，2 色混合光を同軸上で集光する直前に，信号光波長に相当する光をフィルターにて落としてしまえば済む。勿論，フィルター自体が固体物質である以上，生成と吸収のイタチごっこになるのであるが，吸収型のフィルターを用いることにより，フィルター内で生成する信号光波長域の光量とフィルター内で吸収される同波長域の光量を比較すれば，後者のほうが桁違いに大きいため，これも適度に重ねていけば落とせる。

最後に残るのは，集光点領域を囲む真空チェンバー内の残留ガスからの四光波混合光である。これについては，真空度を上げる以外に手がない。現在，実験室内で達成可能と考えられている真空度は，10^{-11} Pa 程度である。原子数にして，$10^{4}/\mathrm{cm}^{3}$ 程度。しかしこの値は実のところ，真空度を測るゲージの精度の限界であるとも言われている。実際には，そのゲージの下限を振り切るほどの真空度を達成できる真空排気系も実存するため，必要に応じてその排気系を導入していけばよい。市販品で，分圧で 10^{-13} Pa まで分解できる四重極質量分析器が存在するが，そのような機器を用いれば，残留ガスの成分と個々の成分の原子数までが実測可能であると見込まれる。あとは，観測された原子種ごとに圧力を上げた状態で四光波混合光量の偏光組み合わせ依存性を実測しておけば，真空内四光波混合量の測定時の真空度に応じた原子起因光量を外挿値として求められることになるであろう。

現在これらの想定を実験的に検証する準備を進めている。これまでに，単一光子感度で希薄大気中の原子起因の四光波検知に成功している。図 4 の 4 つのパネルは，生成場 C，誘導場 I の有無について 4 つの組み合わせ：C+I，C のみ，I のみ，およびペデスタルの各々について四光波混合光の波長域にある光子の 60 ns ゲート内の到達時間分布を示す。速い到達時間帯は，直線偏光状態 $\left\{1\right\}$ を，遅い到達時間帯は

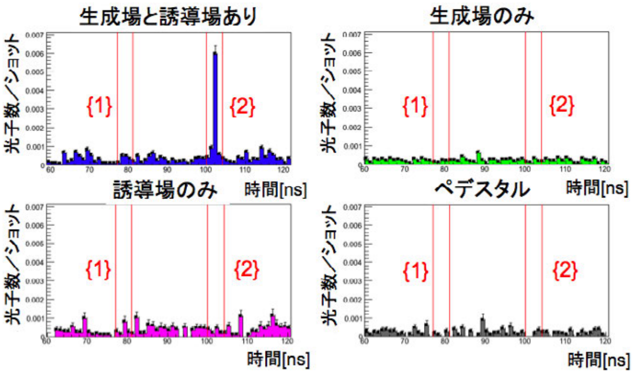

図 4　10^2 Pa 大気起因の四光波混合光の到達時間分布

{1} と直交した {2} の場合に相当し，C+I の時にのみ鋭い時間構造が現れる。同時に信号光の検出効率の見積が可能となっている。

5　展望

上記のように現時点では，テーブルトップの実験として手探りの状態で予備実験を繰り返しているが，その準備段階を経た後，特にヨーロッパで勃興している高強度レーザー場を用いた実験へ拡張することを視野に入れている。

すでに予算措置が行われている Extreme Light Infrastructure (ELI) プロジェクトのうち，著者が直接関与しているルーマニアに建設中の ELI-NP[12]について若干触れておく (図 5 参照)。これには ~ 10 PW(~ 200 J/ ~ 20 fs pulse) のレーザー二基が導入されると同時に，600 MeV の電子線ライナックが備えられる予定のユニークな施設である。2017 年に完成予定で現在プロジェクトが進行している。

図 5　建設中の ELI-NP の完成予想図[12]

もう一つレーザー施設を横に繋ぐ共同体として International Zetta-Exa Watt Science and Technology (IZEST) が存在することは特筆に値する。IZEST は素粒子分野でいう CERN に似た共同体であるが，実験する場所は一拠点に限られない。世界中に存在する施設を IZEST ネットワーク内で柔軟に利用するという思想の組織体である。本稿に特に関連する IZEST 内のプロジェクトとして，高繰り返しかつ高強度のファイバー束を基礎としたレーザー Coherent Amplification Network (CAN) を開発している (図 6 参照)。たとえば，四光波混合の場合，上述したようにパルスあたりのエネルギー（光子数 N）が物理的には最も重要であった。しかし，実験の系統的な側面を加味すると，やはりパルスの統計量も必須となる。CAN は国際プロジェクト ICAN として，50 J/100 fs , 繰り返しレート 10 kHz を目指して開発途上にある。このレーザーが，レーザープラズマ加速技術と融合すると，近未来のコライダー実験に応用する道も開けていくことが見込まれている。その意味においても，本研究をコライダー実験と共に行う利点がある。

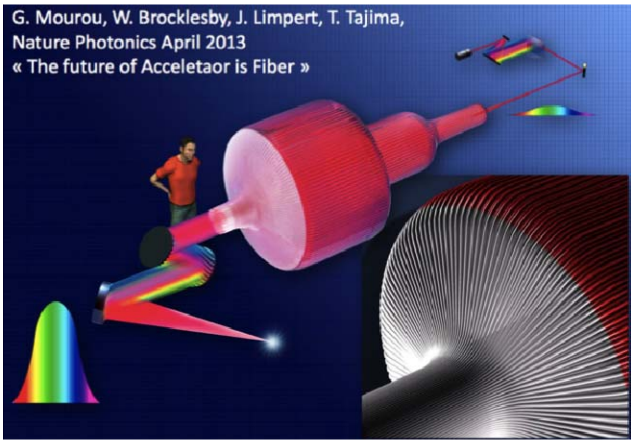
G. Mourou, W. Brocklesby, J. Limpert, T. Tajima,
Nature Photonics April 2013
« The future of Acceletaor is Fiber »

図 6　開発中のファイバー束レーザーCAN のイメージ図[13]

図 7 は，京大化研で予定している 2 段階の高強度レーザー場実験を皮切りに，ELI-NP，ICAN とステップアップした場合に，真空内四光波混合法で期待される未知場の質量 m eV と光との結合 g/M GeV^{-1} に対する 95％信頼度の感度上限値を表している。太いピンクの水平線は，M がプランク質量すなわち重力と同程度の弱結合に相当する。赤の斜線は，ELI-NP による感度領域，緑の斜線は，開発中のファ

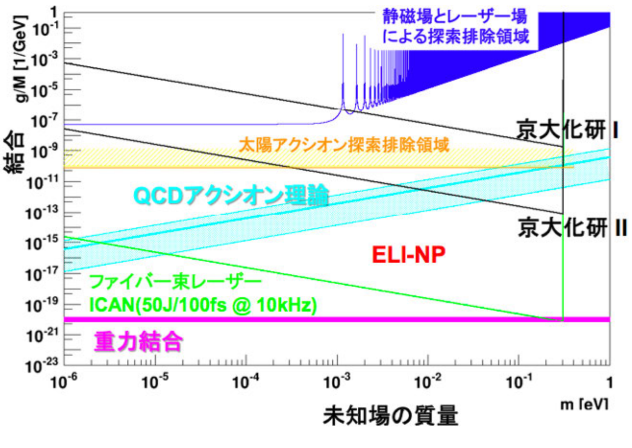

図 7　質量–結合に対する予想感度

イバー束レーザー（ICAN）が利用出来た場合，重力的弱結合の感度限界を超えられることを示す。水色の斜帯は，QCDアクシオン予言域を指している。黒斜線は上記，京大化研のステージIとIIで得られる感度を示しており，レーザーと静磁場を用いた探索の限界値 $g/M \sim 10^{-7}\,\mathrm{GeV}^{-1}$ [13]や太陽アクシオン観測による限界値 $g/M \sim 10^{-10}\,\mathrm{GeV}^{-1}$ を，比較的重い質量領域で超えられることが見込まれる。いずれも10日間連続運転の統計量に基づく到達感度を示している。

むすび

暗闇をレーザーポインターで照らすことを想像して頂きたい。もしも，暗闇にレーザービームの色のついた軌道を想像したならば，SF映画の見過ぎである。実は，暗闇に散乱体が存在しないと，光は決して光ってみえることはない。私たちが真空とみなす対象は，物のない状態，すなわち，光らない暗い状態である。私たちの提案は，要するに，暗くて一見何もないようにみえる真空を明るく照らし，もしも，わずかな光の散乱を発見できたならば，真空だと思っていた対象の中に微かな散乱体があることを見出だせるという，至極当たり前のことに過ぎない（映画スターウォーズでは，ダースベーダー周辺には暗黒場があるのだから，光線が見えていてもよいのであろう）。ただし，照らし方には色々あるということである。しかし，この極当たり前のアプローチは，革命的意義を持ち得る。ニュートンはリンゴの落下により万有引力を着想したといわれるが，これはアボガドロ数を超える質点質量の2乗程度の感度で重力が顕在化する好運な状況にあったからといえよう。一方，レーザー強度を200 kJ以上に上げられた場合，このコヒーレント場中には，平均値としてアボガドロ数以上の光学波長域の光子が存在することになる。人類がこの強度のレーザー場を制御できた場合，本研究の提案は，アボガドロ数の3乗で垣間見られる極微弱な現象に感度をもつ展望を与えられる。自然界に重力よりも弱い力が身近に存在することは，通常は想像すらしないであろう。将来，より高強度かつ高繰り返しのレーザーが開発され，もしも，重力結合よりも弱い領域で共鳴場が見つかれば，DMおよびDEのための解釈を超えた，ガリレオ・ガリレイ以来の最大級の実験的成果に到達できるかもしれない。

最後に，さらに別の視点を追加して本稿を閉じよう。量子光学では，分極に関する感受率を基準に，物質の光応答を議論する。物質内において四光波混合は3次の分極係数に起因している。この係数は電場の3乗に応答する項として理解される。それ故，強度の3乗に比例した四光波混合光量が現れるのである。ここまでの議論では，真空中の共鳴場に光子が2個結合するケースのみを考えてきたが，2個以上の光子が同時に結合するケースも一般的にはあり得る。その場合，相互作用レートはレーザー強度に鋭く依存し，比較的弱い光強度でも予想外に何かを見つけられるかもしれない。もしも，真空起因の光波混合が起こる事例が1つでも示せれば，真空量子光学の幕開けとなろう[14]。

参考文献

[1] 湯川秀樹監修，内山龍雄訳編，アインシュタイン選集 **2**, 28; A. Einstein und W. Mayer, S. B. Preuss. Akad. Wiss. , 541-557 (1933).

[2] Y. Fujii and K. Maeda, *The Scalar-Tensor Theory of Gravitation* Cambridge Univ. Press (2003).

[3] 読みやすいものとして，以下の文献を挙げておく。藤井保憲著，「基本定数の宇宙論的変動をめぐって」数理科学2013年5月号.

[4] Mark P. Hertzberg, Max Tegmark, and Frank Wilczek, Phys. Rev. D **78**, 083507 (2008).

[5] Y. Fujii and K. Homma, Prog. Theor. Phys. **126**, 531-553 (2011); K. Homma, D. Habs, T. Tajima, Appl. Phys. B **106**, 229-240 (2012); K. Homma, Prog. Theor. Exp. Phys. 04D004 (2012).

[6] Y. Fujii, Nature Phys. Sci. **234**, 5 (1971); E. Fischbach and C. Talmadge, *The search for non-Newtonian gravity*, AIP Press, Springer-Verlag, New York (1998).

[7] D. Bernard et al., Eur. Phys. J. D**10**, 141 (2000).

[8] M. Minowa et al., Phys. Lett. B**668**, 93 (2008); E. Arik et al. (CAST Collab.), Phys. Rev. Lett. **107**, 261302 (2011).

[9] K. Ehret et al. (ALPS Collab.), Phys. Lett. B **689**, 149 (2010).

[10] R. J. Glauber, Phys. Rev. **131** , 2766 (1963).

[11] Sylvie A. J. Druet and Jean-Pierre E. Taran, Prog. Quant. Electr. **7**, 1-72 (1981).

[12] http://www.eli-np.ro

[13] Gerard Mourou, Bill Brocklesby, Toshiki Tajima and Jens Limpert, Nature Photonics **7**, 258–261 (2013).

[14] T. Tajima and K. Homma, Int. J. Mod. Phys. A **27**, No. 25, 1230027 (2012).